Valorization of Natural Fibers and Municipal Solid Waste Incineration (MSWI) Bottom Ash in Building Composites

Helong Song

Bouwstenen 395

Valorization of Natural Fibers and Municipal Solid Waste Incineration (MSWI) Bottom Ash in Building Composites

Helong Song

CIP-DATA LIBRARY TECHNISCHE UNIVERSITEIT EINDHOVEN

Title: Valorization of Natural Fibers and Municipal Solid Waste Incineration (MSWI) Bottom Ash in Building Composites/ by Helong Song

ISBN: 978-90-386-6181-0

Bouwstenen 395

NUR 955

Ph.D. thesis, Eindhoven University of Technology, the Netherlands

Cover design: Helong Song

A catalogue record is available from the Eindhoven University of Technology Library

Valorization of Natural Fibers and Municipal Solid Waste Incineration (MSWI) Bottom Ash in Building Composites

PROEFSCHRIFT

ter verkrijging van de graad van doctor

aan de Technische Universiteit Eindhoven,

op gezag van de rector magnificus prof.dr.ir. S.K. Lenaerts,

voor een commissie aangewezen door het College voor Promoties,

in het openbaar te verdedigen op 31 oktober 2024 om 16:00 uur

door

Helong Song

geboren te Dengzhou, China

Dit proefschrift is goedgekeurd door de promotoren en de samenstelling van de promotiecommissie is als volgt:

Voorzitter:	Prof. dr. ir. M. Hornikx
1e Promotor:	Prof. dr. ir. H.J.H. Brouwers
2e Promotor:	Prof. dr. W. Chen
Copromotor:	Dr. F. Gauvin
Promotiecommissieleden:	Prof. dr. S. Amziane (University of Clermont Auvergne)
	Prof. dr. M. Robert (Sherbrooke University)
	Prof. dr. I. Merta (Vienna University of Technology)
	Dr.ir. R.H.J. Peerlings

Het onderzoek of ontwerp dat in dit proefschrift wordt beschreven is uitgevoerd in overeenstemming met de TU/e Gedragscode Wetenschapsbeoefening.

Preface

Time flies, and in the blink of an eye, I find myself at the end point of my PhD journey. While writing this thesis, I often sunk in thought unconsciously, many happy moments passed that seemed to have happened yesterday which unbelievably richly weaved my 4 four-year time.

First and foremost, I would like to express my deepest gratitude to my promotor, Prof. dr. ir. H.J.H. (Jos) Brouwers. You provided me with a valuable opportunity to further pursue my studies, encouraged me to improve my spoken English, and helped a lot of support in translating the research into potential real-engineering applications. Your hard work and positive spirit have greatly impressed me and inspired me to through this PhD journey. Often, your interesting pieces of advice effectively guided me in a clear and right direction. Through 4-year study, I grew a lot and got motivated for my future career and life. I would like to also express my warmest thanks to my second promoter, Prof. dr. Wei Chen. First to see you in Wuhan with Prof. Brouwers, thank you for your nice dinner that night. That visit was my first time in Wuhan. Your careful review of my thesis and valuable suggestions for improvement were greatly appreciated.

Secondly, I truly and warmly appreciate my daily supervisor Dr. Florent Gauvin. You always try your best to provide me with endless support and advice from my tough starting to final stage. For example, when I struggled with the experimental design and reviewer comments replies, you always gave me insightful and useful suggestions. When I was in trouble and having a confused mind, you could understand me and provide me useful suggestions from your point and experiences such as English-speaking improvement. It is always a pleasure to work with you, like a friend.

I would also like to thank the committee members, Prof. dr. ir. M. Hornikx, Prof. dr. S. Amziane, Prof. dr. M. Robert, Prof. dr. I. Merta, and Dr. R.H.J. Peerlings for the invitation acceptance to be members of my PhD committee and their constructive comments for the improvement of my thesis quality.

Dr. Katrin Schollbach is a very nice daily supervisor in our group. I enjoy talking with you, very thanks for helping me receive bottom ash for my research and for teaching me excellent

quantitative XRD lessons. Prof. dr. Qingliang Yu is a nice and knowledgeable daily supervisor. Although we did not communicate much, I believe that there will be more opportunities in the future. Prof. dr. Sieger van der Laan is also kind and knowledgeable. Thank you very much for pointing out my true problem in English pronunciation and giving some useful improvement suggestions. Do you remember we drank a lot with you, Prof. Brouwers, and the other two professors in the bar one evening at the 2023 Wuhan conference? To tell you the truth, all of you have a high tolerance for alcohol and seemed perfectly normal, while I was getting tipsy. Happy memory haha.

Certainly, I deeply appreciate our technicians Anneke Delsing and Harrie Smulders, who gave me a lot of support in the lab. It was not aggregate to say without your help and support, the experiments in my thesis could not have been presented.

More importantly, I sincerely appreciate our building materials group colleagues. Through 4-year Ph.D. journey, thank you very much for together with you: Anna, Hoss, Yuxuan, Shaohua, Winne, Kinga, Tao, Jaward, Xuan, Yan, Daoru, Yanjie, Zhihan, Felix, Ricardo, Iris, Charles, Naomi, Zixing, Jia, Chuen Hon, Marina, Samuel, Samantha, Leila, Beatrice, Jinyang, Yanshuo, Shashank, Ceren, Jiale, Quan, and newcomer Yilu. I wish you all the best and brightest future and that you achieve your dreams. Furthermore, I sincerely give my thanks to my master's student Theun Luinenburg for your hard work in doing experiments and writing the report.

Of utmost significance, I am grateful to my family (my father Yunji Song, my mother Xiaoli Zhou, and my brother Hewen Song) for their unconditional support, care, and endless love, especially my parents. You are great parents, who raised me and supported me all the time. Sincerely thank my parents again! I must also appreciate my wife Xiao Wu, who always stood by me patiently, sent me my favorite food, and encouraged me through the tough and stressful stage of my PhD journey, despite the thousands of kilometers between us.

山高路远，江湖再见！

Written by Helong Song

Eindhoven, February 2024 (Lunar Chinese New Year)

Summary

Nowadays, driven by the global imperative for sustainability, the construction sector has shifted its attention towards developing green, eco-friendly, and valorized building materials. Facing the barriers encountered in the development of sustainable building materials, this thesis focuses on the technology solutions in two key areas: challenges associated with utilizing natural fibers in sustainable building composites, and the development of an eco-friendly solution for recycling waste residue-Municipal Solid Waste Incineration Bottom Ash (MSWI BA)-in practical engineering applications.

In the **first section**, hemp fiber-reinforced cement composites (HFRCCs) are studied. Compared to traditional cement-based materials, HFRCCs offer excellent properties, e.g., higher flexural strength, lower cost, and carbon footprint. The performances of reinforced cementitious composites are closely related to the physicochemical properties of hemp fibers. Among these properties, the swelling-shrinking behavior and alkali degradation of hemp fibers contribute to a decline in mechanical properties. To address these challenges, fiber modification treatment is necessary. First, alkyl ketene dimer as a low-cost hydrophobic agent is proposed to modify the surface of hemp fibers to reduce swelling-shrinking behavior associated with its hydrophilic nature (**Chapter 2**). This modification effectively maintains the strength properties of HFRCCs by avoiding the swelling-shrinking behavior of embedded fibers. Then, to mitigate the alkali degradation of embedded hemp fibers and understand the degradation process, zirconia is synthesized to coat the fiber surface and to increase the alkali resistance from the cement matrix (**Chapter 3**). The study thoroughly investigates the evolution of cement hydration products on the fiber surface, the compatibility between cement and fibers, and strength performance under accelerated aging conditions, demonstrating the effectiveness of zirconia modification in mitigating fiber degradation and maintaining high-strength properties. Additionally, natural fiber can be manufactured into composites without a cement binder (known as bio-based composites) for application in building thermal insulation. These bio-based insulation composites are susceptible to moisture absorption and mould growth, thus shortening their product-service cycles. To enhance their durability, the abovementioned AKD is utilized to modify the bio-based composites (**Chapter 4**). This enables improved

hygrothermal performances and resistance to mould growth, as evidenced by experimental and simulation results.

The **second section** moves towards the recycling potential of solid waste as sustainable building materials, specifically addressing bottom ash, a primary by-product of municipal waste incineration plants. Despite its abundance, MSWI BA has not yet been practically utilized in cementitious composites, due to its low strength and contaminant leaching. These issues arise from the high metallic alumina content of MSWI BA, which reacts under an alkaline matrix, leading to strength reduction and readily contaminant leaching. To address the above issues, a simple, eco-friendly, and practical strategy is proposed for solidifying cementitious composites containing MSWI BA which are applied to cementitious binders (**Chapter 5**), manufactured lightweight aggregates (**Chapter 6**), and natural sand alternatives in mortars (**Chapter 7**). Taking into account the porous microstructure of MSWI BA under an alkali cement matrix, natural fibers are introduced into the MSWI BA-based composites. This incorporation significantly reduces the pore amount/volume of the composites and enhances mechanical strength. By applying the leaching test technique, it is observed that contaminant ions such as some heavy metal ions, sulfate, and chloride anions are effectively immobilized due to fiber capillary absorption. Finally, both environmental impact and economic assessment of the resulting composites are quantified to evaluate the feasibility of this strategy.

Contents

CHAPTER 1

1. Introduction

1.1 Background and motivation

As urbanization evolves and the population grows worldwide, the demand for building materials is increasing [1]. This demand manifests in two aspects: the refurbishment of public infrastructure, such as roads and buildings in developed nations, and the construction of new infrastructure and residential units in developing countries like China. Among these building materials, cement-based composites play an important role in infrastructure developments due to their excellent compressive strength, low cost, and long service life. However, cement-based composites face both technological and environmental challenges. Technologically, they suffer from low tensile strength, limited cracking resistance, and insufficient fracture toughness. Traditionally, these weaknesses can be addressed by the incorporation of uniformly distributed or randomly oriented short fibers [2]. Commonly used fibers are made from materials such as steel, glass, polypropylene or other polymers, and they can substantially improve the fracture toughness of the resulting composite. Despite their benefits, these fibers also have disadvantages, such as high costs and carbon footprint. Environmentally, the production of cement-based composites is associated with CO_2 emissions and the depletion of mineral resources. Currently, the global cement production has reached about 4.1 billion tonnes, with projections indicating an increase to 8.2 billion tonnes by 2030 [3, 4]. During cement manufacturing, the decomposition of limestone and the combustion of fuel contribute to the total CO_2 emissions. According to the Global Carbon Atlas, the cement sector, as the second-largest industrial source of CO_2, emitted about 1605 million metric tons in 2022 [5]. Thus, the cement industry faces the challenge of reducing CO_2 emissions to meet the targets set by the

Paris Agreement in 2015 [6]. Moreover, natural mineral resources (e.g., limestone, clay, and river sand) are facing shortage due to the rapid and massive consumption of raw building materials, leading to ecological deterioration such as increased soil erosion, flooding, and loss of biodiversity.

In order to address these challenges, two approaches are selected in this work. One approach is using renewable natural fibers derived from agricultural waste streams as reinforcement for deficiencies in the tension behavior of traditional cement composites [7]. Additionally, loose fiber composites offer potential applications in specific building sectors, particularly thermal insulation.

Another alternative involves replacing a significant portion of cement or aggregate materials like natural (river) sands in cementitious composites with various solid wastes, including silica fume [8], fly ash [9], and ground granulated blast furnace slag [10], which have been markedly utilized. Further exploring the feasibility of incorporating additional types of solid waste streams into cementitious materials is necessary [11]. Expanding the application fields of solid waste, such as sustainable lightweight aggregate production, is also a meaningful strategy for the cement sector from both environmental and economic perspectives [12].

In conclusion, the objective of this thesis is divided into two main sections: (1) utilizing natural fibers in sustainable building composites and (2) recycling solid wastes into sustainable building composites.

1.1.1 Utilizing natural fibers in sustainable building composites

Hemp fiber-reinforced cement composites (HFRCCs)

Natural (plant) fibers, as shown in **Fig. 1.1**, have been considered as potential alternatives to conventional synthetic fibers for reinforcing structural cement-based composite due to their significantly lower cost, ready availability, and being renewable [7, 13-16]. In countries where various natural fibers are abundantly available, it is economically sensible to develop technologies that utilize these fibers as reinforcement in cement composites for housing and other construction applications. Due to their excellent mechanical properties, natural fiber-reinforced cement composites (NFRCCs) represent a new and distinct category of building

materials with performance comparable to conventional concrete composites reinforced with synthetic fibers.

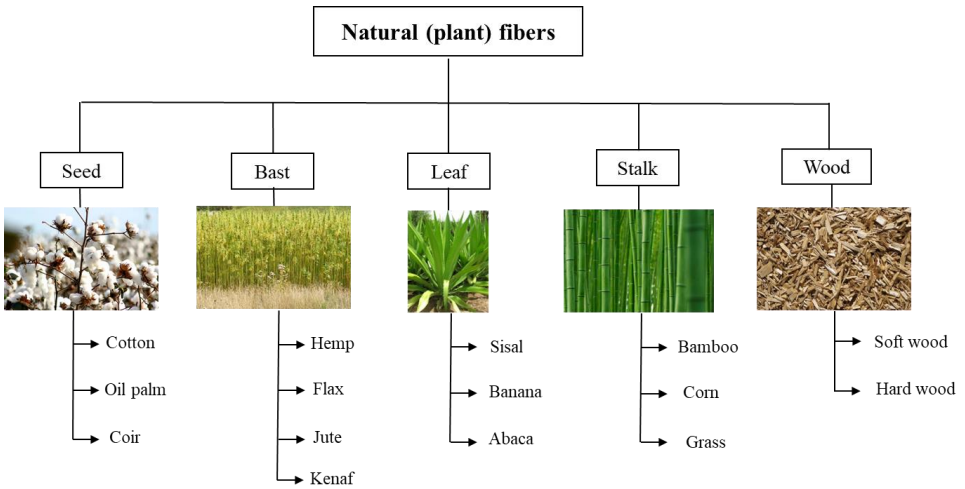

Fig. 1.1 Classification of natural (plant) fibers, based on reference [17].

The ongoing development of NFRCCs has been named "tomorrow's growth product" in the construction industry [18]. Among these composites, utilizing hemp fibers as reinforcement in cement composites has recently gained considerable attention in recent years. This is owing to the exceptional mechanical strength of hemp fibers and their worldwide availability due to the strong adaptability of hemp plants to diverse environmental conditions [19, 20].

However, the practical application of NFRCCs, including Hemp Fiber-Reinforced Cement Composites (HFRCCs), is hindered by two primary technical barriers. Firstly, organic natural fibers possess inherent hydrophilic properties that affect the interfacial bonding of fiber-cement composites [21]. Specifically, natural (plant) fibers are primarily composed of cellulose, hemicellulose, lignin, and pectin [22, 23]. Cellulose, hemicellulose, and lignin contain different amounts of hydroxyl groups available that interact with adsorbed water molecules, causing the cellulose fibers to swell and generate microcracks in the matrix [24-26]. Over time, as free water of swollen fibers is absorbed excessively via capillarity and transport of microcracks in the matrix, they start shrinking, eventually leading to debonding between fiber and matrix [26]. This process, summarised in **Fig. 1.2**, weakens the interface bonding and reduces the mechanical strength of the resulting composites [25].

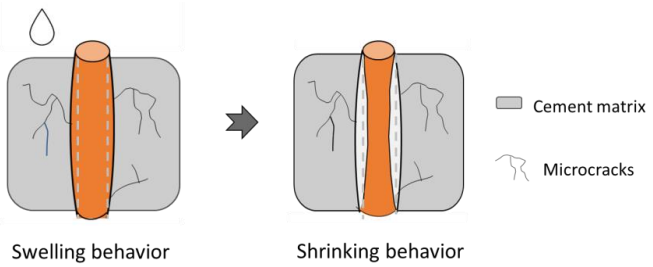

Fig. 1.2 The swelling-shrinking behavior of hemp fibers within cement matrix, based on reference [26].

Secondly, natural (plant) fibers are readily attacked and degraded when exposed to the alkaline cementitious matrix [27, 28]. The structure and components of the fibers primarily influence the degradation process. According to reported literature [29], Wei and Meyer describe the degradation process of natural fiber embedded in the cement-based matrix in four steps, as shown in **Fig. 1.3**: (1) degradation of lignin and partial degradation of hemicellulose in the primary wall; (2) complete degradation of hemicellulose in the primary wall; (3) disintegration into microfibrils due to the loss of adhesive hemicellulose in the secondary wall; and (4) broken into fine microfibrils, until to the complete degradation of the fibers. The degradation results in poor mechanical performance and durability of NFRCCs (including HFRCCs).

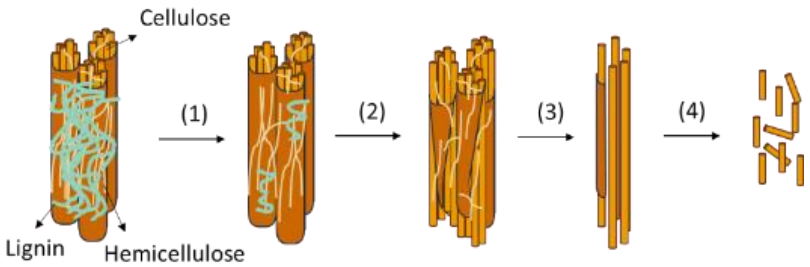

Fig. 1.3 Schematic diagram of the degradation mechanism of natural fibers within an alkaline cement matrix [29].

Accordingly, addressing these barriers requires altering the surface properties of fibers through modification treatments.

Bio-based insulation composites

Considerable attention has recently been directed towards the application of bio-based composites for thermal insulation components in building assemblies. This interest is due to their environmental friendliness, cost-effectiveness, and thermal insulation capacity comparable to traditional materials. Nevertheless, practical applications remain limited primarily due to concerns regarding the durability of bio-based composites under harsh weather conditions. The main reason is that mould grows easily on bio-based composites, influenced by factors such as the fiber type used and their high moisture absorption properties, consequently shortening their lifespan. As highlighted in the study of Koh et al [30], the rapid and extensive mould growth on mycelium-based composites is experimentally observed over a short time, attributed to their highly hydrophilic nature. This mould growth adversely affects both their thermal insulation capacity and durability. Thus, before widespread practical application in the field, the durability aspect should be thoroughly enhanced through fiber modification, to ensure the prolonged lifespan of thermal insulation building components.

1.1.2 Recycling solid wastes (MSWI BA) into sustainable building composites

Bottom ash (BA) is the largest by-product generated after the complete incineration of municipal solid waste [31]. One scenario illustrating the generation process of incinerator bottom ash is depicted in Fig. 1.4. Over the past few decades, the management of municipal solid waste incineration residue (bottom ash) has become a pressing concern due to the rapid expansion of waste-to-energy incineration projects. In the United States alone, approximately 9 million tons of MSWI ashes (mostly MSWI bottom ash) were generated in 2017 [32]. Similarly, in Europe, municipal solid waste incineration plants produce about 20 million tons of bottom ash [33]. In China, more than 13 million tons of MSWI BA are generated annually [34]. Thus, the effective utilization of MSWI BA has driven much research interest from academia and industry due to its widespread availability and high quantity [35].

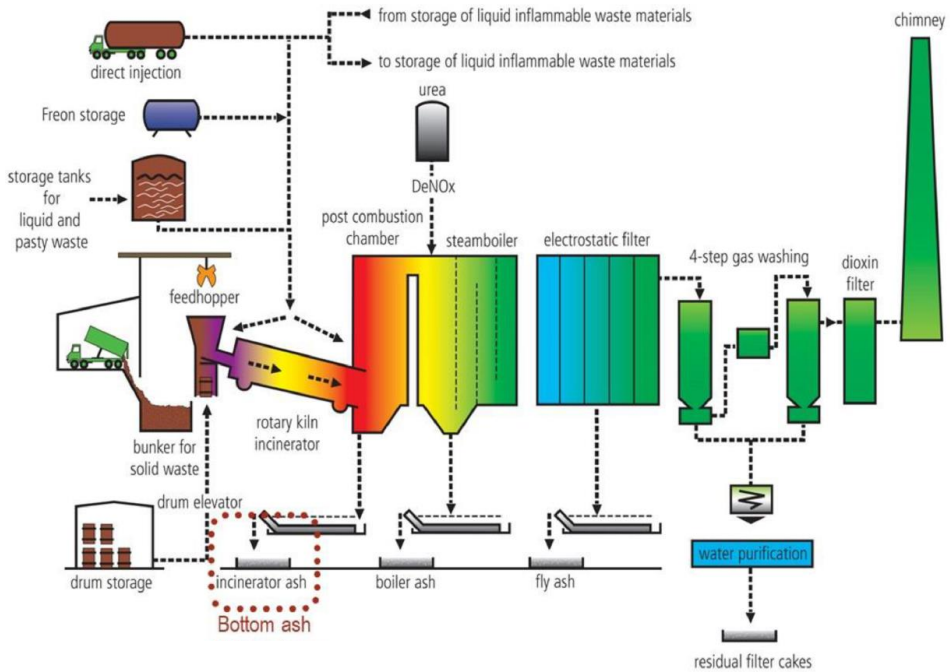

Fig. 1.4 Schematic representation of the bottom ash generation process in a grate incinerator [36].

From the perspective of its physicochemical properties, MSWI BA can typically be used as a building material. Regarding physical properties, the particle size distribution of the main fraction of MSWI BA (60-90%) falls within the typical range of sand and gravel, between 20 μm and 10 mm [37]. Engineering properties tests have also demonstrated that MSWI BA exhibits properties similar to those of natural aggregates. Therefore, MSWI BA is well-suited for replacing conventional aggregate [38, 39]. Regarding chemical components, the element composition of MSWI BA is generally consistent, although variations in concentrations among areas [37]. Common elements found in MSWI BA include Si, Al, Fe, Mg, Ca, K, Na, and Cl, mainly existing in their respective oxide. These elements are present within relatively predictable ranges as, SiO_2>CaO>Fe_2O_3~Al_2O_3~Na_2O>MgO~K_2O. Besides, MSWI BA contains some soluble salts, heavy metals, and organic compounds. Due to its chemical composition being similar to cement and exhibiting a certain pozzolanic reaction [11], MSWI BA has great potential and feasibility for recycling as a cementitious material.

Despite this, the effective utilization rate of MSWI BA in cement-based materials remains insufficient [40]. Primarily, MSWI BA generally contains a higher content of metallic

aluminum compared to common cementitious materials, triggering the aluminum reaction (also known as swelling) within the alkali cement matrix. This reaction releases hydrogen gas and results in the formation of porous structures, consequently decreasing the compressive strength of resulting cementitious products [36]. Current technologies for removing aluminum from MSWI BA are laborious and high-cost, thereby weakening the competitive advantages within the market. Additionally, MSWI BA contains a substantial quality of hazardous substances, including various heavy metal ions, sulfate, and chloride anions [41, 42]. These containments severely hinder its practical application rate in cement-based materials [43]. Hence, the aforementioned barriers need to be addressed.

1.2 Scope and objectives

This thesis aims to develop high-performance sustainable building materials for the future construction sector. The research concept of this work can be generally divided into two topics.

1.2.1 Durability of natural fiber-reinforced composites

Durability of hemp fiber-reinforced cement composites (HFRCCs)

Both poor interface bonding and readily alkaline degradation of fibers lead to poor durability of HFRCCs, which limits their application in the building and construction industry. To overcome the first issue, alkyl ketene dimer (AKD) is used to treat fibers, enhancing their hydrophobicity and improving interface properties with cement-based materials. The mechanical properties of the treated fibers on reinforcing cement-based materials are investigated. Additionally, to mitigate hemp fiber alkaline degradation, the zirconia coating modification of the fibers is adapted drawing from the successful application of zirconia on glass fibers. The effect of zirconia modification on the durability of HFRCCs is examined upon accelerated aging conditions.

Durability of bio-based insulation composites

Since bio-based composites require good resistance to mould growth to ensure their durability as thermal insulation components, specific treatment of bio-based composites is needed. Considering the mould growth caused by inherent moisture absorption, AKD hydrophobic treatment is performed on bio-based composites (mycelium composites and grass composites, here). Specifically, the impact of AKD hydrophobic modification on the hygrothermal

properties and its subsequent effect on mould growth of bio-based composites are investigated. Furthermore, through simulating exposure to real weather conditions in various regions over ten years, the potential mould growth risk of the modified bio-based composites is assessed. This evaluation aims to determine the durability of these materials when applied as thermal insulation and their feasibility for use in different geographic areas.

1.2.2 Recycling MSWI BA into building composites

Currently, implementing MSWI BA as new building materials is necessary for the sustainable development of the building sector. The characteristics of MSWI BA, as mentioned in the above section 1.1.2, indicate its potential to be applied as a building material substitute. In this context, MSWI BA after milling is used as supplementary cementitious materials and manufactured lightweight aggregates through the cold-bonded technique, respectively. Also, MSWI BA is directly employed to replace natural silica sand. However, whether milled or unmilled, the simple substitution of MSWI BA for building materials can result in the generation of inner porous structures and the leaching of contaminants. To address these concerns, natural (plant) fibers, with the advantages of high stiffness and special mico-scale hollow lumen structure, are proposed as both pore fillers and hazardous substance absorbents when MSWI BA is used as above three building material substitutes i.e. cementitious materials, cold-bonded lightweight aggregates, and sand. The mechanical properties of the resulting different composites are comprehensively investigated, alongside an evaluation of their leaching risk. Finally, the environmental and economic effects of fiber incorporation on cement-based composites containing MSWI BA are evaluated through life cycle assessment simulation.

1.3 Outline of the thesis

The experimental framework of this thesis is schematically shown in **Fig. 1.5**. The content of each chapter is briefly introduced as follows:

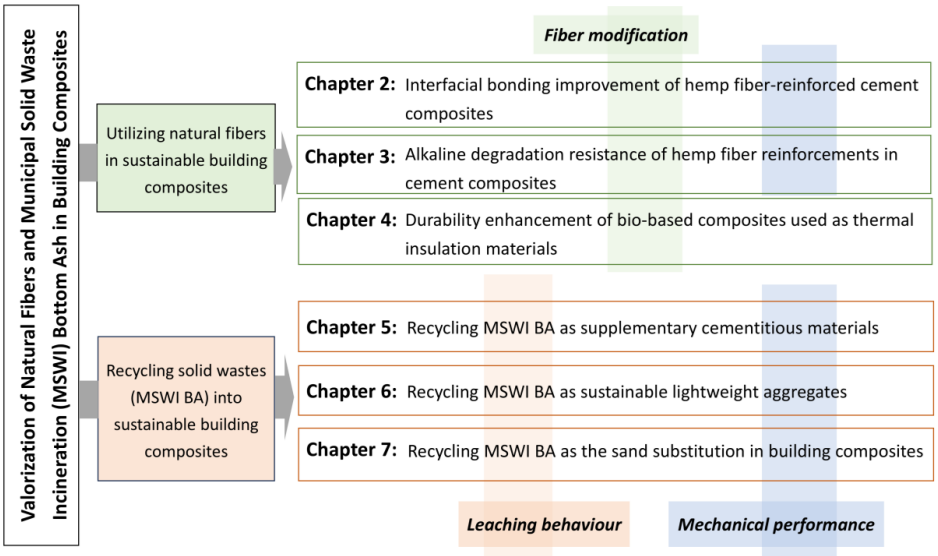

Fig. 1.5 Outline of the thesis.

Chapter 2 introduces a cost-effective hydrophobic agent, alkyl ketene dimer (AKD), to modify hemp fibers for interface property improvement of reinforced cement composites. The hydrophobic effect of AKD grafting modification on hemp fibers is identified and assessed. The interface property between the fibers and the matrix is revealed by characterizing microstructural properties, cross-compatibility index calculation, and mechanical strength.

Chapter 3 describes the fiber surface coating with zirconia (ZrO_2) to resist the fiber degradation within the cementitious matrix. The durability of the resulting composites is evaluated through mechanical strength tests under different curing times and wetting-drying cycles. The thermal stability of embedded fibers and the evolution of cement hydration products on the fiber surface are also discussed.

Chapter 4 investigates the effect of AKD hydrophobic modification on the durability of both grass composites and mycelium composites, making them suitable to be applied as thermal insulation in buildings. Their physical properties, thermal conductivity, and mould growth evaluation before and after the modification are discussed. Furthermore, the potential mould growth risk over ten years is evaluated under different real weather conditions using the hygrothermal simulation software (WUFI) with the bio-function.

Chapter 5 presents the engineering application of incorporated natural fibers, such as sisal fibers and oil palm fibers, into MSWI BA (milled) blended cement binder. The compressive strength of the resulting blended binders is evaluated, and the microstructure properties, including pore distribution, are priority studied. The effect of natural fiber incorporation on the leaching immobilization of contaminant ions is also assessed.

Chapter 6 investigates the effect of sisal fiber incorporation on the mechanical performance and sustainability of cold-bonded lightweight aggregates with a high fraction of milled MSWI BA. The mechanical strength of individual pellets with and without fiber incorporation is statistically analyzed and compared. The hydration kinetics of different design systems are examined using isothermal calorimetry, and the leaching behaviors of heavy metal ions, chloride, and sulfate are evaluated.

Chapter 7 aims to improve the substitution rate of natural sand with MSWI BA in mortar composites by incorporating sisal fibers. The correlation between compressive strength, Young's modulus, and ultrasonic pulse velocity (UPV) of the resulting composites is investigated. Hirsch's theoretical model is employed to predict the tensile modulus and strength, comparing these predictions with practical values obtained by the three-point bending test. Finally, the microstructure properties of the mortar composites are thoroughly analyzed.

Chapter 8 concludes the presented work and proposes some recommendations for future study.

CHAPTER 2

2. Improving the interface property and mechanical performances of the cementitious composites by low-cost alkyl ketene dimer-modified fibers

Based on this paper:

H. Song, T. Liu, F. Gauvin, and H.J.H. Brouwers. Improving the interface compatibility and mechanical performances of the cementitious composites by low-cost alkyl ketene dimer modified fibers. Construction and Building Materials 395, 132186 (2023).

2.1 Introduction

In recent years, natural fiber-reinforced cement composites (NFRCCs) have attracted significant attention from researchers in both academia and industry due to their excellent flexural strength, low cost, and low carbon footprint. Among these fiber-reinforced cement composites, hemp fiber-reinforced cement composites (HFRCCs) are a good candidate taking into account the relatively good mechanical strength of hemp fibers and their worldwide availability owing to the excellent suitability of hemp plants in soil and environmental conditions [19, 44]. Li et al. [45] concluded that incorporating hemp fibers with 20 mm length significantly improved the mechanical strength and toughness index with only a 0.36 % (by weight) fiber addition. Comak et al. [46] reported that the inclusion of hemp fibers in mortars increased flexural strength and found that 12 mm fiber length and 2–3% of hemp fiber addition positively impacted flexural strength and splitting tensile strength. Ruano et al. [47] stated that

adding hemp fibers could increase the toughness of cementitious composites, characterized by pull-out testing. However, the hydrophilic nature of HF makes it sensitive to moisture variations, leading to swelling-shrinking behavior [48, 49]. Ultimately, this behavior would weaken the interfacial bonding, thus negatively affecting the mechanical properties of HFRCCs.

Surface modification of hemp fibers becomes necessary to improve the interfacial bonding between the fiber and the matrix, obtaining better performance of the resulting composites [50, 51]. Sepe and Bollino [52, 53] studied the influence of chemical treatments on the mechanical behavior of epoxy matrix composite reinforced with woven hemp. Test results show that silane treatment of hemp fibers improves both tensile and flexural properties of the composites and silane treatment is more effective in preventing the failure of the composite induced by water uptake. In theory, reducing the fiber's hydrophilic nature to minimize its swelling-shrinking behavior in cementitious composites, is an effective approach to enhance the interfacial adhesion of HFRCCs. Various fiber surface treatments have been explored for reinforcing cementitious composites, including the horrification treatment [54, 55], polymer coating [56, 57], and silane treatment [58]. These treatments have demonstrated positive effects on the fiber-matrix bond and the mechanical properties of the cementitious composites. Yet, such treatment does not show long-term performance as cellulose-O-Si-O-bonds are not stable against hydrolysis [59, 60]. Especially under the alkaline condition of the cement hydration process, the chemical bond rupture between silanes and cellulose occurs readily as acids and bases are known to be powerful catalysts for the hydrolysis of siloxane bonds [61]. In addition to these technical difficulties, the cost of fiber modifying agents also has to be considered (commonly silane coupling agents, 20–50 €/kg) Therefore, it is urgent to look for a new and low-cost modifying agent to treat the fibers which can (1) bind chemically to cellulosic fibers to change the hygroscopic character of natural fibers; (2) be stable under alkaline conditions; (3) be economic.

Hydrophobic modification of natural fiber is a common treatment to resist liquid penetration in papermaking, which is called surface sizing. low-cost alkyl ketene dimer (AKD, 1–10 €/kg) is a main sizing agent resulting in enhanced water resistance [62]. Zhang et al [63] investigated the effect of bamboo flour with alkyl ketene dimer (AKD) on the polyethylene/bamboo flour composites. It was observed that AKD-modified wood-plastic composites had high water resistance, low swelling ratio, and excellent mechanical properties. Angin et al [64] analyzed the chemical and thermal properties of using AKD as a coupling agent for natural fiber and

glass fiber-reinforced poly composites. The results indicated that the crystallinity of the hybrid composites was increased by 18% compared to neat composites. Missoum et al [65] used AKD to chemically modify nano-fibrillated cellulose (NFC) and found that AKD modification can increase the mechanical property of the resulting NFC. Though most researchers are focusing on utilizing AKD for improving the properties of natural fibers, to our knowledge none of them has reported AKD-modified fiber used in cementitious composites. Furthermore, given the alkaline resistance of the embedded fiber in fiber-reinforced cement composites and its relatively low cost, AKD seems to be a promising candidate.

Thus, this work aims to investigate the grafting modification (physical immersing) of HF with AKD and its impact on the fiber-matrix interface bonding. FTIR analysis and water absorption tests were employed to characterize the grafting effect of HF. Furthermore, to better understand the impact of the modification on the overall properties of HFRCCs, the mechanical properties such as compressive strength, flexural strength, and toughness capacity, as well as the interfacial performance of the fiber-reinforced cement composites, were analyzed. This treatment will accelerate the industrial-scale practical application of HFRCCs in the construction sector and pave the way toward sustainability in the circular economy.

2.2 Experimental

2.2.1 Materials

Hemp fiber products (designated “H”) were supplied by HempFlax (The Netherlands). Before the experiments, hemp fibers were sieved, washed, and dried because many broken inner stems and fine fibers (<1 cm length) existed. In addition, the chemical compositions of hemp fibers are mainly cellulose, lignin, hemicellulose, waxes, and water-soluble substances. The detailed physical properties and chemical components of the hemp fiber are listed in **Table 2.1** and **Table 2.2**, respectively.

Table 2.1 Physical properties of hemp fibers.

Diameter (mm)	Density (g/cm^3)	Average length (mm)	Aspect ratio	Water absorption (%)	Young’s modulus (GPa)
0.25 ± 0.08	1.34	4.23	8-28	141	20.5

Table 2.2 Chemical compositions of hemp fibers (wt. %) [66].

Fiber type	Cellulose	Lignin	Hemicellulose	Pectin	Wax
Hemp fiber	70.2 - 74.4	3.7-5.7	17.9 - 22.4	0.9	0.8

The commercial alkyl ketene dimers emulsion was provided by Kemira (Finland). Commercial ordinary Portland cement (OPC) CEM I 52.5R (Specific surface area 1.34 m^2/g) was supplied by ENCI (The Netherlands). The oxide compositions, phase compositions, and particle size distribution of the OPC are shown in **Table 2.3** and **Fig. 2.1**. The standard sands with a granulometry of 0/2 were used according to EN 196-1. The particle size distribution of used sand is shown in **Fig. 2.2**.

Table 2.3 Chemical composition of OPC (wt. %).

Compounds	MgO	Al_2O_3	SiO_2	K_2O	CaO	TiO_2	Fe_2O_3	SO_3	In_2O_3	Rest
CEM I	1.48	4.25	17.32	0.5	67.62	0.4	3.26	3.03	1.32	0.82

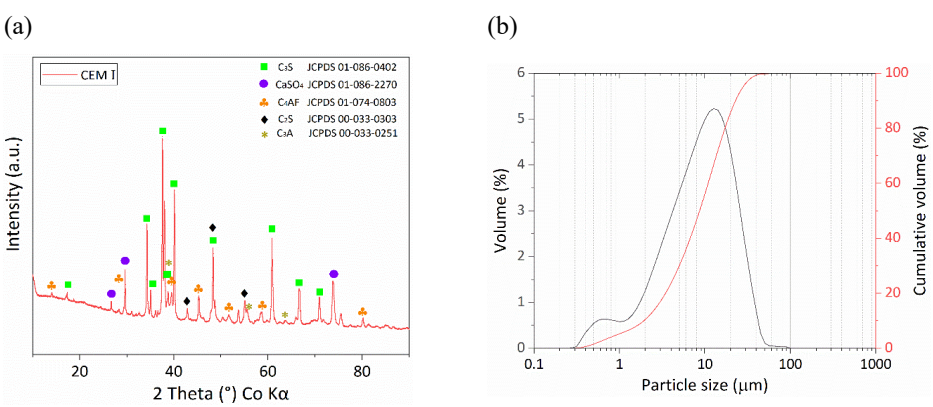

Fig. 2.1 The phase composition (a) and the particle size distribution (b) of OPC.

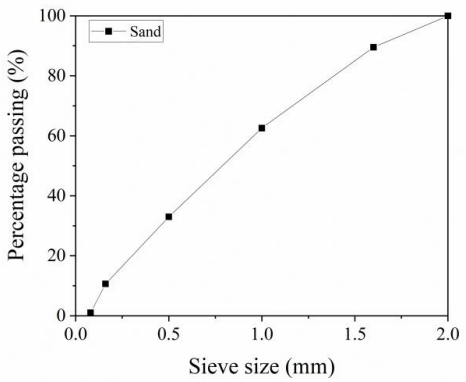

Fig. 2.2 The particle size distribution of the standard sands used.

2.2.2 Methods

Fiber treatment

To better modify hemp fiber, pre-treatments were employed on hemp fiber. Pre-treatment involves two steps: de-waxing, and alkali treatment [61]. Firstly, the wax was almost entirely taken out of the fibers (90% of 2–4 mm length, around 125 μm diameter) using ultra-pure acetone. The fibers were kept in jacketed Erlenmeyer flasks with boiling acetone for 45 min. Then, the fibers were immersed in 5 wt.% sodium hydroxide solution for 30 mins and immediately washed with distilled water. To fully neutralize the effect of NaOH, a weak acetic acid solution was applied to reach the neutral pH. Subsequently, distilled water was utilized to rinse the fibers. After that, the fibers were dried at room temperature for 48 h and then in an oven at 70 ℃ for 8 h.

The fiber modification was carried out using a similar procedure proposed by H. Zhang et al. [67]. Hemp fibers (H) and hemp fibers after pretreatment (HP) were impregnated with a 2.4% AKD emulsion for 1.5 h, and then impregnated fibers were filtered by vacuum filtration equipment. Finally, these modified fibers (HPM) were dried in the oven at 90 ℃ for 6 h.

Preparation of fiber-reinforced composites

Hemp fiber-reinforced composites with 1% (by weight relative to cement weight) of short hemp fibers (0.2 ~ 0.8 cm) were prepared from the untreated and treated fibers. Firstly, this amount of fiber addition is determined based on the optimal addition of the literature [68, 69]. Secondly,

the selection of short fibers in this study is considered: one is a lot of short fibers are wasted, not applied in the textile industry like long hemp fibers [70]; the other is to take advantage of easily random dispersion, which plays an effective role in preventing the growth of the cracks in the composites [71]. In terms of the preparation process, the fibers were first introduced in the cement and sand and mixed for 90 s in a blender (Perrier Labotest, type 32, France) to obtain a homogenous sample followed by water addition. The matrices, treatments, and weight fractions of fibers are presented in **Table 2.4**. After 2 mins, the mixture was cast into a plastic mold (40 mm × 40 mm × 160 mm size) and covered with a damp polyethylene film to avoid water evaporation. One day later, the samples were demolded and cured in a climatic chamber at 20 ± 2 ℃ and 50 ± 5% humidity.

Table 2.4 Sample codes of the different treated fiber-cement composites.

Code	Sand/cement	Water/cement	Fiber addition (wt.% of cement)	Hemp fiber surface treatment
Control	3	0.5	-	-
C-H	3	0.5	1%	Not treated
C-HP	3	0.5	1%	Pretreated only (de-waxing and alkaline treated)
C-HPM	3	0.5	1%	Pretreated and then modified with AKD emulsion

2.2.3 Characterization

Texture

The surface microphase and structure of modified fibers were analyzed using a Zeiss optical microscope combined with a scanning electron microscope mentioned below. The analyses of the fibers' surface were performed with a Camera/Detector Axiocam 305. Before testing, the fiber samples were made as flat as possible and put on dark paper.

Water absorption test (WAT)

Fiber samples were contained in a steel tea bag and then immersed in distilled water at room temperature. Weight change was recorded by balance every second by a computer program [35],

as is shown in **Fig. 2.3**. Before measurement, all tested samples were put into the oven (40 ℃, 6 hours) to balance the moisture of the fibers.

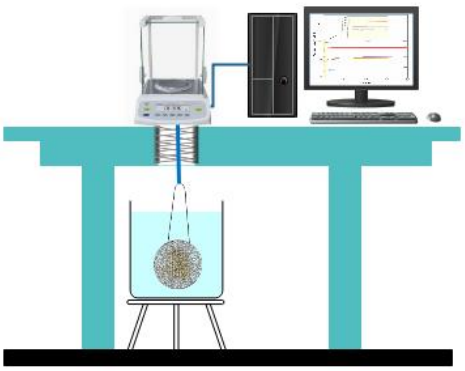

Fig. 2.3 Schematic diagram of water absorption.

Fourier transform infrared spectroscopy (FTIR)

The measurements were performed using a Perkin-Elmer spectrometer with wavenumbers ranging from 4000 to 400 cm^{-1}. A total of 4 scans were taken for each fiber sample and corresponding cement composite powder with a resolution of 1 cm^{-1}. To prepare the samples for the FTIR test, AKD-modified fibers were first extracted with acetone to remove the unreacted AKD for 24 hours. Then the unmodified and modified fibers were oven-dried at 65 °C for 48 hours. More details in some cases are described in ref [72].

Scanning electron microscope coupled with energy dispersive (SEM-EDS)

The surface topography of the fracture surfaces of untreated/treated fibers and fiber-reinforced cement composites was investigated using SEM. The micro-surface analyses were performed on specimens covered with Au by using a Thermo Fisher Phenom Pro-X microscope under an accelerating voltage of 15 kV. The chemical composition was identified using energy dispersive spectrometry (EDS) on different spots to verify the presence of hydrated cement on the surface of embedded hemp fibers. For a better representation of the elements present, each sample was chosen to measure in five different embedded fiber regions and an average of forty values was obtained.

X-ray diffraction (XRD)

The X-ray diffraction (XRD) patterns of fiber-reinforced cement mortars were carried out on ground powder using a Bruker D4 with a Co tube. The angular range was between 10° and 45° (2θ). Before milling into powder for testing, all mortars were cured at ambient temperature after 7 and 28 days. At specific curing ages, the mortar samples were crushed and then immersed in isopropanol. Afterward, the powdered samples were dried in the oven for 24 h at 60 ℃ to stop the hydration process of cement.

Mechanical strength test

The compressive strength and flexural strength were carried out according to EN 196–1 [73]. The three-point bending test was carried out using the EZ 20 Lloyd Instrument (AMETEK) testing machine by AFNOR NF-EN-993–6. All tests were performed using a consistent span of 100 mm and a deflection rate of 0.1 mm per minute. At least 5 specimens were tested in a three-point bending configuration for each composite formulation. The value of the load and bending were simultaneously recorded. As we assume that the material is homogeneous, the normal stress σ_{xx} in a rectangular beam of length l between supports is:

$$\sigma_{xx} = \frac{3}{2}\frac{Fl}{wh^2}\ , \tag{2.1}$$

in which F is the applied force, and w and h are the width and the height of the beam, respectively.

Significant differences in strength properties between the groups were evaluated using Tukey's HSD test ($P < 0.05$) in JMP Pro 11 software [74]. A new method developed by Barr et al. [75], which is based on ACI Committee Report 544.2R, was adopted to calculate the toughness index (I_t) of the composites in this work. The reason is that the traditional method of calculated toughness index could not be applied with a small percentage of fiber addition which could not provide the typical load-deflection curve. In order to supplementary evaluate the toughness capacity, the post-crack energy absorbed, calculating the area under the load-deflection curve ranging from the post-peak to the end [68]. In addition, the stiffness deriving from the slope of the linear curve represents an efficient load transfer process, associated with a good fiber–matrix interface bonding.

2.3 Results and discussion

2.3.1 Analysis of fiber modification

Fiber modification mechanism

Previous studies [61, 76] showed that the pretreatment of both sole diluted alkaline solution and a hybrid combination of acetone and alkaline solution could promote the partial removal of lignin, waxes, pectin, hemicellulose, and oils on the surface of natural fiber, and leads to more cellulose OH groups exposed on the fiber surface. It means that the extra hydroxide ions from the alkaline solution readily react with the OH groups on the cellulose chains:

$$Cell - OH + NaOH \rightarrow Cell - O^{-}Na^{+} + H_2O \quad . \tag{2.2}$$

Therefore, in the second step of modification, the pretreated procedure improves the grafting reaction between the lactone ring of AKD and free OH^{-} groups on cellulosic fibers to form a hydrophobic layer on the fiber surface attributed to a lot of alkyl groups introduced [63, 77], as presented in **Fig. 2.4**. In this study, the acetone-alkaline pretreatment and AKD modification were performed on hemp fibers. Then the mortar composites reinforced by fibers subjected to different treatments were obtained and analyzed in terms of interface bond and strength performance.

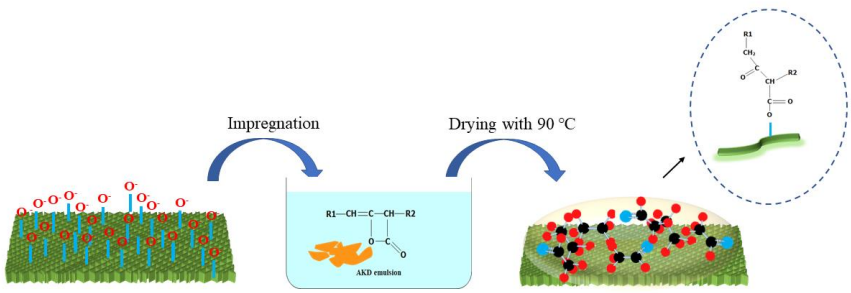

Fig. 2.4 The schematic illustration of the grafting reaction between pretreated fibers and AKD.

Microstructure of fibers with treatments

The change of the fiber surface morphology is the most direct reflection of treatments. **Fig. 2.5** shows the optical morphology of untreated/treated fibers (Zeiss) and related microstructures under SEM. There are some yellowish substances on the fiber surface presented in **Fig. 2.5a**,

which are lignin and waxy substances based on the analyses of FTIR. After pretreatment, this layer of yellow substance almost has been removed, as is presented in **Fig. 2.5b**. Meanwhile, it is observed from the corresponding SEM picture, that the surface of the fiber became rougher on account of the removal of partial lignin and other impurities [78].

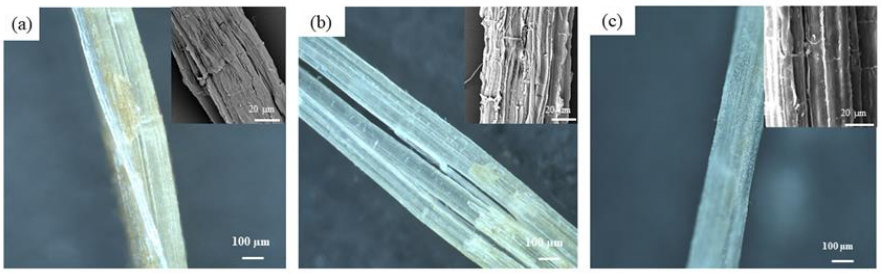

Fig. 2.5 Micro morphology and structure of fibers with different treatments (a) H, (b) HP, and (c) HPM.

For the modified fibers, a whitish waxy layer is uniquely coated on the fiber surface which was seen in **Fig. 2.5c**. The micro-level surface of fibers after impregnating has gotten a little smoother but still rather rough. These behaviors are in line with the optical measurements within the CIE Lab system and SEM observation performed by Arminger et al. [79] on the wood surface sprayed with alkyl ketene dimer dispersion.

FTIR characterization of fiber modification

The FTIR analyses reveal the AKD grafting modification on hemp fibers. **Fig. 2.6** shows the infrared spectra of untreated/treated fibers. Plant fibers are primarily composed of three main components: cellulose, lignin, and hemicellulose. In the hemp fibers (H), the peak at around 3270 cm^{-1} represents the stretches of O-H bonds from cellulose and hemicellulose; the O-H bending of absorbed moisture is at 1640 cm^{-1}. The peaks around 1026 cm^{-1} correspond to the C-O of a secondary alcohol, as well as the stretch at 2915 cm^{-1} is the C-H bond from -CH_2- of cellulose [80]. In addition, the H spectrum shows that 1160 cm^{-1} and 896 cm^{-1} represent C-O-C stretching at the β-(1→4)-glycosidic linkages in cellulose and hemicellulose [81]. After pretreatment, almost all peaks become weakened and some peaks disappear, which is likely due to the removal of impurities from fibers (e.g. lignin, certain hemicellulose, and wax) [61, 76]. For example, the peak at 1239 cm^{-1} of HP is significantly lower than that in the H. The decrease in the peak intensity represents the reduced C-O stretching of the acetyl group of lignin [82,

83]. In addition, the peak intensity at 3270 cm^{-1} weakens and even the peak at 1730 cm^{-1}, corresponding to the C=O stretching of the acetyl groups, disappears in the HP [82, 84]. These indicate the degradation of lignin and hemicellulose on the hemp fiber surface [82].

In terms of AKD-modified fibers (HPM), this curve, in general, is similar to those of the H and HP but there are still some obvious differences between them. This suggests that the modification treatment of hemp fibers just changes the chemical groups characteristic of the fibers' surface instead of their structure. The stronger intensity of the sharp peaks at around 2915 cm^{-1} and 2849 cm^{-1}, representing symmetric and asymmetric C-H stretching vibrations of -CH_2- groups, respectively [85]; the occurrence of new peaks at 1472 cm^{-1} and 720 cm^{-1} is related to C-H scissoring vibration and C-H rock mode [85, 86]. These changes indicate that the molecular structure of the HPM surface contains more than four CH_2. This is because the introduction of long-chain AKD molecular provides more alkyl groups and can give good hydrophobicity [85]. Here, it is also worth mentioning that the sharp peaks at 1721 cm^{-1} and 1845 cm^{-1} stand for the C=C double bond and the C=O double bond of the carboxyl group in the AKD lactone ring [77]. Therefore, the above analysis verified that AKD was successfully grafted on the fiber surface.

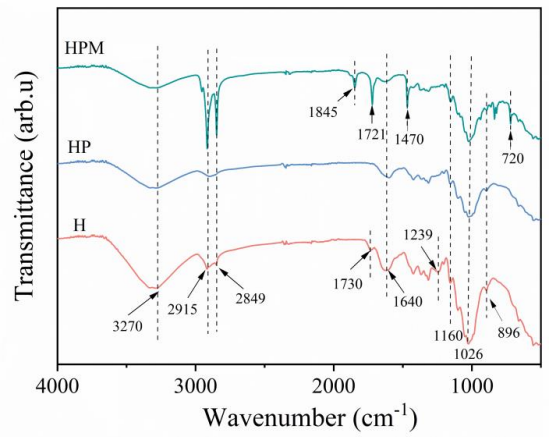

Fig. 2.6 FTIR curves of H, HP, and HPM.

Water absorption of fibers with treatments

The effect of hydrophobic modification of fibers is justified by water absorption measurement. **Fig. 2.7** shows the water absorption curves for various treated hemp fibers. In general, this result

shows that the fibers absorb water very rapidly at first, and later a saturation level was attained without any further increase. This process of absorbing water, at first, is dependent on both chemical compositions (the hydrophilic groups of the fiber surface) and physical structure (the interweaving gaps among fibers, and fiber voids) and short after mainly on chemistry compositions of fibers (the hydrophilic hydroxyl groups) until the end.

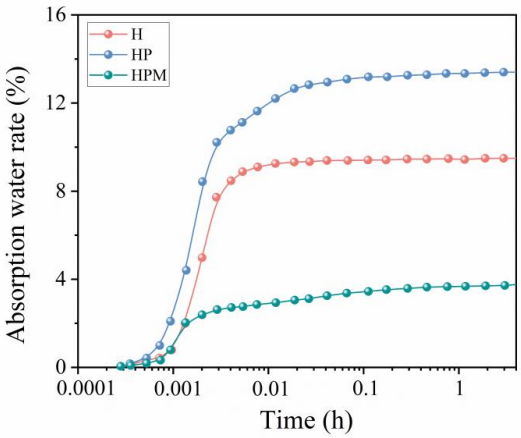

Fig. 2.7 Absorption water rate curves of fibers with different treatments.

As the treatment varies the water uptake nature of the fibers also varies. The HP has the highest water absorption rate while the HPM has the poorest water absorption ability (good hydrophobic effect). This is because the pretreated (alkaline pretreated and acetone pretreated) makes the more cellulosic hydroxyl groups exposed on the fiber surface via the removal of lignin and some impurities in the former; however, these hydrophilic groups were replaced with long-chain alkyl groups after the AKD treated in the latter. Therefore, HPM has the best water resistance. This result is consistent with previous findings in the literature [62, 77].

2.3.2 The analysis of fiber-reinforced composites

Workability

The flowability plays an important role in the workability of cement composites, which is reported in **Fig. 2.8**. It is clearly shown that fiber-reinforced mortars have relatively poor flowability (120 mm < flow value < 150 mm), compared to the reference mortar without fibers (> 160 mm). That could be related to the water absorption of the embedded fibers [87].

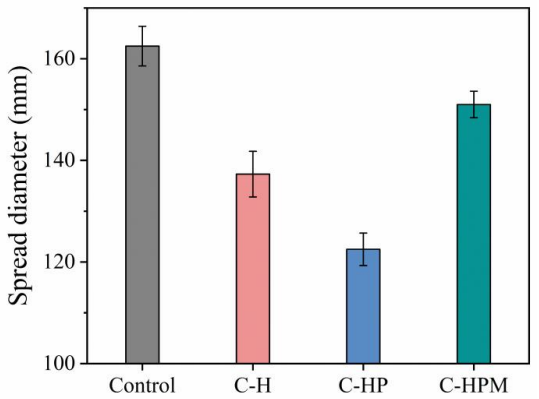

Fig. 2.8 Variation of spreading of the cement mortar reinforced with or without fibers with different treatments (see **Table 2.4**).

Meanwhile, as it can be noted the hydrophobic modification of AKD on fibers somewhat increases the workability of fiber-cement composites (C-HPM>C-H>C-HP) due to the decrease of water demand by the fibers. To some extent, this behavior further confirms the water absorption measurement of fibers.

The fiber-reinforced cement composites are then investigated in terms of interface property, reaction products, and mechanical strength.

The interfacial property analysis

To directly understand the interfacial property of hemp fiber-cement composites, it is crucial to judge the compatibility by a quantitative indicator and qualitative characterization. In this study, the cross-compatibility index (CX) method proposed by Sorin et al. [88] was employed to evaluate the compatibility between hemp fiber and cement matrix:

$$CX = \sqrt[3]{\frac{HR_{max}\, H_{3.5-24} t'_{max}}{HR'_{max} H'_{3.5-24} t_{max}}}, \tag{2.3}$$

in which HR_{max} = maximum heat rate of hemp fiber-cement composite (mW/g); HR'_{max} = maximum heat rate of neat cement paste (mW/g); $H_{3.5\text{-}24}$ = total heat (the area under heat rate curve) released by hemp fiber-cement composite in 3.5 -24 h interval (J/g); $H'_{3.5\text{-}24}$ = total heat

(the area under heat rate curve) released by neat cement paste in 3.5 - 24 h interval (J/g); t_{max} = time to reach maximum heat rate of hemp fiber-cement composite (h); t'_{max} = time to reach maximum heat rate of hemp fiber-cement composite (h).

To interpret the above equation, a typical heat hydration curve is given in **Fig. 2.9**.

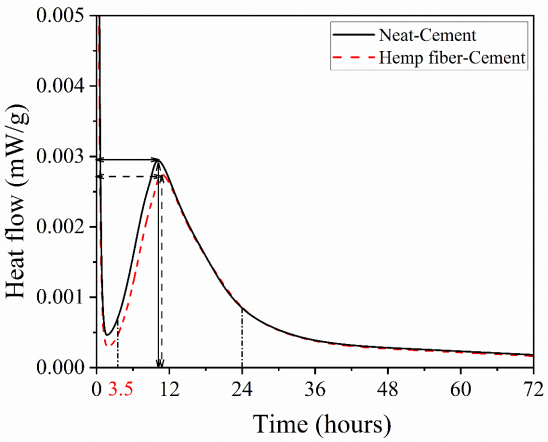

Fig. 2.9 Heat flow versus time for a typical hemp fiber-cement (dashed curve) and neat-cement paste (solid curve).

Table 2.5 presents the level of compatibility of the cement composites reinforced with different treated hemp fibers. The hemp fiber-reinforced cement composites exhibit high compatibility index values (above 95.0%), indicating good compatibility between hemp fibers and cement matrix. This could be attributed to the lower content of organic extractives in hemp fibers, resulting in a less inhibitory degree of cement hydration when compared to other plant fibers [89, 90]. Among hemp fiber-reinforced cement composites, C-HP and C-HPM have better compatibility levels. This is associated with the fibers' pretreatment which removes those cement-hardening inhibitory components (some sugars and extractives) from the hemp fiber surface. Further, C-HPM has the best compatibility level due to the presence of AKD grafted on the fiber surface. This modification layer hinders the capture of Ca^{2+} present in the cement solution by cellulose fibers, benefiting the nucleation of $Ca(OH)_2$ and C-S-H gel and then mitigating the retarding degree of cement hydration [91]. Therefore, the main conclusion is that AKD modification has a positive influence on the compatibility between hemp fiber and cement matrix.

Table 2.5 The cross-compatibility indexes of hemp fiber-reinforced cement composites.

	Hemp fiber-reinforced cement composites		
	C-H	C-HP	C-HPM
Cross compatibility indexes (CX)	95.9%	97.3%	99.5%

Apart from that, the microstructure and appearance of fiber-cement composites are important for characterizing the interface link situation between the fiber and cement matrix. Results are shown in **Fig. 2.10**, different interactions occur between hemp fibers and cement matrices. In all cases, C-HPM (**Fig. 2.10c**) reveals the tightest gaps between the fiber and the cement matrix indicating the strongest interfacial adhesion. This behavior is in accordance with the compatibility index calculation mentioned above. However, as for the C-H (**Fig. 2.10a**) and C-HP (**Fig. 2.10b**), the gaps between the fibers and the cement matrix are visibly wider. This is due to the shrinking behavior after swelling of embedded H and HP, which leads to the debonding of the fiber-matrix interface. Especially for C-HP, the degree caused by the shrinking of fiber cells after moisture loss is very significant on account of the higher water absorption rate after the pretreatment leading to increased swelling. On the other hand, AKD modification can reduce this swelling-shrinking behavior of the fiber by improving the hydrophobic properties. Thus, C-HPM has the best interface bonding.

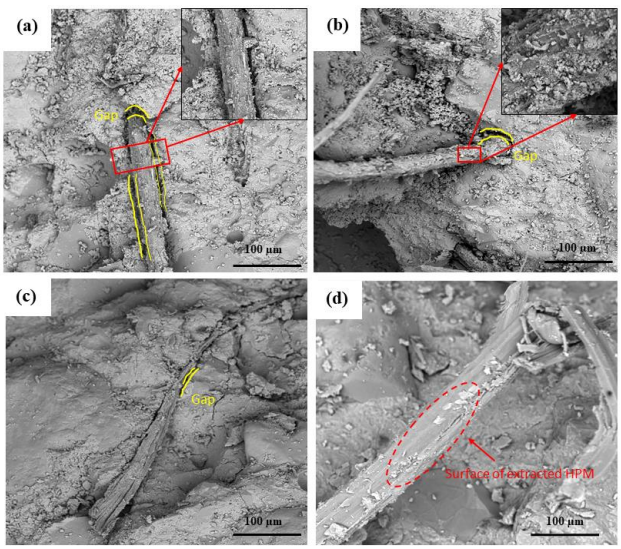

Fig. 2.10 Interface area of fiber-reinforced cement composites (a) C-H and (b) C-HP, applied zoom indicates the location of cement hydration products, and (c) C-HPM (d) Extracted HPM.

Regarding the surface appearance of the embedded fibers, **Fig. 2.10d** shows that the HP surface has the largest amount of attached cement hydration products, whereas the surface of HPM has a few hydration products. The amount of hydration products on the H surface is between those of HP and HPM. Therefore, the amount of hydration products on the different fiber surfaces is closely associated with the physiochemical properties of their surfaces. The cement hydration products deposited on the fiber surface are a process of heterogeneous nucleation and growth. The extent of this process depends on the fiber substrate properties. To be more specific, the low free energy (both the wetting surface and the rough surface) of the fiber substrate facilitates the heterogeneous nucleation and growth of the cement hydration products [92, 93]. Among the three fibers, HP with the roughest and most wettable surface has the most hydration products. Compared with H and HP, HPM has the most hydrophobic and relatively smooth surface; thereby, the cement hydration products are rarely deposited on the surface of HPM. The chemical components of hydration products on the fiber surfaces will be discussed below.

Analysis of the reaction products

To further clearly clarify the interface reaction products, the surface products of the embedded fibers were analyzed through EDS. Based on the elements of cement hydration products like C-S(A)-H, portlandite (CH), and ettringite, the atomic ratios of several elements with respect to calcium are investigated and shown in **Fig. 2.11**.

As seen in **Fig. 2.11a**, the Al/Si molar ratio (0.11) of the hydration products on the HPM surface is lower than those of H (0.21) and HP (0.16), respectively, indicating that less amount of SiO_4 tetrahedrons was replaced with AlO_4^- tetrahedrons in the amorphous C-S(A)-H deposited on the HPM surface. It was well known that Si-O-Si bonds were stronger than Si-O-Al bonds in terms of the C-S(A)-H [94]. This also assistant confirms the strong interface bond in the C-HPM. Besides, most data points of HP are concentrated near zero point and on the X-axis (Si/Ca), which means more portlandite was precipitated on the surface of HP, which agrees with the literature [95-97]. In **Fig. 2.11b**, the embedded-H data is along the theoretical composition line representing the mix of CH and ettringite, which is average higher than the data distribution of the embedded-HPM. In detail, the range of the S/Ca ratio is similar between both but in terms of the Al/Ca ratio, the data range of the embedded H is higher than that of the embedded HPM. This suggests the composite of CH and ettringite, perhaps more ettringites, on the embedded HPM surface. As regards the alkali content ratio in **Fig. 2.11c**, it can be seen that the data plots

of the K+Na/Ca ratio of the embedded-HPM (above approx. 0.40) exceed those of the embedded-H (0.18-0.38) and the embedded-HP (0.06-0.21). This reason for this phenomenon most likely lies in the fact that the hydrophobic characteristic of the HPM surface hinders the alkali ions from entering into the fiber's inner lumen by reducing the swelling capacity, hence more alkali ions stay on the fiber surface. Another potential reason is that the increased formation of the C-S-H phase (as discussed earlier) on the HPM surface enhances the adsorption of alkalis such as K^+ and Na^+, thereby reducing their leaching [98]. The surface of the embedded H has the second-highest K+Na/Ca ratio maybe since the extractives (i.e., pectin and wax) of the H surface ascribed to the untreated also have a certain hydrophobicity, playing a similar behavior to the HPM. On the other hand, the embedded HP facilitates the entry of alkali ions into the fiber structure due to its high-water absorption capacity, resulting in less amount of these ions attached to the fiber surface.

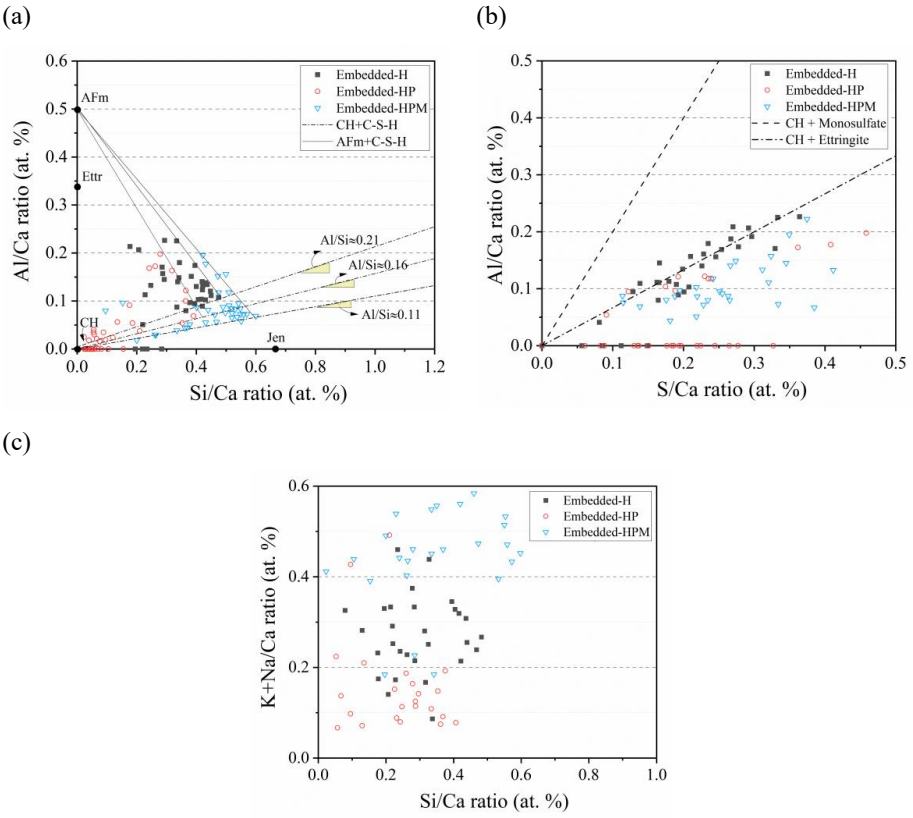

Fig. 2.11 Al/Ca versus Si/Ca (a), Al/Ca versus S/Ca (b), and K+Na/Ca (c) atomic ratios of hydration products deposited on the surface of the embedded fiber.

To further investigate the impact of different fiber treatments on the hydration products of cement matrices, XRD and FTIR analyses were also carried out in this study. **Fig. 2.12** displays the phase compositions of different samples after 7 and 28 days of curing. In general, all peaks still occur at the same positions irrespective of fiber treatments and the curing time (**Fig. 2.12a** and **b**). That means, fiber treatments in this study cannot cause the formation of new cement hydration products, which is mainly because the fiber components and chemistry AKD molecular are not involved with the cement hydration reactions. In addition, the intensity of two peaks, representing portlandite and calcite or C-S-H, become stronger due to the cement hydration. It is also interesting to note that no distinct peaks for the embedded fibers were identified. This could be due to the small percentage of fibers compared to cementitious materials.

(a)

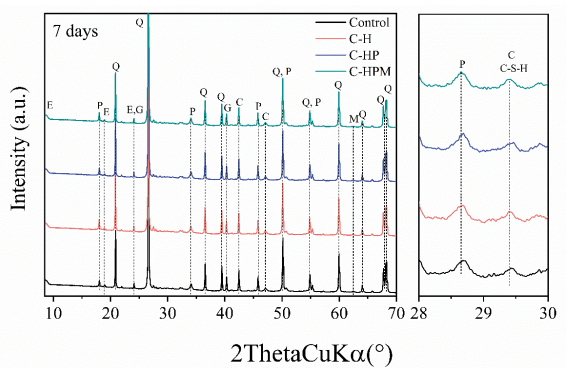

(b)

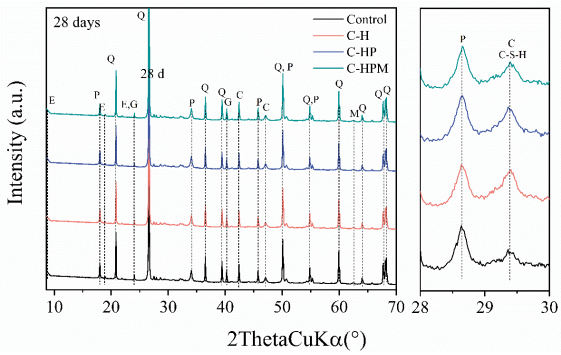

Fig. 2.12 XRD curves of the cement composites reinforced with or without fibers after curing 7 days (a) & 28 days (b), respectively.

Another, **Fig. 2.13** depicts the FTIR curves of the fiber-cement composites at different curing stages. In the present experiment, the major vibration bands are identified for cement hydration products. To be more specific, at the 7-day curing stage as is shown in **Fig. 2.13a-d**, the band at 3645 cm^{-1} is due to the OH band from $Ca(OH)_2$ [99]. Whereas the band at around 3405 cm^{-1}, representing hydrogen-bonded OH species, is very wide and weak. To explain this phenomenon, one reason possibly is that the distance forming the hydrogen bonds could be not met as the network of C-S-H gel is relatively loose during 7-day curing. Another possible reason is most OH is presented in the form of free water involved in the early hydration reaction of cement. The band centering at about 1652 cm^{-1} is caused by the bending vibration (V_2) of irregularly bound water [100, 101]. **Fig. 2.13c** shows the carbonate bands, 1420-1480 cm^{-1}, which arise from the reactions of atmospheric CO_2 with calcium hydroxide [102, 103]. The sulfate absorption bands (S-O stretching bands) are assigned at 1097 cm^{-1} and 1151 cm^{-1}, respectively [103]. For the Si-O from the cement, Si-O asymmetric stretching vibration (V_3) of silicate, Si-O out-of-plane bending vibration (V_4) of silicate, and Si-O in-plane bending vibration (V_2) of silicate centered at 925, 522, and 452 cm^{-1}, respectively. These band assignments are in good agreement with those studies in the literature [104, 105]. Moreover, the presence of the bands located at 776 cm^{-1} and 692 cm^{-1} is due to the quartz sand [106, 107].

At the curing stage of 28 days, the band at approximately 3400 cm^{-1} is stronger than that of 7 days of curing in **Fig. 2.13a'**. The hydrogen bonds formed are probably from the interface of the embedded fibers and the cementitious matrix since the interface distance is closer as the cement hydration develops. Also, the shifting characteristics of the absorption peaks in the range 1650-1660 cm^{-1} representing the irregularly bound water (**Fig. 2.13b'**) are influenced by the hydrophobic treatment of fiber with AKD. For other main peaks, the peaks with the carbonate bands become stronger (**Fig. 2.13c'**) while those peaks corresponding to the S-O (sulfate) presented in **Fig. 2.13d'** are relatively weaker in comparison with the curves of 7 days. The reason for this phenomenon most likely lies in the fact that as the cement hydration proceeds, more calcium carbonate is produced and the sulfate is consumed, respectively [108]. Therefore, the main conclusion is that the fiber treatments have a certain impact on the hydration products deposited on their surfaces but little influence on the hydration of the cement matrix.

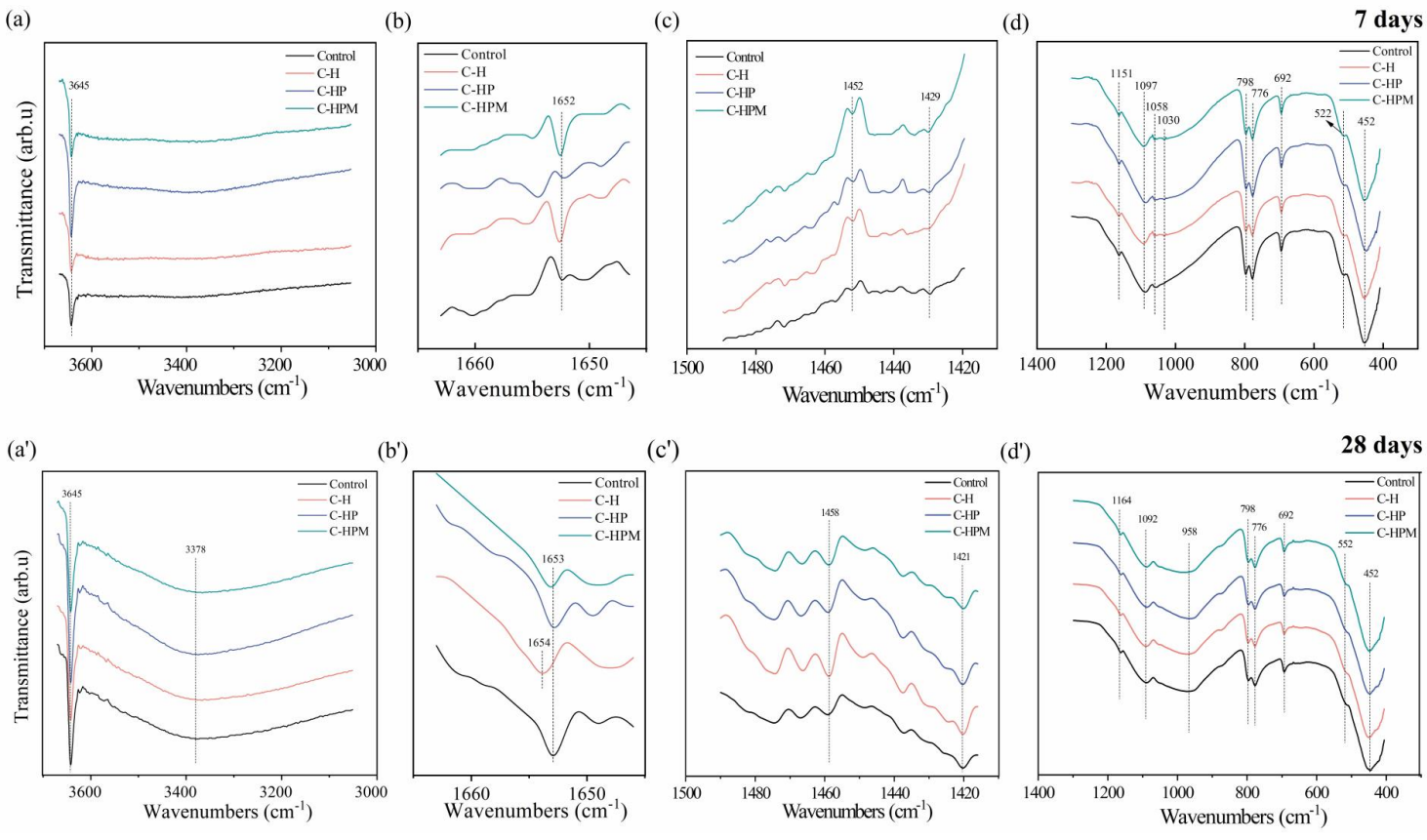

Fig. 2.13 FTIR curves of the cement composites reinforced with or without fibers (see Table 2.4) after 7 days (a-d) & 28 days (a'-d').

Mechanical properties of fiber-reinforced composites

Strength performance is an important reflection of the interface property of fiber-reinforced cement composites. The results of the mechanical strength of the samples are displayed in **Fig. 2.14** and summarized in **Table 2.6**.

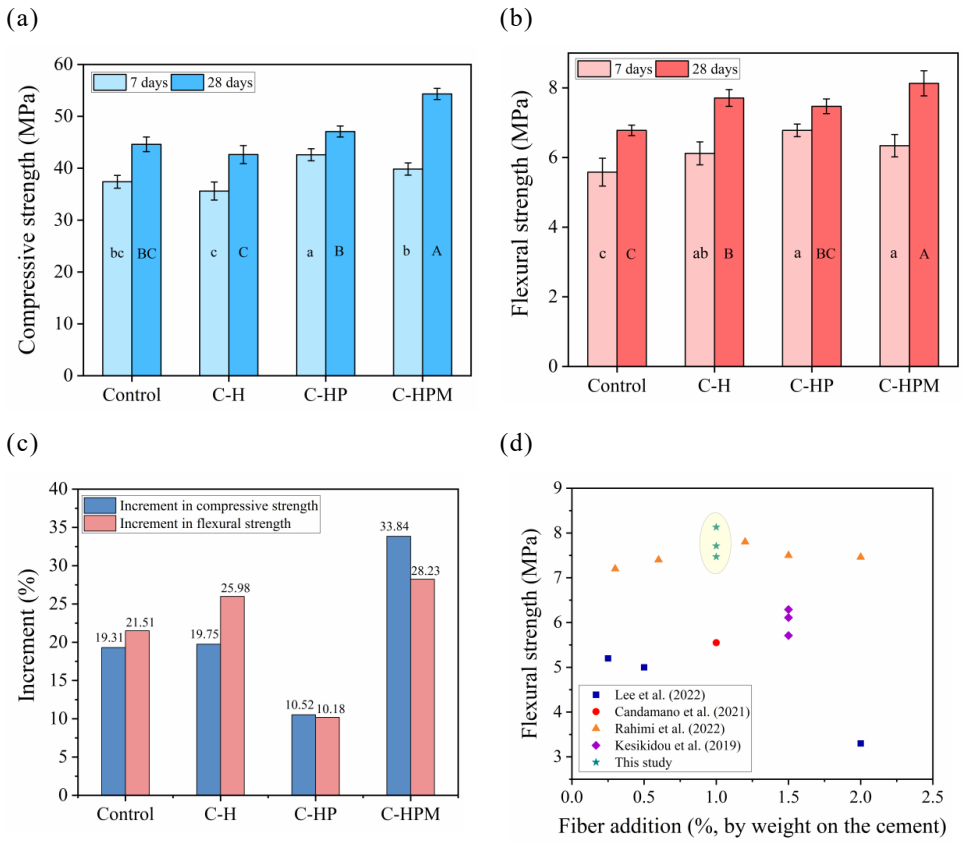

Fig. 2.14 Compressive strength (a) and Flexural strength (b) of fiber-reinforced cement composites (see **Table 2.4**). The composite samples with or part with the same letter in the middle of the columns are not statistically different by Tukey's HSD test; increment percentage in both strength (c) and the comparison of flexural strength data obtained from this study with that of other studies (d) [68, 69, 109, 110].

In **Fig. 2.14a** and **b**, almost all fiber-reinforced cement composites are better than the control at all ages (7 days and 28 days) when hemp fibers at 1.0% by weight of cement weight are mixed into mortars. This may be due to the filling effect of the embedded fibers in the matrix [111]. Similar results have further been reported by other researchers [112, 113]: Balasubramanian et

al. [112] suggested that the addition of fibers by a dosage of 1.5% could show an increase in compressive strength as compared to conventional concrete. By contrast, the compressive strength of the C-H is slightly lower than that of the control sample at all curing ages. This can be due to the retarding effects caused by hemicellulose-type polysaccharides of hemp fiber, which overtakes its filling effect. Compared to the C-H statistically, C-HP shows significantly higher strength performance. This is related to the pretreatment of embedded fibers which can not only decrease the air-entraining effect [114], which is reflected by the density results but also reduce the delaying effect due to some polysaccharides [115, 116]. Regarding the effect of decreased air entraining, this is due to the fiber pretreatment which leads to the destruction of the surface structure of fibers, thus allowing water to penetrate and displace air that may have been trapped in the voids or lumen structures of the fibers. Finally, this displacement contributes to reducing the overall entrapped air content in the composites. Moreover, it has to be mentioned that the C-HPM in this study has the highest strength properties in all fiber-reinforced cement composites statistically. This could be justified because of the best interface property between the fiber and the matrix. Interestingly, it can be seen that control samples at 3 and 28 days of curing do not present ideal strength performance. The reason for this phenomenon is unclear but could be attributed to high air humidity that increases the underlying water-cement ratio. This results in a little negative impact on mechanical strength development. In addition, such a phenomenon of low expected strength was also found in the previous study [117].

As shown in **Fig. 2.14c**, C-HPM exhibits the highest strength increment, about 33.84% in compressive strength and approximately 28.23% in flexural strength from 7 to 28 days of curing, among all specimens. This can be attributed to the fact that both the AKD modification reduces the swelling-shrinking capacity of fibers and the pretreatment densifies the microstructure of the cement matrix [114, 118]. In the same period, the increment of C-HP is the lowest in compressive strength and flexural strength, which are 10.52% and 10.18%, respectively. In fact, this phenomenon is caused by the characteristic of high-water absorption of HP, resulting in the higher swelling-shrinking degree of the embedded fibers and then poor interface bonding between the fiber and the cement matrix. The results in **Fig. 2.14d** indicate that in previous studies the flexural strength improvement of the natural fiber-reinforced cement composites is quite limited even though the addition of fiber content increases. However, the flexural strength in this work (the addition of 1 wt.% of cement) is relatively higher due to the swelling-resistant behavior. This increases the potential of hemp fiber-reinforced cement composites applied in the construction field.

The response curves can be described by identifying two domains shown in **Fig. 2.15**. The first linear region represents the uncracked stage, and the second region is identified by the development of cement matrix crack (non-linear response is magnified in **Fig. 2.15b**), fiber pull-out process, and cracked stage, in which crack pattern is completely developed up to failure [68]. The non-linear range is quite limited, which is attributed to the small dosage of fiber in the composites. In general, all cement composites reinforced by hemp fibers show higher peak response and longer displacement compared to the control specimen without fiber addition. Interestingly, C-HP has the highest peak response and longest displacement elongation at 7 days but cured to 28 days is quite low or short in both, just slightly above that of the control in terms of the peak. The reason for this phenomenon most likely lies in the fact that the mechanical interlock is formed between the rough surface of HP and the cement matrix at the early curing time; whereas the high swelling and shrinkage behaviors of HP take responsibility for this as time goes by.

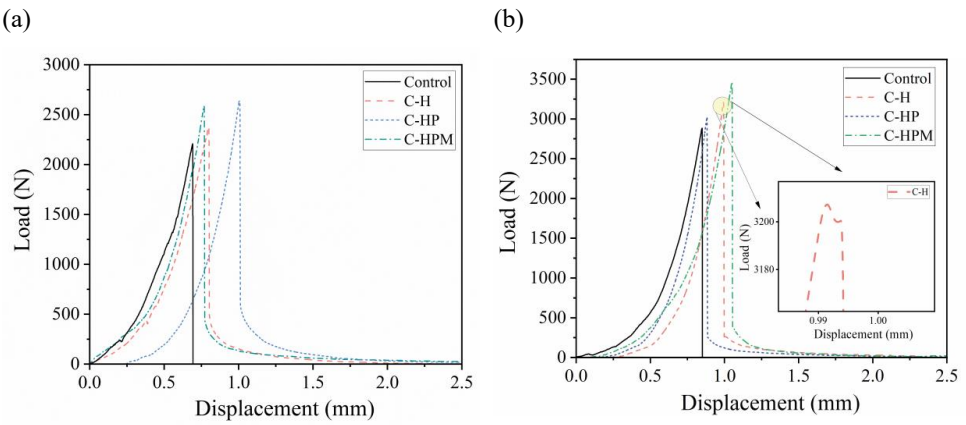

Fig. 2.15 The load vs. displacement curves of fiber-reinforced cement composites (see Table 2.4) after 7 days (a) and 28 days (b) of curing.

In addition, combined with the results of the toughness index and post-crack energy absorbed in **Table 2.6**, the fiber-reinforced cement composites have an increase in both toughness and ductility compared to the plain. Indeed, hemp fibers not only improve the resistance to micro-crack initiation but also bridge the macro-cracks of the cement matrix, thereby delaying the fatigue-crack propagation of composites and increasing the toughness capacity. It is also noted that the C-HPM exhibits the highest stiffness, which is approximately 65% and 12% higher than that of the C-H at 7 days and 28 days, respectively. This indicates that the interface bonding

between HPM and the cement matrix promotes efficient transfer under loading (from the cement matrix to the fibers). This analysis is also confirmed by SEM observation and the relevant compatibility calculation mentioned above.

Table 2.6 Physical and mechanical properties of the fiber-reinforced cement composites (see **Table 2.4**).

		Control	**Hemp fiber reinforced composites** (1 wt.% of binders)		
			C-H	C-HP	C-HPM
Density (Kg/m^3)	7 d	2007 ± 3.4	1979 ± 5.3	2053 ± 5.5	2031 ± 10.9
	28 d	2180 ± 7.4	2095 ± 8.1	2177 ± 10.5	2237 ± 6.2
Compressive strength (MPa)	7 d	37.39 ± 1.23	35.60± 1.74	42.59 ± 1.16	39.84 ± 1.18
	28 d	44.61 ± 1.41	42.63 ± 1.74	47.07 ± 1.06	53.32 ± 1.08
Increment (%)		19.31%	19.75%	10.52%	33.84%
Flexural strength (MPa)	7 d	5.58 ± 0.40	6.12 ± 0.33	6.78 ± 0.18	6.34 ± 0.32
	28 d	6.78 ± 0.15	7.71 ± 0.24	7.47 ± 0.21	8.13 ± 0.36
Increment (%)		21.51%	25.98%	10.18%	28.23%
Post-crack energy absorbed (10^{-3}J)	7 d	-	96.22	169.89	107.87
	28 d	-	114.41	82.89	140.98
Toughness Index(I_t)	7 d	1	1.06	1.14	1.09
	28 d	1	1.07	1.08	1.16
Stiffness (kN/mm)	7 d	7.59	6.96	9.12	11.46
	28 d	11.17	12.48	11.88	13.95

2.4 Conclusion

In this chapter, the interface properties and mechanical properties of the hemp fiber-cement composites were improved by different treatments of the fiber surface. Optical microscope, SEM, FTIR, and WAT were used to characterize the fibers.

In terms of the composites, the CX calculation and SEM were employed to evaluate the interface properties; Both the EDS test of the embedded fiber surface and the XRD and FTIR characterization of the composites were used to study the cement reaction products; The mechanical strength, toughness index and stiffness of the composites were also tested. Based on the results obtained in this work, the conclusions are summarized as follows:

(1) The alkali and acetone pretreatments enhance the roughness of the fiber surface but also lead to an increase in the water absorption capacity, which could be related to the removal of lignin and some extractives. However, after AKD modification, the fiber became quite hydrophobic thanks to the presence of alkyl groups.

(2) The CX index calculation and SEM observation show that after pretreatment and AKD treatment, the compatibility and interface bonding of the composites are effectively improved. Therefore, reducing the swelling-shrinking capacity of the fiber is an effective way to strengthen the interface bonding.

(3) Compared with H and HP, less amount of cement hydration products were deposited on the HPM surface. Due to the hydrophobic property (low free energy), the HPM can effectively reduce the heterogeneous nucleation and growth of hydration products on its surface. Furthermore, the portlandite precipitated on the HPM surface accounts for the lower percentage of cement hydration products according to the results of EDS.

(4) There are no significant differences in the hydration products of the cement matrix in the three different composites, indicating that AKD is not involved with cement hydration reaction, a good candidate agent of fiber modification.

(5) The characterization of the mechanical properties showed an increase in the strength performance, toughness capacity, and stiffness for the cement composites reinforced with hemp fibers, especially for the AKD-modified fibers. Thus, this is also a response to the better interface bonding between HPM and the cement matrix.

From these results, it can be concluded that AKD-modified could effectively improve the mechanical properties by strengthening the interface bonding and be probable in the practical application of the building field.

CHAPTER 3

3. Effects of zirconia modification on the durability of hemp fiber-reinforced cement composites under accelerated aging

Based on this paper:
H. Song, T. Liu, F. Gauvin, and H.J.H. Brouwers. Evaluation of zirconia modification on the durability of natural fiber-reinforced cement composites using accelerated aging. Journal of Building Engineering 84, 108632 (2024).

3.1 Introduction

Natural fiber-reinforced cement composites (NFRCCs), including hemp fiber-reinforced cement composites (HFRCCs), are being actively explored for applications in the civil engineering and building fields [119-121]. However, the poor durability of NFRCCs, attributed to the alkaline hydrolysis and the mineralization of the embedded natural fiber, greatly limits their practical application.

To address this problem, two strategies have been employed to increase long-term durability, namely (1) modification of the cementitious matrix [27, 122] and (2) fiber treatment [123]. The second approach has been widely adopted due to the additional advantage of optimizing the fiber-matrix interface. Therefore, this study is also focused on fiber treatment. In terms of fiber treatment used in NFRCCs, there are various methods including thermal treatment [124], alkali treatment [125], and physical-chemical impregnation [126, 127] among others. In particular, introducing functional substances through dip coating on natural fibers has been considered an

effective and low-cost route to improve the durability of NFRCCs by protecting the embedded fibers from the alkaline pore solution. For example, Canovas et al. [128] enhanced the durability of Portland cement mortars reinforced with sisal fibers by coating timber extracts (e.g. colophony, tannin, and vegetable oil) onto sisal fibers and the flexural strength results of the composites showed that mortars reinforced with impregnated fibers exhibited better durability. Bilba and his co-worker used an emulsion of silane to coat bagasse fibers for reinforcement of cementitious composites, which concluded that 6% weight of silane is capable of reducing the water absorption potential of fibers, hence increasing the durability [58]. Although these treatment methods can prolong the durability of NFRCCs a certain, some new problems such as the high cost and complicated treatments are introduced.

Given that zirconium dioxide (ZrO_2) has been successfully applied on glass fibers, which is known as alkali-resistance (AR) glass fibers, to improve their durability in cement matrix [127, 129], several researchers have used zirconium dioxide (ZrO_2) on natural fiber modification to improve the durability of the fiber-reinforced cement composites [129, 130], and it was reported that ZrO_2-treated yarn fibers can effectively prolonger the durability of reinforced cement composites at room conditions [127]. However, the durability of NFRCCs under harsh environments has yet to be performed. In addition, the alkali resistance behaviors (alkali hydrolysis and mineralization) of ZrO_2 on natural fiber were not fully unclear.

Hence, the goal of this chapter is to evaluate the durability of ZrO_2-modified fiber-reinforced cement composites under harsh conditions and reveal the related mechanism. In this study, hemp fiber is selected as the research objective considering the overabundant waste of hemp fibers produced annually in Europe [131]. The ZrO_2 sol was employed to modify hemp fibers by dipping method. Subsequently, hemp fiber-reinforced cement composites (HFRCCs) were obtained by randomly mixing short fibers with cement-based materials. To assess the durability of the composites under harsh conditions, the mechanical strength of the composites was tested at different wetting-drying cycles. Meanwhile, to fully understand the mechanism, the property performances of the embedded fibers were characterized by the thermogravimetric measurement and the element components tests on hydration products of fiber surfaces. Furthermore, to compare the performance of ZrO_2 in terms of its resistance to alkali hydrolysis and resistance to mineralization, the tensile strengths of the fibers exposed in different designed alkali solutions were investigated. The outcomes of this study can provide the theoretical

guidance to accelerate the industrial application of the HFRCCs such as pavement blocks and low-cost housing.

3.2 Experimental

The durability of HFRCCs under accelerated aging conditions is assessed by analyzing the properties of embedded fibers, the mechanical strength of entire HFRCCs, and fiber-matrix compatibility, as illustrated in **Fig. 3.1**. The alkali resistance behaviors of fibers under different alkali mediums were compared to further evaluate the fiber surface treatment on the durability of entire composites.

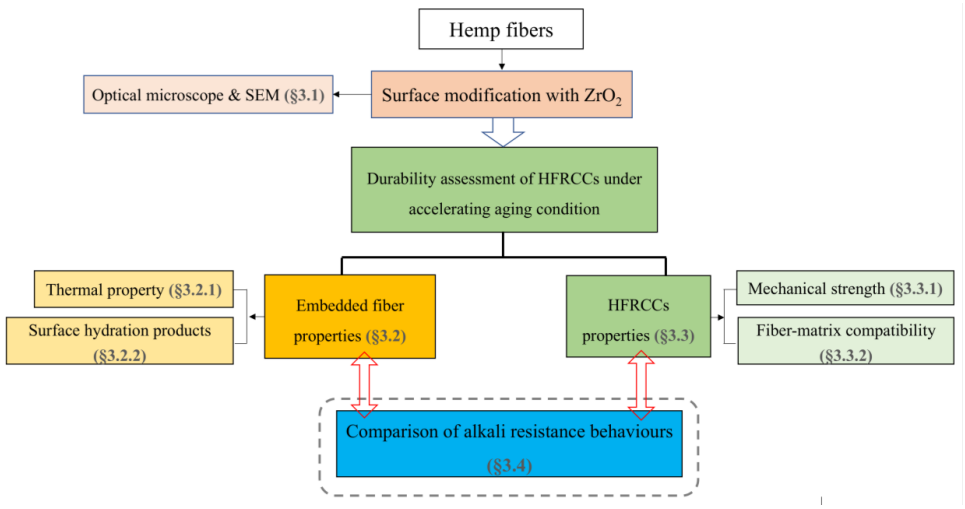

Fig. 3.1 Overview of the work in this chapter.

3.2.1 Materials

Technical hemp fibers were supplied by HempFlax Group B.V. (The Netherlands). All the chemical components used for the pretreatment and the preparation of the ZrO_2 sol like zirconyl chloride octahydrate ($ZrOCl_2 \cdot 8H_2O$), Polyethylene glycol (PEG400), Hydrogen peroxide (30 wt.%) and absolute alcohol were purchased from the VWR®, part of Avantor. The commercial ordinary Portland cement (OPC) CEM I was provided by ENCI B.V, (The Netherlands).

3.2.2 Methods

3.2.2.1 Fiber treatment

Prior to the experiment, some long hemp fibers were washed and cut (length = 12 cm) for the single fiber tensile testing, which will be specifically described in the following section. The remaining shorter fibers were cut (length ≈ 2 cm) for the preparation of fiber-cement composites. Subsequently, these fibers were pretreated with both acetone and diluted alkaline solution to remove the impurities on the fiber surface (i.e. pectin, lignin, and hemicellulose). This step was detailed in the previous work.

The method used to prepare the ZrO_2 sol follows the work of Wang et al. [132]: The ZrO_2 sol was prepared and aged for 1 day for coating. The pretreated fibers were completely immersed in the ZrO_2 sol for 5 minutes, filtered twice, and dried at 70 °C for 1 day. A ZrO_2 layer was formed on the fiber surface. The treatment process is schematically shown in **Fig. 3.2**.

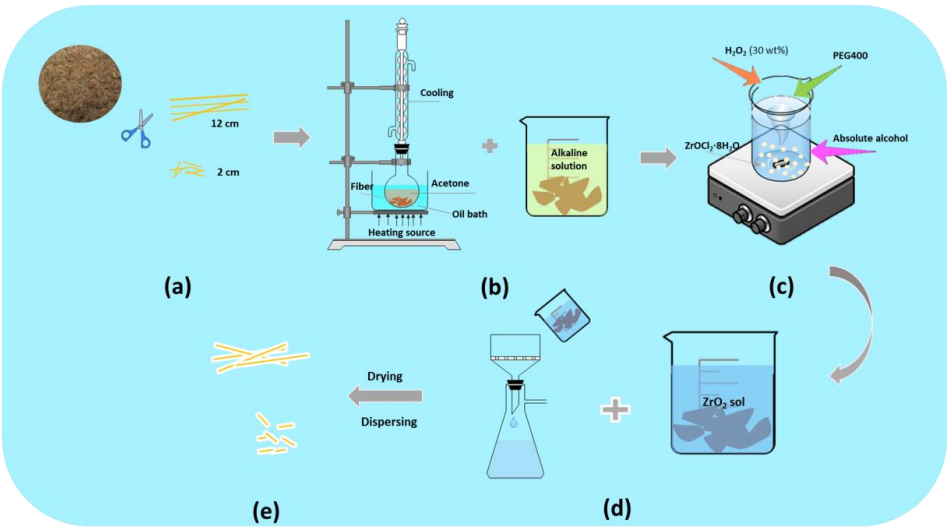

Fig. 3.2 Schematic illustration for the process of the pretreatment and ZrO_2 modification on fibers. (a) Cutting raw fibers. (b) fibers pretreating. (c) Preparing ZrO_2 sol. (d) fibers immersed and filtered. (e) ZrO_2 coated on fibers.

3.2.2.2 Fiber composites preparation

HFRCCs with 2% (by weight, relative to cement weight) were prepared from original, pretreated, and ZrO_2-treated fibers. Corresponding codes of their composite were shown in **Table 3.1**. The hemp fibers used were around 2 cm in length, and their distribution in the composites was random orientation. The sand-cement ratio and water-cement ratio used in this work were 3 and 0.5, respectively. The main purpose of sand addition is to ensure the fibers randomly disperse. In addition to that, the short fibers were also distributed by hand followed by mixing continued at middle speed for 2 mins to disperse uniformly. The flowability of all mortars was adjusted and kept around 18 mm using a polycarboxylic ether-based superplasticizer, which is to avoid the influence of the absorbing water of fiber on the water-cement ratio. The specimens were demolded after 24 h and kept in a climatic chamber at 20 ± 2 ℃ and 50 ± 5% humidity for 28 days.

Table 3.1 Sample codes of the fiber-cement composites.

Code	Sand/ Cement	Water/ Cement	Fiber addition (wt.% of cement)	Hemp fiber surface treatment
Control	3	0.5	-	-
C-R	3	0.5	1%	R: Raw (no treated)
C-P	3	0.5	1%	P: Pretreated
C-Z	3	0.5	1%	Z: Modified with ZrO_2 sol

After that, the mortar specimens were subjected to wetting-drying cycles to accelerate aging. The wetting-drying cycling approach in our study was adopted based on the literature [133]. In detail, one cycle includes the wetting step (submerged in sealed tap water at room temperature for 7 days), the drying step (dried in a circulating air environment at 60 ℃ for 4 days), and the cooling step (cooled down at room temperature for 3 h). Finally, the investigated specimens were repeatedly exposed to different cycles for the later tests.

3.2.2.3 Alkali resistance test

The deterioration of untreated, pretreated, and ZrO_2-treated long fibers exposed to different alkali environments gave important information concerning the durability of fiber-cement mixture specimens. The degradation of the fibers was measured as strength loss occurred over time, for different treated fibers under three kinds of environments: fibers stored in water; fibers

stored in a saturated solution of calcium hydroxide of pH 12.6; and fibers stored in a solution of sodium hydroxide of pH 12.6. These fibers were stored in small containers with tap water or chemical solutions for up to 90 days, as is shown in **Fig. 3.3**. The container was covered, and the pH of the solutions was checked at regular intervals; solutions that had not retained the initial pH value were replaced. In addition, considering the security risk of the Lab room, the fog equipment is turned on and set for 6 hours every day. After different storing days, the fibers were dried in the oven at 60 ℃ for 24 h and then tensile tested.

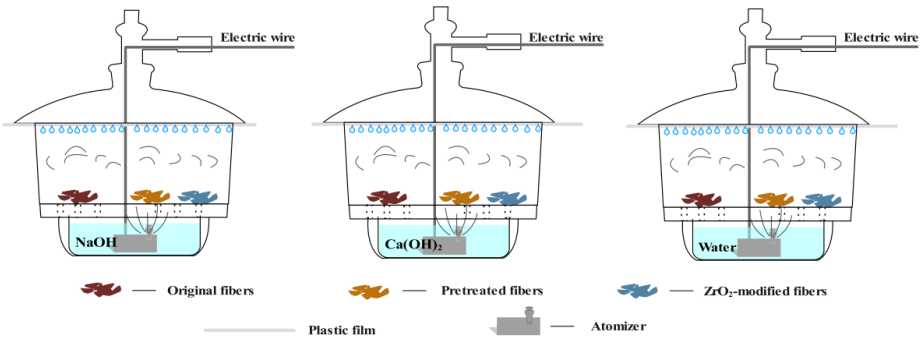

Fig. 3.3 Schematic illustration for different treated fibers processed in three types of environments: NaOH solution, saturation $Ca(OH)_2$ solution, and water.

3.2.3 Characterization

Both optical microscope and SEM measurements for fiber observation and EDS measurement for the cement hydration products on the fiber surface were conducted according to the procedure described in Section 2.2.3. The thermogravimetric analysis (TGA, NETZSCH STA 449 F1) was performed on both unembedded fibers and the extracted fibers from the cementitious matrix to evaluate the thermal behavior of these fiber samples. The temperature was set between 50 ℃ and 700 ℃ and the environment was in a nitrogen flow of 100 mL/min at a heating rate of 20 ℃/min. The isothermal calorimeter (TAM air, Thermometric) is employed to study the compatibility between the fibers and the cement. In the sample preparation, we thoroughly shook and mixed the fibers and dried powders homogeneously. This was done to ensure the uniform dispersion of fibers in the fresh slurry, all while shortening the stirring time after adding water to enhance the accuracy of the tested results. The compressive strength and flexural strength of NFRCCs in this work were conducted following EN 196-1 [73]. The tests were repeated three times. Besides, the tensile strength of long fibers was

determined using the EZ 20 Lloyd Instrument (AMETEK) testing machine with a maximum capacity of 100 N. The load was applied at a constant rate of about 0.2 mm/min. The tests were carried out after 0, 12 d, 30 d, and 90 d of immersion in the two solutions or the water. For each test, three different treated fiber samples (raw/untreated, pretreated, and ZrO_2-treated) were prepared, with the tests being replicated ten times.

3.3 Results

3.3.1 Fiber surface modification

The fibers, subjected to various treatments including untreated, only pretreatment, and both pretreatment and ZrO_2 coating, exhibit distinct differences in both colors and surface morphology, as illustrated in **Fig. 3.4**.

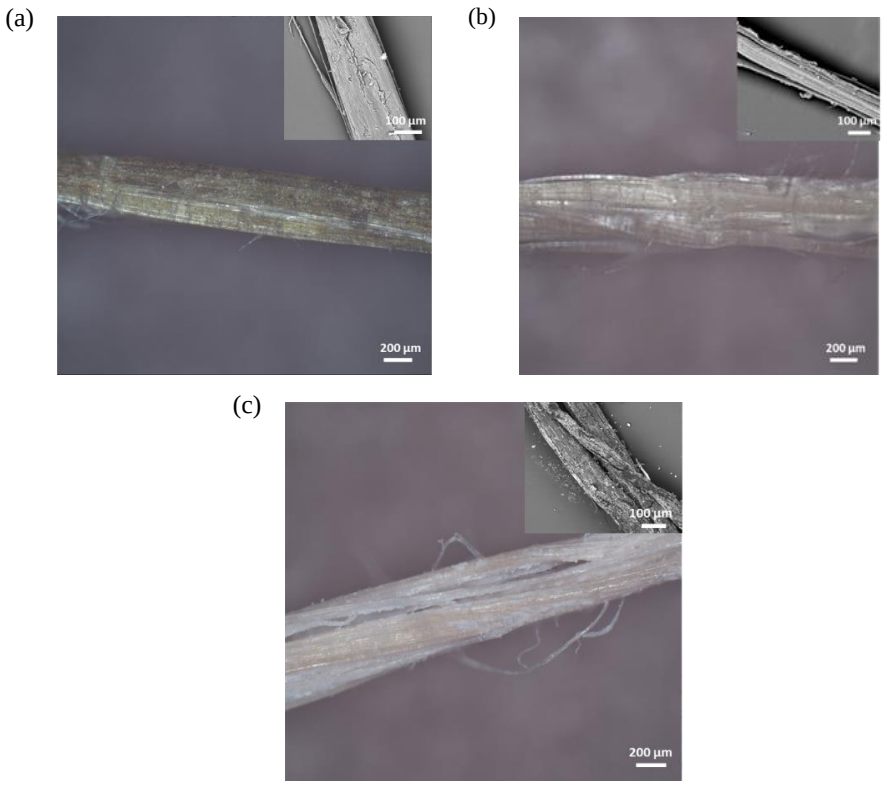

Fig. 3.4 Surface morphology of fibers with different treatments (a) Raw, (b) Pre-treated, and (c) ZrO_2-modified.

In **Fig. 3.4a**, optical and corresponding SEM images of raw hemp fibers are presented. The fiber surface is observed to have a dark yellow color, attributed to non-cellulosic substances such as pectin and lignin, as confirmed by IR-spectroscopy [134]. Meanwhile, a smooth surface was observed from the corresponding SEM image. After the alkali-acetone pretreatment, the color of the fiber surface became brighter, more microfibril fibers appeared and the surface became rough relief as illustrated in **Fig. 3.4b**. These phenomena can be explained by the removal of some non-cellulosic substances under the pretreatment process. To be more specific, some impurities (i.e. wax and pectin) of fiber surfaces were removed by the acetone extraction procedure [135]. Furthermore, sodium hydroxide was employed to remove the other impurities (i.e. lignin, pectin, and hemicellulose) in the first layer of the fiber cell wall [61]. In addition, the rough surface of the pre-treated fiber is more beneficial for the physical attachment of following ZrO_2. As seen in **Fig. 3.4c**, a unique modified layer of ZrO_2 was coated on the pre-treated fibers which could resist the alkaline attack and degradation from the cement matrix [136]. Also, the surface became quite rough, which could benefit the increase of the interface bonding between fibers and the cement matrix [68].

3.3.2 Effect of ZrO_2 modification on the properties of embedded fibers

To better understand the actual degradation evolution of different treated hemp fibers embedded in the cementitious matrix throughout normal curing time and accelerated aging, thermogravimetric analysis (TGA) was performed on embedded fibers, and energy dispersive spectrometry (EDS) was performed on the hydration products precipitated on the embedded fibers surface.

Thermal stability analysis of embedded fibers

Thermogravimetric analysis was carried out to investigate the degradation of embedded hemp fibers caused by a mortar matrix throughout 28 d curing, not including the part wetting/drying cycles. This is because the embedded fibers due to the mineralized degradation, are stuck on the cementitious matrix and are difficult to separate.

Fig. 3.5 shows TG and DTG plots for the investigated degradation of fiber components under nitrogen atmospheres. TG Several distinct thermal degradations are observed on the DTG cures of the fibers: (1) the slight peak between 100 and 180 ℃ represented a loss of free water and combined water which comes from fibers structure and/or cement hydration products (C-S-H

and ettringite). (2) a sharp peak was observed between 250 and 370 ℃ which corresponds to the degradation of hemicellulose and lignin, followed by cellulose [137, 138]. (3) an evident shoulder observed around 400-550 ℃ for the embedded fibers in the cementitious matrix might be due to the decomposition of portlandite from the cement hydration products [139]. (4) Finally, the peak of about 650 ℃ corresponds to the residue decomposition of calcium carbonate residues on the extracted fiber surface.

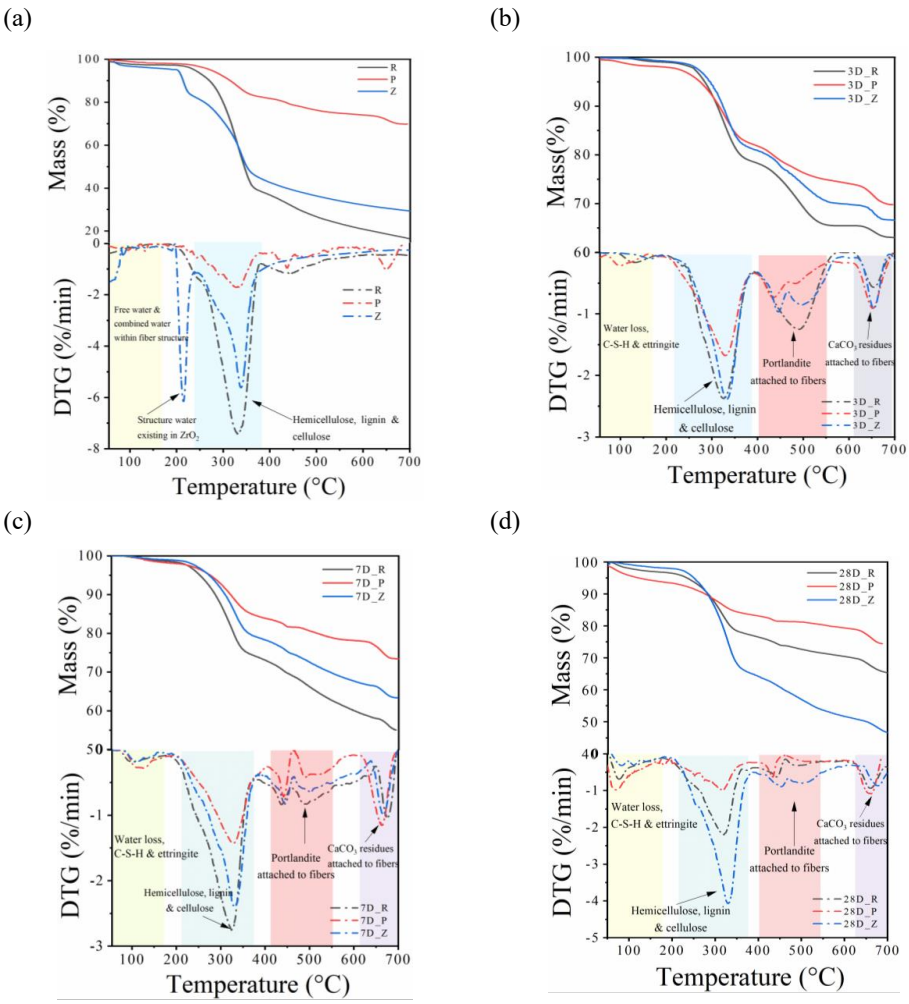

Fig. 3.5 Mass loss curves and DTG curves (b) of different treated fibers (R, Raw fibers; P, Pretreated fibers; Z, ZrO_2-modified fibers) before and after being subjected to different aging stages in cement mortars: (a) 0 d, (b) 3 d, (c) 7 d, and (d) 28 d.

Interestingly, before embedding, a small shoulder peak of the pre-treated fiber and the ZrO_2-modified fiber both occur at around 440 ℃ shown in **Fig. 3.5a**. This is because this peak is the shoulder peak of cellulose degradation caused by the removal of the hemicellulose and extractives and then the improvement of the cellulose crystallinity index. The behavior is consistent with the DTG measurement of Almeida Melo Filho et al.[140]. In addition, the strong narrow peak of the ZrO_2 modified fibers non-embedded in cement matrix around 180-210 ℃ is observed. This is due to the removal of structural water molecules existing on the zirconia, corresponding to M-OH bonding [141, 142].

Based on the literature [127], a slightly small peak between 220 and 300 ℃, which is associated with the degradation of hemicellulose, is observed in the DTG curves although the peak is not evident. It can also be seen from TG curves that pre-treated fibers have low mass loss no matter if embedded in the cement matrix. It is well known that the semi-crystalline cellulose components have better thermal stability than amorphous hemicellulose. After raw hemp fibers are alkali extracted, the semi-crystalline cellulose amount achieves a higher percentage of total components. Therefore, the pretreated step before fiber modification is quite necessary to improve thermal stability. More importantly, the embedded raw fibers have the highest rate of cellulose degradation at 3 and 7 days of aging but aging to 28 days the embedded ZrO_2-modified fibers present the highest degradation rate. This indicates that the ZrO_2 modification delays its cellulose decomposition which implies the ZrO_2-modified fiber has better alkali resistance when subjected to the cementitious environment.

Table 3.2 DTG peaks the temperature of cellulose of non-embedded/embedded hemp fibers under different curing stages.

	DTG peak temperature (℃)			
	Before	3 days	7 days	28 days
Raw	332	326	324	320
Pre-treated	336	328	328	316
ZrO_2-modified	338	332	332	330

Table 3.2 presents the change in thermal temperature representing the maximum rate of cellulose decomposition under different treatments and curing ages. After the initial 3 days of embedding in the cementitious matrix, the major shift to lower temperature of the DTG peaks occurred in

both raw and pre-treated fibers and a small shift for the ZrO_2-modified fibers. This indicates that cellulose is prone to undergo major degradation without the thermal insulation protection of ZrO_2 film. Subsequently, a considerable reduction in the DTG peak temperature of the pre-treated fibers at 28 days of embedded in the cement mortars. However, for the ZrO_2 modified fibers, the DTG peak at 7 days curing appears to keep the same level as the 3 days curing and then slightly shift to a lower temperature at 28 days (330 ℃). In general, a decrease in the peak temperature of cellulose was obtained for raw (3.6%), pre-treated (6.0%), and ZrO_2-modified fibers (2.3%) during the 28 days of curing. This small peak shift suggests the ZrO_2 film acts as a thermal insulator protection to mitigate or even avoid the rapid degradation of cellulose. Also, the lower peak of DTG presented in the pre-treated fibers can be explained by the fact that cellulosic microfibrils' direct exposure to the cementitious alkali environment after the removal of extractives and hemicellulose, leading to the easy mineralization of surface microfibrils and then the decrease in the crystallinity degree of cellulose [127].

Hydration products analysis on the embedded fiber surface

To better understand the underlying effect of different treated fiber surfaces on cement hydration products, and assess their alkaline resistance, EDS analyses were conducted on the surface of embedded fibers to investigate any changes in the chemical composition before and after the wetting-drying cycling.

The effective element ratios of the materials were determined by two lines in **Fig. 3.6a**, **Fig. 3.7a**, **Fig. 3.8a**, **Fig. 3.10a**, and **Fig. 3.11a**. Results indicate that the dominant phases present on all fiber surfaces are typical of cement hydration products: CH, C-S-H, and AFm/AFt phase. The Al/Si ratio of C-S-H was determined by the slope of a dash-dot line, which is drawn through the points with the lowest Al/Ca ratio and represents mixed analyses of portlandite and C-S-H without AFm or ettringite. The solid line was drawn from the AFm element point (0, 0.5) and through the upper bound of the distribution of the Al/Ca atomic ratio. The range of Ca/Si ratios of C-S-H was roughly represented by the interior zone with dense bulk data points along the two lines. The discrete points with much lower Si/Ca ratio or higher Al/Ca ratio are due to deviations of EDS spectra caused by the pores, or thin C-S-H which is not sufficiently thick to minimize the contribution of adjacent phases [143].

From the below EDS, the Si/Ca in C-S-H was determined to be 0.56 ± 0.03 both before and after wetting-drying cycling. The determined ratio decreases within the range of previously reported data [144]. Richardson investigated that some Al^{+3} was substituted for Si^{+4} in the C-S-H. In addition, according to the following linear relationship formula developed by Richardson and Groves [145], a theoretical Al/Ca trace composition was estimated to be in the range from 0.04-0.06 based on the Si/Ca found in this work:

$$\frac{Si}{Ca} = 0.444 + 2.25\frac{\mathrm{R}}{Ca}\ , \tag{3.1}$$

where R is mainly Al (as Fe is presented in minor amounts)

Bonen and Diamond [146] observed that the mean Al/Ca and S/Ca ratios were in the range from 0.034-0.066 and 0.037-0.06, respectively, and in C-S-H with Si/Ca approximately 0.43-0.48. Therefore, in this study, before wetting-drying cycling, Al/Ca and S/Ca were determined to be C-S-(A)-H phase and other phases like ettringite or monosulfate in the cement hydration products.

- Prior to wetting/drying cycles

As seen in **Fig. 3.6a**, the Al/Ca and Si/Ca ratios of the hydration products precipitated on the ZrO_2-modified fiber surface are higher than the remaining two fibers after 3 days of curing. This appears to indicate that higher levels of the AFm/AFt phase and lower levels of portlandite are attached to the embedded fiber surface under the ZrO_2 modification. The calculated Ca/Si and Al/Si ratios of C-S-H on the ZrO_2-modified fiber surface are 2.65 ± 0.32 and 0.16, respectively, and the mean value of Ca/(Si+Al) is 2.28. Meanwhile, among the three treated fibers, the ZrO_2 treatment increased the relative amount of C-S-H phase precipitated on the fiber surfaces, as indicated by a relatively higher Si/Ca ratio. As for **Fig. 3.6b**, it appears that the major pots were concerned below the line of CH + ettringite mightily since the sulfate is loosely absorbed within the C-S-H. Furthermore, a relatively higher amount of CH appears on the embedded raw fiber and pre-treated fiber surface. This implies that these two embedded fibers are more easily attacked by the alkaline ions or mineralized by the portlandite from cement hydration products.

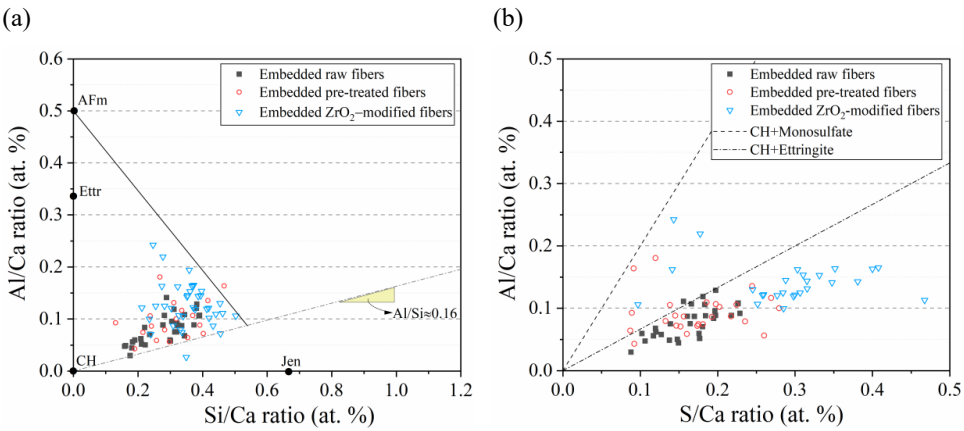

Fig. 3.6 Average Al/Ca versus Si/Ca molar ratios (a) and average Al/Ca versus S/Ca ratios (b) after 3 d curing, respectively.

Based on the observation of **Fig. 3.7a**, there is no distinct difference in the Al/Ca and Si/Ca ratios for each type of fiber surface, only a slightly lower level of Al/Ca ratio in the embedded pre-treated fiber surface at 7 days of curing. The calculated Ca/Si and Al/Si ratios of C-S-H in all fiber surfaces are 3.17 ± 0.47 and 0.17, respectively. That means that the value of Ca/(Si+Al) is 2.71, which increases from 2.28 at 3 days due to the development of cement hydration. In addition, ettringite intermixed with more portlandite precipitated on the pre-treated fiber surface, as indicated by the relatively lower Al/Ca and S/Ca ratios in **Fig. 3.7b**.

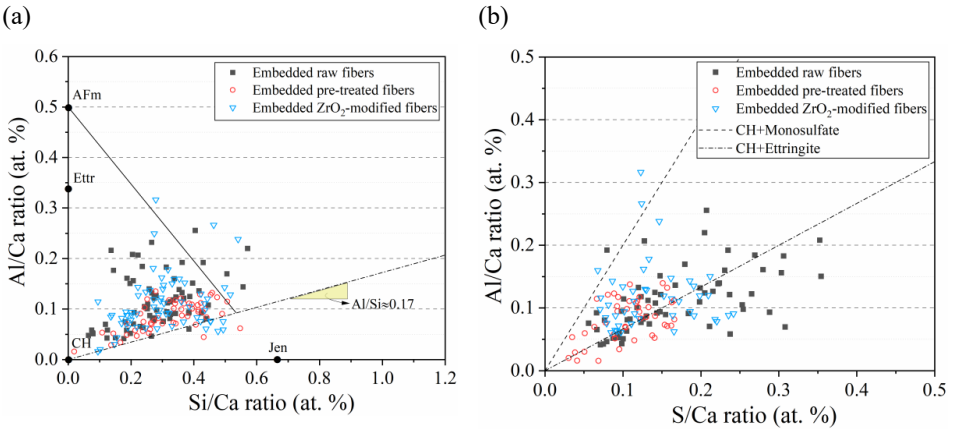

Fig. 3.7 Average Al/Ca versus Si/Ca molar ratios (a) and Average Al/Ca versus S/Ca ratios (b) after 7 d curing, respectively.

As seen in **Fig. 3.8a**, the range of Si/Ca ratio of C-S-H on the fiber surfaces at 28 d is similar to that at 7 days of curing, but the Al/Si ratio was increased up to 0.22. The calculated mean value of Ca/(Si+Al) is 2.60. That means, more SiO4 tetrahedrons of C-S(A)-H was replaced by $AlO4^-$ tetrahedroa as the cement hydration developed. Besides, the S/Ca ratio range at 28 d is slightly higher than that at 7 days as illustrated in **Fig. 3.8b**. It is possibly related to the release of sulfate-containing liquid absorbed from the cement matrix, in the cavity of the embedded hemp fibers.

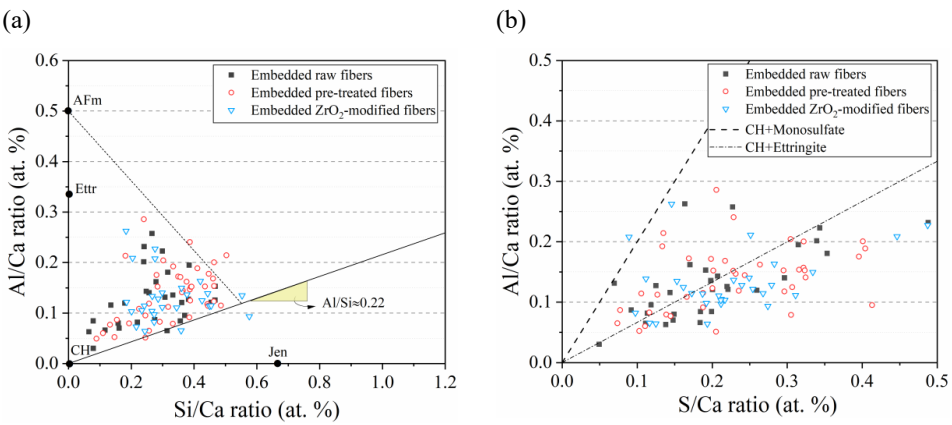

Fig. 3.8 Average Al/Ca versus Si/Ca molar ratios (a) and Average Al/Ca versus S/Ca (b) after 28 d curing, respectively.

Fig. 3.9 illustrates the alkali content on the different treated fiber surfaces embedded in the cementitious matrix. The results obtained show that the major portion of Si/Ca ratio data focuses on below the value 0.5 and all K/Ca ratios are lower than 0.6 in both 7 d and 28 d of curing. As seen in **Fig. 3.9a**, all ZrO_2-modified fiber data fell on or around the K/Ca Y-axis with the lowest Si/Ca ratio while most pretreated fiber data distributed on the Si/Ca X-axis with a relatively higher Si/Ca ratio. This was probably related to the ion exchange due to the ionic species like ZrO^{2+} or Zr^{4+} existing in an alkali environment [147, 148]. As also explained in Ref. [98] and Ref. [149], the alkali ions can be absorbed by the C-S-H gel. Thus, the C-S-H phase precipitated on the surface of the ZrO_2-modified fiber mainly exists in the formation of non-expansive C-K-S-H. At 28 d of curing, there was little difference in the Si/Ca ratio among the three fibers, but the K/Ca ratio in the raw fiber and pre-treated fiber almost fell to zero (**Fig. 3.9b**). The reason for this phenomenon possibly is that the fiber surface without the barrier of ZrO_2 film is prone to absorb the K ions into the fiber lumen, especially for the pre-treated fibers, resulting in the K element not being detected by the EDS technique.

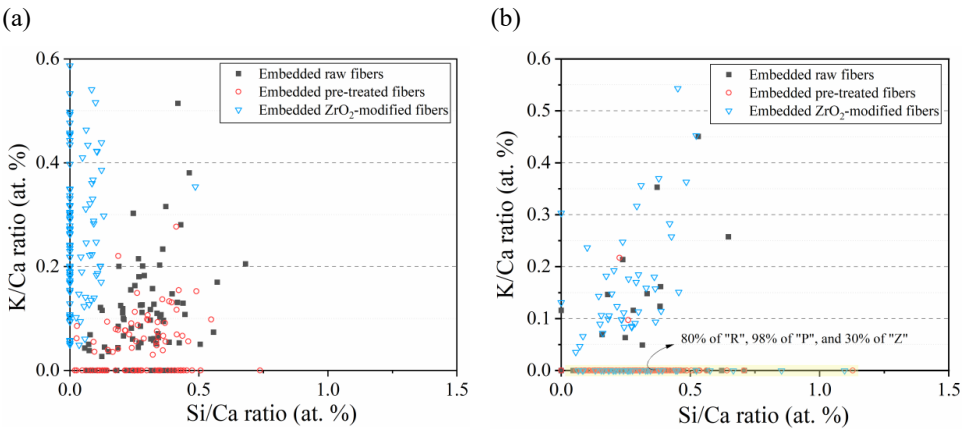

Fig. 3.9 Average K/Ca versus Si/Ca molar ratios after 7 d curing (a) and 28 d curing (b).

To summarize, during 28 d, the mineralization of the embedded pre-treated fiber is more serious compared to the other two embedded fibers. The hydration products precipitated on the pre-treated fiber surface are mainly portlandite intermixed with ettringite with increasing curing time. Whereas the hydration products on the surface of ZrO_2-modified fiber are mainly C-S-H phases, which exist in the form of non-expansive C-K-S-H.

- After wetting/drying cycles

After 3 wetting-drying cycles, the embedded ZrO_2-modified fiber surface showed a significantly superior Al/Ca ratio and Si/Ca ratio (**Fig. 3.10a**), and a lower S/Ca ratio (**Fig. 3.10b**) compared to the other two fiber cases. This indicates that after ZrO_2 modification the production deposited on the embedded fiber surface mainly exists in the form of the alumina-rich phase (e.g., mono sulfate). In general, the calculated Ca/Si ratio and Al/Si ratio of C-S-H on the fiber surfaces are 1.95 ± 0.22 and 0.11, respectively, and the mean value of Ca/(Si+Al) is 1.76, which notably decreased compared to those values before cycling. This could be possibly related to the transverting of more Ca sources into portlandite and calcite due to the curing under harsh environments (high temperature and cold water)

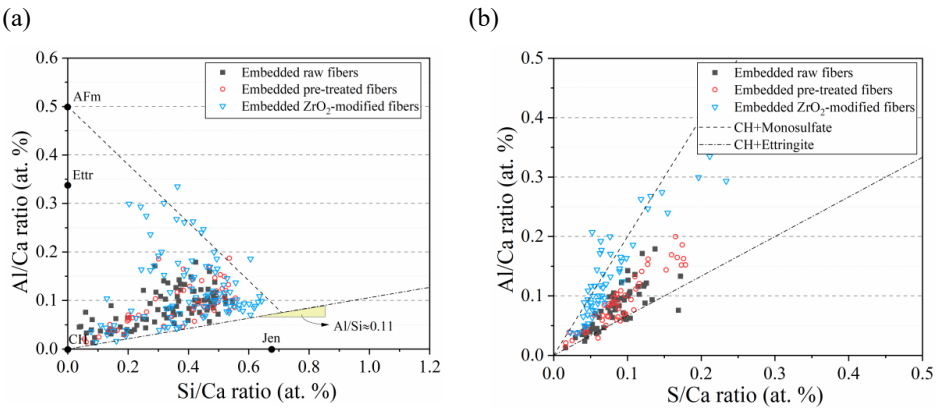

Fig. 3.10 Average Al/Ca versus Si/Ca molar ratios (a) and Average Al/Ca versus S/Ca (b) after 3 cycles, respectively.

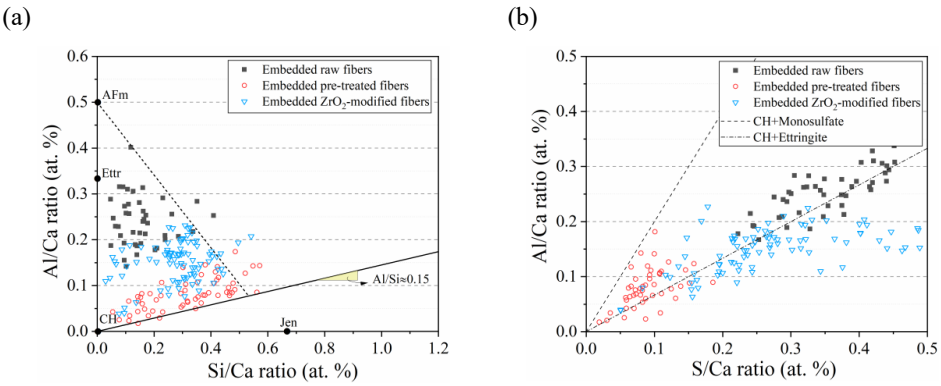

Fig. 3.11 Average Al/Ca versus Si/Ca molar ratios (a) and Average Al/Ca versus S/Ca (b) after 5 cycles, respectively.

Up to 5 cycles, it can be seen in **Fig. 3.11** that the data of the embedded raw fibers are in the highest zone regarding both the Al/Ca ratio and S/Ca but the relatively lower Si/Ca ratio. This phenomenon implies that more ettringite and C-S(A)-H phases in which the SiO4 tetrahedrons of C-S(A)-H were replaced by $AlO4^-$ tetrahedrons, precipitated on the raw fiber surfaces. Compared to the raw fibers, both the pretreated fibers and ZrO_2-modified fibers have a relatively higher Si/Ca ratio as illustrated in **Fig. 3.11a**. This indicates that the SiO4 tetrahedrons of C-S-H were little or even not substituted by $AlO4^-$ tetrahedrons for both fiber surfaces. In addition, the lowest Al/Ca ratio and S/Ca ratio in **Fig. 3.11b** indicates that more amount of portlandite or calcite and C-S-H phases exist on the pre-treated fiber surfaces. The phenomenon that increased the Al/Ca ratio and S/Ca ratio after ZrO_2 modification compared to the pre-treated

fibers probably could be less amount of Ca existing on the phases on the fiber surfaces due to the alkali resistance of ZrO_2.

As a result, during wetting-drying cycles, the more ettringite and amorphous C-S(A)-H phases precipitated on the embedded raw fiber. Moreover, many SiO4 tetrahedrons in C-S-H are substituted by $AlO4^-$ tetrahedrons. However, the pre-treated fibers still retain a significant amount of portlandite or calcite, along with partial C-S-H phases on their surface. In the case of ZrO_2-modified fibers, after the initial 3 cycles, predominant alumina-rich phases like monosulfate exist on their surface. Subsequently, as the wetting/drying continues, the less-Ca-contained phases precipitate on the fiber surface compared to the other embedded fibers. The resistance to alkali ions is attributed to the presence of the ZrO_2 film.

3.3.3 Effect of ZrO_2 modification on the durability of the composites

Mechanical Strength of the Composites

The mechanical strengths of HFRCCs are the most important criterion to assess the durability of the composites. Therefore, the compressive strength and flexural strength of the mortar composites reinforced with different treated fibers, after various curing days and wetting-drying cycles were investigated and the results were illustrated in **Fig. 3.12**.

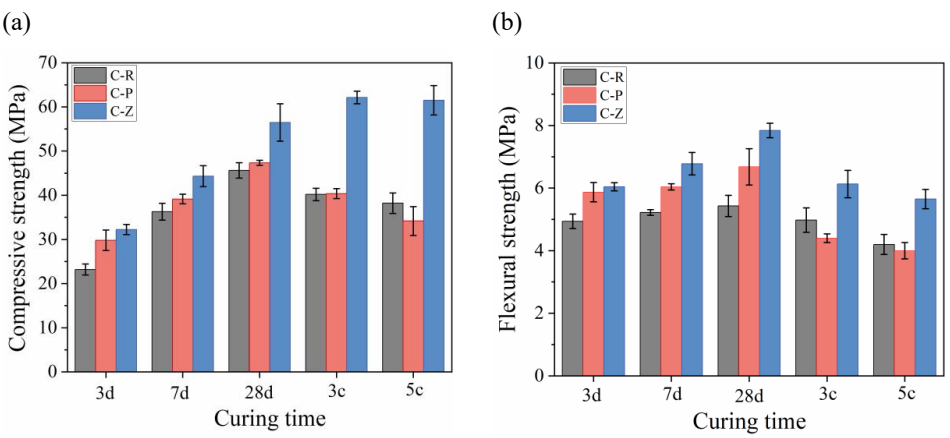

Fig. 3.12 Compressive strength (a) and flexural strength (b) of the mortar composites reinforced with hemp fibers (**Table 3.1**).

It was seen that the compressive strength (**Fig. 3.12a**) and flexural strength (**Fig. 3.12b**) increase with increasing curing time before the wetting-drying cycle. In addition, it is worth mentioning that the mortar composites reinforced with the fibers that underwent the pretreatment process (pretreated fibers and ZrO_2-modified fibers) have a somewhat higher flexural strength and compressive strength than the composites reinforced with raw fiber. This is possibly related to the difference in fiber stiffness with or without the pretreatment. The pretreatment can improve fiber flexibility, thus benefiting the flexural strength increase of the composites [150]. Meanwhile, this can result in more readily mechanical interlocking between the fiber and the matrix due to the rougher surface, leading to sufficient compaction at high loading [118, 151]. Further, the mortars reinforced with ZrO_2-modified fibers retain significantly higher mechanical strengths compared to those mortars reinforced with raw fiber or pre-treated fibers. That means ZrO_2-modified fibers can effectively improve the durability of their cement-based composites. This could be related to the compatibility between the fiber and the cement matrix, which will be discussed in the following section. As seen in **Fig. 3.12a**, the compressive strengths of C-R and C-P increased within the 28-d normal curing, followed by a considerable decrease during the wetting-drying cycles, a 16.3 % decrease for C-R and a 27.8 % decrease for C-P, respectively. However, for C-Z, the compressive strength continuously increased to 62.1 MPa until the third wetting-drying cycle and then only slightly reduced at the fifth cycle. It can be explained that the ZrO_2-modified fibers embedded into the cement matrix can provide an alkali-resistance film from the attack from the alkali cement hydration products as explained above. In terms of flexural strength shown in **Fig. 3.12b**, a similar trend, an increase within 28-d curing but a decrease in the period of the wetting-drying cycles, is observed for all the investigated composites. However, the degree of the trend is different, which is associated with fiber treatments. C-Z has an obvious increase in flexural strength within the initial 28-d curing and a slower reduction in the period of accelerated aging compared to C-R and C-P. By contrast, a sharp decrease in the initial three wetting-drying cycles was observed for C-P, which is attributed to the mineralization of the embedded pre-treated fibers, which has been explained in the section on thermal stability. Similar results are also reported in the literature [127]. Therefore, the ZrO_2 modification would be a quite potential approach to improve the durability of the NFRCCs.

Compatibility Analysis of the Composites

The interface property between fiber and cementitious matrix can directly influence the durability and mechanical strength of HFRCCs. Thus, in this work, it is necessary to evaluate the effect of ZrO_2 modification on the compatibility between the fibers and the cement matrix. The cross-compatibility index (CX) has been described in Chapter 2.3.

Table 3.3 presents the level of compatibility of the HFRCCs with different fibers (raw fiber, pre-treated fibers, and ZrO_2-modified fibers). According to the literature [88], three compatibility levels are divided: incompatibility level when the CX value is <40, moderate compatibility level when the CX value is between 40 and 80, and compatibility level when the CX value is> 80. It was seen that all HFRCCs have high compatibility index values, which exceed 90%. This can be attributed to the fact that hemp fibers have a relatively small amount of non-cellulosic substances (i.e. pectin, wax, and lignin) in comparison with other biomass fibers [89], which means less inhibition of the cement hydration. In comparison with C-R, both C-P and C-Z have relatively higher compatibility levels, which could be related to the removal of some extractives and sugars. Furthermore, for the case of C-Z with the highest compatibility level, there are several possible reasons associated with the synthesized ZrO_2 deposited on the fiber surface. Firstly, the ZrO_2 has a certain catalyze capacity which might accelerate the cement hydration reaction [136]; secondly, the fiber surface after ZrO_2 modification becomes quite rough (**Fig. 3.4**), which could benefit the mechanical interlocking of the interface in the composites [152] and increase the compatibility. Finally, the retardation effect on cement hydration reaction might be mitigated by the synthesized ZrO_2 layer that could prevent the fiber sugars components from directly contacting the cement matrix. Hence, the main conclusion is that ZrO_2 modification can benefit the compatibility increase between the fiber and cement matrix.

Table 3.3 The cross-compatibility indexes of hemp fiber-reinforced cement composites (see **Table 3.1**).

	Hemp fiber-reinforced cement composites		
	C-R	C-P	C-Z
Cross compatibility indexes (CX)	90.1%	94.2%	99.8%

3.3.4 Alkali resistance behaviors of ZrO_2: alkali hydrolysis and mineralization

To compare the alkali resistance behaviors (alkaline hydrolysis and mineralization) of different treated fibers particularly ZrO_2-modified fibers, the strength stability of the fibers immersed in different alkaline mediums was studied. The following results will describe the peak tensile strength of different treated fibers immersed in different liquid environments (Water, NaOH solution, and saturation $Ca(OH)_2$ solution) as a function of the days. In this research, the pH value (pH $\approx$ 12.5) in the NaOH solution was kept the same value as that in the saturation $Ca(OH)_2$ solution to compare the alkali hydrolysis of the fibers (from attacking of hydroxide ions) [29] with the fiber mineralization caused by $Ca(OH)_2$ [153]. Besides, to minimize the influence of the water content of fibers on their tensile strength, the investigated fibers should be dried at 60 °C before the test every time according to the literature [154]. Three different treated long fibers were used as investigated objects: raw fibers, pretreated fibers, and ZrO_2-modified fibers.

Fig. 3.13 shows the tensile strength of different treated fibers under various conditions. Before fogging, an increase in the peak tensile strength after the pretreatment (acetone treatment and alkali treatment) compared to that of raw fibers (126.9 ± 4.3 MPa). This was because the pretreatment process makes the fiber more flexible and softer by removing some non-cellulosic compounds. This result was also consistent with the literature [155, 156]. However, a slight reduction (5%) in the tensile strength after the ZrO_2 modification in comparison with that of pre-treated fibers. It is reasonably assumed that ZrO_2 particles attached to the fiber surface would restrict the movement of microfibril when the fiber is tensile, which is also confirmed by the SEM observation. Similar results are found in Ref [157].

As expected, only a small decrease in tensile strength as the increase of the days was observed for the ZrO_2-modified fibers regardless of immersion in any medium. In the water fogging environment depicted in **Fig. 3.13a**, the gradual decrease in the tensile peak of three different treated fibers may be related to microbiological action [158]. Meanwhile, the decreasing trend in ZrO_2-modified fibers is no remark compared to the other two fibers, which is attributed to the antibacterial property of synthesized ZrO_2 [159].

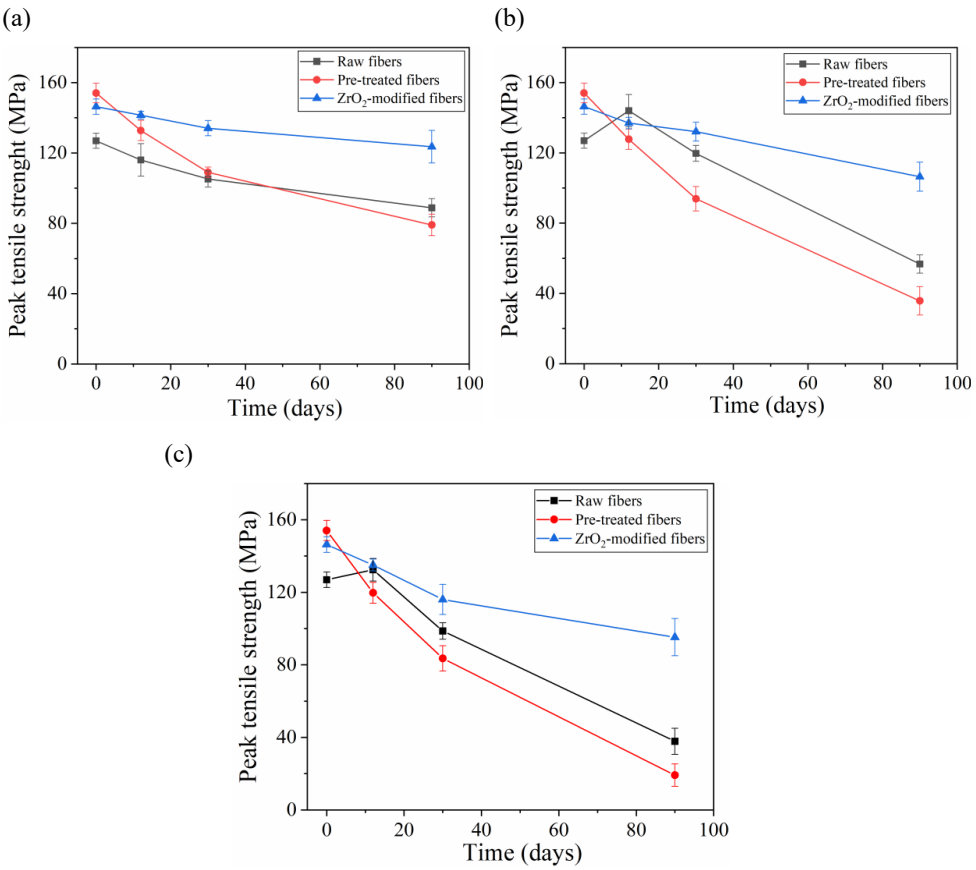

Fig. 3.13 Comparison of the peak tensile strength of untreated and treated hemp fibers (raw, pre-treated, and ZrO_2-treated) before (0 days) and after being immersed in the water (a), NaOH solution (b), and saturation $Ca(OH)_2$ (c) and for 12, 30 and 90 days.

As seen in **Fig. 3.13b** and **Table 3.4**, the pre-treated fibers experienced the most serious deterioration in the sodium hydroxide solution and decreased down to 76.8% of their initial strength after 90 days, whereas the fibers after ZrO_2 modification had the slowest drop in tensile strength (27.3%). Interestingly, it was observed that the peak tensile strength of raw fibers seems to be increased at the initial 3 days of storing in the alkali mediums. The reason is due to the removal of non-cellulosic substances from the fiber surface, which has already been mentioned above. In the case of the saturation calcium hydroxide environment (**Fig. 3.13c**), the fiber degradation suffers more severely than that in the sodium hydroxide solution, reflected by the data of tensile strength downtrend. It is well-known that saturation $Ca(OH)_2$ additionally leads to fiber mineralization [160] except for the alkali hydrolysis, thus providing a more aggressive

environment for the fiber. In comparison between the NaOH solution medium and saturation $Ca(OH)_2$ medium, it was seen that the decrease in tensile strength caused by only the mineralization was not considerable compared to the alkali hydrolysis. In addition, it was observed that after 90 days raw and pre-treated fibers retained, respectively, 70.2% and 87.6% of their original strength which have been lost completely after 200 days. The flexibility of the air-dried fibers could be pulled apart fairly easily by finger force. For the ZrO_2-modified fibers, the loss of the original tensile strength of fibers was relatively less (retaining 65.1%). Therefore, ZrO_2 modification not only could provide better alkali resistance behaviors (alkaline hydrolysis and mineralization).

Table 3.4 Strength loss of different treated fibers suffering in various alkali mediums after 90 d.

		Water	**NaOH**	**$Ca(OH)_2$**
Strength loss (%)	Raw	30.0	55.3	70.2
	Pre-treated	48.7	76.8	87.6
	ZrO_2 modified	15.6	27.3	34.9

3.4 Discussion

Durability tests on ZrO_2 modified fiber reinforced cement composites under accelerated aging conditions are an innovative measurement previously not focused on in the literature. Mechanical strength tests of the composites reinforced with different treated fibers (C-R, C-P, and C-Z) were conducted to evaluate their durability comparison. The mechanical strength behaviors of the composites can be well supported by the alkali resistance performances of embedded fibers and their compatibility with the cement matrix. In addition, the tensile strength measurement of different treated fibers (raw, pretreated, and ZrO_2-modified) in various controlled alkali solutions was carried out to compare alkali resistance behaviors: hydrolysis and mineralization. The results revealed the higher strengths of C-Z compared to C-R and C-P. It is caused by the presence of ZrO_2 which not only can prevent the degradation of fibers but also improve the compatibility between the fiber and the cement matrix. On the pre-treated fiber surface, according to EDS data, much portlandite and ettringite were observed which are prone to mineralization fibers, while the C-S-H phase is the main product precipitated on the ZrO_2-modified fiber which facilitates the interface adhesion (**Fig. 3.14**). Furthermore, the ZrO_2 modification exhibits greater resistance to the degradation caused by the alkali hydrolysis compared to the fiber mineralization.

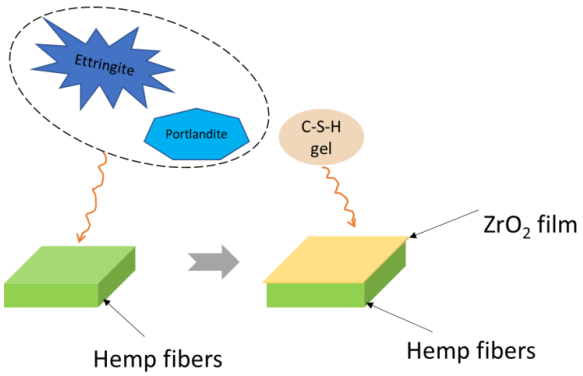

Fig. 3.14 The schematic of cement hydration products precipitated on the surfaces of unmodified and modified fibers.

The analyzed literature did not conduct the durability test on ZrO_2-modified reinforced cement composites under accelerated aging conditions. Boulos et al. [136] tested the mechanical strength of the composites reinforced with different treated fabrics within 90 days under normal conditions. The strength results of ZrO_2-treated fabric-reinforced cement composites were higher than untreated and pre-treated specimens. Nevertheless, the literature confirmed the alkali resistance effect of ZrO_2-treated fabrics and good interfacial adhesion to the matrix.

The literature [127, 136] demonstrated that the use of ZrO_2 can effectively reduce the degradation of natural fibers in cementitious materials by its resistance behaviours. However, without comparing the resistance of ZrO_2 to alkali hydrolysis and mineralization, it is difficult to fundamentally explain the alkali resistance behaviours in the cement matrix.

In some literature [158, 161, 162], the comparison of alkali hydrolysis resistance and the mineralization resistance of natural fibers was determined based on their strength loss immersing into the NaOH and $Ca(OH)_2$ solutions, respectively. The results show the strength loss of fibers in the $Ca(OH)_2$ solution is more severe than that in the NaOH solution. This is mainly attributed to the crystallization of lime in the fiber lumen, voids, and walls in addition to alkaline hydrolysis. As expected, the above deliberations prove the alkaline resistance comparisons of the unmodified fibers in this study (**Table 3.4**). However, there is no statement about the alkaline resistance comparisons of the ZrO_2-modified fibers. In light of this, the tensile strength measurement of the ZrO2-modified fibers after immersing in various alkali mediums, was carried out in this work. When the ZrO_2-modified fibers suffered in the NaOH solution, the

OH^- attack from the solution was effectively inhibited by forming a stable hydrated layer on the fiber surface due to the presence of ZrO_2 [163]. On the other hand, when exposed to $Ca(OH)_2$ solution, the strength loss of three fibers only caused by the mineralization was smaller than that caused by the alkali hydrolysis. This is because the fiber mineralization resulted from only $Ca(OH)_2$ here, rather than the complex cement hydration products ($Ca(OH)_2$, ettringite, and monosulfate) [160]. It is worth noting that only considering the strength loss caused by the mineralization, the degradation of ZrO_2-modified fibers is smaller compared to those of the other two treated fibers. This could be related to the formed ZrO_2 hydrated layer with selective permeability which is a certain resistance to the migration of (OH-, Ca^{2+}, and $Ca(OH)_2$) to the inner structure of the fibers, meaning the mitigated degradation process. Therefore, ZrO_2 modification not only could provide better resistance to alkali hydrolysis of fibers but also a certain extent alleviate the fiber mineralization.

In this study, an innovative fogging setup is designed to compare the alkali resistance behaviors mentioned above. If the modified/coated fibers were long-term immersed in the solutions, the modified/coated layer would be prone to be detached, affecting the experimental accuracy. Therefore, the common experimental setup (directly immersed fibers into various alkali solutions) used in the literature [158, 161, 162], is not suitable for modified/coated fibers. On the other hand, the fogging solution in the setup of this work avoids the problem of the peel-off of modified/coated layers from the fiber surfaces.

To sum up, ZrO_2-modified fibers reinforced cement composites, even under accelerated aging conditions, could efficiently improve durability due to their high alkali resistance performances and good interfacial adhesion to cement matrix. The use of NFRCCs is a good alternative to the high-carbon footprint production of traditional mortar/concrete materials, offering environmental and economic advantages. The results of this study can accelerate the practical application of NFRCCs, in particular in outdoor environments.

In this study, the feasibility of using ZrO_2 modification to enhance the durability of the composites under wetting-drying cycles was proven. However, the correlation between this accelerating aging and practical weather environment requires further study.

3.5 Conclusion

This work aimed to investigate the durability of hemp fiber (raw, pretreated, and ZrO_2-modified) reinforced cement composites under accelerating aging conditions. Relevant mechanical properties and micro-analyses of the composites were deeply investigated. The following findings are drawn.

(1) The pretreatment resulted in the decoloration of hemp fibers from dark brown to yellow mainly due to the removal of the non-cellulosic substances. Further, the modified fibers presented a white-yellow color and rough surface, which is related to the ZrO_2 film owing to the existing ZrO_2 film.

(2) The pretreatment and ZrO_2 modification of the fibers promoted their thermal stability, because of improved cellulose crystallinity index after hemicellulose and partial cellulose amorphous area removal, and the presence of insulator ZrO_2 film.

(3) During the normal curing period, the mineralization of the pre-treated fibers embedded in cement suffers the most severely evidenced by the much portlandite and ettringite precipitated on their surfaces. Whereas the C-S-H phases are the main products precipitated on the ZrO_2-modified fiber.

(4) Compared to the other two untreated and pretreated-fiber reinforced cement composites, ZrO_2-modified fiber-reinforced cement composites under accelerated aging conditions still maintain the highest mechanical strength. Cross-compatibility index calculations have proven that the compatibility level is better for the mortars containing ZrO_2-modified fibers which support higher mechanical properties when hemp fibers are within the cement.

(5) The alkali resistance test has demonstrated that alkali hydrolysis results in more significant degradation of fibers compared to mineralization. Importantly, the ZrO_2 modification exhibits excellent alkali resistance, regardless of both hydrolysis and mineralization.

It is necessary to highlight that the ZrO_2 modification can effectively improve the durability of hemp fiber-reinforced cement composites even though the composites are cured under harsh environmental conditions and the related alkali resistance mechanism of ZrO_2 in the NFRCCs

is revealed. We believe that these findings will help guide the practical application of NFRCCs. Nevertheless, it has to be mentioned that the current study still has some limitations the composites in this study have not yet been conducted into a practical application to test and related application cost lacks calculation. Thus, in future research, it is necessary to investigate the feasibility of the practical application of ZrO_2-modified hemp fiber-reinforced cement composites and expand the range of target natural fibers to increase the widespread application of the composites.

CHAPTER 4

4. Durability assessment of alkyl ketene dimer hydrophobic treatment of bio-based thermal insulation materials

Based on this paper:

H. Song, K. Hon, F. Gauvin, S. Pantaleo, F. Berger, W. Chen, and H.J.H. Brouwers. Durability assessment of alkyl ketene dimer hydrophobic treatment of bio-based thermal insulation materials (Submitted).

4.1 Introduction

In the building field, thermal insulation plays a role in achieving good building energy efficiency [164], by reducing heating and cooling loads under different climate zones. Current commercial insulation materials are mainly non-renewable materials such as mineral wool, polyurethane, polystyrene (expanded & extruded), aerogels, and other novel materials and designs like aerogels, gas insulation panels, and vacuum insulation panels [165]. Although exhibiting good thermal insulation capacity, these traditional materials still have different disadvantages: high production cost for aerogels; environmental pollution for fossil fuel-based materials, complex processing, and difficulty adjusted cutting for vacuum insulation panels and the like [165-167].

In recent years, in the context of climate change and a series of low-carbon policies announced [168], researchers in both academia and industry have been motivated to develop sustainable

insulation materials of biomass origin [169-171]. Bio-based materials are not only cost-effective and environment-friendly but also exhibit comparable hygroscopic, acoustic, and thermal insulation properties with commercial insulation materials. Panyakaew et al. [172] designed a new thermal insulation board using coconut husk and bagasse. The results showed that the bio-based composite board can meet the requirements of insulation fireboards except for swelling thickness. Kumfu et al. [173] evaluated the thermal properties of the insulation board compositing pineapple lead fiber and natural rubber latex. It was found that the thermal conductivity of this insulation board was 0.057 W/m*K with a low density of 338 kg/m^3. These studies confirm that bio-based composites have huge potential for insulation layer application.

Grass is a fast and easy-growing plant. There are large amounts of tonnes of grass mowed in the world per year. As reported by the water board [174], about 800 tonnes of grass is mowed annually in the Netherlands. Part can be used for composting, but large amounts of grass residues are still left, become biomass waste, and are stacked in the open air, which occupies a lot of land resources. Several studies [175-177] have explored the potential of manufacturing grass fibers into composites for thermal insulation. However, it has been observed that grass fibers experience significant deterioration under high humidity conditions [175].

Mycelium composites are comprised of organic fiber wastes through mycelium binding [178]. A lot of literature [178-180] has reported that mycelium composites can be exploited as insulation materials given that they feature excellent thermal performance, low density, biodegradability, low-carbon footprint, and low cost [181]. Appels et al. [182] manufactured the mycelium composites with different substrates: straw, sawdust, and cotton, and found that the mycelium composites are feasible as foam-like and natural materials in terms of density and elastic modulus. Besides, mycelium composites with multiscale hierarchical porous structures, constructed by randomly disordered poplar and birch sawdust, were found that lower thermal conductivity and high mechanical properties [183]. Yet, the critical disadvantage of high susceptibility to mould growth hinders the practical application in some structural materials such as panelling, flooring, and furniture [184].

According to the analysis of some researchers [175, 185-187], the above two bio-based insulation composites, due to their hydrophilic nature and high moisture absorption capacity, may feature poor thermal insulation properties and high mould growth risk. To address this,

various hydrophobic modification treatments have been undertaken to alter the moisture absorption characteristic of bio-based composites. For example, Lozhechnikova et al. [188] used carbauba wax particles to physically coat the wooden board toward energy efficiency. The results showed that the wax coating can effectively improve the hydrophobicity of the board surface. Kumar et al. [165] investigated the hydrophobic modification on the wood fibrous insulator surface using octadecyltrichlorosilane (OTS). They found that the modified wood fibers have higher resistance to fungi growth and condensate adsorption. These treatments achieve different levels of the hydrophobic effect, but they simultaneously bring some disadvantages: nonuniform coating, poor durability of the hydrophobic modification effect, and expensive modified agents. Thus, looking for a cost-effective hydrophobic modification agent is urgent for improving thermal insulation properties and mould resistance capacity to accelerate grass and mycelium composites in practical applications.

In Chapter 2, alkyl ketene dimer (AKD) has successfully been used to modify hemp fibers, demonstrating an excellent hydrophobic effect. To our knowledge, this AKD hydrophobic treatment has not yet been used in bio-based thermal insulation materials (grass and mycelium composites) in the building field. Furthermore, the effects of this hydrophobic treatment on the hygrothermal properties and mould growth resistance of both composites have not been investigated.

Thus, the main purpose of this work is to address research gaps concerning the use of two common bio-based composites, grass and mycelium composites, as thermal insulation materials. For this purpose, we investigate the physicochemical properties, hygroscopic properties, thermal performance, and mould growth resistance of applying AKD modification to enhance their durability. A simulated building envelope is presented to assess durability by analyzing the hygric properties and mould growth risk in different climates for years. The results found in this study provide insights into effectively upgrading the durability of common grass and mycelium composites through AKD modification, resulting in accelerating their practical application as thermal insulation materials.

4.2 Experimental

4.2.1 Materials

In this work, mycelium and grass bio-based composites were supplied by Fairm (the Netherlands) and Gramitherm (Belgium), respectively. The thickness in both mycelium and grass composites was measured at 35 mm and 60 mm, respectively. The physical appearances of both composites are characterized in **Fig. 4.1**. The mycelium composites mainly consist of Dutch agricultural biomass including miscanthus, flax, and straw bounded together by the fungal mycelium growth as the natural connector. For the grass composites, 72% grass fibers, 20% jute fibers from waste cocoa and coffee sacks, and partially waste polyester fibers are bounded through air laying and thermal press processes. The commercial Alkyl Ketene Dimer (AKD) emulsion was provided by Kemira ora (Finland).

(a) (b)

Fig. 4.1 Physical appearances of as-received mycelium composites (a) and as-received grass composites (b).

4.2.2 Methodology and relevant characterizations

The durability of mycelium and grass composites under AKD hydrophobic modification was evaluated. In particular, the basic physio-chemical properties, hygrothermal performances, and mould growth risk of both composites are tested using the following methodology (**Fig. 4.2**).

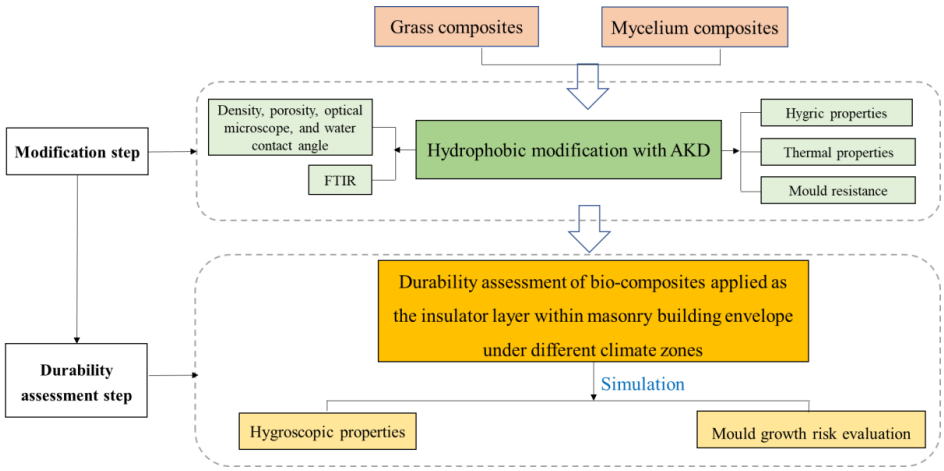

Fig. 4.2 Overview of this chapter.

Hydrophobic modification

Before the modification, mycelium composites (15 cm ×10 cm ×3.5 cm) and grass composites (15 cm ×10 cm ×6 cm) underwent an oven-drying process at 60 °C for 8 h. Subsequently, the dried composites were immersed in a 2.4% AKD emulsion for 12 h and token out. Following this, they were positioned in a fume hood to facilitate the evaporation of excess water before being transferred to an oven set at 105 °C for 6 h to promote the reaction between the fibers and AKD. Finally, the modified composites were cooled down to room temperature and seal-bagged for end use.

Performance characterization

The optical microscope observation, SEM plus EDS, and FTIR measurements were conducted according to the procedure described in Section 2.2.3.

Density and porosity

True density (ρ_{true}) measurements were conducted on a helium pycnometer (Micromeritics AccuPyc II 1340). Each composite was milled into the powder to break the existing pores/voids and directly filled in a sample cell (10 cm^3 volume size). The bulk density (ρ_{bulk}) of each

composite was directly calculated according to the shape volume. The total porosity (φ_{total}) of the composites was calculated with:

$$\varphi_{total} = 1 - \frac{\rho_{bulk}}{\rho_{true}} , \quad (4.1)$$

where ρ_{bulk} is bulk density in dry conditions and ρ_{true} is true density in dry conditions.

Water absorption/wettability characterization

According to the literature, the water absorption capacity *(WAC)* of both as-received and modified composites was tested through the weight difference between dry and saturation humidity conditions. Specifically, the unmodified/modified composites were initially dried and weighted (w_{dried}) before being saturated in water for 48 hours. After that, the composite samples were taken out, lightly blotted with a cloth to remove extra surface water, and finally weighted (w_{sat}). The water absorption capacity of the composites was calculated using:

$$WAC = \frac{w_{Sat} - w_{dried}}{w_{dried}} , \quad (4.2)$$

where w_{sat} is saturated weight, and w_{dried} is dried weight.
The wettability of investigated composites was evaluated and compared using the sessile drop method (Water contact angle measuring instrument, Dataphysics OCA30). The measurement was performed with an accuracy of 0.1° reading.

Hygroscopic properties

Given the high porosity resulting from the cellulosic fibers, the sorption isotherms (adsorption and desorption phases) of the bio-based composites are a very important characteristic and necessary to be measured according to the method of gravimetric sorption technique [189]. Before the test, the bio-based composite samples were oven-dried at 60 °C for 24 h to obtain their dry weight. The dried samples were placed into different sealed desiccators with constant relative humidity RH which was controlled by various saturated salt solutions [190]. In this work, the selected saturated salt types at 20 °C and their corresponding relative humidity were as below:

- Magnesium chloride hexahydrate ($MgCl_2$•$6H_2O$): 33% RH.
- Sodium bromide (NaBr): 59% RH.
- Sodium chloride (NaCl): 75% RH.
- Potassium chloride (KCl): 85% RH.
- Potassium sulfate (K_2SO_4): 98% RH

In terms of desorption, the same composites are switched from a high relative humidity chamber to a lower chamber. When the mass difference in consecutive two measurements 24 h apart is less than 0.1%, it was considered that the tested samples have reached the stable state. Simultaneously, the vapor diffusion coefficient (cm^2/S) of the composites is measured. In addition, the water absorption saturation of the composites is measured by immersing them into the water for 7 d, removing the surface water with a sponge, and weighing them.

The water vapor diffusion resistance factor μ is tested using the wet/dry cup methods following the standard EN-ISO 12572 [191]. The setup schematic is shown in **Fig. 4.3**.

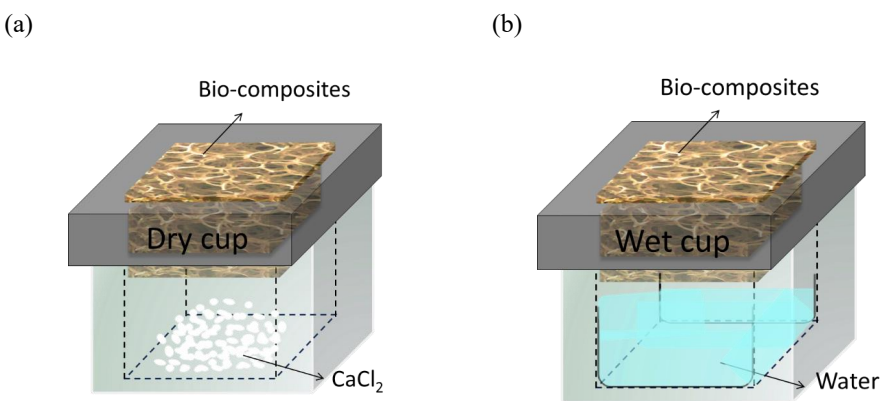

Fig. 4.3 Setup schematics of dry (a) and wet cup (b).

The anhydrous calcium chloride ($CaCl_2$) and water were used to prepare the dry cup and wet cup, respectively. The bio-based composite edges are sealed with aluminum tapers to prevent vapor from diffusing by the sample edges. The bio-based composites with a thickness *D* (m) are attached to the cups with an exposed area A (m^2). The test chamber environment was set at 20 ℃ and 60% RH. The entire cup containing samples was weighted until the calculated density of water vapor transmission rate g ($kg/m^2 \cdot s$) difference between two consecutive times (8 h

apart) was less than 5%. This was assumed that the steady state was reached. The density of water vapor transmission rate g is obtained according to:

$$g = \frac{\Delta m}{A * \Delta t}, \tag{4.3}$$

in which Δm is the mass changes of the entire cup; A is the exposed sample area and Δt is the time interval for testing specimen weight.

Accordingly, the water vapor diffusion resistance factor μ can be obtained using

$$\mu = \frac{\Delta P * \delta_{air}}{g * D}, \tag{4.4}$$

in which ΔP (Pa) is the partial pressure difference of water vapor; δ_{air} (kg/m*s*Pa) is the water vapor permeability of air.

Thermal properties

Thermal conductivity λ [W/(m*k)] was measured using the transient line source method equipped with a thermal needle probe (AP ISOMET heat transfer analyzer model 2104). The measurement device has an accurate of 5%. Before the test, the samples were first oven-dried at 50 ℃ for 24 h and then turned into a desiccator within silica gel. The purpose of this step is to keep an almost 0% RH environment. In the next step, the dried samples were also in controlled humidity chambers (50% and 80% RH) until their weight was unchanged. To avoid the disturbance of exterior moisture on the λ measurement, the tested samples were wrapped with low-permeability film. During the measurement period, the exterior temperature is set as 20 ℃. The values tested are the average of 5 trials.

Mould growth resistance

The hydrophobic modification on the mould growth resistance was assessed using the European Assessment Document EAD 040005-00-1201 [192]. Specifically, the tested bio-based composites were placed into desiccators filled with water to expose them to a higher humidity. The specimens were inspected at 0, 30, and 60 days later. The mould growth on

unmodified/modified bio-based composites was observed with the naked eye and using an optical microscope (Zeiss) at different magnifications, following ISO 846 [193].

Durability assessment of the composites

To evaluate the durability of the as-received/modified bio-based composites as the insulation layer within cavity walls in realistic weather conditions, a heat and moisture transport software WUFI Pro 6 with plug-in Bio component [194] was employed to simulate the hygrothermal performance and mould growth risk of the composites in ten years. The analysis is focused on the interfaced bio-based composite layers next to the exterior and interior sides. Within WUFI Pro 6, the non-steady heat and moisture transport process can be calculated by following coupled equations:

$$\frac{\partial H}{\partial T}\frac{\partial T}{\partial t} = \frac{\partial}{\partial x}\left[\lambda \frac{\partial T}{\partial x}\right] + h_v \frac{\partial}{\partial x}\left[\frac{\delta}{\mu}\frac{\partial p}{\partial x}\right] \tag{4.5}$$

and

$$\rho_w \frac{\partial w}{\partial \varphi}\frac{\partial \varphi}{\partial t} = \frac{\partial}{\partial x}\left[\rho_w D_w \frac{\partial w}{\partial \varphi}\frac{\partial \varphi}{\partial x}\right] + \frac{\partial}{\partial x}\left[\frac{\delta}{\mu}\frac{\partial p}{\partial x}\right], \tag{4.6}$$

respectively, in which H ($J \cdot m^{-3}$) is the enthalpy, λ ($W \cdot m^{-1} \cdot K^{-1}$) is the thermal conductivity, T (℃) the temperature, h_v ($J \cdot kg^{-1}$) the evaporation enthalpy of water, p (Pa) the water vapor partial pressure, μ (dimensionless) the vapor diffusion resistance factor, ρ_w ($kg \cdot m^{-3}$) the density of water, δ ($kg \cdot m^{-1} \cdot s^{-1} \cdot Pa^{-1}$) the water vapor diffusion coefficient in air, D_w ($m^2 \cdot s^{-1}$) the liquid transport coefficient, and φ (dimensionless) the relative humidity RH.

The profiles of temperature (T) and relative humidity (RH) are set as the boundary conditions:

$$T(x = L, 0 \le t \le 10\ years) = 20\ ℃\ . \tag{4.7}$$

$$RH(x = L, 0 \le t \le 10\ years) = \text{ISO13788}\ with\ humidity\ class\ 3\ \text{(ISO13788, 2012)}\ . \tag{4.8}$$

$$T(x = 0, 0 \le t \le 10\ years) = Climate\ profile\ . \tag{4.9}$$

$$RH(x = 0, 0 \le t \le 10\ years) = Climate\ profile\ . \tag{4.10}$$

The design of the assembly wall was based on the most common solid brick cavity wall type. Specifically, the masonry exterior walls |(2×110 mm) within filling the tested bio-based

composites (60 mm) and air layer (40 mm), as illustrated in **Fig. 4.4**. To evaluate the durability of the bio-based composite specimens confronting different climates, eight distinct climate zones distributed in the world were selected as input for the hygrothermal modeling. **Table 4.1** summarizes the annual weather conditions including temperature, humidity, wind speed, and rainfall precipitation for all eight locations [195]. Climate Cfb is represented by Amsterdam with a marine west coast climate, Climate Aw for Hainan with a tropical wet and dry or savanna climate, Climate Dwb for Heilongjiang with a humid continental, severe dry winter, warm summer climate, Climate Bsh for New South Wales with a subtropical steppe climate, Climate Csa for Alger with Mediterranean, hot summer climate, Climate Bwh for Lima with a subtropical desert climate, Climate Cfa for New York with a humid subtropical, no dry season climate, and Climate Dfc for British Columbia with a subartic, severe winter, no dry season, cool summer climate. The hygrothermal simulation runs for ten years and the data of the final year is extracted for special analysis on hygric content on both interior and exterior surfaces of bio-based composites using WUFI Pro 6. Moreover, according to the hygrothermal results, the mould growth risk is assessed using WUFI Bio 4.0 plug-in component.

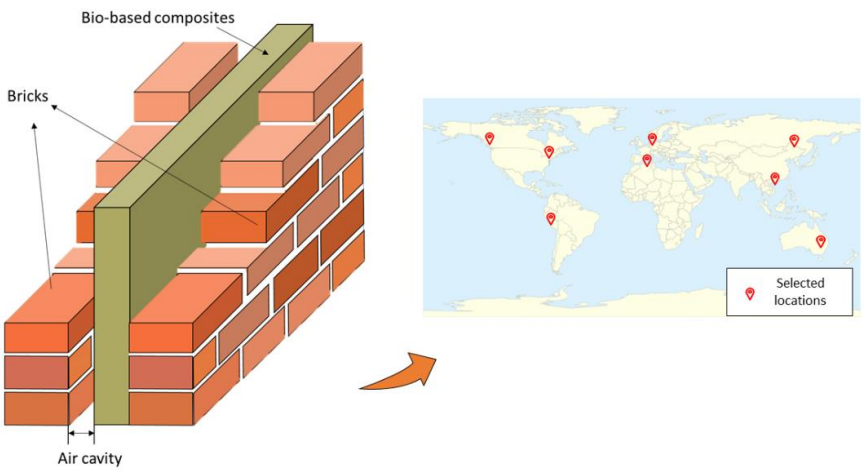

Fig. 4.4 The designed assembly wall and its simulation application under selected locations under distinct climate zones (X_i represents the monitoring point of the bio-based insulation composites facing the interior side, and X_e represents the monitoring point to the exterior side).

Table 4.1 Summary of climate profile for simulated exterior weathers, sourcing from (Kőppen climate classification description: A, tropical; B, arid; C, temperate; D, continental, a, Hot summer; b, Warm summer; c, Cold summer; h, Hot; w, Dry winter; f, No dry season; s, Dry summer.).

Climate zone (Köppen)	Location	Altitude (m)	Average temperature (°C)	Average relative humidity (%)	Average wind speed (kmh)	Average annual rainfall precipitation, (mm)	Driving rain direction, main	Counter radiation, sum ($kWh.m^{-2}$)
Cfb	Amsterdam, NL	None	11.7	79.5	20.9	99.1	SW	2754
Aw	Hainan, CN	44	25.7	81.7	17.5	76.1	East	3566
Dwb	Heilongjiang, CN	386	3.1	76.3	10.5	40.4	NE	2151.4
Bsh	New South Wales, AU	187	21.1	54.7	20.5	24.0	NW/SE	2696.6
Csa	Alger, DZ	31	19.3	65.9	11.9	35.4	West	2895.7
Bwh	Lima, PE	136	20.8	77.3	10.8	2.1	South	3163.3
Cfa	New York, US	13	13.3	72.3	12.7	80.0	NE	2642
Dfc	British Columbia, CA	1121	5.0	85.5	4.4	145.5	SE	2680.6

4.3 Results and discussion

4.3.1 Physical-chemical properties and bio-hygrothermal performances of bio-based insulation composites

Physical properties

The physical properties of bio-based composites, which are affected by the type of natural fibers, chemical characteristics, and manufacturing processing, directly determine their insulation performance. To understand the physical property variance, basic important properties such as thermal conductivity, specific heat, bulk density, apparent density, and porosity of as-received and modified bio-based composites are tested in **Table 4.2**. Although highly different, these basic physical properties can meet the requirements of traditional insulation materials with comparable thermal conductivity in the range of 0.03-0.06 W/m*K. Compared to the mycelium composites, the grass composites have lower thermal conductivity, and higher porosity regardless of the modification treatment. This indicates that grass composites possess better insulation performance. Similarly, after the AKD modification, the general insulation performance has improved in comparison with their as-received mycelium and grass,

respectively. However, the porosity of modified composites gets slightly decreased because the formation of AKD wax membrane can cover the voids of the fiber surface and pores between the interwoven fibers [196]. Despite this, the AKD wax deposited on the fiber surfaces potentially increased thermal insulation performance by increasing the thickness of average fibers, which can be observed via optical microscope imaging (**Fig. 4.5**).

Table 4.2 The basic physical properties of the mycelium composites and grass composites before and after the modification.

	As-received mycelium	**Modified mycelium**	**As-received grass**	**Modified grass**
Thermal conductivity [W/(m*K)]	0.0546	0.0518	0.0484	0.0456
Specific heat capacity [J/(kg*K)]	1084	953	1686	1397
Bulk density [kg/m^3]	174.3	178.1	93.5	100.2
True density [kg/m^3]	1187.7	1165.2	1192.0	1209.4
Porosity [%]	85.3%	84.7%	92.2%	91.7%

Therefore, the morphology of the composite is distinctively different before and after AKD modification. In the case of as-received mycelium composites, the loose and fogging-white mycelium ligaments were covered on the fiber surfaces. While the milky-white substances from dried AKD wax and mycelium ligaments are observed on the surfaces of the modified mycelium composites. In terms of the grass composites, the semi-transparent white wax was coated on the fiber surface after the modification. Noticeably, the surface colour becomes yellow after the AKD modification. This is related to the AKD dispersion solution. One of the dispersions, cationic starch, gets yellow after the water molecules removal during the drying process [197], thus resulting in composite yellowing.

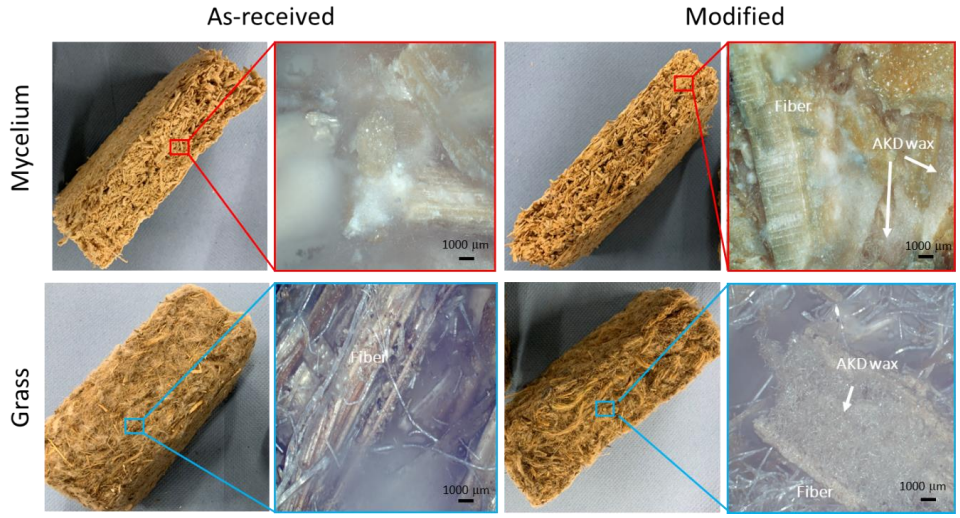

Fig. 4.5 Morphologies of mycelium composites and grass composites before and after the AKD modification.

All these morphology observations suggest that the AKD was covered on the surfaces of fibers within the bio-based composites. To better and deeply understand the chemical reaction mechanism in the modifying process, we analyzed the variation of chemical function groups and element ratio of the fiber surfaces in the following section.

Chemical analyses

The surface OH groups of cellulosic fiber are the dominant reason for the hydrophilicity of bio-based composites. To alter the hydrophilic nature, hydrophobic groups are often introduced on the fiber surfaces. Hence, in this study, the AKD with long-carbon chains (about 12-17 carbon) are grafted on the OH groups of the fibers, as illustrated in **Fig. 4.6a**. The linkage reactions between AKD and OH groups consist of two ways: hydrogen-bonded and covalently bonded [198]. The FTIR spectra curves of as-received and modified composites in this study are displayed in **Fig. 4.6b** and corresponding characteristic peaks are listed in **Table 4.3**. All investigated composites have similar spectra curves because of similar studied bodies: cellulosic fibers. For example, the cellulosic characteristic peaks at 2925 cm^{-1}, 2850 $cm^{-1,}$ and hemicellulose peak at 1728 cm^{-1} are found in all spectra curves. However, the intensity of some peaks is distinct. In the case of mycelium composites, The broad peat at about 3330 cm^{-1} represents the OH stretching: intermolecular hydrogen bonds and intramolecular hydrogen

bonds [199]. After AKD modification, the peak in mycelium composites became flatter, indicating that AKD molecules were primarily covalently bonded to the cellulose molecules. This resulted in a reduction in the number of hydrogen bonds generated by both the cellulose molecules themselves and their interaction with water molecules. In contrast, the peak in the grass composites became thinner and steeper, implying that the combination between AKD molecules and grass cellulose OH was mainly hydrogen bonded. Additionally, the intensities of the peaks at 2920 cm^{-1} and 2850 cm^{-1}, corresponding to C-H antisymmetric stretching and C-H symmetric strength, increased in both modified composites due to the introduction of long-chain alkyl groups. Furthermore, the presence of broken lactone ring peaks at 1703 cm^{-1} in both modified composites indicated that reactive AKD molecules were chemically grafted onto the cellulosic molecules. However, the peak at 1845 cm^{-1} suggests the presence of partially unreacted AKD on the fiber surfaces.

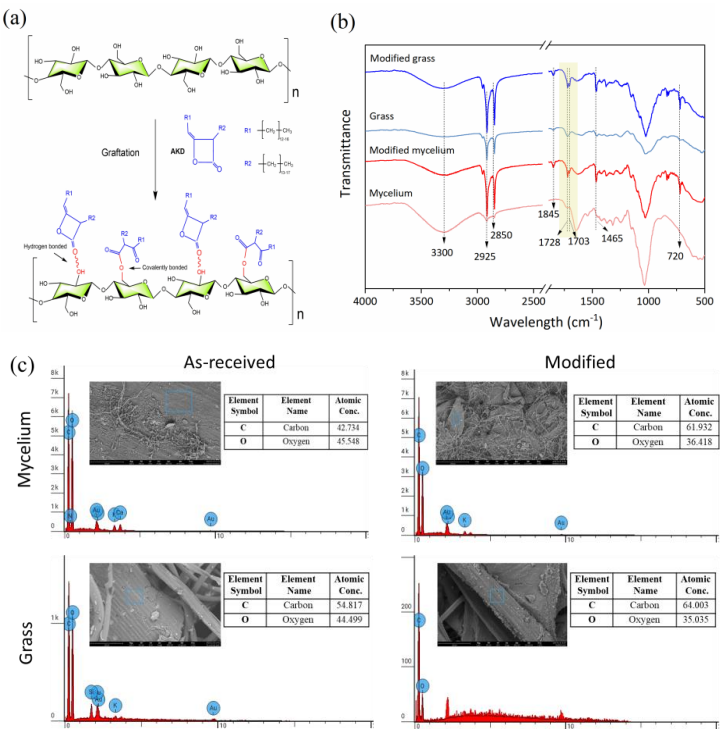

Fig. 4.6 Hydrophobic mechanism for bio-based composites humidity resistance: (a) molecular grafting reaction of AKD on different composites cellulose. (b) the FTIR spectra of as-received/modified bio-based composites. and (c) the C/O element ratio variation before and after the modification.

In addition, the C/O element ratio on the fiber surfaces is an important parameter for identifying surface group variation (**Fig. 4.6**). Before AKD modification, the C/O ratio was approximately consistent with cellulose molecules: $(C_6H_{12}O_6)_n$. However, after the modification, the C/O ratio increased to approximately 2, indicating that more groups containing carbon were covered on the fiber surfaces.

Table 4.3 FTIR peak assignments for as-received and modified bio-based composites.

Wavenumber (cm^{-1})	Assignment	Component	References
3300	O-H stretching vibration of hydroxy groups	Cellulose molecular/or AKD-hydrogen-bonded to cellulose	[63, 198]
2925	C-H asymmetric stretching from CH_3	cellulose and/or AKD molecular	[63]
2850	C-H stretching vibration from CH_2	cellulose and/or AKD molecular	[86]
1845	Lactone ring	lactone ring of AKD (unreacted)	[86]
1728	C=O stretching (unconjugated)	Hemicellulose and/or AKD	[63]
1703	β-ketone ester	Broken lactone ring of AKD (reacted)	[86]
1465	C-H stretching vibration from CH_2	AKD molecular	[86]
720	C-H stretching vibration from CH_2	AKD molecular	[86]

Consequently, all these chemical analysis results suggest that AKD, with a hydrophobic role, has been successfully grafted onto the bio-based composites. Therefore, in the following section, the hydrophobic effect in both composites was investigated.

Hygroscopic properties

The hygroscopic property of bio-based composites plays a key role in the insulation materials. Here, we studied some important hygroscopic properties, i.e., water vapor resistance factor μ, water absorption capacity, and water contact angle results of the bio-based composites. The results are listed in **Table 4.4** and **Fig. 4.7**. The μ factor value of the mycelium composite is twice

that of the grass composite regardless of under dry or wet cup conditions. This distinct μ factor between them is attributed to different apparent densities and thicknesses [200]. However, a neglect influence of the AKD modification under the same condition was found for the μ factor of the composites. In terms of water absorption capacity, AKD modification reduces the hydrophilic nature of the composites, which results in a close to a half-time reduction in water absorption weight, and a more noticeable decrease was observed in the case of grass composites, up to 50.1%. The reduced hydrophilic behavior is also further confirmed by the water contact angle test through the sessile drop method and such relatively substantial alteration is observed in grass composites.

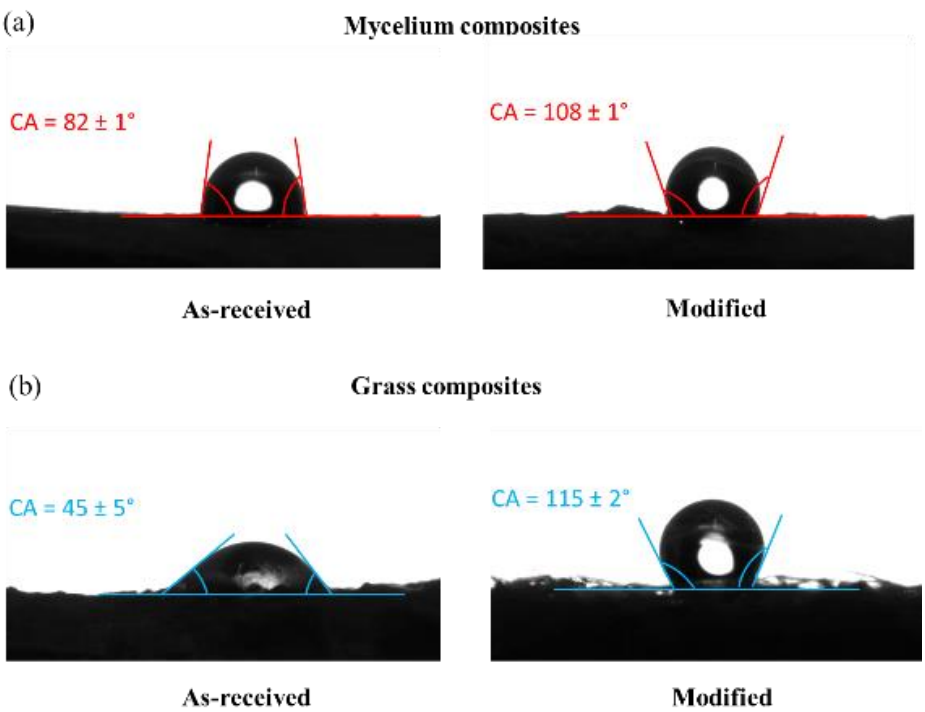

Fig. 4.7 Sessile drop water contact angle images of (a) mycelium and (b) grass composites before and after the AKD modification.

Table 4.4 Hygroscopic properties of unmodified and modified bio-based insulation composites.

		As-received mycelium	Modified mycelium	As-received grass	Modified grass
Water Vapour Resistance Factor μ	"Dry cup" condition	4.0	4.0	1.9	2.0
	"Wet cup" condition	3.1	3.3	1.4	1.5
Water absorption capacity (*WAC*, %)		451	269	776	387
WAC decrement (%)		40.4		50.1	
Water contact angle (°)		82 ± 1	108 ± 1	45 ± 5	115 ± 2

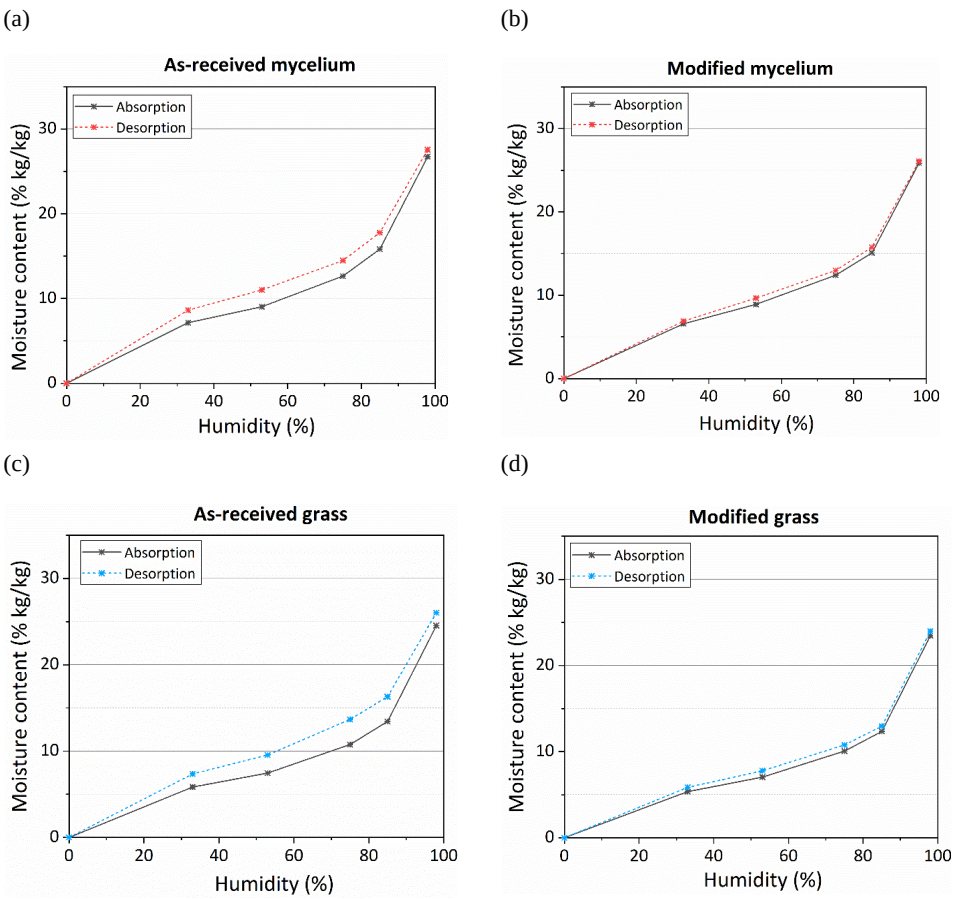

Fig. 4.8 Absorption and desorption isotherm curves: plots of moisture content against relative humidity of mycelium composite (a), modified mycelium composites (b), grass composites (c), and modified grass composites (d).

In addition, both as-received composites exhibited a typical sigmoidal profile and significant hysteresis phenomenon between adsorption and desorption phases (**Fig. 4.8a** and **c**). These are the common features of hygroscopic bio-based composite materials [201, 202]. Specifically, as-received grass composites have a more distinct hysteresis phenomenon at around 75% RH than their counterpart mycelium composites. The smaller pores within the grass composites accelerate the moisture absorption kinetic and maintain the moisture content due to the capillary force role [203]. This explanation is also confirmed by the morphology observation (see **Fig. 4.5**). However, after AKD modification, the non-typical sigmodal profiles, and low hysteresis features are shown in two composites because of the hydrophilic alteration of the cellulosic fibers and pores filled with AKD wax.

In summary, AKD modification comprehensively reduces the hygroscopic properties of bio-based composites, especially grass composites. The reduced hygroscopic behavior will likely affect the thermal conductivity [171] and mould growth [30, 204], so next, we investigate the correlation between thermal conductivity and hygroscopic moisture (section 3.1.4), as well as the association between the mould growth risk and hygroscopic moisture (section 3.1.5), respectively.

Thermal properties

Thermal conductivity λ, is the most direct reflection of thermal insulation materials. A study of changes in the thermal conductivity for two composites before and after the modification at various RH conditions (related to moisture content) is summarized (**Fig. 4.9**). These results illustrate that the thermal conductivity increased with relative humidity, with a general linear trend, which is in accordance with data in the literature [175, 201]. Meanwhile, the linear results are as input for following hygrothermal modelling using WUFI software. In addition, the thermal conductivity λ at various RH was tested with the thermal needle probe under steady-state conditions. The composites after AKD modification show an overall lower thermal conductivity under different RH compared with their corresponding as-received ones. This indicates that AKD introduction can improve the thermal insulation capacity of bio-based composites by reducing hygroscopic moisture. Among all studied composites, modified grass composites have the lowest value of thermal conductivity (47.9 $mW \cdot m^{-1} \cdot K^{-1}$), followed by as-received grass composites (52.1 $mW \cdot m^{-1} \cdot K^{-1}$) and slightly higher value (56.3 $mW \cdot m^{-1} \cdot K^{-1}$) of modified mycelium composites, while as-received mycelium composites have

the highest thermal conductivity, at the mean value of 61.9 $mW \cdot m^{-1} \cdot K^{-1}$. According to these comparative results, grass composites with lower thermal conductivity are recommended, in particular with AKD-modified. Furthermore, these values of conductivity are lower than those of reported other organic insulation materials such as about 105 $mW \cdot m^{-1} \cdot K^{-1}$ for wood chip board and 70 $mW \cdot m^{-1} \cdot K^{-1}$ for wood wool board [205].

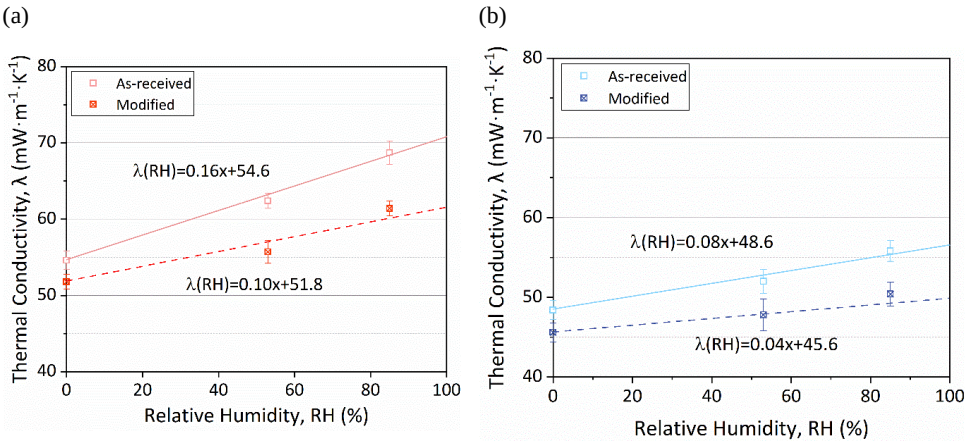

Fig. 4.9 Thermal conductivity λ VS relative humidity RH for mycelium composites (a): as-received and modified, and grass composites (b): as-received and modified.

Mould growth risk

Another moisture-dependent mould growth risk is a key criterion for evaluating the durability of bio-based composites. In this study, the tested bio-based composite samples are subjected to high humidity conditions to inspect the mould growth for two months (60 days). Besides the visual inspection, the mould indexes also called the *VTT* model based on laboratory studies [206], were employed here to quantify the intensity of the mould growth. The photos and their partially magnified microscope images at 0, 30, and 60 days are illustrated in **Fig. 4.10**, and corresponding quantitative results are listed in **Table 4.5**.

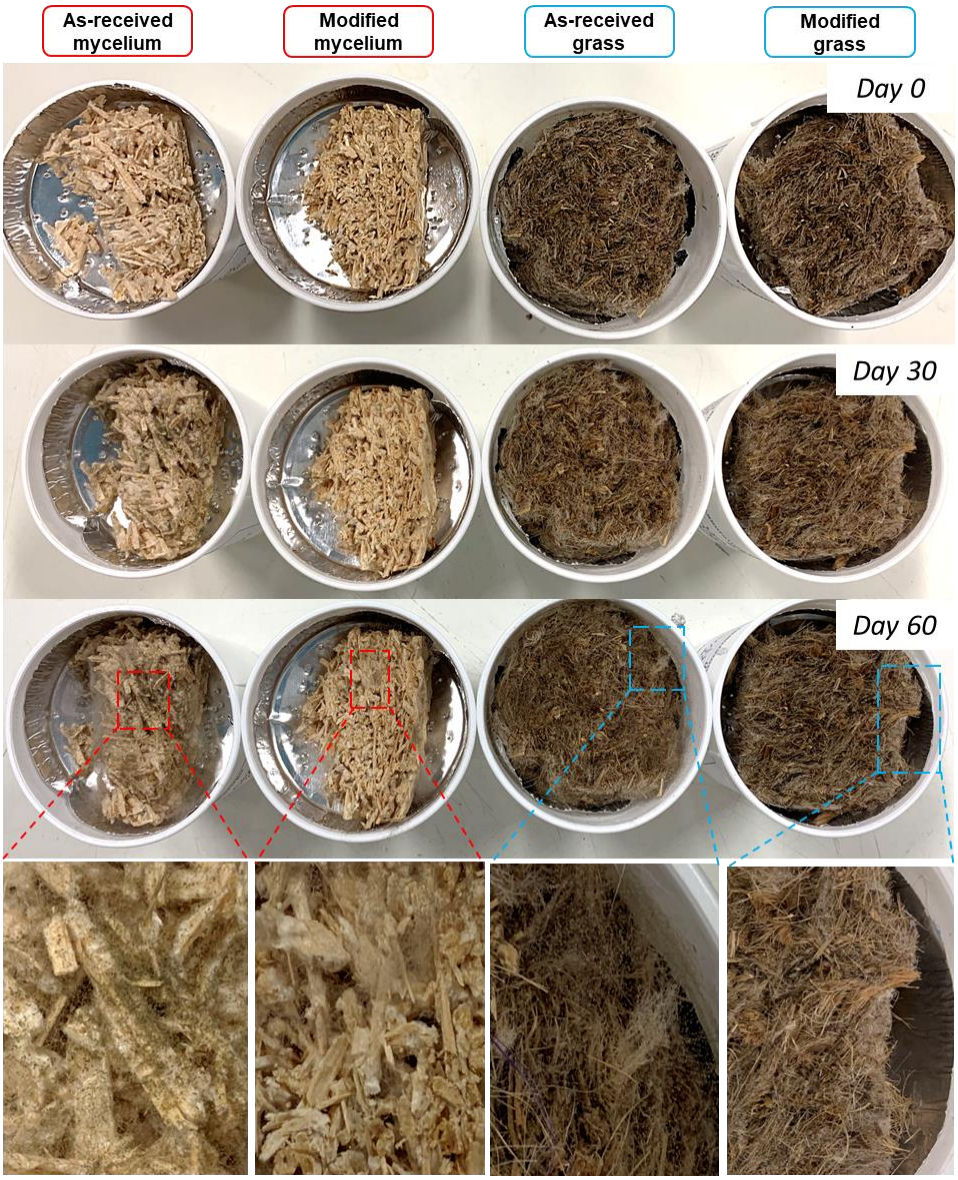

Fig. 4.10 Mould resistance tests on the mycelium and grass composites (as received and modified). Photos and magnificent optical micro photos are taken on day 60.

By the end of the initial 30 days, with the naked eye, a small but significant portion of mould growth on the surface of as-received mycelium composites, while no obvious mould growth is exhibited on the surfaces of the other three composites including as-received grass composites. According to this, three investigated composites such as modified mycelium composites and

both as-received and modified grass composites have good mould-resistance capacity and are suitable to use as insulation components. However, by the end of the 60 days, the as-received mycelium composites have been fully covered by the mould hyphae and intensive spores, but only minor mould hyphae have begun to grow on the surface of modified mycelium composites. In terms of grass composites, a certain area portation of mould with spores visually has been grown on the surface of as-received grass composites, while no mould growth is visibly found on the surface of modified grass composites. These comparative results indicate that AKD hydrophobic modification makes the bio-based composites very resistant to mould growth. This aligns with the literature where the hydrophobic treatment using Octadecyltrichlorosilane (OTS) is resistant to microorganisms attack and against mould growth on the wood fibrous thermal insulator [165]. Additionally, compared to mycelium composites, grass composites exhibited better mould-resistance capacity, which also has been found in the previous study [175]. This is because higher ratios of lignin and wax against sugar content (cellulose-hemicellulose cellulose and hemicellulose) of grass fibers protect their sugar content from attacking by microorganisms and thus delay their degradation into simple sugars that could provide some nutrition for mould growth [207-209].

Table 4.5 Quantity evaluation of mould growth index.

Bio-based insulation composites	The intensity of mould growth	60-day evaluation
As-received mycelium	5(3)	Heavy and tight growth, coverage about 100%
Modified mycelium	1(0)	Small amounts of mould on the surface, the initial stage of local growth
As-received grass	3(0)	Visual finds of mould on the surface, up to 10 % coverage of mould
Modified grass	0(0)	No growth

Noting: The bracket numbers represent the mould growth intensity at the 30-day evaluation and the numbers out of the brackets represent the mould growth intensity at the 60-day evaluation.

Consequently, following AKD modification, both composites, particularly the grass composites, have improved mould-resistant capabilities. In addition, considering future practical

applications, it is necessary to evaluate the durability of bio-based composites used as insulation materials under distinct climates in the next section.

4.3.2 Durability assessment of using bio-based composites simulated as the insulation layer

Hygric performance of the bio-based composite layer

The hygric content of bio-based composites has a positive correlation with mould growth risk that can negatively determine their durability [210-212]. Thus, the moisture contents of two interfaces to both exterior and interior sides of tested bio-based composites are computed considering these interfaces are readily points for moisture accumulation. The simulation period is preset ten years and the hygric results of the final year are extracted and plotted in **Fig. 4.11**. Moreover, to assess the different climate suitability of tested bio-based composites that expand their future application spread, eight distinct climate types i.e., Cfb, Aw, Dwb, Bsh, Csa, Bwh, Cfa, and Dfc distributed in the world are selected (see **Table 4.1**).

Across all climate types, both modified bio-based composites exhibit relatively lower average moisture content regardless of which interface compared to their original ones. In other words, AKD modification can effectively prevent the moisture content from retaining inside the bio-based composites, consequently potentially delaying the mould growth risk and improving durability. Interestingly, the grass composites exhibit higher average moisture content than the mycelium composites under most climate types except for Aw (Hainan). This result is in agreement with their water absorption capacity likely due to smaller size pores and higher porosity of grass composites and the opposite for mycelium composites (**Table 4.2** & **Table 4.4**). Only considering this point of simulated moisture content, therefore, it seems that modified mycelium composites slightly lower the risk potential of mould growth than modified grass composites. However, in fact, besides the moisture content factor, other factors i.e., sorption-desorption rate, fiber types (the ratio of lignin and wax to cellulose and hemicellulose), and binder type influence the mould growth. So next, we use WUFI-Bio to more directly and more accurately predict the mould growth risk.

(a)

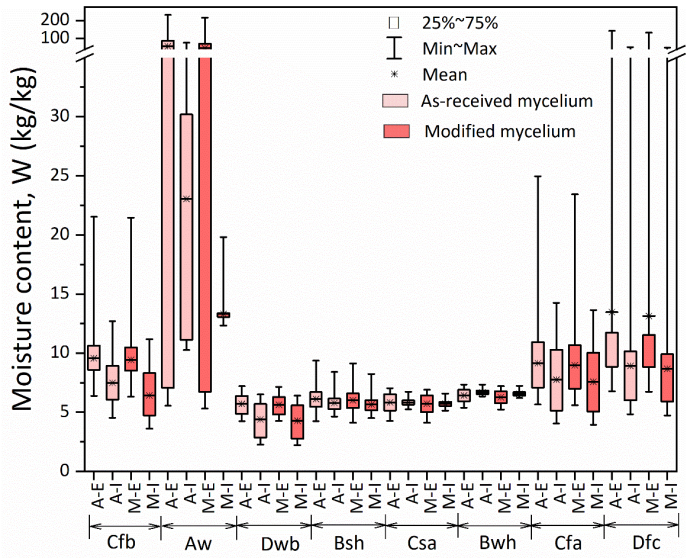

(b)

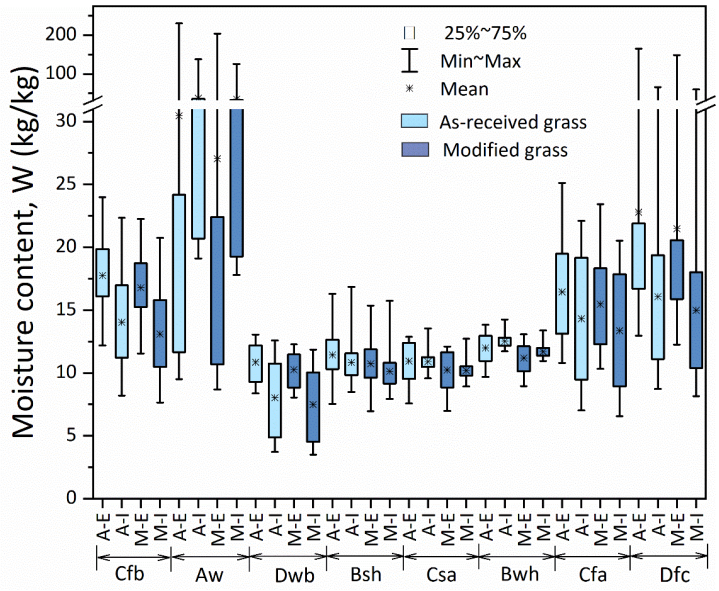

Fig. 4.11 Simulated moisture content results of bio-based composites (a, mycelium composites & b, grass composites) in the designed assembly wall under distinct weather climates (see **Table 4.1**). Noting that A, represents As-received; M, Modified; E, the interface of the bio-based composite layer to the exterior side; and I, the interface of the bio-based composites layer to the interior side.

Mould growth risk evaluation

Fig. 4.12 summarized mould growth risk simulated results of the bio-based composites within the assembly walls under selected distinct climates using WUFI-Bio. Within this simulation, mould growth rate above 239 mm/year represents an unacceptable risk level, while below 176 mm/year represents no risk, and the value between them represents a possible risk and requires a specific evaluation.

Based on the internal comparison of between as-received and modified mycelium composites in **Fig. 4.12a** and between as-received and modified in **Fig. 4.12c**, these results support the hypothesis that the reduced hygric property in bio-based composites, which resulted from AKD hydrophobic modification, contribute to their higher resistance to mould growth compared to their as-received ones. According to **Fig. 4.12a** and **b**. out of the eight cases that represent typical climates, modified mycelium composites can be applied to three climate types: Dwb (Heilongjiang), Bsh (New South Wales), and Csa (Alger), in which their values are almost all below the green line (176 mm/year) with no mould growth risk. Whereas only the Dwb (Heilongjiang) case is possibly suited for original mycelium composites because the mould growth risk of the interface to the exterior is between the thresholds. Similar behavior is found in the grass composites (**Fig. 4.12c** and **d**). For modified grass composites, up to four climate cases have no mould growth risk. Besides the three climate cases above, the additional Bwh (Lima) case can be suited for modified grass composites. However, this Bwh (Lima) case could not be suited for original grass composites as the mould growth rate of their interface to the interior side is exceedingly over the mould growth threshold. To sum up, these findings indicate that AKD hydrophobic modification can not only effectively decrease the mould growth risk, enhancing the durability of bio-based composites, but also broaden the climate suitability range and application range of the bio-based composites when used as insulation materials in multi-assembly walls.

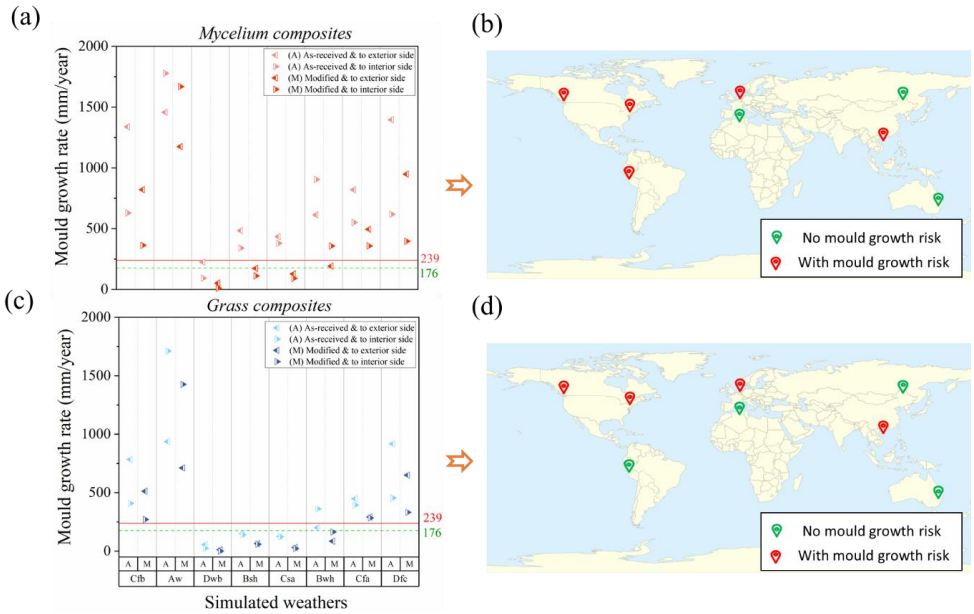

Fig. 4.12 Simulated results of bio-based composites as the insulated layer (a) mould growth rate of two interfaces of mycelium composites (as-received & modified) to both exterior and interior sides under distinct climate types, (b) their mould growth risk evaluation in corresponding locations, (c) mould growth rate of two interfaces of grass composites (as-received & modified) to both exterior and interior sides under distinct climate types and (d) their mould growth risk evaluation in corresponding locations.

4.4 Conclusion

This present work aims to explore the feasibility of using renewable bio-based composites, namely mycelium and grass composites, as substitutes for conventional insulation materials. The study investigates the effectiveness of hydrophobic treatment on two bio-based insulation with AKD on the physicochemical properties, hygrothermal performance, and mould growth risk. Furthermore, the study evaluates the durability of the bio-based insulation composite layer within assembly walls under different climate types by analyzing hygric property and mould growth risk using a bio-hygrothermal simulation approach. The main findings from this study are as follows.

(1) The optical microscope observation confirmed the deposition of AKD wax on the cellulosic fiber surfaces and FTIR analysis and element ratio variation from EDS revealed the bonded

mechanism: hydrogen-bonded and covalent-bonded between the AKD and cellulosic OH groups. The long-chain alkyl groups of AKD were introduced on the fiber surfaces, enhancing the hydrophobic effect which was confirmed by water absorption capacity and sessile drop water contact angle results.

(2) After the AKD modification, some hygroscopic properties and thermal conductivity of both bio-based insulation composites were not only reduced but also significantly improved the resistance of their cellulosic fibers towards the mould growth under high humidity conditions.

(3) According to the simulation results of application in different climate types, AKD modification can decrease the hygric property of both composites within the designed assembly wall regardless of the climate types. Meanwhile, we found that decreased hygric properties of modified composites were advantageous to prevent mould growth, increasing suitability under distinct climate types.

To conclude, both modified bio-based insulation composites, in particular modified grass composites, demonstrate significant potential as thermal insulation materials, characterized by lower hygric performance, lower thermal conductivities, higher mould-resistance ability, and better suitability to climate types compared to as-received composites. Further experimental investigations are warranted to assess the feasibility of AKD-modified bio-based composites used within real assembly walls and under real weather conditions.

CHAPTER 5

5. Effects of plant fibers incorporation on blended binders containing MSWI bottom ash

Based on this paper:
H. Song, T. Liu, and F. Gauvin. Application of plant fibers incorporation on municipal solid waste incineration bottom ash (MSWI BA) as binder substitute: mechanical strength and leaching evaluation (submitted and related patent filed).

5.1 Introduction

The municipal solid waste (MSW) globally increased from 2.3 to 3.1 billion tonnes in recent years (2014-2019) and the MSW produced worldwide is projected to be around 4.54 billion tonnes by 2050 [213]. An enormous amount of MSW is deposited by landfilling or incineration. The treatment approach of landfilling has higher fees, largely occupied lands, and environmental pollutants, but the incineration of MSW can decrease its mass (by 70%) and volume (90%) [214]. Therefore, incineration is an effective way to treat solid waste and is more widely accepted. In developed countries, the percentage of incineration treatment can reach up to 62% [215]. However, after the incineration, a considerable amount of bottom ash is left, which accounts for around 80% by weight among all solid residues [216].

Previous studies [217, 218] have shown that Municipal Solid Waste Incineration Bottom Ash (MSWI BA) has similar chemical components and pozzolanic reactions to other supplementary

cementitious materials like fly ash silica fume, and ground-granulated blast-furnace slag. These studies indicate that MSWI BA can be directly used as a cementitious material to partially replace cement [219]. Nevertheless, it was also widely agreed that the leaching problem and low compressive strength of MSWI BA hinder its application in the building field. For instance, a study showed that the low strength is caused by the amount of metallic aluminum that existed in MSWI BA [220]. In fact, when MSWI BA was mixed into the cementitious matrix, the aluminum could react under the alkaline environment to generate hydrogen gas, which results in porous formation and affects strength properties. To solve this, there are several approaches: (1) physically removing the aluminum from the stony fraction [221]; (2) mechanically milling and sieving out of aluminum fraction [36]; (3) oxidizing the metallic aluminum before utilization [222-224]. For example, Joseph et al. [225] reported that the oxidization reaction of metallic aluminum of milled MSWI BA could be accelerated by increasing the water temperature. Although these treatment approaches can effectively reduce the content of metallic aluminum in MSWI BA, they also bring some new disadvantages: complex treatment process and expensive cost. The other challenge is the leaching of contaminants from MSWI BA. Bottom ash after the complex MSW incineration contains enormous heavy metals (e.g. Pb, Cu, and Zn) and anions (e.g. soluble chloride and sulphates), which pose a risk on the environment and human health [36, 226, 227]. Thus, the concentration of these heavy metal ions and anions need to be decreased to meet the requirement of local legislation before the MSWI BA was used as building material. Therefore, a series of common solutions such as washing repeatedly [228], weathering [229], and other treatments [230, 231] are applied. However, large amounts of water usage and strict requirements of treatment conditions in these solutions increase the cost of waste BA exploitation, further obstructing its practical application. Hence, a simple and cost-efficient approach is urgent to achieve both the strength enhancement environment compliance.

Plant fibers have been widely applied as biomass sorbent materials for heavy metal ion removal in wastewater [232, 233]. Currently, there are two main mechanisms for explaining the absorption process. One mechanism is physically attractive forces due to the unique hollow lumen structure; the other mechanism is ion exchange. The positive cations of heavy metal ions are easily attached to the negative charge at the surface of plant fibers due to electrostatic interactions [234]. In this study, therefore, it is proposed that plant fibers have the potential to absorb the leachate when MSWI BA is applied to partially replace cement. Furthermore, it is reported that plant fibers have the advantage of filling the pores caused by the swelling of coal bottom ash [235] or wood bottom ash [236]. In addition, plant fiber incorporation brings other

benefits such as sustainability and low cost. Considering the above factors, plant fiber incorporation appears to be the most feasible solution for solving the above bottle-necked problems when MSWI BA partially replaces the cement. However, to date, there has been no research on this idea.

Hence, this chapter aims to evaluate the feasibility of a novel approach for solving the leaching and low mechanical strength problems of MSWI BA-based cementitious binders (MSWI BA-BCBs) via the incorporation of plant fibers. Sisal fiber (SF) and oil palm fiber (OPF) were selected as the research objects of this experiment. This is because we obtained that SF and OPF have relatively better absorption capacity of leachate from MSWI BA compared to other common fibers (bamboo fibers, hemp fibers, coconut fibers, and wood wool fibers) in our preliminary experiments. The replacement level of cement by BA is 15% and 30% (in weight of binders), respectively. The compressive strength and macro-micro pore distribution properties of the BA-based cement binders (different replacement rates and different plant fibers) were studied and explained, and the microscopic characteristics of the blended binders were explored by isothermal calorimetry, XRD, and TGA. Additionally, both ICP-AES and IC are employed to investigate the leaching of the heavy metal ions and anions from the BA-based cement binders. Finally, the environmental impact of such binders is evaluated through the greenhouse gas (GHG) emissions indicator in life cycle assessment (LCA) and cost estimation is performed.

5.2 Experimental

5.2.1 Materials and selection

In this research, the raw materials used to prepare the cement-based binders were the OPC (CEM 52.5 R, ENCI, the Netherlands), MSWI BA (Heros, the Netherlands), and a small number of plant fibers (Wageningen University). The reasons for the addition of plant fibers are that: one is to mitigate the leaching of heavy metal ions from the MSWI BA, and the other is to improve the mechanical strength of the cement-based binders.

Before mixing, MSWI BA was dried and milled for 5 mins to meet the PSD requirement as a cementitious supplementary material, as is shown in **Fig. 5.1**. The chemical composition of the CEM I 52.5 R and milled MSWI BA, determined by using the XRF, is given in **Table 5.1**. The summation of the oxides ($SiO_2 + Al_2O_3 + Fe_2O_3$) sample was found to be 69.3% close to 70%,

the sulfur content SO_3 was 1.24% less than 4%, and LOI was 8.14 % less than 10%. So, according to ASTM C618, this type of MSWI BA almost meets all the requirements to be used as a cementitious material. Regarding the plant fiber selection, sisal fibers and oil palm fiber were selected in this study considering the fiber microstructure (**Fig. 5.2**). Besides, the chemical composition of these fibers is given (in **Table 5.2**) for further analysis.

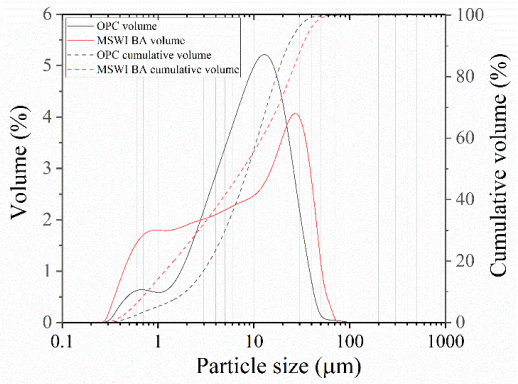

Fig. 5.1 Particle size distribution of cement and milled MSWI BA.

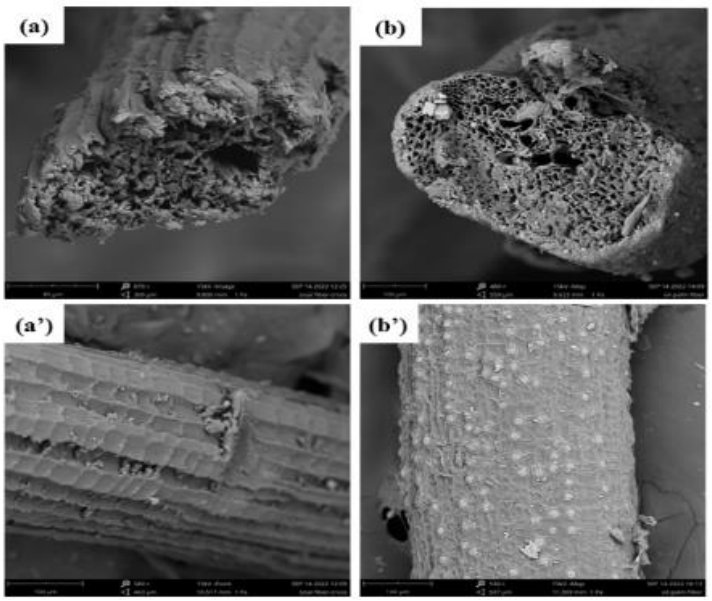

Fig. 5.2 Microstructure of sisal fiber (a cross-section; a', surface) and oil palm fiber (b, cross-section: b' surface).

Table 5.1 Chemical compositions of the CEM 52.5 R and milled MSWI BA.

Oxides (%)	Milled MSWI BA	Cement 52.5 R
SiO_2	37.9	15.8
CaO	21.9	68.2
Al_2O_3	13.8	6.9
Fe_2O_3	17.7	3.9
K_2O	1.3	0.2
MgO	1.5	1.3
P_2O_5	1.1	-
SO_3	1.3	2.8
CuO	0.7	-
ZnO	0.9	0.1
TiO_2	-	0.4
Other	1.8	0.6
LOI	8.2	1.4
Specific density	2.2 ± 0.1	2.5 ± 0.1

Table 5.2 Chemical composition of fibers.

Type	Cellulose (%)	Hemicellulose (%)	Lignin (%)	Ash (%)	Extractive (%)	Average diameter (um)
Sisal fiber [237]	67.0 - 78.0	10.0 - 14.2	8.0 - 11.0	10.0	2.0	150 - 320
Oil palm fiber [238]	32.8 ± 1.9	42.7 ± 2.0	14.9 ± 0.21	7.8	11.3 ± 0.1	410 - 650

Noting: the average diameter of sisal fibers and oil palm fibers used in this experiment is statistically calculated.

5.2.2 Samples preparation

The composition of the MSWI BA-Based Cement Binders (MSWI BA-BCBs) is shown in **Table 5.3**. Several BA-BCBs mixed with plant fibers were designed to solve the bottleneck problems (leaching & low strength) caused when MSWI BA was directly used as the replacement for cement. Therefore, two kinds of 'reference' binders only mixed MSWI BA with cement are considered and denoted as Ref-15 and Ref-30, respectively.

For the case of the blended binders with two different fibers, the design aimed to further compare the impact of the difference in the cellulosic microstructure and chemical components

on the leaching problem and strength property of these binders. The blended binders with sisal fibers were denoted as S-15 and S-30, while those binders with oil palm fibers were denoted as O-15 and O-30. Moreover, to increase the higher possible amount of MSWI BA application, 30% wt. of the cement was replaced by MSWI BA in this study which is referred to as the number '30'. Similarly, the number '15' means that the cement replacement ratio with MSWI BA is 15%. The design of the binders also considered the potential effect of plant fibers on the actual water/cement ratio, hence the water absorption capacity of the two plant fibers was tested according to ASTM procedure D570-99 (ASTM 1999). The obtained results were that the water absorption of sisal fiber and oil palm fiber was 3.58% and 2.51%, respectively. Finally, because of the poor absorbing-water ability and low amount of fiber addition, the effect of the plant fibers on the water/cement ratio in this study could be ignored. However, to keep the similar workability of all specimens and low water usage, the water/cement ratio (0.45) was determined after many preliminary attempts. The CEM 52.5 R was only employed in this work since the effect is faster to achieve the high early-age strength.

Table 5.3 Composition of the MSWI BA-BCBs with or without plant fibers.

Samples	Fibers		Cementitious matrix		
	Oil palm	Sisal	Milled MSWI BA	OPC	Water/Binder
Ref-15	-	-	15	85%	0.45
Ref-30	-	-	30	70%	0.45
S-15		2%	15%	85%	0.45
S-30		2%	30%	70%	0.45
O-15	2%		15%	85%	0.45
O-30	2%		30%	70%	0.45

5.2.3 Characterization

Physical properties

Regarding the raw materials: cement and milled MSWI BA, the specific densities were tested by a Helium pycnometer (Accupyc II 1340), and the chemical compositions were measured by X-ray Fluorescence spectrometer (XRF). Loss on ignition (LOI) was evaluated by oven drying 10 g of MSWI BA at 105 ℃ to constant mass before calcining at 1000 ℃ for 1 h, cooling, and re-weighing. The particle size distributions (PSD) were measured by laser diffraction

(Mastersizer 2000, Malvern). The absorption coefficient of 0.1 was used for both materials, a particle refractive index of 1.68 was used for cement and 1.54 for milled MSWI BA. In terms of plant fibers, their microstructures were characterized by scanning electron microscopy (SEM). The micro-size pores distribution of the cut specimens (15 × 15 × 10 mm^3) was characterized by Micro-CT 100 (Scanco Medical AG, Switzerland). The detailed parameters for testing are following the literature [239].

Thermogravimetric analysis (TGA)

The thermogravimetric analysis (TGA) and differential thermogravimetry (DTG) study were performed by a Q2000 TA Instrument to illustrate the chemical composition of selected paste samples, the powdered paste samples were heated under the nitrogen gas protection from normal temperature to 800 °C, with a rate of 10 °C/min.

Standard leaching test

The leaching test, according to EN 12457-4, 2002, was performed on the original MSWI BA and six cement paste samples cured at 28 days. The levels of potentially toxic elements (Ba, Cr, Cu, Zn, Mo, Sb), chloride, and sulfate were evaluated in this work. The detailed test process was similar to the method of Loginova et al. [240].

Compressive strength

All binder samples of 40×40×160 mm^3 were submitted to compressive strength testing according to the standard EN 12390-3:2019. All samples were tested after 3 and 28 days of curing. The data is gained by repeatedly testing three times to guarantee reproducibility. The significance of the difference between the experimental samples and reference samples was statistically analyzed by one-way ANOVA and P -value<0.05 was considered statistically significant.

Life cycle assessment (LCA)

The LCA approach has been used to assess the environmental impact of supplementary cementitious composites [241, 242]. The process includes three stages for LCA execution: Goal and scope definition, inventory analysis, impact assessment, and interpretation [243]. In this

study, the LCA was conducted using the cradle-to-gate method, to evaluate the environmental impact of incorporating plant fibers in the MSWI BA-based binders' production. The functional unit is considered as one ton of blended binders. This evaluation only focuses on the impact category of greenhouse gas (GHG). LCA modelling was performed using SimaPro software (version 9.0.0.48).

In this study, unit processes in the LCI were sourced from the Ecoinvent databases shown in **Table 5.4**. The built data of the MSWI BA (including the electricity use in the milling process) was modified based on the literature. Additionally, the properties of sisal fibers and oil palm fibers were modified according to the system database of jute and kenaf fibers. The other environmental impacts were not considered in the experiment.

Table 5.4 Source of unit process.

Type of Input data	Source
Water	Ecoinvent 3 database, water, NL
Sisal fibers	Ecoinvent 3 database, jute modified
Oil palm fibers	Ecoinvent 3 database, kenaf modified
Electricity	Ecoinvent 3 database, natural gas, conventional power plant, NL
MSWI bottom ash	Ecoinvent 3 database, MSWI BA built based on the literature [244]
Cement	Ecoinvent 3 database, cement, portland Europe without Switzerland production
Transportation	Ecoinvent 3 database, lorry 16-32 metric tons, EURO5.

5.3 Results and Discussion

In this research, the purposes of plant fiber addition are to solve the low compressive performance and the leaching of heavy metal ions issues when MSWI BA is directly incorporated in cement. Therefore, the study is split into two aspects: one is the effect of plant fiber addition on the compressive performance (compressive strength and pore distribution) of the binders at different curing stages; the other part analyses the microstructural properties (Hydration products and the leaching) of the blended binders. Lastly, the sustainability of the binders was evaluated by Life cycle assessment (LCA) for practical application in the future.

5.3.1 Compressive performance

Compressive strength

The compressive strength of all binder samples is shown in **Fig. 5.3**. The compressive strength of the MSWI BA-BCBs is considerably reduced as the amount of replacement with MSWI BA increases at both 3 days and 28 days after curing. The fact can be explained by the higher porosity created in the cementitious matrix due to the larger amount of metallic aluminum presented in MSWI BA, resulting in the poor strength property of the binders. This finding is consistent with Meyer's. [245] showed that the detrimental effect of metallic aluminum existed in MSWI BA on the compressive strength of concrete due to the releasing of the hydrogen gas generated by the reaction between metal specimens (e.g., aluminum) and alkali salts. It is also confirmed by the following analysis of pore distribution. In addition, another potential reason is the lower pozzolanic reaction of MSWI BA [246], meaning that large unreacted particles of MSWI BA also loosen the compressive strength of the blended binders. Therefore, the reasons for this compressive strength phenomenon are not a single parameter [247] and will specifically be discussed later.

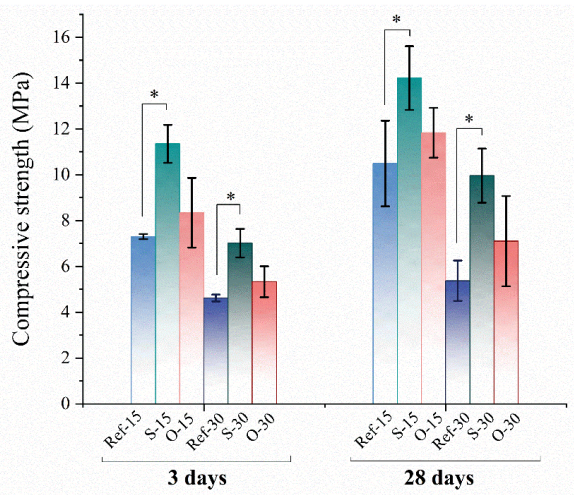

Fig. 5.3 Compressive strength of the MSWI BA-BCBs with different replacements and different plant fibers (see Table 5.3). Noting: the symbol * represents a significant difference.

The mechanical strength of MSWI BA-BCBs increases to some extent with the addition of plant fibers at both stages. This is likely due to the filling effect of the fibers. [248]. Further, it is noted that a significant difference ($p<0.05$) between the sisal fiber samples and the reference

samples. This holds true irrespective of the level of cement replacement and the duration of curing. The compressive strength for SF incorporation is significantly superior to that for counterpart reference samples. For samples with the replacement of 30 wt. % MSWI BA after 28 d curing, S-30 gains the highest compressive strength (about 10 MPa), an 85% increase compared to the Ref-30. On the other hand, no statistically significant difference between the samples with OPF and reference samples was observed, although the OPF incorporation helped in the increment of the MSWI BA-BCBs in terms of compressive strength. This phenomenon may be associated with the difference in the organic component contents of different plant fibers, which delays the cement hydration reaction. To discuss further, the cement hydration, setting, and hardening mainly depend on the concentration of lignin and extractives in the plant fiber [249]. Therefore, the binders with sisal fibers due to the low content of lignin and extractives have relatively higher compressive strength. From the application of MSWI BA for road pavement, the remained binder groups except Ref-30 and O-30 can meet the compressive strength requirement of road paving in garden parks [250]. Meanwhile, combined with considering the consumption amount of MSWI BA, the S-30 is the best candidate.

Pore size distribution

To further evaluate the effect of the physical properties of pores (i.e., numbers, shapes, and size) and factors of the hydration reaction degree on the compressive strength of the binder mixtures, it is important to identify three different phases: pores, reacted and untreated products in the blended binder samples.

The cross-section slices of different samples are characterized with using the software ImageJ (**Fig. 5.4**). It should be mentioned that the word 'pores' here is regarded as the naked-eye visible pores. The pore structures are visible with dark phases in the physical photos, and with circles shown in schematic pictures. In the physical photos, the light phases represent the unreacted particles (almost unhydrated MSWI BA powders due to being less reactive than cement [251]), and the colour degree represents the reacted phases between the pores and unreacted particles. For the physical structures of pores, the larger-round pores and irregular-narrow pores are observed, and the pore number is higher in Ref-15 and Ref-30. While the other binder samples with plant fibers have relatively few tiny circle pores. Because plant fiber incorporation can function as filler for large pores. For instance, when cement replacement by MSWI BA is 15 wt. %, S-15, and O-15 are quite denser, with only several fine pores compared to the

counterpart's reference, which indicates both SF and OPF play a good role in filling pores. However, when the replacement rate increases to 30 wt. %, these two fibers exhibit different filling effects: SF effectively reduces the size and number of pores, but OPF has a relatively poor filling effect, still leaving some visible large pores. This behavior is difficult to explain, and the most likely reason can be related to the chemical components of plant fibers. As can be seen in **Table 5.2**, compared to SF, OPF has more content of lignin and extractives, which significantly delay the cement hydration reaction [252]. Especially when there are fewer cement proportions, the delaying effect is more manifested. It results in a looser skeleton (reacted products) of the MSWI BA-based cement binders. Consequently, OPF incorporation could not effectively improve the mechanical strength of the MSWI BA-BCB. This view is also consistent with the result of the above-tested compressive strength.

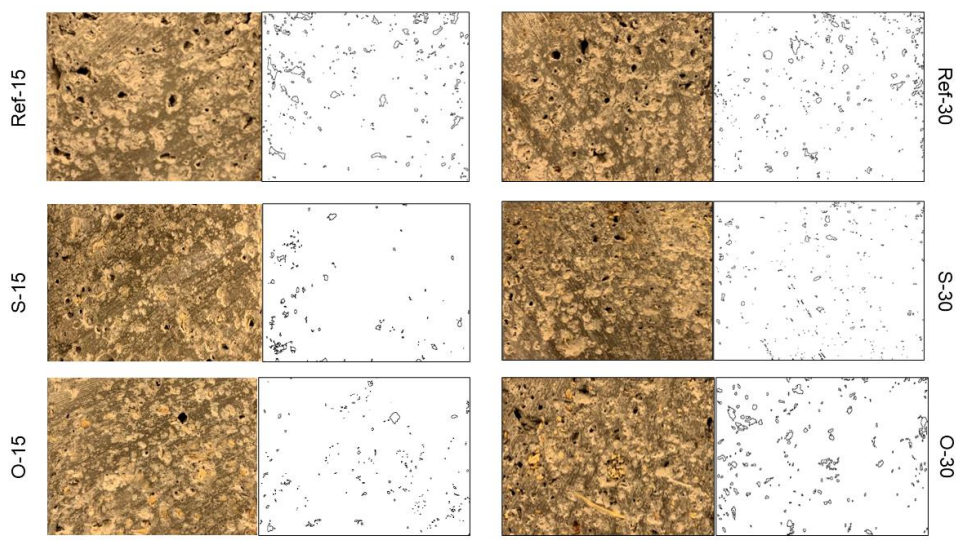

Fig. 5.4 The distribution of pore areas in different samples (see Table 5.3) using ImageJ software.

Fig. 5.5a presents a typical greyscale histogram from a 28-d cured binder mixture (O-15). The histogram was transformed into the Gaussian curves using the PeakFit function in the software OriginPro version, in which the Gausses 1, 2, and 3 represent the pores, reacted products, and unreacted products. The threshold values (intersections) between Gauss 1 and Gauss 2 and between Gauss 2 and Gauss 3 were thought to distinguish the pores, reacted products, and unreacted particles, which is shown in **Fig. 5.5b**. With this approach according to Fang et al.

[253], the threshold values and relevant area fractions of all binder samples were listed in **Table 5.5**. It can be seen that reference samples without plant fibers have a wider threshold range and higher pore area fraction than other samples with plant fibers. That means plant fiber incorporation can reduce the porosity of the MSWI BA-based cement binders through the filling effect, thus contributing to the improvement of compressive strength. However, the incorporation of plant fibers into the MSWI BA-based cement matrix also brings about the retardation of the cement hydration, negatively influencing the strength development. For the S-30 sample, the threshold range representing unreacted particles is wider and the area fraction of reacted products is lower compared to the Ref-30 sample. From this point of view, the compressive strength of S-30 should be lower than that of the Ref-30 sample. With opposite this expectation, the tested strength results from **Fig. 5.3** show that the compressive strength of S-30 is significantly higher than that of Ref-30. This indicates that the positive effect of SF as a filler role on the compressive strength of the MSWI BA-BCBs considerably exceeds the negative effect of it as a "cement retarder". Similar behavior was visible in the case of OPF incorporation, but the exceeding degree is not evident (as shown in **Fig. 5.3**), which probably could be explained by the fact that the higher organic components of lignin and extractives (**Table 5.2**) enhance the influence of it as a 'cement retarder'.

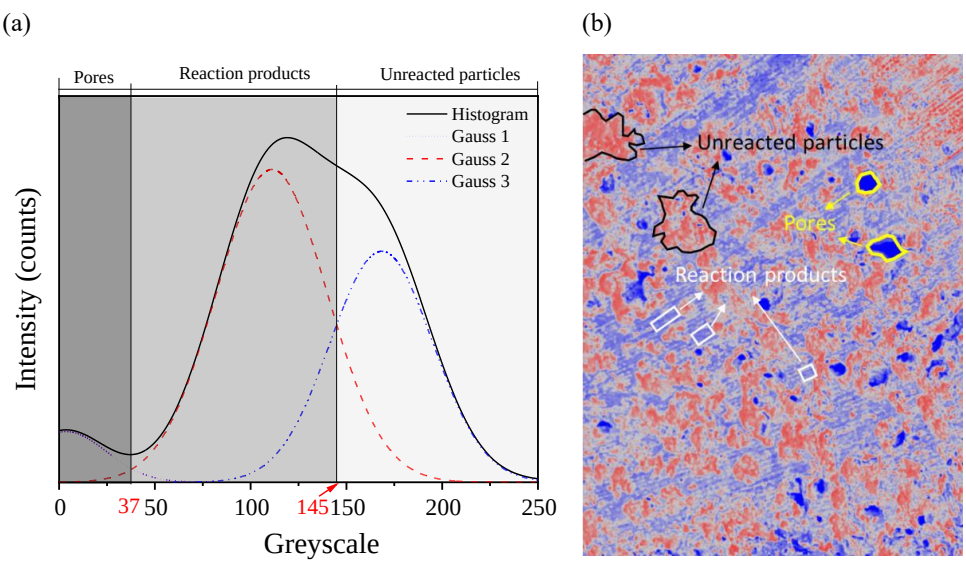

Fig. 5.5 A typical polychromatic greyscale histogram (a) and a typical cross-section (b) of different phases in the binder samples after 28 days of curing. Noting: Red zones represent unreacted particles; Purple represents reaction products; Blue represents pores.

Table 5.5 Threshold values and related area fractions for identifying different phases in different samples (see **Table 5.3**).

Samples		Pores		Reaction products		Unreacted particles	
		Threshold value range	Area fraction (mm^2/mm^2, %)	Threshold value range	Area fraction (mm^2/mm^2, %)	Threshold value range	Area fraction (mm^2/mm^2, %)
28 d	Ref-15	0-53	10.50 ± 0.08	53-154	55.42 ± 2.03	154-255	32.13 ± 3.08
	S-15	0-43	4.82 ± 0.16	43-136	53.13 ± 1.76	136-255	41.07 ± 2.23
	O-15	0-37	2.04 ± 0.11	37-145	45.39 ± 2.21	145-255	54.36 ± 3.01
	Ref-30	0-57	14.54 ± 1.08	57-132	51.63 ± 2.70	132-255	35.83 ± 2.69
	S-30	0-41	6.03 ± 0.25	41-126	48.53 ± 2.35	126-255	42.48 ± 2.18
	O-30	0-42	9.74 ± 0.07	42-129	39.14 ± 1.68	129-255	55.16 ± 3.15

In order to further investigate the influence of the plant fibers incorporation on the micro-size range pores in the MSWI BA-based cement binders, Micro-CT is employed to analyze the fine pores (the size of diameter below 2 mm) in all samples after 28-d curing.

The results of micro-size pore distribution and 3-dimensional volume of all binder samples are displayed in **Fig. 5.6**. It can be clearly observed from the 3D volumes that the percentage of the large pores in the blended binders with 30% replacement is higher than that of 15% replacement. The increment of MSWI BA mixing could release more hydrogen gas, leading to more and larger pores being generated. In addition, it can be seen from the corresponding data that the pore count distribution in the MSWI BA-BCBs with plant fibers is more concentrated in the small-size range compared to those binders without plant fibers (Ref-15 and Ref-30). This indicates that plant fiber filling can reduce certain the formation of larger pores. On the one hand, due to the existence of plant fibers, some small pores can be prevented from interconnecting to form large pores. On the other hand, plant fibers due to the hollow lumen structure can allow gas to enter. That means, the diffusion from the hydrogen gas can be reduced to form large-size pores during the curing period of MSWI BA-BCBs. Therefore, the larger the diameter size of plant fibers (SF versus OPF, **Table 5.2**) leads to a better large pore-filling effect. For samples with OPF, the pore diameter distribution is mostly focused on the smaller size range compared to those samples with SF.

To summarize, when only considering the micro-pore filling (below 2 mm), OPF incorporation has a more significant effect than SF incorporation regardless of MSWI BA addition level. However, when considering the naked-eye pores, the filling effect of OPF is less apparent as the increase of MSWI BA; while SF is still relatively evident due to fewer organic components (lignin and extractives). Thus, considering the stability of the filling effect at high MSWI BA utilization, it is recommended to incorporate SF into MSWI BA-BCBs.

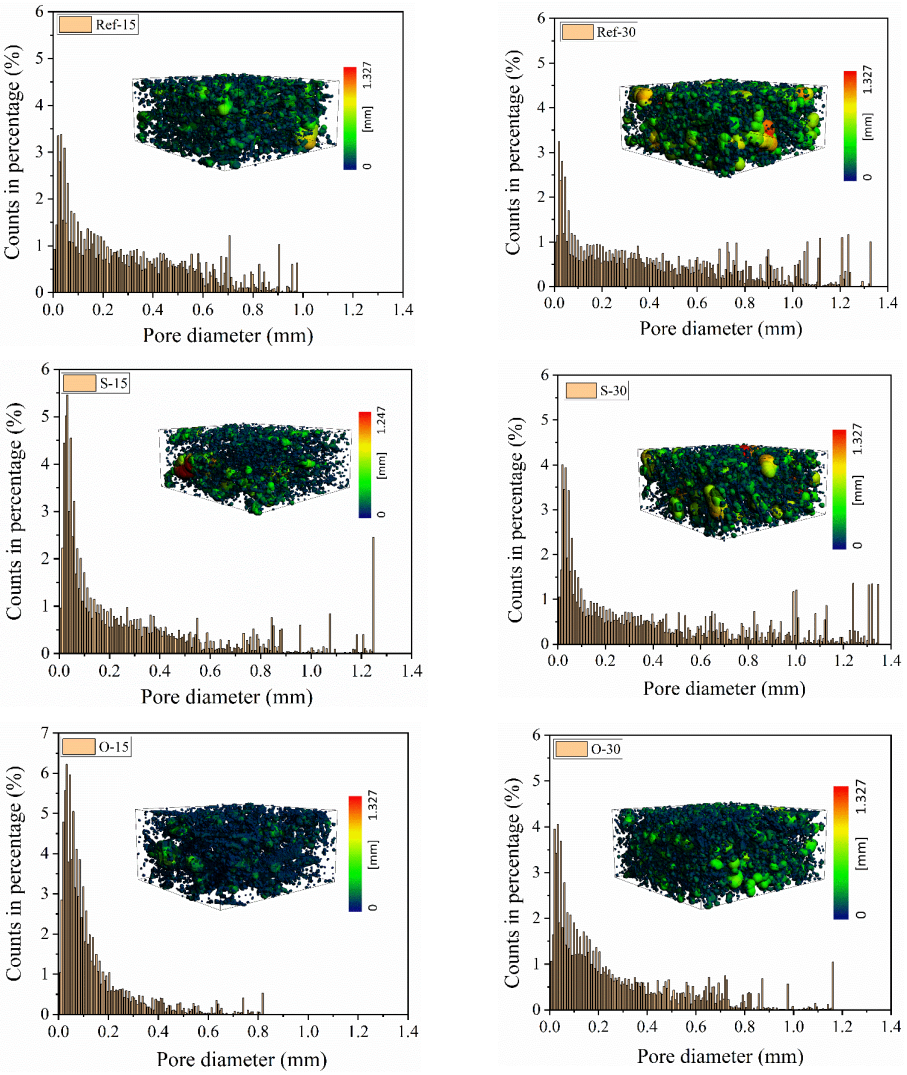

Fig. 5.6 The porosity of different MSWI BA-BCB samples (Table 5.3) by Micro CT.

5.3.2 Microstructural properties

Hydration process

To study the influence of plant fiber additions on the hydration process of MSWI BA-BCBs, the MSWI BA-BCBs hydration heat release was determined by using an isothermal calorimeter. The results of hydration heat release are illustrated in **Fig. 5.7.**

The entire hydration process generally consists of four periods: dissolution period, induction period, acceleration/deceleration period, and stable period [254]. The first exothermic peak formation is due to rapid dissolution and the reaction of aluminates and sulfate from MSWI BA and the cement clinker initially one hour after mixing with water. Then the second exothermic peak comes with the hydration of C_3S and the formation of secondary C-S-H gel [255]. It can be seen from the enlarged picture in **Fig. 5.7a** that the samples with plant fibers have longer second-peak reached time and lower second-maximum heat release rates than their corresponding reference samples. This is mainly due to the plant fibers' addition, which leads to the retardation of the CEM-MSWI BA hydration. Especially for samples with oil palm fibers, the retardation is considerably prolonged by approximately 8 h for the O-15, and the second peaks for both O-15 and O-30 are the lowest in their groups (one group is a 15% replacement level, and the other group is a 30% replacement level), respectively. This is attributed to the high proportion of lignin and extractives in the oil palm fibers, which retard the cement hydration reaction by forming an organic layer coating around the anhydrous or partially hydrated cement grains [256, 257]. In addition, with the increase of MSWI BA, the second exothermic peak of the binders with 30% MSWI BA was greatly decreased and the arrival time of their second peaks was delayed. This indicated that MSWI BA addition also results in a certain degree retarding of cement hydrations. In fact, MSWI BA due to lower reactivity would dilute the clinker contents (Alite and Belites) when the equivalent cement was replaced [258]. Interestingly, it has to be mentioned that the time reaching the second exothermic peak for O-30 is shorter than that for O-15. This behavior is difficult to explain, and the most likely reason is that more and larger pores generated due to the increase of MSWI BA, lead to the looser interface linking between the embedded oil palm fibers and the CEM-MSWI BA matrix. That means the oil palm fibers in the sample with a higher amount of MSWI BA are difficult to sufficiently inhibit the CEM-MSWI BA hydration reaction. Thus, the delaying effect in O-30 is relatively stronger.

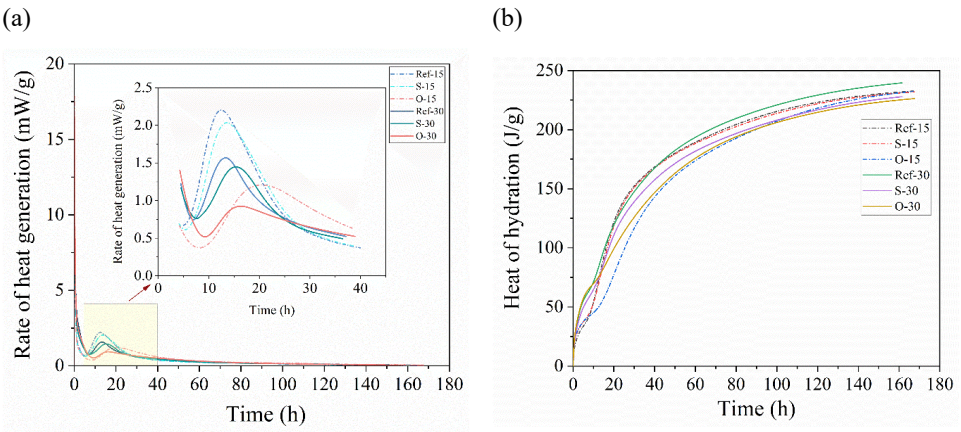

Fig. 5.7 Heat of hydration: (a) heat flow (b) total heat release.

As can be seen from **Fig. 5.7b**, Ref-30 has the highest total released heat, followed by Ref-15. This indicates that increasing the replacement level generates more heat released. That means, a 15% MSWI BA extra addition in the CEM-MSWI BA system could contribute more heat cumulative than 15% of pure cement, which is dominantly attributed to more silica and alumina sources provided by MSWI BA for the pozzolanic reaction. This is confirmed by the result of the above XRF. On the other hand, both S-15 and O-15 are higher than both S-30 and O-30 regarding the total heat release. This suggests that when plant fibers are incorporated, the increasing replacement level with MSWI BA causes relatively poor pozzolanic reactivity in the MSWI BA-BCBs. The reason for this phenomenon is not yet clear until now, but this behavior is possibly related to the calcium source decreasing caused by both less cement amount and the capture of plant fibers on calcium.

XRD analysis

The XRD results in **Fig. 5.8** compare the hydration products of different samples at 3-d and 28-d curing. Compared with the samples in the early 3-d curing, the peak of portlandite shows a certain increase in the 28-d curing samples with plant fibers incorporation whereas no significant difference among the blended binders without plant fibers. It illustrates that the organic components of plant fibers delay the hydration reaction, thus reducing the developing consumption of CH in the secondary hydration reaction period [259]. This behavior is also in line with the analysis of the calorimeter. In addition, the inner quartz peak intensity increases with the extra addition of MSWI BA, which is due to the large amount of quartz contained in

the MSWI BA. It is noteworthy that the wide peak representing the Cl-LDH phase formed is more obvious as the replacement level increases, which is probably because relatively higher alumina content and lower SO_4^{2-} content contained in the MSWI BA compared to the cement promote the LDH formation. This product is well-known to be beneficial for the trapping of inorganic anions like chlorides. The formation of Cl-LDH is not only characterized in this study but also reported and confirmed by [214, 260].

(a) (b)

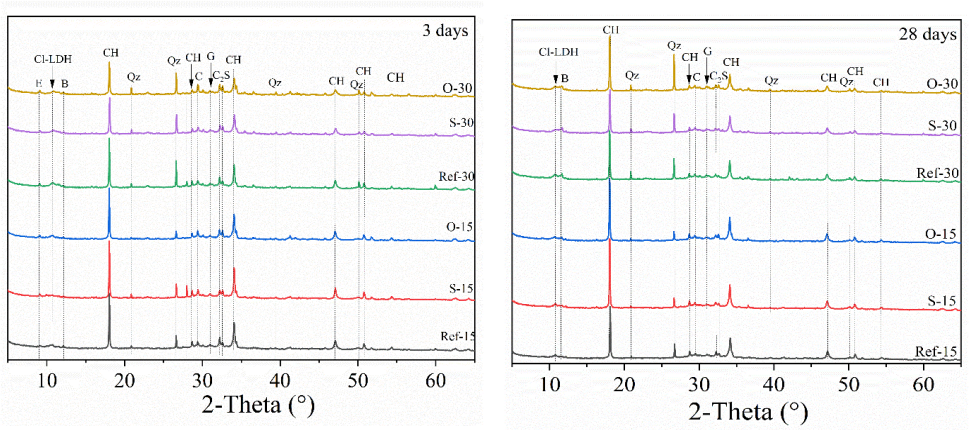

Fig. 5.8 XRD of all tested samples at 3 days and 28 days. Abbreviations associated with the mineralogical phase are: E-ettringite, Cl-LDH-chloride layered double hydroxide, B-brownmillite, G-gypsum, CH-portlandite, Qz-quartz, C_2S-dicalcium silicate phase.

TG-DTG analysis

The TG and DTG results of all tested samples for 28 d curing are shown in **Fig. 5.9**. Comparing the TG curves shown in **Fig. 5.9a** and **b**, it can be seen that the mass loss of each binder sample is quite similar when the cement replacement ratio is 15%, but when the replacement ratio is 30% the degree of mass loss is obviously different. This indicates that when the MSWI BA addition is too large, the effect of plant fiber on the CEM-MSWI BA reaction is more evident.

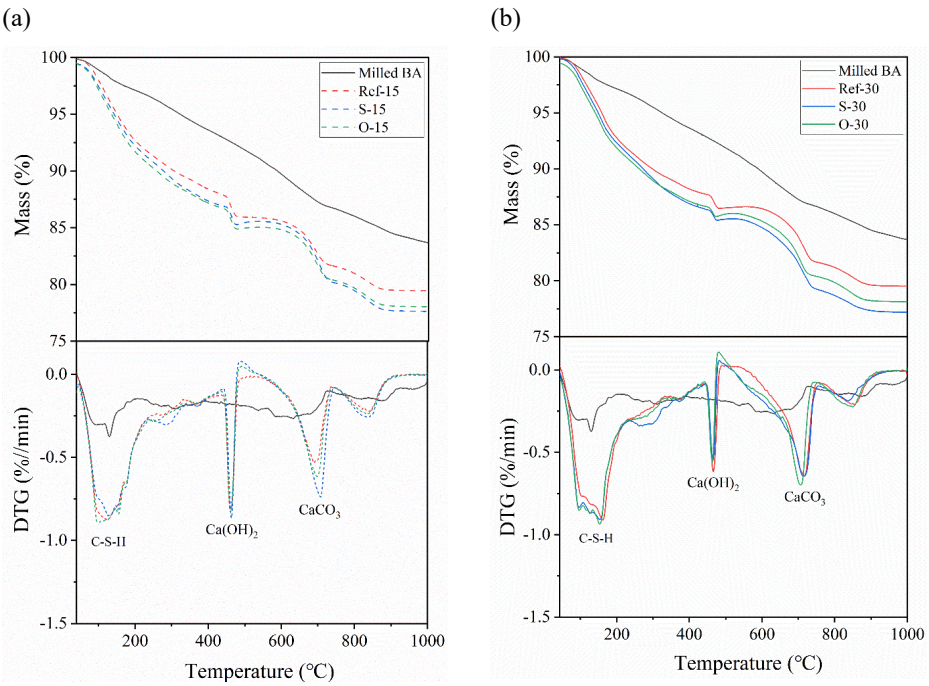

Fig. 5.9 TG-DTG results of all tested samples (see **Table 5.3**) for 28 days.

The DTG curves could be generally divided into four stages. The first wide peaks at 40–200 C were attributed to the vaporization of unbound water (40 -105 °C) and the decomposition of the hydration product C-S-H (105-200 °C); the second sharp peaks at 400-500 °C are the decomposition of portlandite ($Ca(OH)_2 \rightarrow CaO + H_2O$), and the peaks at 600–800 °C are related to calcite decarbonization $CaCO_3 \rightarrow CaO + CO_2$. Lastly, rare literature about the peak at 800-850 °C is reported. According to the metallic zinc that existed in MSWI BA. it was assumed that this peak was probably related to the great volatilization of $ZnCl_2$ formed when the temperature was above 800 °C [261-263]. Besides, it is noted that the small exothermic peaks located at around 280 °C due to the degradation of cellulose and lignin [264].

In comparison with the DTG curves, the peak of C-(A)-S-H for a 30% replacement level is higher than that for a 15% replacement level, while the peaks of both portlandite (CH) and calcite are reduced. This phenomenon also verifies the results of the XRD, which suggested that the portlandite produced by cement hydration was consumed due to the pozzolanic reaction of extra MSWI BA, thereby leading to a decrease in calcite and more amorphous C-(A)-S-H transformed.

Heavy metal ions leaching

The results of heavy metal ions and anions leaching of all samples are presented in **Table 5.6**. Even though the milled MSWI BA and CEM I have very high leaching of heavy metal ions and anions, almost all these ions in all MSWI BA-BCBs much lower the legislative limit except for Cu. With regard to the slightly exceeding standard limit of Cu leaching, it could be caused by the fine-size crushed samples selected for the leaching test. Yang et al., [265] reported that the smaller the particle size of the crushed MSWI BA-based cement composites the higher the concentration of Cu leached. Therefore, the Cu leaching can be declined by increasing the relatively big-size crushed samples (still meeting the requirement of below 4 mm) for the leaching test. For another solution, it is known that the heavy metal composition distribution is much related to the size of raw MSWI BA. Thus, the metallic Cu of MSWI BA can be recovered by sieving before the MSWI BA is milled and used in cementitious binders. Here, we do not further study the recovery techniques, which is out of the scope of this investigation.

Table 5.6 Leaching of anions (sulfate and chloride) and heavy metal ions present in the leachates cations for milled MSWI BA, CEM I 52.5 R, and all binder samples after 28 d curing; the units for concentrations given as mg per kg of dry matter; LL is the legislation limit [266].

Samples	Leaching value (mg/kg d.m.)							
	Chloride	Sulfate	Ni	Cu	Zn	Mo	Pb	pH
Milled MSWI BA	8682	13865	0.18	7.01	0.84	3.77	0.56	9.8
CEM I 52.5 R [240]	322	52	20.5	< 0.01	0.05	0.2	17	-
Ref-15	291.4	38.4	0.23	1.52	0.21	0.1	0.69	13.68
S-15	252.3	28.5	0.09	1.06	0.17	0.09	0.58	13.64
O-15	242.8	27.7	0.15	1.1	0.18	0.1	0.58	13.6
Ref-30	533.3	36.9	0.12	1.84	0.38	0.13	0.89	13.51
S-30	477.9	31.6	0.1	1.3	0.33	0.11	0.72	13.25
O-30	455.1	21.7	0.11	1.31	0.36	0.12	0.75	13.18
LL	616	1730	0.44	0.9	4.5	1	2.3	-

- *Not measured*

Noticeably, when plant fibers are incorporated into the MSWI BA-BCBs, the leaching of anions (chloride and sulfate) is considerably decreased. That means, plant fibers can promote the absorption of chloride and sulfate by capillary suction [122], which thus reduces the risks of

steel reinforcement and the expansion issue caused by excessive sulfate. Comparing SF to OPF, the OPF has a more obvious absorption capacity of the anions. This could be explained by the denser lumen structures efficiently exerting the fiber capillary force to absorb the chloride and sulfate anions. In comparison with the above absorption effect, plant fiber addition has a less reduction in the leaching of heavy metal ions. This is unexpected since it is usually considered that positive charges of heavy metal ions are more easily attracted to the plant fiber surfaces with negative charges due to electrostatic interactions. Combined with capillary absorption, therefore, the leaching of heavy metal ions should be considerably reduced. A possible reason for this phenomenon is the fact that the existence of heavy metal ions in the alkali environment mainly are the forms of their hydroxides ($Pb(OH)_3^-$, $Zn(OH)_4^{2-}$, $Cu(OH)_4^{2-}$), resulting in electrostatic repulsion with negatively charged plant fiber surfaces. Eventually, the electrostatic repulsion decreases the absorption effect of capillary suction on the heavy metal ions. Nonetheless, the leaching results of heavy metal ions absorbed by incorporated plant fibers can basically comply with the Dutch soil environmental legislation.

5.3.3 Environmental and economic assessment

Greenhouse gas (GHG) emissions

GHG emissions for one ton of binder composites are shown in **Fig. 5.10**. The data show that the MSWI BA-based binders with or without plant fibers have lower GHG emissions than pure cement binders. This is because the MSWI BA or plant fibers incorporation reduces the dosage of cement in the binder, hence decreasing the GHG emission from the production of cement. Additionally, it has to be mentioned that the incorporation of plant fibers mixed into binders can reduce GHG emissions when the cement replacement keeps the same level. Especially SF reinforcement has a better decrease in GHG emissions than OPF. For samples with 30% replacement, the GHG emissions of S-30 are reduced by around 63 kg CO_2 eq./ton compared to the Ref-30, exceeding the relative reduction of O-30 emissions (45 kg CO_2 eq./ton). This indicates that S-30 has an advantage in carbon dioxide emissions compared to other samples, which have great potential for building applications.

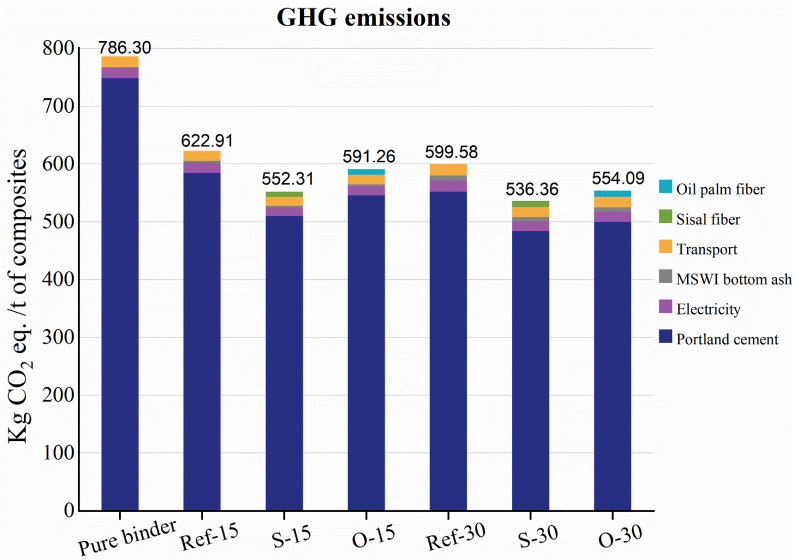

Fig. 5.10 GHG emissions of all tested samples (see **Table 5.3**).

Economic evaluation

To evaluate the cost-benefit of the MSWI BA-based binders containing SF and OF, a cost-benefit analysis is carried out for pure cement binders and six different binder samples. The price of raw materials for binders comes from the local market price in Europe (the Netherlands) shown in **Table 5.7**. It is noted that the cost of MSWI BA and its relevant transport is free. One reason is that MSWI BA is a waste material. Another, for the municipal waste incineration plant, the fee of MSWI BA landfilling or other treatments is far higher than that of transport for the MSWI BA-based binders' preparation. **Fig. 5.11** shows a cost-benefit analysis of all binder samples. As shown in **Fig. 5.11**, the cost of the MSWI BA-based binders remarkably reduced with the increase of the replacement level of MSWI BA. In addition, it can be seen that even though plant fibers were incorporated into the relevant MSWI BA-based binders, the cost gap between them was almost negligible. This is because plant fibers chosen in our current work are a bulk commodity and very cheap (**Table 5.7**). In the future, if this technique is matured, the waste plant fibers will be chosen, which not only receive huge economic benefits but also mitigate the impact of waste plant fibers on the environment. Thus, S-30 can be considered to be a suitable mix design considering its compressive strength, leaching, economic benefit, and waste utilization rate.

Table 5.7 Prices of raw materials and processing for all tested samples.

	Raw materials					Process	
	OPC	MSWI BA	Water	Plant fibers		Electricity	Transport
				SF	OPF		
$Price_{(approx.)}$	123 €/ton	-	0.87 €/m^3	10 €/ton	15 €/ton	0.32 €/kWh	0.348 €/tkm

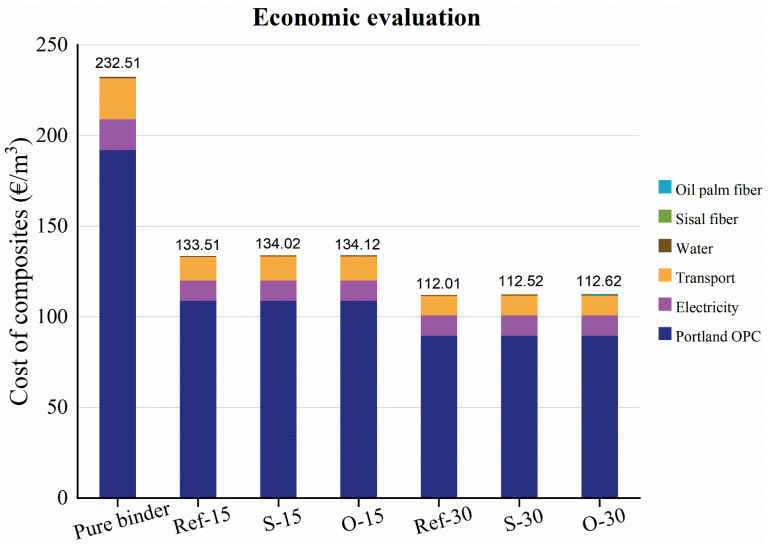

Fig. 5.11 Cost of one cubic meter of MSWI BA-BCB samples (see **Table 5.3**).

5.4 Conclusion

Two types of plant fibers (SF and OPF) were compared and analyzed to assess the effect of their incorporation on the mechanical property and leaching of the MSWI BA-BCB. The different replacement of MSWI BA was also studied. Moreover, the environmental and economic feasibility of the plant fibers reinforced binders is evaluated. The following conclusions can be drawn:

(1) In the MSWI BA-based cement binders, plant fiber incorporation has a positive impact on the compressive strength of the MSWI BA-BCBs, due to the filling effect. Especially the compressive strength of SF incorporation increases by 85% compared to the reference sample at 28-day curing when the replacement level is 30 wt.%. Further, it is found that S-30 has

acceptable compressive strength which meets some types of road pavement requirements under the premise of MSWI BA maximum consumption.

(2) The increase of cement replacement with MSWI BA leads to larger and more pores generated in the MSWI BA-BCBs, which is attributed to more hydrogen gas release, while plant fiber incorporation considerably reduces the size and numbers of the pores on account of the obstacle of plant fiber on gas diffusion and pore interconnection. Furthermore, the micro-CT study has proved plant fiber with a larger diameter size is more beneficial to the pore filling in the MSWI BA-BCBs.

(3) Although the filling effect of plant fibers effectively enhances the strength of MSWI BA-BCBs, the fiber addition also delays the cement hydration due to some organic components (extractives and lignin) as cement retarders, consequently, it negatively affects the strength of MSWI BA-BCBs development. Eventually, OPF with a higher content of those organic components reduces the contribution to compressive strength by the filling effect.

(4) It is noted that the leaching of heavy metal ions, chloride, and sulfate anions is lowered when plant fibers are incorporated due to capillary suction. This effect is very remark for anions leaching and to a lesser extent for heavy metal ions leaching.

(5) The results of GHG emission in the LCA tool show the waste MSWI BA and plant fibers incorporation notably reduce the GHG emission reduction by increasing the cement replacement level, mitigating the environmental impact.

In terms of economic feasibility, the cement replacement with BA helped in reducing the cost of the MSWI BA-BCBs (around 52%) even though plant fibers incorporation brings an almost negligible cost increment. If this technique is successful, the waste plant fiber could be applied, which saves huge costs for MSWI BA-BCB production.

CHAPTER 6

6. Effects of sisal fiber incorporation on lightweight aggregates made using MSWI bottom ash

Based on this paper:
H. Song, T. Liu, F. Gauvin, and H.J.H. Brouwers. Investigation of sisal fiber incorporation on engineering properties and sustainability of lightweight aggregates produced from municipal solid waste incinerated bottom ash. Construction and Building Materials 413, 134943 (2024).

6.1 Introduction

Municipal solid waste incinerated bottom ash (MSWI BA) is the largest residue fraction from waste-to-energy plants. Because of its physical-chemical properties and pozzolanic reaction, incorporating MSWI BA for the production of building materials has attracted more and more interest [240, 267]. The primary forms of MSWI BA employed in mortars/concrete were commonly categorized in two ways: supplementary cementitious material [268, 269], which was investigated in Chapter 5, and artificial aggregates [12, 270, 271]. Currently, the technique of cold-bonded pelletization for aggregate production is the most commonly adopted by many researchers due to a series of advantages (low energy consumption, low cost, and low carbon footprint) [272]. Furthermore, to maximize the utilization of MSWI BA, some scholars attempted to improve the proportion of MSWI BA in artificial aggregates. For instance, Liu et al. [273] explored different amounts (10% - 60% of the total solid) of the binder (cement and ground granulated blast furnace slag) to bond MSWI BA for artificial lightweight production.

The results showed that 30% of the total solid reached the optimal condition considering the production efficiency and MSWI BA recycling rate. However, the building products prepared by MSWI BA were found to have low strength due to the undesirable swelling of metallic aluminum under the alkaline environment with hydrogen emission [271], and serious contaminating ions leaching (e.g., heavy metal ions, chloride, and sulfate anions). Two main drawbacks would limit its practical application in the building industry. To address them, many attempts have been made but introduced a series of new challenges, inlcuding high treatment cost (see Chapter 5.1).

Given the positive effects of sisal fiber incorporation on the mechanical strength and leaching immobilization of MSWI BA-based cementitious binders discussed in Chapter 5, the incorporation of sisal fibers can be anticipated to address the abovementioned two drawbacks when utilizing MSWI BA to manufactured lightweight aggregates. Meanwhile, to the best of the authors' knowledge, no studies have analyzed the effect of sisal fiber incorporation into artificial aggregates with MSWI BA.

Considering the above, the purpose of this study is to explore the feasibility of the MSWI BA-based aggregates incorporated with sisal fibers and provide scientific insight for developing a new solidification technology from the strength properties and contaminant leaching. A cold-bonded pelletizing technique was employed in this work. A comprehensive experiment work including physical properties, mechanical strength, and microstructure characteristics of aggregates was conducted. Then the mechanisms of strength development and contaminants immobilization were also explored in depth. Finally, the impacts of MSWI BA-based synthesized aggregates on the environment and related manufacture cost evaluation were investigated.

6.2 Experimental

6.2.1 Materials

The MSWI BA, CEM I 52.5 R, and sisal fibers used here are the same as Chapter 5. The corresponding properties have been detailed in the previous section 5.2.1.

6.2.2 Methods

6.2.2.1 Pretreatment

In this experiment, the same batch of SF was cut twice into very fine fibers using a cutting mill (SM 100, Retsch) to ensure a homogeneous dispersion within the cement and MSWI BA particles. The raw MSWI BA from the plant was first dried in the oven at 60 °C due to some water content according to EN 933-1. The moisture content was tested at approximately 8%. The carbon emissions and fees during the drying process were also calculated into the carbon emissions and cost assessment in the subsequent section. After that, the MSWI BA was milled (Vibratory disc mill RS300, Retsch) for the powder to the effective and homogeneous aggregate production. The particle size distribution of milled MSWI BA is also the same as in section 5.2.1.

6.2.2.2 Synthesized sustainable lightweight aggregate

In view that the pozzolan activity is slightly low and the hydration capacity is weak [214, 237], it is necessary to add OPC to stimulate pozzolanic activity, and then the gelling and bonding effect of the chemical reaction was applied to combine MSWI BA to form synthesized lightweight aggregates (SLWAs). This principle has been also reported in the literature [274]. To ensure that the cut sisal fibers and MSWI BA can be fully bonded by the binders, it is necessary to find a suitable water/cement ratio before manufacturing. After several trials, the liquid-solid (cement and MSWI BA) ratio was determined at about 25% on the weight of the cementitious materials. However, a slight variation in the practical liquid-solid ratio was observed among groups (**Table 6.1**). This is primarily attributed to practical operational factors. Occasionally, some of the fogged water may spray on the inner wall or even out of the pelletizer, rather than all targeting the dried particle surfaces. This results in a minor loss of water loss or a minor addition of water supplementary, leading to a deviation in the calculated liquid-solid ratio. However, the practical liquid-solid ratio used to produce the aggregates should be considered consistent.

In addition, it was found that the bonding effect of SLWAs was very loosened when the mass percentage of MSWI BA constituent occupied over 80%. Thus, the replacement proportions with MSWI BA range from 60% to 80% here. In this work, the cold bonded method was adapted to manufacture the aggregate. The size of the disc pelletizer (ERWEKA-AR 403) is specified as follows: 100 cm diameter and 15 cm high. The detailed parameters were modified based on

the information from the literature from Tang [275], and the practical manufacturing effect. The coordination of synthesized LWA is illustrated in **Table 6.1**. The manufacturing process is presented in **Fig. 6.1**. Before manufacturing lightweights, the raw solid materials were first mixed sufficiently within a plastic bucket by shaking up and down for 3 minutes. Partly mixed materials (around 30% of total solid weight) were placed on the running disc at 60 rpm. The water was sprayed continuously onto the surface of dried materials. This process lasted about 15 minutes. After that, the running disc speed was changed to 70 rpm and then the rest 70% of the raw materials were slowly and continuously placed on the running disc, and the water was still slowly sprayed on the dried materials surfaces. This process lasted 20 minutes until no new aggregates were produced, and then the produced aggregates were collected. The production efficiency of the aggregates is calculated as follows:

$$\text{Production efficiency} = \frac{W_{certain\ size}}{W_{total\ size}} \times 100\%\ , \tag{6.1}$$

where $W_{certain\ size}$ is the weight (g) of the synthesized aggregates at a certain size and $W_{total\ size}$ is the total weight (g) of the synthesized aggregates of all sizes.

Table 6.1 The fraction of raw materials to synthesize green LWA.

Item		W/C (%)	Fibers (wt.%)	MSWI BA (wt.%)	Cement (wt.%)
S1	S1-C	24.20	-	60	40
	S1-F	24.74	2		
S2	S2-C	23.66	-	70	30
	S2-F	28.62	2		
S3	S3-C	26.54	-	80	20
	S3-F	24.35	2		

Noting: (1) The unit: wt.% means the weight percentage relative to the total inorganic mass (MSWI BA and cement).

The obtained aggregates need to be sealed by plastic bags to harden and form for 24 hours to avoid the loss of water evaporation. Finally, the aggregates were cured in an environment (21 ℃ and 98% relative humidity) for 28 days to get the necessary strength. In addition, high humidity was chosen as the curing condition in this experiment considering the report by Shafigh et al.

[276], which concluded that moist curing could reduce the decrease of strength in oil pal shell-blended fly ash lightweight concrete than air curing.

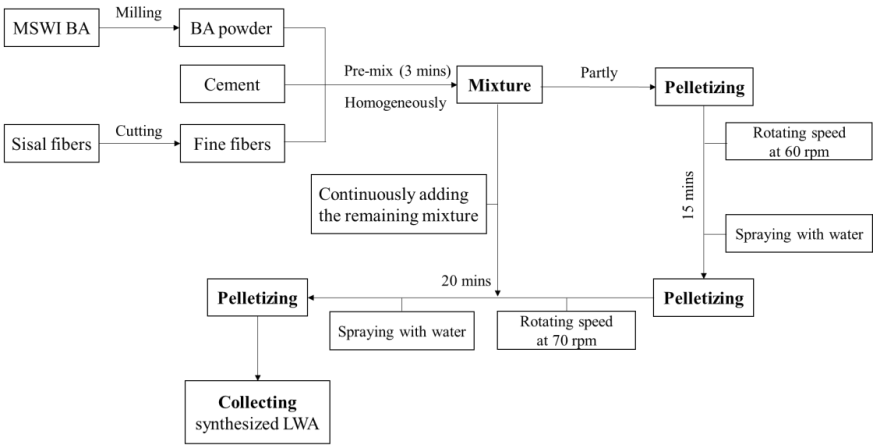

Fig. 6.1 The manufacturing process of SLWAs.

6.2.3 Characterization

Physical properties

Prior to the below characterizations, the aggregates were put into the oven at 105 ℃ for 24 h. The loose-filled bulk density was tested according to EN 1097-3. The bulk density (ρ_{bulk}) of a single aggregate was calculated and obtained via the cross-section image processed by ImageJ software. The description is detailed in the literature [277, 278]. The apparent density ($\rho_{apparent}$) and true density (ρ_{true}) are measured using a helium pycnometer performed on the aggregate and the milled powder, respectively. The closed porosity (φ_{closed}) of the aggregate was calculated following:

$$\varphi_{closed} = \rho_{bulk} * \left(\frac{1}{\rho_{apparent}} - \frac{1}{\rho_{true}}\right) \times 100\% \ . \tag{6.2}$$

The total porosity (φ_{total}) of the aggregate was calculated according to eq. (4.1). The water content and water absorption test of SLWAs were determined following the ASTM C-127. To evaluate the shape of SLWAs, the flattening coefficient p, was as follows:

$$p = \frac{\text{e (thickness)}}{\text{I (width)}} \ . \tag{6.3}$$

The elongation coefficient q, was as follows:

$$q = \frac{\text{I (width)}}{\text{L (length)}} \ . \tag{6.4}$$

For each granular fraction, 20 aggregates were measured based on the literature [279]. According to Zingg's classification method [280], the shape of aggregates is categorized into four types: disk, spherical, blade, and rod (**Fig. 6.2**).

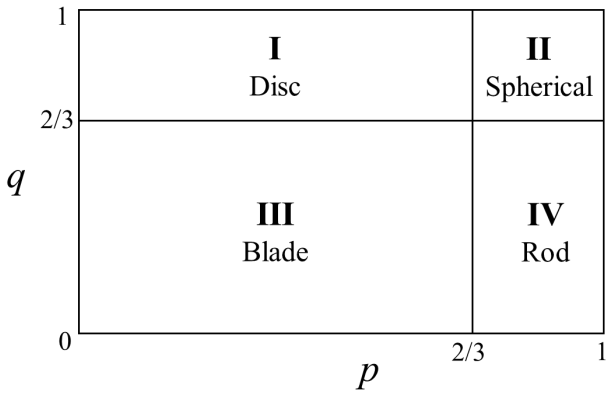

Fig. 6.2 Zingg's classification of particle shape.

Furthermore, the sphericity (Ψ) of aggregates is calculated following Wadell's formula:

$$\Psi = \sqrt[3]{q^2 \times p} \ . \tag{6.5}$$

Mechanical performance

The crushing strength of a single synthesized aggregate in this study is obtained by adapting a modeling calculation proposed by [281]. The test was conducted using the EZ 20 Lloyd Instrument machine with a 30 kN loading cell, accurate to 1/1000 of the load cell capacity, at a loading speed of 0.8 mm/min until it is broken, as shown in **Fig. 6.3**.

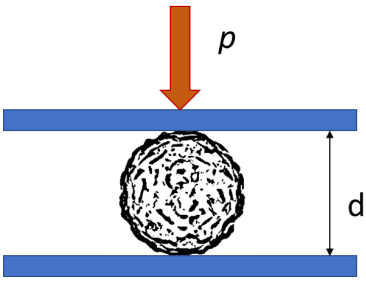

Fig. 6.3 Crushing strength of individual pellet.

20 pellets in each subgroup were statistically tested and the results of peak force were recorded. According to the literature [281], the crushing strength was calculated following the relation

$$\sigma_{crushing} = \frac{2.8P}{\pi d^2}, \tag{6.6}$$

where σ is the crushing strength of individual aggregate (MPa), *P* is the peak force (N), and d (mm) is the distance between the points of loading.

The above equation was built on the hypothesis that the fracture along the middle part of the test samples. As can be seen from **Fig. 6.4**, the crack propagated along the middle axis, which proves that it is reasonable to employ this modeling formula performed on the synthesized aggregates in this experiment.

(a) (b)

Fig. 6.4 Crack propagation of typical aggregates without SF (a) and with SF (b).

Microscopic properties

To analyze the microscopic performance difference of SLWAs with or without sisal fibers, the

cross-section microstructure of crushed aggregates was characterized with a Zeiss optical microscope and scanning electron microscopy (SEM, Phenom ProX, PhenomWorld). The surface roughness of the SLWAs was quantified by phenom 3D roughness reconstruction software. The field of view is between 10 μm and 2 mm. Ra (average roughness) is automatically calculated and obtained. In addition, to better understand the underlying effect of the hydration kinetic of aggregates on strength development, the isothermal calorimeter (TAM air, Thermometric) is employed to study the hydration reaction of synthesizing the aggregates. However, the mixtures for producing aggregations are difficult to disperse due to the low water/solid (MSWI BA and cement) ratio. To address this problem, the water/solid ratio is increased to 0.5 to prepare the samples for calorimeter measurement. Various ratios of MSWI BA, cement, and/or SF were blended in glass bottles. Following 3 minutes of manual shaking, water was added to the glass bottles, and mixing was performed using a glass rod. The mixed samples were then sealed and loaded into an isothermal calorimeter that had reached thermal equilibrium at 20 ℃. After nearly 2 weeks, the test was stopped, and the samples were removed. The obtained data were subsequently analyzed and compared.

Leaching evaluation of SLWAs

The environmental impact of the investigated SLWAs is evaluated by the leaching test according to the Dutch legislative standard NEN 7383, 2003. The crushed aggregates after a single compressive strength test are sized below 4 mm before the test. The crushed aggregates were placed into a sealed plastic bottle (L/S = 10) and shaken at 200 rpm for 24 hours. After that, the leachates were filtered through the 0.2-um filter to prepare solutions for the heavy metal ions test (Inductively coupled plasma atomic emission spectrometry, ICP-AES) and anion test (Ion chromatography, IC).

Environmental and Economic Evaluation

According to the literature [282] [283], [284], the approach of life cycle assessment (LCA) has been employed to evaluate the environmental impact of lightweight aggregates synthesized by solid waste. In this work, the cradle-to-gate method within the LCA was employed to evaluate the environmental impact of synthesized MSWI BA-based aggregates. Detailed calculation procedures are the same as those in the section 5.2.3.

6.3 Results and discussion

6.3.1 Physical properties

The aggregates with different replacement substitutes of MSWI BA were produced and the obtained production efficiency results are illustrated in **Fig. 6.5**. In general, synthesized coarse aggregates with 4 mm more (4-8 mm and >8 mm) account for the major percentage of produced aggregates. Therefore, considering the effective utilizing ratio of aggregates, coarse aggregates are chosen more than 4 mm in diameter size as the research objectives in this study. When SF is incorporated, the production efficiency of coarse aggregates synthesized is obviously increased. In particular, the fraction of coarse aggregates in the S2-F is 60.54%, with the highest increment of 66.5% compared to the control S2-C. This indicates that SF can provide a bond effect in mixed powder (cement powder and MSWI BA powder) in the preparation process. According to the literature [285, 286], cement powder and MSWI BA powder have positive charges, leading to the appearance of electrostatic repulsion forces. That means such forces would be set off to some extent the driving force produced from the hydrophilic characteristics of powders. Whereas, sisal fiber with both hydrophilic characteristics and negative charges [287] can not only take water absorption force to bind inorganic powder but also attract these negative-charged powder agglomerations to form aggregates. Furthermore, when cement replacement with MSWI BA increases, the production efficiency of the coarse aggregates without fiber incorporated generally decreases. This is in accordance with the previous study. However, it was noticed that sisal fibers incorporated have the best effect on production efficiency when the proportion of MSWI BA increases to 70 wt.%. This could be because when the amount of MSWI BA is lower, the water is easily absorbed by a higher proportion of cement, which leads to less bonding effect provided by sisal fibers due to their lower wetting surfaces. On the other hand, when the amount of MSWI BA exceeds 70 wt.%, the cement binder is insufficient for the system, resulting in synthesized aggregate powder being prone to loosening and finally reducing the production efficiency of aggregations. Therefore, considering the efficient production, the 70 wt.% MSWI BA with sisal fibers is the optimum design ratio in this study.

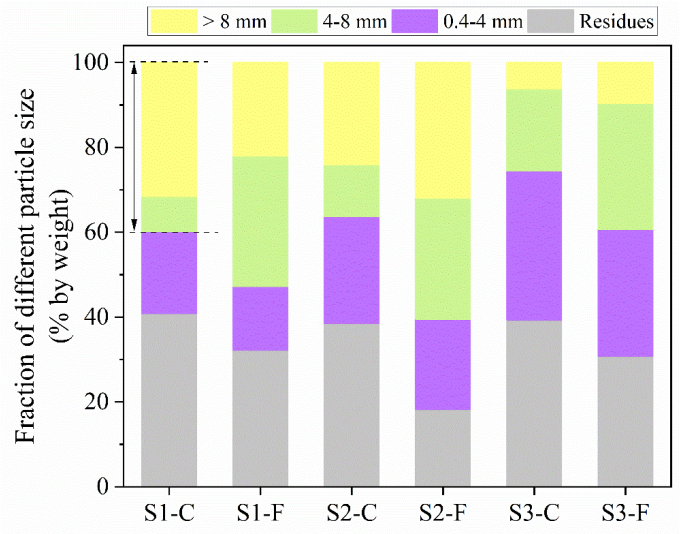

Fig. 6.5 Production efficiency of SLWA (equivalent diameter > 4 mm) under different proportions.

Shape characteristics and physical properties of aggregates are significant parameters for assessing synthesized lightweight aggregates. **Table 6.2** shows the morphological and physical properties of all studied aggregates. In terms of morphological performances, three main parameters: flakiness ratio, elongation ratio, and sphericity are focused on. According to Zingg's classification, three groups are categorized as spherical (flakiness ratio > 2/3., elongation > 2/3). Meanwhile, the shape of aggregates in the S2 group is the nearest closest to the spheric, with the highest levels of sphericity (0.87). The reason for this is unclear but it is possibly related to the design ratio of S2. The resulting early strength can effectively be resistant to impact force in the course of pelletizing. Besides, such a spherical shape can improve workability and affect the stress concentration of corresponding LWA concrete under loading [288]. The results of surface roughness show that sisal fiber incorporation can increase the roughness degree of synthesized aggregates, which can improve the interface property of concrete in the future. Among all the MSWI BA replacement groups, the S2-C and S2-F in the S2 group have the most significant difference in surface roughness as can be seen in **Table 6.2**. The corresponding surface roughness profiles are depicted in **Fig. 6.6**.

Table 6.2 Geometrical characteristics and physical properties of synthesized coarse aggregates under different proportions (**Table 6.1**).

		S1		S2		S3	
		C	F	C	F	C	F
Shape parameters	Flakiness ratio	0.89	0.86	0.92	0.90	0.85	0.86
	Elongation ratio	0.88	0.83	0.86	0.86	0.81	0.86
	Sphericity	0.87	0.84	0.87	0.87	0.82	0.86
Surface roughness (Ra, μm)		2.92	4.07	3.20	5.09	2.91	3.18
Water absorption (%)		22.81	28.17	24.17	29.55	32.23	36.23
Loose-filled bulk density (kg/m^3)		720.92	882.81	675.50	695.42	633.52	652.61

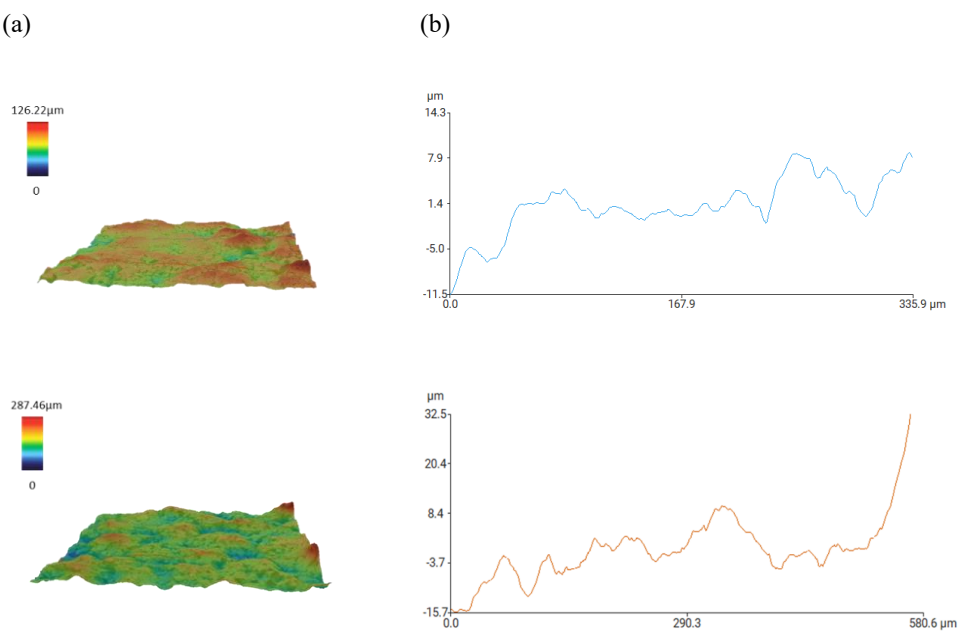

Fig. 6.6 Surface roughness appearances and corresponding type lines of coarse aggregates: S2-C(a) and S2-F(b).

In terms of water absorption, the data presents that SLWAs produced with S1-F, S2-F, and S3-F perform relatively higher compared to those without SF. This could be related to their microstructure changes due to the SF incorporation. Commonly, plant fibers have a hollow

lumen structure, which is prone to absorb water via capillary force [289]. The detailed explanation is further discussed in the following sections. In addition, the loose bulk density of the aggregates is also shown in **Table 6.2**. This shows that the loose bulk density of all aggregate samples is in the range of 633.52-882.81 kg/m^3, which meets the density requirement (between 500 and 1200 kg/m^3) of LWAs according to UNI EN 13055-1:2005 standard. High replacement levels result in a decreased density of the aggregates, which is attributed to the binder content decreases [12]. Whereas, at each substitution level, the SF added can increase the loose bulk density of synthesized aggregates. In fact, there are certain macro and micro pores generation resulting from hydrogen gas release of the metallic aluminum contained MSWI BA, reacted with alkali [269]. SF incorporation can fill the pore spaces and increase the density to some extent. This will be further proved by the following cross-section observation with SEM. Meanwhile, this analysis implied the pore structures are likely to affect the mechanical performance of the SLWAs. To under the effect, the strength of single aggregates is studied in the subsequent section.

6.3.2 Strength of individual aggregate

The strength property of synthesized aggregates is likely to depend on two fundamental aspects. First, the low-activity MSWI BA replacement can negatively influence the hydration kinetics of the binder cement, thus leading to a reduction of strength [290]. Second, the mixture of MSWI BA and cement results in pores generation from metallic aluminum reacting in the alkali environment, seriously hindering the development of structural strength [271, 290].

The strength results of individual aggregate with 4-15 mm are presented in **Fig. 6.7**. The data of the individual aggregate strengths are relatively dispersed since this strength test would be affected by the chosen single aggregate [275]. Therefore, to more clearly exhibit the correlation between the strength properties and the aggregate size, we fitted these dispersed data to analyze and compare. According to the data of the peak force and particle size (**Fig. 6.7a**, **b**, and **c**), the peak force statistically increases with the rising equivalent diameter of individual SLWA regardless of with/without SF incorporation. This trend is well in agreement with the reports of [291, 292]. However, as the replacement level with MSWI BA increases, the average peak forces of the aggregates gradually decrease. Increased MSWI BA content not only reduces the potential degree of pozzolanic reaction within the CEM-MSWI BA system [214, 237] but also generates more pore spaces due to the increase in the metallic aluminum content [36, 293]. The

combination of both factors leads to serious negative effects on the load force. This can be in line with the loose density measurement. According to the data regression analysis, the addition of SF enhances the peak force of individual particles, which is highly related to the filling role of plant fiber. Here, the filler role of SF in the CEM-MSWI BA system is thought a combination of both a physically filling effect and a seeding effect (hetero nucleation and growth). The deep analysis will be discussed in the following sections. In addition to filling the pores, incorporated SF has high stiffness that helps in resistance to compression force. It has to be noted from the fitting non-linear curves that the strengthening effect of SF becomes more significant when the equivalent diameter increases. This could depend on the MSWI BA content of the individual aggregate.

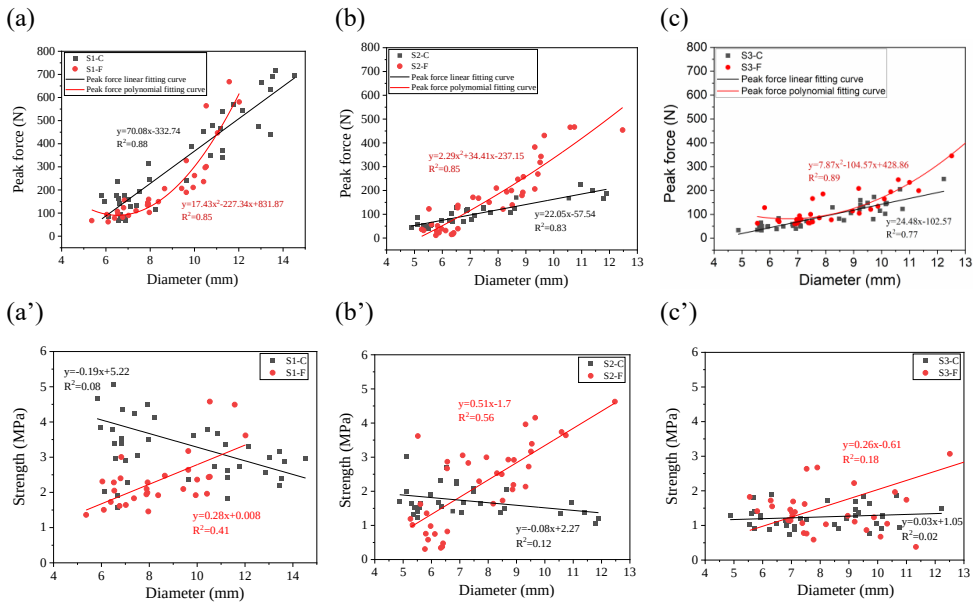

Fig. 6.7 Relationships between SLWA size and peak force (a, b, and c), and strength (a', b' and c'); different SLWAs represented in **Table 6.1**.

The correlations between crushing strength and pellet diameter size were calculated and obtained in **Fig. 6.7a'**, **b'**, and **c'**. The crushing strength of SLWAs decreases with the increase of the aggregate size, which is consistent with the discovery of Liu et al.[292] .investigated the single-particle compression test of artificial MSWI BA-based aggregates and found the peak force increases with the increase of the single-aggregate size. In contrast, the relation between the crushing strength and the aggregate size is a positive correlation for the SF addition. In

particular, in the S2 group (70% replacement), SF addition exhibited the most significant strengthening effect on the SLWAs. In general, plant fiber added to the cementitious matrix can improve the flexural strength of the composites by resisting cracking destruction.

To deeply understand the effect of the SF addition on the CEM-MSWI BA system, we analyze the hydration kinetics of the mixtures and micro-structures of SLWAs in subsequent sections.

6.3.3 Microscopic properties analysis

Calorimetry

The calorimetry results are shown in **Fig. 6.8**. It can be seen from **Fig. 6.8a** that the heat flow rate is quite low, which is mainly due to the major content of low-active MSWI BA incorporation. In addition, several peaks derived from one curve appeared at different hydration times, as shown in **Fig. 6.8b** and **c**. It is unclear but it is probably related to the accelerating/retarding effect of some element components of MSWI BA. Kumar et al. [32] concluded that some heavy metal elements like Cu and Fe can retard cement hydration while the others like Pb and Br appear to accelerate cement hydration. Interestingly, the total heat release of the mixture with SF exceeds that of the mixture without SF at all substitution levels as the hydration time increases. There are two potential reasons for this phenomenon, one is likely because of the internal curing role of SF [294, 295]. SF, due to the hollow lumen structure, absorbs the alkali pore solution containing OH- inside its structure in the initial hydration period. However, at the later period of hydration time, as the moisture of the system is lost, the solution absorbed by SF is slowly released. At this time, the hydroxyl ion in the alkali pore solution can continue to dissolve the metallic aluminum from MSWI BA, forming alumina tetrahedral and finally participating in the system cementitious reaction. These exothermic processes of dissolution and reaction further increase the total heat release. The other is closely related to the extra hetero nucleation sites due to the presence of the SF, which can accelerate the system hydration reaction. The deep mechanism explanation will be discussed in the following section.

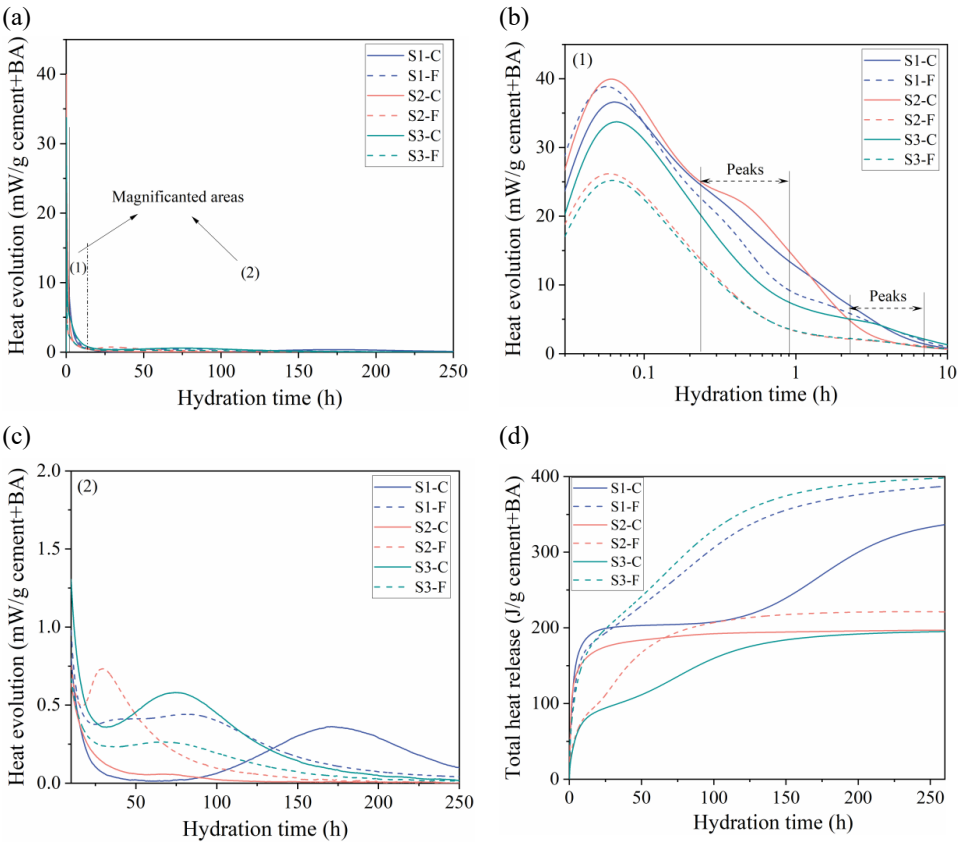

Fig. 6.8 Heat evolution: (a) entire-period curves (b) the curve in the initial 10 h and (c) the curves between 10 and 250 h, and total heat release (d) normalized to the solid mass (cement plus MSWI BA).

To clearly observe the influence of SF incorporation on the system hydration parameters, the correlation between hydration parameters and SF at the different replacement levels of MSWI BA was depicted in **Fig. 6.9**. The SF incorporation is positively correlated with the time at the maximum heat flow (final setting time), as shown in **Fig. 6.9a**. The time advance suggests that fiber incorporation can accelerate the hydration reaction via increased hetero nucleation sites, which is in line with the above analysis of total heat release. The cumulative heat result (**Fig. 6.9b**) indicated that SF added can significantly promote the hydration kinetics of the CEM-BA system. In particular, the SF incorporation under the 70% substitution level achieves the highest cumulative heat, indicating the added SF plays the best optimal role in this substituted system.

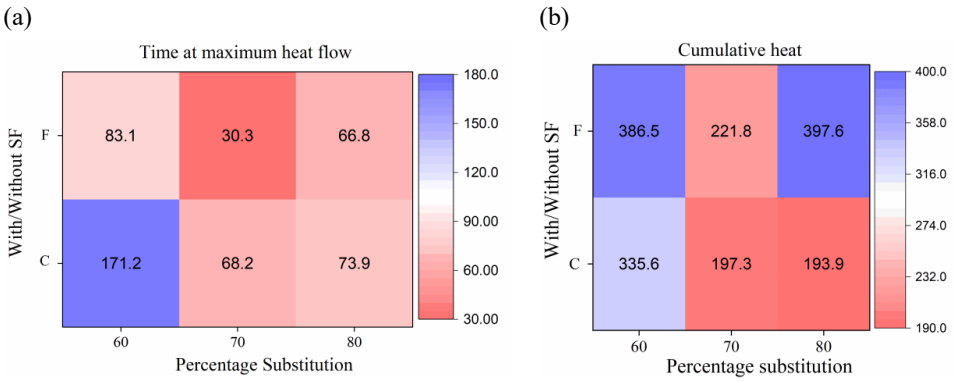

Fig. 6.9 Heat map of correlation between SF contained at the different substitution of MSWI BA and hydration parameters: (a) final setting time and (b) cumulative heat of SLWAs.

Microstructure and pore structure

The optical microscope and SEM images of S2-C and S2-F are shown in **Fig. 6.10**. According to the optical images, the synthesized aggregates without fibers have many micropores and some small pores, whereas only several small pores were observed in the aggregates with fibers. Meanwhile, the fiber and the cementitious matrix are well-bonded. The reason for this phenomenon could be due to the hydroxyl and carbonyl groups on the fiber surfaces, which can promote the nucleation and growth of the calcium silicate hydrate C-S-H gel and chemical bonding with cementitious matrix [296, 297].

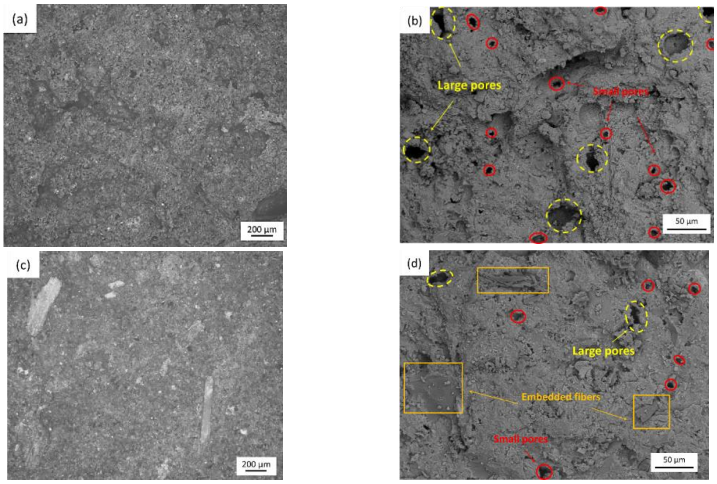

Fig. 6.10 The optical microscope cross-section images of S2-C (a) and S2-F (c); the SEM images of S2-C (b) and S2-F (d).

The SEM images of samples S2-C and S2-F are depicted in **Fig. 6.10b** and **d**. It can be observed that both the amount and size of pores in S2-C are much more than those of sample S2-F. This indicates that the sisal fiber incorporation can densify the aggregates, which is attributed to the pore filling and accelerated hydration through extra hetero-nucleation sites provided.

To quantify the proportion of pore spaces, the porosity of aggregates under different replacements with/without fibers is measured, as shown in **Fig. 6.11**. The total porosities of the aggregate samples (S1-S3) generally increase as the replacement level with BA increases. This is consistent with the strength behaviors of the aggregates at different replacement levels. However, in terms of closed porosity, S2-F at a 70% replacement level, displays the lowest (1.97%). There are possibly two reasons for this. One is related to the closed pore size, which matches the size of the fiber diameter. This is well confirmed by the above optical microscope observation. Another possible reason is when the replacement level is from 60% to 70%, the increased BA tends to lead to increased pore amount and expanded pore size, which means many open pore amounts are generated and closed pore amounts are relatively reduced. As it continues to increase to 80%, the expanding degree of the pore size and the increase of the pore amount gets relatively weak due to much less cement incorporation. Therefore, this is why the increasing trend of total porosity trend is kept, not presenting the same turning point as the closed porosity.

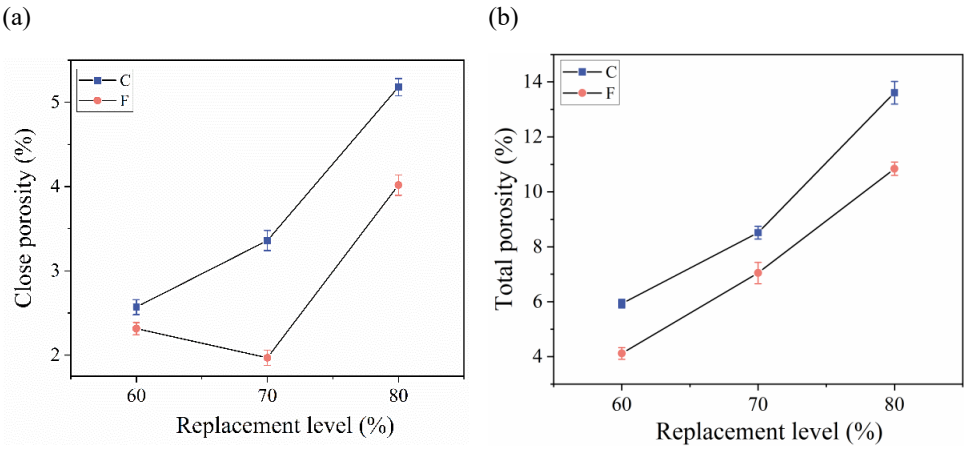

Fig. 6.11 Porosites of the synthesized aggregates with different replacement levels (60%-S1, 70%-S2, and 80%-S3; see Table 6.1): closed porosity (a) and total porosity (b).

Leaching behavior

Considering some hazardous substances contained in MSWI BA, it is necessary to assess the potential environmental impact of the synthesized aggregates in this study. The leaching test was performed on the leachate from the SLWAs, focusing on the concentration of the type of harmful anions (chloride and sulphate) and certain hazardous heavy metal cations. The leaching data is shown in **Table 6.3**.

Table 6.3 Leaching of chloride and sulphate, and heavy metal cations present in the leachates for raw materials (cement and ground MSWI BA) and SLWAs. LL is the legislation limit of building materials in the Netherlands [266].

Samples	Leaching value (mg/kg d.m.)						
	Chloride	Sulphate	Ba	Cr	Cu	Mo	Zn
Ground MSWI BA	8682	13865	0.98	0.4	7.01	3.77	0.84
CEM I 52.5 R [240]	322	52	30000	0.5	<0.01	0.2	0.04
S1-C	2410	75.4	13.32	0.35	3.46	0.81	0.36
S1-F	2260	207	9.45	0.26	3.21	0.67	0.22
S2-C	3320	429	3.16	1.19	4.91	2.43	0.2
S2-F	2710	878	2.1	0.82	4.77	2.27	0.18
S3-C	4800	874	2.25	1.01	7.28	3.04	0.16
S3-F	4570	757	1.62	0.78	7.06	2.82	0.13
LL[a]	616	1730	22	0.63	0.9	1	4.5
LL[b]	8800	20000	100	7	10	15	14

mg/kg d.m. *refers to the mg per kg of dry matter.*

LL[a] *refers to the legislation limit of the building materials that have not been molded.*

LL[b] *refers to the legislation limit of the building materials that only can be applied in insulating facilities.*

It can be seen from the comparison of the leaching data with the legislation limitation values, that the values for the SLWAs are far below the legislation limitation of building materials applied in insulation facilities. This suggests that the synthesized aggregates can be applied in certain construction facilities by enclosing them with an outer layer such as in the liquid-tight

paving application. Compared to the limit values of unmolded materials, the leaching emissions of partially harmful elements in the SLWAs have not yet met the legislation criteria, but it is not difficult to estimate that when the aggregates used as lightweight concrete, the leaching emissions of the resulting composites will be considerably reduced or even below the limit values.

The results show that the leaching values of tested hazardous element ions are significantly decreased after ground MSWI BA is processed into the SLWAs. This is likely to be the fact that the hydration products like C-S-H gel and ettringite generated from the reaction of cement and MSWI BA immobilize these harmful ions, thus reducing their release [11]. As regards the comparison of the experimental aggregates with reference aggregates, the leaching values of the aggregates reinforced with SF can effectively decrease the release of contaminated ions, except for the sulphate anions. The reason for this unusual phenomenon is unclear but is possibly related to the polysaccharides of sisal fibers. This could capture the Ca^{2+} from gypsum, leading to the potential release of sulphate [298].

Overall, after ground MSWI BA is processed into SLWAs, their leaching values of hazardous ions can satisfy the environmental-friendly requirement.

6.3.4 Further mechanism analysis

It is well known that the water-soluble extractives and polysaccharides of plant fiber retard the normal setting and then influence the strength development of the fiber/cement composites [299, 300]. However, in this study, plant fiber added in the CEM-MSWI BA system comprehensively exhibits a positive role in the strength property of the synthesized aggregates, although the retarder effect also possibly exists. To better understand the underlying positive effects of plant fiber in the CEM-MSWI BA matrix, it is important to familiarize the chemical compositions of MSWI BA and its performance within an alkali cement environment. Unlike common supplementary cementitious materials (SCMs), MSWI BA contains a relatively higher amount of metallic aluminum, which readily reacts with alkali and then releases hydrogen gas. This release leads to pore generation, which can detriment the ultimate strength of the resulting CEM-MSWI BA composites [36]. To address it, SF was incorporated into the CEM-MSWI BA matrix for the production of lightweight aggregates.

Based on the characterization and analysis conducted in this study, two mechanisms of SF reinforcement are proposed: the filling effect and the seeding effect, as illustrated in **Fig. 6.12**. For the former, plant fiber incorporation can physically fill the pores produced from the reaction of MSWI BA in the cement system. For the latter, plant fiber can act as seeds, providing additional nucleation sites for the growth of hydration products such as portlandite and the calcium silicate hydrate C-S-H gel, as is shown in **Fig. 6.13**. Similar to the behavior reported in [301, 302]. Meanwhile, plant fiber, as the internal curing agent [302], can more effectively and persistently induce the hetero nucleation and growth of inorganic matrix substances on its surface through the slow release of pore solution. and Ultimately, these two ways can help improve the overall density and compactness of the aggregates.

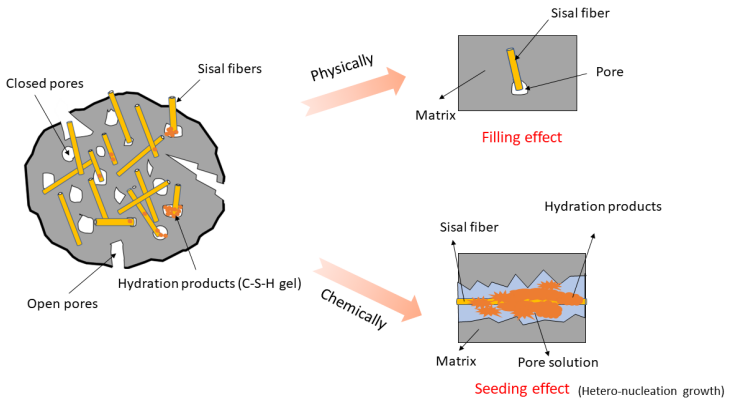

Fig. 6.12 Mechanism schematic in strength development of the SLWAs with SF.

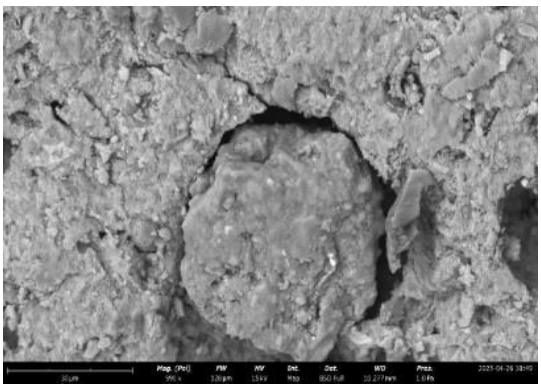

Fig. 6.13 A scanning electron micrograph (SEM) of the cross-section of S2-F.

In terms of contaminant immobilization, plant fibers with hollow structures are prone to absorb wastewater containing heavy metal ions by the capillary force [303]. This suggests that when SF was incorporated into the MSWI BA-OPC system, the pore solution containing heavy metal cations from MSWI BA also could be absorbed into the inner structure of the fiber (**Fig. 6.14**). Subsequently, the heavy metal cations absorbed will be well fixed on the inner surface of the fibers due to the electrical attraction. It is known that plant fiber is negatively charged due to the existence of some functional groups like carboxylic groups [304, 305]. Also, it was reported that heavy metal elements are in the form of their cations distributed in MSWI BA [306]. That means it is probably theoretically possible for the heavy metal cations to be absorbed onto the inner surface of the fibers. Finally, The leaching data of the SLWAs confirmed the above hypothesis of the immobilization mechanism.

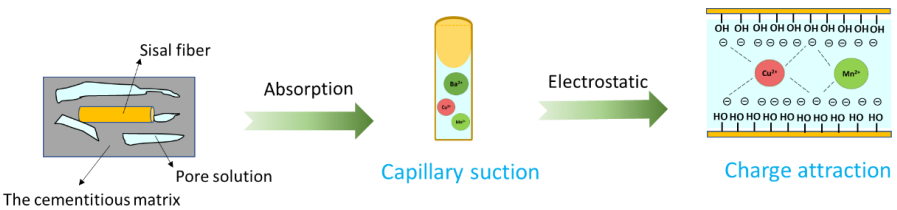

Fig. 6.14 Mechanism schematic in contaminant immobilization of the SLWAs with SF.

6.3.5 Environmental and economic evaluation

Environmental assessment

The greenhouse gas emission generated by the manufactured aggregates was evaluated as an indicator of environmental impact. To quantify the greenhouse gas emission of SLWAs, life cycle assessment (LCA) was employed in this study according to ISO 14040. Because the MSWI BA is one waste substance, the energy consumption and greenhouse gas emissions generated by MSWI BA production are not considered in the following LCA calculation. The transportation distance for delivering raw materials was considered 200 km, (252 km is the longest straight line distance in the Netherlands, referring to [307].

The global warming impact of SLWAs is shown in **Fig. 6.15**. It can be seen that the greenhouse gas emissions comprehensively continue to decrease as the replacement rate with MSWI bottom ash increases. In addition, SF incorporation can help reduce the global warming impact when

the replacement level is the same. This is highly related to the enhanced production efficiency of the SLWAs due to the bridging effect of the fibers. For example, with the S2 group (70% replacement), the global warming impact of S2-F is significantly decreased by about 156 g CO_2 eq./kg (a decrease of 21%) in comparison with the S2-C. That means, S2-F is the best candidate among them considering the global warming impact, which has great potential for the sustainable building industry.

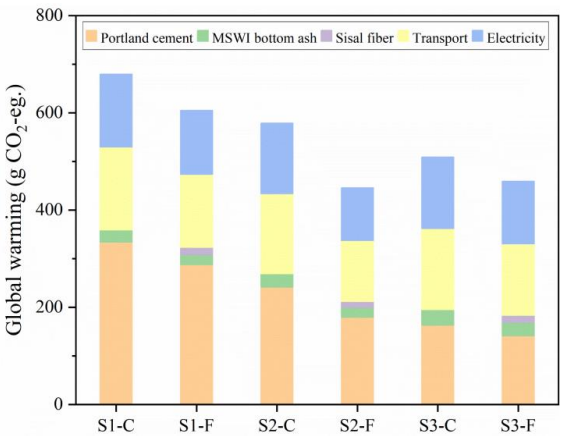

Fig. 6.15 Global warming impacts per 1 kg of aggregate preparation (see **Table 6.1**).

Cost evaluation

The cost data for the materials and their corresponding processing are sourced from the Alibaba online website in the Netherlands region or the broader European area [308]. The detailed price date is referred to in **Table 5.7**.

The cost of synthesized aggregates at different substitutions with MSWI BA is shown in **Fig. 6.16**. The cost data shows that as the substitution level increases, the cost of the SLWAs exhibits a decreased trend. This suggests that the dosage of MSWI BA used plays an important role in reduced cost. Comparing the S2 group and S3 group, the cost gaps of the SLWAs are smaller, which is attributed to the decreased production efficiency with increased MSWI BA. In addition, it is because of the production efficiency sisal fiber can promote, the aggregates reinforced with fiber generally lower cost advantages at the same replacement level. Expanded clay aggregates common commercial LWAs. The price is between €90/m^3 and €120/m^3, which averages far above the cost of the SLWA (both S2 and S3). That means, in the aspect of materials cost, such

SLWA aggregates have the potential to be competitive. Finally, combined with the strength analysis above, the S2-F is the best candidate for the SLWAs production.

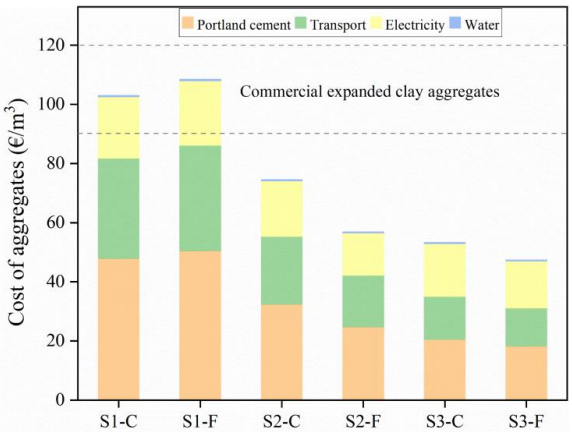

Fig. 6.16 The cost of the SLWAs under different replacement levels (see **Table 6.1**).

In conclusion, the studied SLWAs can not only be friendly to the environment in terms of the green housing gas emission and hazardous contaminant leaching but also have huge economic benefits in the lightweight aggregates market.

6.4 Conclusion

This comparative experiment aims to study the feasibility of the SF incorporation into synthesized MSWI BA aggregates in terms of strength improvement and contaminant leaching solidification. 2 wt. % SF was added into the SLWAs with different replacement levels of MSWI BA. The impacts of SF on the physical characteristics, strength performance, microscopic properties, and sustainability of the produced aggregates were investigated. The following conclusions are drawn:

(1) The incorporation of SF can promote the production efficiency improvement of SLWAs by both hydrophilic nature and charge attraction of the fiber. The surface roughness extent of aggregates containing SF is obviously increased, which benefits the improved interface property of further concrete engineering.

(2) With increased MSWI BA content, the strength properties of SLWAs are reduced. However, the SF addition can considerably strengthen the strength performance of relatively large-

diameter SLWAs, by improving the cement hydration kinetic (seeding effect) and reducing the porosity-filling effect. Especially, the SF shows the most remarkable strengthening effect of the SLWAs at the 70% replacement level of MSWI BA.

(3) The SF added into the aggregates can effectively absorb chloride anions and some harmful heavy metal ions from BA. Combined with the cement solidification effect, the harmful ion leaching requirement of some building applications like insulated facilities can be satisfied.

(4) Through the greenhouse gas emission calculation, it is concluded that the SF incorporation can evidently reduce greenhouse gas emissions when the SLWAs are prepared, particularly the S2-F (a decrease of 23%) compared to S2-C. In addition, for the cost evaluation, the cost of SLWAs has been greatly decreased in comparison with the commercial expanded clay aggregates.

Therefore, our results support the feasibility of the SF as reinforcement for the cold-bonded granulation of MSWI BA. The SF incorporation not only enhances the strength properties of the SLWAs but also contributes to environmental benefits by reducing harmful ion leaching and greenhouse gas emissions. Furthermore, it is evaluated that the cost of SLWAs reinforced with SF is remarkably low, which has huge economic benefits.

CHAPTER 7

7. MSWI bottom ash as natural sand in mortars: the effect of sisal fibers

Based on this paper:
H. Song, T. Liu, F. Gauvin, and H.J.H. Brouwers. Upgrading sand replacement with MSWI bottom ash in mortar applications: A green solution of sisal fiber incorporation (Submitted).

7.1 Introduction

Natural silica sand, especially river silica sand, plays a crucial role in the growth of urbanization and infrastructure, particularly in the construction industry. Globally, an estimated 10.5 billion tons of river sand are consumed annually for the production of mortar and concrete [309]. With the rapid growth of the construction sector, this demand is projected to continue rising. However, excessive excavation of river silica sand can bring remarkable economic benefits, but in turn, simultaneously leads to many environmental threats such as riverbank erosion, river bed depletion, risk to bridge safety, and negative impacts on biodiversity and ecosystems along riverbanks [310, 311]. Moreover, due to its non-renewable nature, the exploitation of river sand is subject to regulation by governments and environmental protection legislation in many countries [311]. As a result, in the present scenario, an alternative material to replace the river silica sand is urgently needed to identify for making mortar and concrete.

In recent years, the use of MSWI BA as a direct replacement for river silica sand in virgin building composite materials, such as mortar and concrete, has attracted large attention in the

context of promoting a circular economy [312-314]. This is because of similar chemical compositions and grain size distribution between MSWI BA and river sands used in building materials [315]. Sani et al. [316] investigated the effect of different sand replacement ratios with bottom ash on the strength properties of the concretes. The results showed that 30% bottom ash replacement, as an optimum usage, could get a favorable strength property. Minane et al. [315] explored the mechanical properties of the mortar by utilizing 100% bottom ash for the substitution of natural sand (<2 mm). Compared with the bottom ash-based mortar without superplasticizer addition, the compressive strength of the bottom ash-based mortar with 3% superplasticizer addition exhibited a significant increase while flexural strength showed a slight increase. Moreover, Tang et al. [227] studied the strength and environmental impacts of the MSWI BA use as sand replacement (maximum replacement ratio of 30%) in the mortar application. It was found that the sand replacement with MSWI BA harmed cement hydration and decreased the strength properties of the mortars. In addition, the leaching contaminants exceed the Dutch legislative limit, which threatens environmentally friendly. Thus, ensuring both sufficient strength performance and effective control of pollutant leaching presents a significant challenge in practical application within the construction industry [314].

In light of the challenges mentioned above, which are similar to those encountered in both Chapter 5 and Chapter 6, the incorporation of sisal fibers can be expected to address these challenges when substituting MSWI BA for natural sands substitution in mortar or concretes.

Consequently, this chapter aims to investigate the effects of sisal fiber incorporation on the mechanical properties and leaching behaviors of the mortar using MSWI BA as a replacement for sand. In this work, the replacement level of sand with MSWI BA in the mortar ranges from 0 -100 vol. %. Flexural strength and fracture toughness of the mortar specimens without or without sisal fibers were obtained by the three-point bending test. The fracture morphology of the specimens was characterized. In addition, the leaching behaviors of the mortars with/without sisal fibers were evaluated. The findings of this study will further accelerate the potential of the practical application of MSWI BA in civil engineering.

7.2 Experimental

7.2.1 Materials

The cement was used 52.5 R grade; The standard silica sand with particle size distribution was used following the UNI EN 196-1:2005 [73]; The employed MSWI BA was supplied by the company Heros (the Netherlands), with already dried treatment. Sisal fibers were provided by Wageningen Food & Biobased Research, the Netherlands. Detailed information on these materials will be given in the following subsection.

Physical properties

The particle size distribution of MSWI BA within 2 mm and standard sands is shown in **Fig. 7.1**. It can be seen that the distribution is similar between them. In addition, the fineness modulus (FM) of MSWI BA and standard sands is 3.7 and 2.4, respectively.

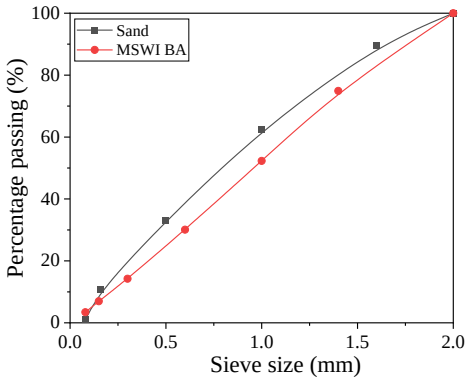

Fig. 7.1 Particle size distribution of MSWI bottom ash and standard sand.

The bulk density (ρ_{bulk}) of the MSWI BA was obtained from the 40*40*40 mm^3 mold filling. For true density (ρ_{true}) and apparent density ($\rho_{apparent}$), a helium pycnometer was employed for measuring the ground MSWI BA powder and dried MSWI BA particles, respectively. For envelop density, the surface dried MSWI BA sample was put into a graduated container, the envelop volume of the sample could be measured by Archimedes method and then calculated to obtain the envelop density ($\rho_{envelop}$). The MSWI BA sample was oven-dried for 24 h at 105 °C, recording the weight as M_{dried}, The dried sample was soaked in water for 24 h, and then the surface water by the absorbed papers, recording the weight as M_{water}. The water absorption

rate (*W*) of the MSWI BA could be calculated by eq. (4.2). According to the abovementioned calculation, the basic physical properties of MSWI BA and standard sands used are given in **Table 7.1**. The characteristics of sisal fibers in this study are provided in **Table 7.2**.

Table 7.1 Basic physical properties of MSWI BA and standard sand.

	Bulk density (g/cm^3)	**Apparent density (g/cm^3)**	**Envelop density (g/cm3)**	**Water absorption (%)**
MSWI BA	1.02	2.65	1.52	24.3
Sand	1.66	2.54	-	2.3

- *unmeasurement*

Table 7.2 Characteristics of sisal fibers.

Properties	**Values**
Fiber length (cm)	0.5-4.5
Fiber diameter (μm)	191-235
Density (g/cm^3)	1.41
Water absorption rate (%)	3.58
Tensile strength (MPa)	430-710

Surface appearance

The microscopic appearance of MSWI BA was observed under scanning electron microscopy (**Fig. 7.2**). Many mineral agglomerations are condensed together and the shapes are irregular including spherical-like and cubic and geometric size. Also, the surface texture of MSWI BA is rough which promotes better bonding and higher strength of mortar or concrete [317]. Further, many fine mico-pores were observed on the surface of MSWI BA. Thus, that is why the coefficient of water absorption is higher compared with fine aggregate sands. This is also confirmed by the literature [318].

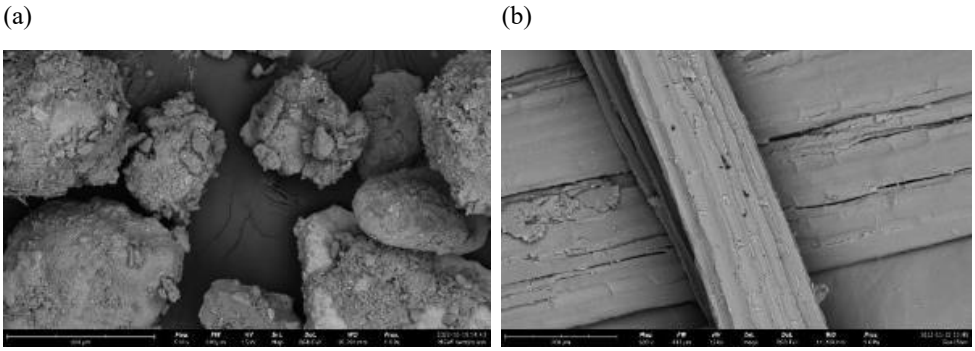

Fig. 7.2 Microscopic appearance of MSWI BA (a) and SF (b).

7.2.2 Methods

Ten types of mortar were produced with various levels of MSWI BA substitution for sand by volume (0%, 25%, 50%, 75%, and 100%). These mortar mixtures were prepared both with and without the SF incorporation. The capital letters, "C" and "F", represent the mortars with and without SF, respectively. The mix proportion example is given in **Fig. 7.3**. The amount of SF is 2 wt.% of cement, and the water/cement ratio was 0.5. It has to be noted that extra water was added in the mixing process to compensate for the water absorption amount of MSWI BA. This step aims to solely focus on the effect of MSWI BA replacement on our research results, excluding the effect of actual w/c ratio variation resulting from the water absorption of MSWI BA and SF.

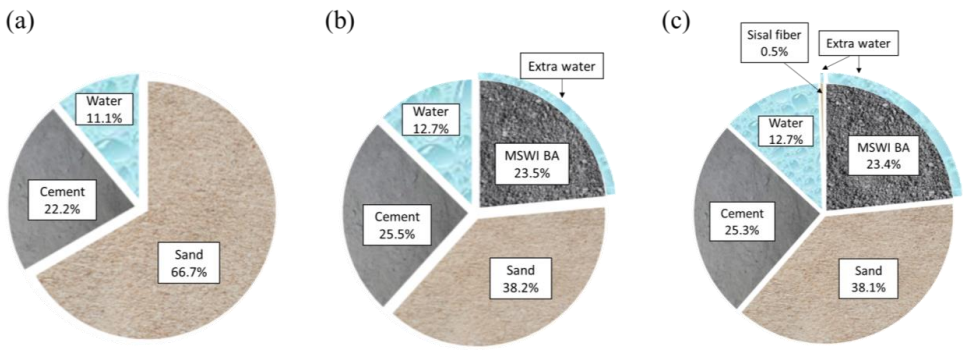

Fig. 7.3 Volume proportions of representative mixes from left to right: (a) control; (b) 50% MSWI BA sand replacement; (c) 50% MSWI BA sand replacement added with sisal fibers.

For the mortar preparation, all dry materials containing cement, MSWI BA, and/or sisal fiber were mixed at a low speed for 1 minute to obtain a perfect homogeneous mixture. The calculated water was added to the mixture slowly. After that, the speed was changed to the middle level at about 120 rpm for the 120 s, to the high level at about 480 rpm for the 60 s, and finally back to the intermediate level for the 30 s. The workability of obtained mortars was measured by a flow table test following the EN 1015-3 [319] and the size of the slump cone used is specifically 60 mm in height with an internal diameter of 100 mm at the bottom and 70 mm at the top. For each mix proportion, three prisms (40*40*160 mm) were cast and covered by the cling film to avoid water evaporation. After 24 h, they were demolded and stored in a curing room at a temperature of 20 ± 1 °C and relative humidity at 96±2% for different ages.

7.2.3 Characterization

Mechanical properties

The mechanical strengths of all mortar samples were tested after 28 days of curing. The compressive strength was carried on broken specimens after a three-point bending test. Three-point bending test was carried out according to the standard EN 196-1[73], which evaluates the flexural strength and fracture toughness of mortars. The EZ 20 Lloyd Instrument (AMETEK) testing machine, equipped with a loading capacity of 50 kN was performed on the mortar samples. More precisely, the displacement of the specimen is driven by the loading cell, with a rate of 0.5 mm per minute. Furthermore, the curves of applied load P versus the mid-span deflection δ of the beam were recorded during the tests, till the complete failure of the specimen [320, 321]. The flexural strength can be calculated according to eq. (2.1). The experimental setup and related testing parameters are shown in **Fig. 7.4a** and **b**, respectively.

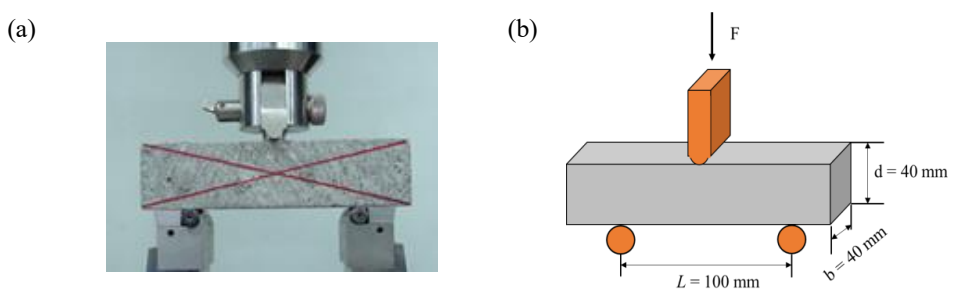

Fig. 7.4 Experimental setup (a) and geometrical sizes and loading configuration (b) for three-point bending test.

Fracture toughness was performed on the current mortars according to the extending provision of ASTMC C1018 [322]. The corresponding toughness index was computed through the following

$$I = \frac{CMOD(3\delta)}{CMOD_{con}(\delta)}\ , \tag{7.1}$$

where δ refers to the mid-span deflection when the first crack of the specimen occurs; $CMOD(3\delta)$ refers to the area under the Crack Mouth Opening Displacement (*CMOD*) from the origin to 3δ; and $CMOD_{con}(\delta)$ refers to the area under the *CMOD* of the control specimens till the crack opening. Therefore, the above formula represents the relative value of energy absorption capacity of the sisal fiber-reinforced mortars compared to the unreinforced mortars. The elasticity modules of the mortars are related to the following ultrasonic pulse velocity test and the corresponding results were obtained based on the following

$$E = (10^5 \times V^2) \times \left(\frac{\Delta}{9.81}\right)\ , \tag{7.2}$$

where E stands for elasticity modulus (GPa), V stands for ultrasonic pulse velocity (km/s), and Δ stands for unit weight (g/cm^3).

Ultrasonic Pulse Velocity (UPV)

Mortar specimens at 28 days of curing were measured using the IP-8 ultrasonic measuring system (Ultratest GmbH, Germany) [323]. Before the measurement, the system was calibrated based on the UPV of 343±3 m/s at 20 °C. Consequently, the mixing mortar was poured into the silicon mold. The inside of the ∅50 mm × 50 mm mortar in the silicon was measured every minute for 72 h through P waves with a measuring distance of 40 mm.

The ultrasonic wave velocity (Vs, km/s) was calculated using:

$$V = L/T\ , \tag{7.3}$$

in which V represents the ultrasonic pulse velocity (km/s), L represents the distance between centers of transducer faces (mm), and T represents the velocity time (μs).

Microstructural analysis

To better understand the microstructure and the interfacial bonding between cement and sand/MSWI BA in mortars, the microstructure of mortar samples was investigated with scanning electron microscopy (SEM). Typical mortar samples were broken into small pieces. These pieces were immersed in isopropanol for 24 h and then over-dried in an oven at 45 °C for 24 h. The dried specimens were sputtered with Au. Finally, a Thermo Fisher Phenom Pro-X microscope was employed to observe the microstructure of prepared samples under an accelerating voltage of 15 kV. The crack propagation on the surfaces of the broken specimens, observed after the compressive strength test, was photographed. Image processing and analysis were conducted using ImageJ software. The original images of the cracked samples were digitally processed to identify cracks for the resistance-deformation capacity analysis. In the analyzed area, contrast and sharpness filters were applied. The images were then converted to 8-bit grayscale binary images and thresholded to obtain grayscale outlines.

7.3 Results and discussion

7.3.1 Workability

Due to the various physical characteristics of MSWI BA and river sands, the workability of fresh mortars is necessary to be evaluated to ensure the feasibility of MSWI BA and/or added SF on the application of the mortar. The results are shown in **Fig. 7.5**. At the MSWI BA substitution rate of 0%, the mortars with/without fibers have remarkably low fluidity. With the increase of MSWI BA replacement level, the spread diameter of fresh mortars expanded gradually. The higher the replacement ratio of MSWI BA is, the higher the fluidity degree of corresponding mortars is. The smaller-sized silica sand tends to absorb water more rapidly at the initial mixing period in light of higher surface areas, somewhat hindering the grain flowability [324]. In contrast, the larger-sized MSWI BA sand enhances grain flowability, particularly in the case of higher replacement of silica sand by MSWI BA. This could be confirmed by the particle size distribution data of cement and MSWI BA. Also, the spherical-like shape of MSWI BA readily flows compared with angular sands.

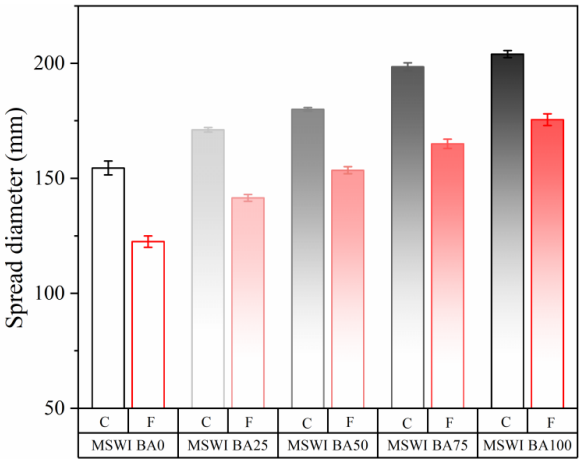

Fig. 7.5 Spread diameter of fresh mortar containing MSWI BA (0%, 25%, 50%, 75%, and 100%) and/or sisal fibers. Noting: C-control; F- fibers.

Compared with the control mortars, the flowing diameters of all mortars reinforced with SF were remarkably reduced regardless of the MSWI BA contention. Taking the MSWI BA75 group as an example, the flowing diameter of MSWI BA75-C is 198 mm, while MSWI BA75-F is 165 mm in flowing diameter, dropping by about 17%. The drop in the workability can result from the combined effect of rough surface, irregular shape, bridging effect, and porosity structure of SF [325, 326]. This is consistent with the study of Wongsa et al. [327] on the characteristics of sisal fiber-reinforced geopolymer mortars, which demonstrated that the geopolymer mortars reinforced with sisal fibers exhibited low flow values.

7.3.2 Mechanical properties of the MSWI BA-based composites

Correlation between compressive strength and non-destructive test

We studied the variation of compressive strength and ultrasonic pulse velocity of the examined mortars under different MSWI BA replacement levels, shown in **Fig. 7.6a** and **b**. As detailed in **Fig. 7.6a**, the compressive strength of mortars exhibited a continuously decreasing trend with an increasing amount of MSWI BA. In all mortars containing MSWI BA, the highest compressive strength was observed with a 25% replacement of MSWI BA, whereas the lowest was observed with a 100% replacement of MSWI BA. This is because the metallic aluminum present in MSWI BA can be reacted in the alkaline cementitious medium, releasing hydrogen gas, forming porous structures, and finally lowering compressive strength [328]. This is also

called the swelling of metallic aluminum [220]. Therefore, higher MSWI BA replacement is poorer strength of the resulting mortars.

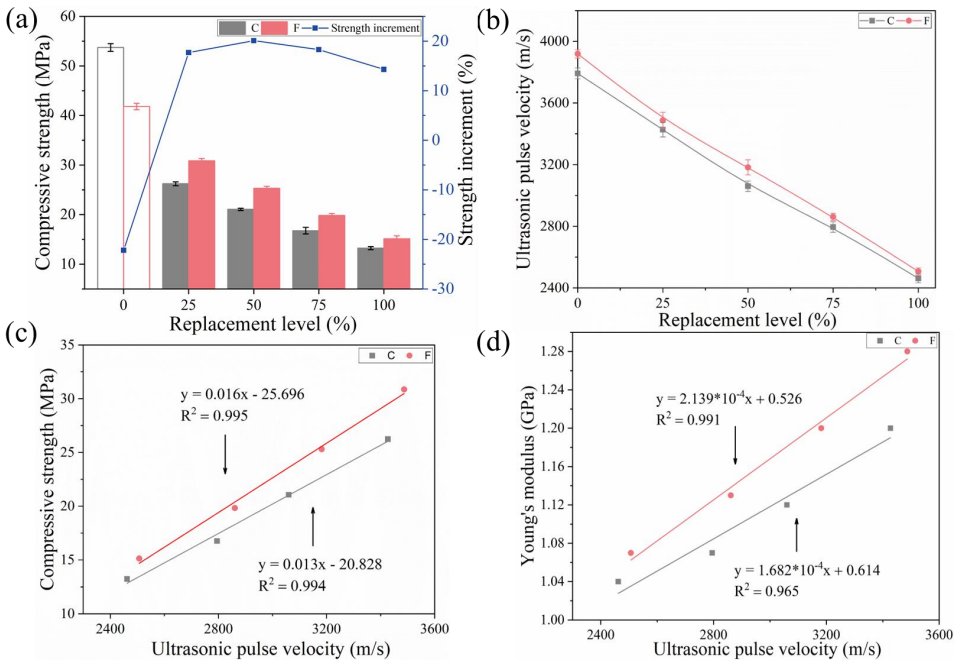

Fig. 7.6 The relation of compressive strength, ultrasonic pulse velocity, and Young's modulus versus different replacements of the two types of mortars with/without SF (C-control and F- fibers). (a) the relation between compressive strength and MSWI BA replacement level; (b) the relation between ultrasonic pulse velocity and MSWI BA replacement level; (c) the relation between compressive strength and ultrasonic pulse velocity, and (d) the relation between Young's modulus and ultrasonic pulse velocity.

Moreover, it can be seen that under 0% MSWI BA replacement level (pure mortars), the fiber addition lowers the compressive strength of the mortar. The compressive strengths of the control mortar and the fiber-reinforced mortar are 53.73 MPa and 41.81 MPa, respectively. similar behavior has been found in the literature [329]. The polysaccharides of SF can delay the cement hydration via hydrolyzed and transform into some carboxylic acids, negatively impacting the strength development. By contrast, in all mortar specimens containing MSWI BA, the compressive strengths of the fiber-reinforced mortar are higher than those of the counterpart control mortars. Notably, the highest strength increment (25.1%) is observed for the MSWI BA 25 group. MSWI BA25-F and MSWI BA75-F are 30.8 MPa and 19.8 MPa, higher than their

counterpart mortars. The increments for the MSWI BA25 group and MSWI BA50 group are 5.7% and 8.6%, respectively. This differs from the common reduced strength of cement-based materials caused by the polysaccharide fibers [116, 330]. In our study, this controversial phenomenon seems to be mainly related to the cementitious system. The structure of the pure cement hydration system is dense, which is ready to be negatively influenced by the fiber polysaccharide dissolution. Whereas, the MSWI BA-based cement system exhibited a porous structure resulting from the swelling of metallic aluminum [220]. This loose structure not only slows the negative impact of the polysaccharide cement hydration reaction but also plays the filling role in the porous matrix due to incorporated SF. Consequently, this combined effect exceeds the retarder effect brought by the fiber polysaccharide, contributing to strength improvement.

Fig. 7.6b compares the non-destructive UPV values of the control mortars and the fiber-reinforced mortars under 0-100% replacement of MSWI BA. The UPV is positively associated with the mortar density (see **Table 7.3**), reflecting the pore structure of the mortars as the presence of such pores can prevent and slow down the pulse velocity [331]. It can be also observed that all fiber-reinforced mortars have higher UPV values than their counterpart control mortars. With a 50% replacement, the fiber-reinforced mortar has a 4.0% higher UPV value in comparison with the control mortar (3060 m/s). A similar result was also found by Wongsa et al. [327] who found that the presence of SF in mortar could increase the ultrasonic wave travel speed. In addition, Mohammed et al. [332] discovered that ultrasonic wave speed in dense concrete (excellent quality) was higher compared to loose concrete (poor quality). Therefore, it can be concluded that SF addition can effectively improve the quality of the mortars containing MSWI BA. Interestingly, the trend of the UPV results is in line with the compressive strength data, except for the control group.

Consequently, to further understand the relationship between these two factors: compressive strength and the UPV value. The results are illustrated in **Fig. 7.6c**. Both correlation coefficient values ($R^2 \geq 0.995$) indicate a closely high correlation between compressive strength and the UPV. It can be also observed that there are the best-fitted positive linear relations between these two factors. The compressive strength increases as the ultrasonic wave travel speed increases. Notice, that the slope value of the regression equation for the fiber-reinforced mortar (0.016) is higher than that for the control mortar, at 0.013.

In addition, Young's modulus, highly related to mechanical strength property, is one of the essential properties for mortar engineering applications. The results of Young's modulus versus the UPV are plotted in **Fig. 7.6d**. The UPV data points to are positive correlation with Young's modulus, which is in line with the correlation with compressive strength. Similar to this, the mortar reinforced with SF exhibits a higher slope value in comparison with the slope of the control mortars ($1.682*10^{-4}$). This indicates that SF addition can somewhat improve the resistance to deformation under loading.

Lastly, to directly characterize the deformation-resistance capacity of the mortars, **Fig. 7.7** compares the side-surface morphology and corresponding grayscale outlines of the examined mortars (MSWI BA 25 replacement and MSWI BA75 replacement) after loading. The grayscale images were obtained through a grey value threshold process in ImageJ software [333].

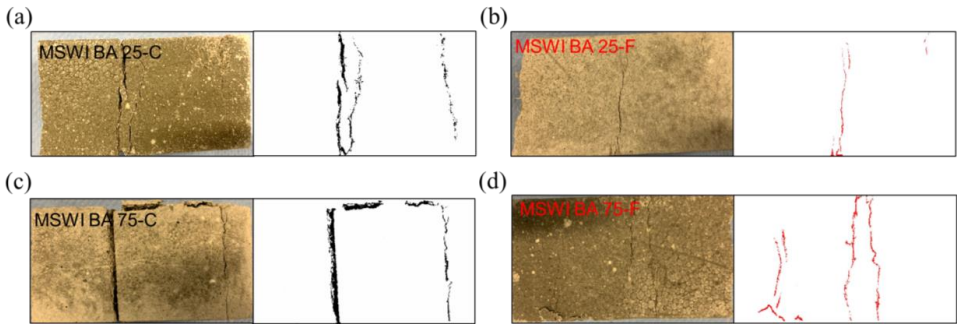

Fig. 7.7 The side surfaces of the mortar specimens with 25% MSWI BA replacement: (a) control mortar; (b) fiber-reinforced mortar) and with 75% MSIW BA replacement: (c) control mortar; (d) fiber-reinforced mortar, after the compressive strength test.

With both MSWI BA replacement levels, the fiber-reinforced mortars (**Fig. 7.7b** and **d**) exhibit fine and fewer cracks after the compressive test, as compared to their counterpart control mortars (**Fig. 7.7a** and **d**). This is because the fiber addition restrains the deformation of mortar under high loading by bridging effect and also because sharing the load force, transferring to the matrix [334]. From the aspect of different substitution levels with MSWI BA, a trend can be concluded that higher substitution corresponds to more serious damages such as wider crack width, bigger crack opening, and more crack number. The increased amount of MSWI BA effectively reduces the resistance-deformation capacity of the mortars.

In summary, the increased replacement levels of MSWI BA can decrease the compressive strength, the UPV, and Young's modulus (deformation resistance). Whereas, the fiber addition can effectively improve the mortar quality in terms of compressive strength, UPV, and resistance-deformation capacity of the mortar composites.

Three-point bending test

The mechanical response of the mortars (containing MSWI BA) reinforced with/without SF is carried out three-point bending test. We took the MSWI BA25 specimens as an example to record an in-situ video of its three-point bending test. The corresponding synchronization of the video frames and the load force-displacement curves is illustrated in **Fig. 7.8**. Through this test, the applied load versus mid-span displacement curves of all investigated mortars were determined and depicted in **Fig. 7.9** and **Fig. 7.10**, respectively. Accordingly, flexural strength and fracture toughness were calculated. Meanwhile, the mortar density and calculated porosity were obtained by helium pycnometer. The results are in **Table 7.3**.

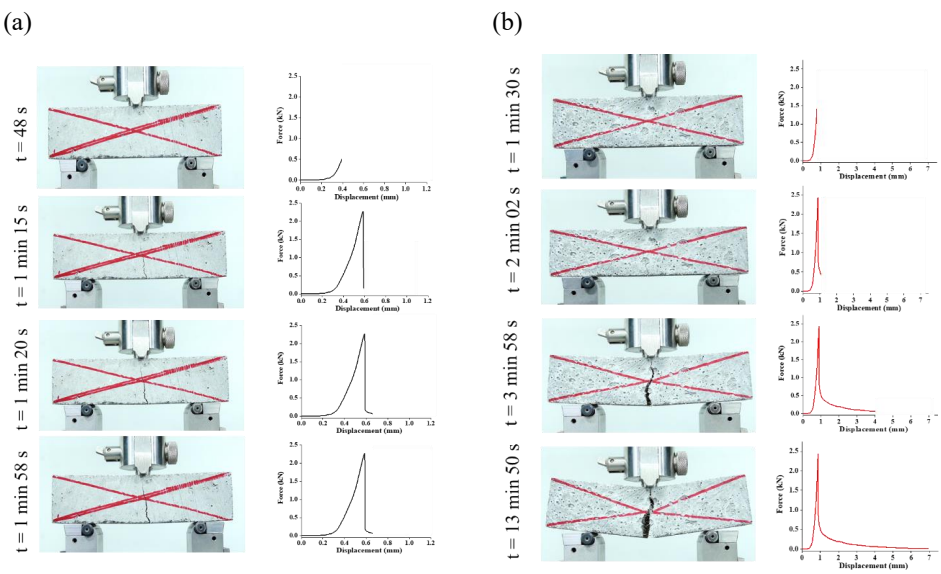

Fig. 7.8 Synchronization of frames from in-situ record video and the corresponding load-displacement curves of a three-point bending test on the mortars within 25% replacement (C-control and F- fibers): (a) MSWI BA25-C and (b) MSWI BA25-F.

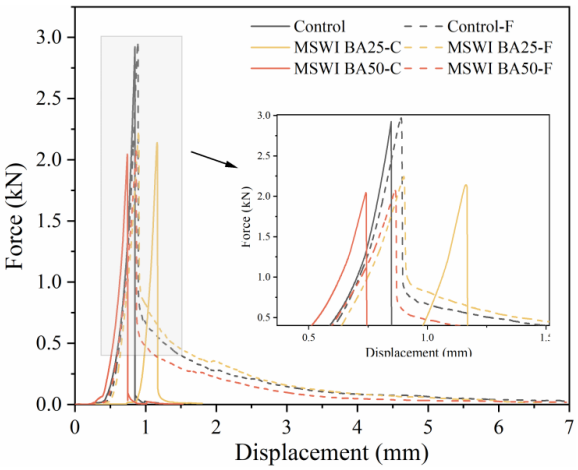

Fig. 7.9 Force vs. displacement curves of the examined mortars (control mortars and fiber-reinforced mortars) within 0%, 25%, and 50% MSWI BA replacements.

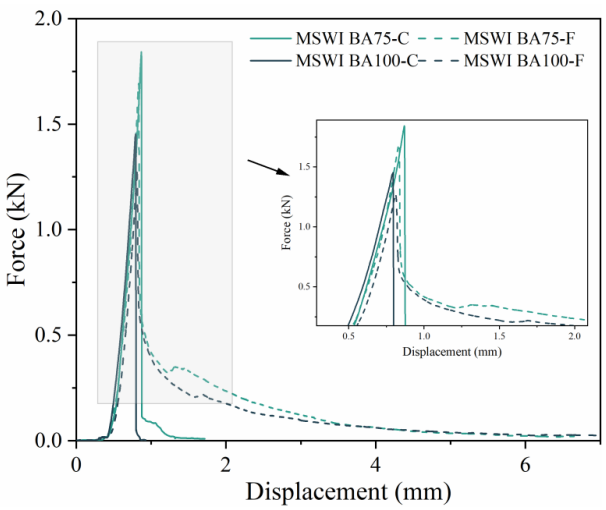

Fig. 7.10 Force vs. displacement curves of the examined mortars (control mortars and fiber-reinforced mortars) within 75% and 100% MSWI BA replacements.

It can be highlighted from the load-displacement curve evolution of the control mortar (**Fig. 7.8a**) that the maximum load force is at the crack appears, and falls rocketly to zero residual strength. This indicates such specimens without the fibers perform quite a brittle failure. Unlike the control mortar, the load force slowly decreased after the peak although a sharp drop load also occurred resulting from less fiber incorporation (see **Fig. 7.8b**). This is because the fibers

began to take over the load in the post-crack area, and the fiber bridging effect benefits controlling the rate of energy release, thus retaining a certain load-carrying capacity of the specimen. Meanwhile, compared with the control mortar, the crack opening of the fiber-reinforced mortar is remarkably wider which indicates higher energy absorption capacity. Similar behavior can be found by Ding et al. [335] reported the crack spacing of the 3D concrete specimens with fibers increased when the force was loaded as compared with the 3D concrete specimens without fibers.

Table 7.3 Tensile properties, densities, and porosities of different mortar specimens (C-control and F-fibers).

Specimen		Flexural strength (MPa)	Fracture toughness	Bulk density (g/cm^3)	True density (g/cm^3)	Porosity (%)
MSWI BA0	C	6.70 ± 0.13	-	2.06	2.47	16.49
	F	6.87 ± 0.11	2.48 ± 0.18	1.99	2.45	18.54
MSWI BA25	C	5.17 ± 0.15	-	1.82	2.43	25.08
	F	5.48 ± 0.18	3.66 ± 0.31	1.86	2.42	23.08
MSWI BA50	C	4.16 ± 0.14	-	1.66	2.35	29.45
	F	4.41 ± 0.20	4.00 ± 0.17	1.72	2.40	28.09
MSWI BA75	C	4.10 ± 0.05	-	1.50	2.34	35.77
	F	3.96 ± 0.07	2.85 ± 0.16	1.59	2.42	34.51
MSWI BA100	C	3.22 ± 0.08	-	1.29	2.40	46.19
	F	3.16 ± 0.10	2.60 ± 0.37	1.39	2.39	41.76

The results in **Fig. 7.9**, **Fig. 7.10**, and **Table 7.3** emphasize that when below the 50% MSWI BA replacement the flexural strength of the fiber-reinforced mortars is higher as compared to the counterpart control mortar, while the slightly lower trend is observed when over the 50% substitution level. This probably be related to the magnified retarder effect of polysaccharide fibers, exceeding the filling effect as the MSWI BA content increases, which hinders the hydration degree of the matrix and weakens the flexural strength. From the fracture toughness data, it can be found that fiber inclusion increases the toughness of the mortar specimens regardless of MSWI BA replacement levels. Noticeably, the reinforcement effect of SF within the mortars containing MSWI BA is more significant than that in control mortars only without MSWI BA. The reinforcement effect depends on the filling effect of SF, highly associated with

void/pore size within the mortars. For the control mortar, the fine pores/voids are generated from the water evaporation and air entrapping when mixing or casting; However, the relatively larger pores/voids for the mortars containing MSWI BA are attributed to the reaction between cement and the metallic aluminum within MSWI BA. The latter pore/void size is better matched for the diameter of SF, which facilitates the specimen reinforcement. Among all mortar specimens containing MSWI BA, the highest fracture toughness was seen at 50% replacement. This phenomenon indicates that the combined effects: the filling effect and interface bonding between the fiber and the matrix, achieve the optimality under such replacement.

Table 7.4 Comparison of the mechanical strength of MSWI BA-based cementitious composites at 28 d curing.

Composite type	MSWI BA content (%)	Fiber type	Fiber percentage (%)	Mechanical strength		References
				Compressive strength (MPa)	Flexural strength (MPa)	
Mortar	20, 40, 60	-	-	37.8, 27.7, 24.2	-	[336]
Mortar	25	-	-	38.4	6.2	[337]
Mortar	50, 100	-	-	12.5, 7.5	-	[338]
Mortar	10, 20, 30	-	-	30.4, 31.4, 33, 5	0.61, 0.62, 0.61	[339]
Paste	5, 10, 15, 20, 30, 40, 50	Wood wool	-	-	4.0, 4.3, 4.9, 2.5, 2.2	[258]
Paste	30, 40, 50	-	-	27.2, 21.4, 15.1	4.9, 4.5, 3.6	[340]
Mortar	25, 50, 75, 100	-	-	28.2, 22.1, 17.8, 13.5	5.2, 4.2, 4.1, 3.2	This study
Mortar	25, 50, 75, 100	Sisal fibers	2 % wt.	29.8, 24.0, 19,1, 15.1	5.5, 4.4, 4.0, 3.2	This study

From the perspectives of porosity aspect and density, a rising trend of porosity and a decreasing trend of density can be identified as MSWI BA replacement increases. This can be explained by more amount of micro-small pores due to an increased aluminum-swelling reaction between

cement and MSWI BA [328]. However, the addition of fibers generally reduced the porosity of fiber-reinforced mortars compared to their counterparts due to the filler effect. The only exception to this was observed in the MSWI BA0 specimens. A comparison of the mechanical strength of MSWI BA-based cementitious composites is also presented in **Table 7.4**. The flexural strength of the mortars in this study is relatively higher compared to the pastes or mortars in other studies, while the compressive strength remains at a similar level across the studies.

Theoretical modeling

To reduce cost and time-consuming experiments, many theoretical models have been developed to predict the mechanical properties of natural fiber-reinforced cement composites [341, 342]. To investigate the feasibility of the model on natural fiber-reinforced composites incorporating MSWI BA, Hirsch's model [343] was employed to predict the tensile modulus and strength of the composites and compare it with the practical results in this study. The calculation equations are as follows:

$$M_C = x\left(M_m V_m + M_f V_f\right) + (1-x)\frac{M_m M_f}{M_m V_f + M_f V_m}\ , \tag{7.4}$$

$$T_C = x\left(T_m V_m + T_f V_f\right) + (1-x)\frac{T_m T_f}{T_m V_f + T_f V_m}\ , \tag{7.5}$$

in which x in both equations is 0.1 for randomly oriented composites. M_c and T_c are the modulus and tensile strength of the composites. V_f and V_m are the fiber volume fraction and matrix volume fraction, respectively. The subscript letters *c*, *f*, and *m* refer to composite, fiber, and matrix, respectively.

Fig. 7.11 compares the predicted mechanical property results and practical results of the investigated composites. The modeling results show good agreement with practical tested results. This is attributed to the uniform distribution of random fiber at loading, which ensures the reasonability of the modeling equations. Similar behavior was also found by Munde et al. [342] reported at low fiber fraction, the model shows a good agreement. More importantly, the comparative results suggest that Hirsch's model can be applied to natural fiber-reinforced composites containing MSWI BA.

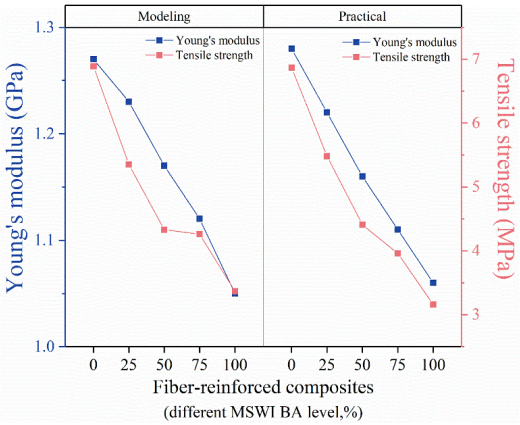

Fig. 7.11 Variation of modeling-calculated Young's modulus values and tensile strength values in comparison with their corresponding practical values of the fiber-reinforced composites.

7.3.3 Microstructure analysis

To directly reflect the variation of inner porous structures with different replacement levels, the cross-section surfaces of fractured mortars were observed in **Fig. 7.12**. **Fig. 7.12** shows optical images of the fracture surfaces after the three-point bending test. Through comparing these images, it can be highlighted that the structure of mortars gets loosened with increasing pores as the replacement level with MSWI BA increases. In all cases of mortars containing MSWI BA, However, the inner structure of mortar gets denser with reduced pore amounts when SF was added into mortars. These results are well in line with the density and porosity data (see **Table 7.3**). From the viewpoint of fracture surface color in all mortars, the color of fracture surfaces gets darker grey as MSWI BA increases under 50% substitution, representing more cement/MSWI BA matrix hydrated, whereas the mortar fracture surfaces present lighter grey with increased MSWI BA over 50% replacement, standing for more cement/MSWI BA matrix unhydrated. This indicates that when exceeding 50% replacement MSWI BA performs significant inert characteristics, not much involving the hydration reaction. It is worth noting that multiple narrow cracks exist in the MSWI BA75-C and the MSWI BA100-C specimens while no visible cracks were observed in the counterpart fiber-reinforced mortar specimens. The crack generation resulted from the over-thermal expansion generated by the reaction of over-amount metallic aluminum from MSWI BA with cement as the replacement level increases [271]. For the fiber-reinforced mortars, the fiber inclusion can absorb certain alkali hydroxyl ions from cement pore solution, thereby reducing the thermal expansion reaction with aluminum and crack generation [344].

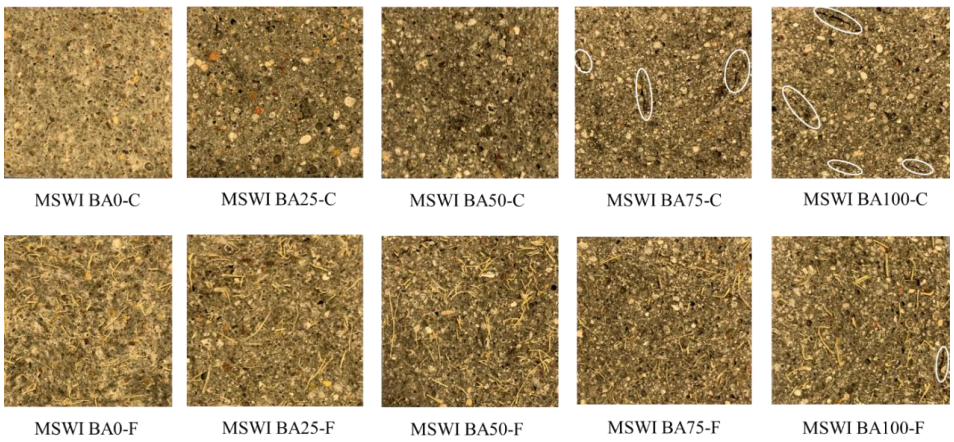

Fig. 7.12 The fracture surface of all mortar specimens (C-control and F- fibers) after the three-point bending test.

To further analyze and compare the microstructure of different mortar specimens, the mortars with 25% and 75% MSWI BA replacement and/or SF were selected to investigate. The results are shown in **Fig. 7.13**. It is evident that the mortars at 25% MSWI BA replacement have fewer pores and denser matrix structure as compared with the mortars at 75% MSWI BA replacement. Also from **Fig. 7.13a**, an ITZ between the sand particle and the cement matrix is dense, owing to the growth into the interface gaps of cement hydration products and the reacted cementitious products between the cement and MSWI BA. wide micro-cracks are exhibited on the fracture surface of the control mortar, while finer micro-cracks are shown on the fracture surface of the fiber-reinforced mortar (**Fig. 7.13b**). Meanwhile, the interface bonding between the fiber and the matrix is quite strong, which can be visible from both the dense fiber-matrix interface microstructure and broken matrix pieces resulting from the fiber being pulled out.

In **Fig. 7.13c** and **d**, many visible holes occur due to the sand particles dropped. This implies that the matrix becomes loosened when low-active MSIW BA is incorporated up to a certain level. However, the fiber incorporation can reduce the pore size and amount through the filling role and internal curing effect of SF. The phenomenon is also consistent with the optical microscope observation (see **Fig. 7.12**).

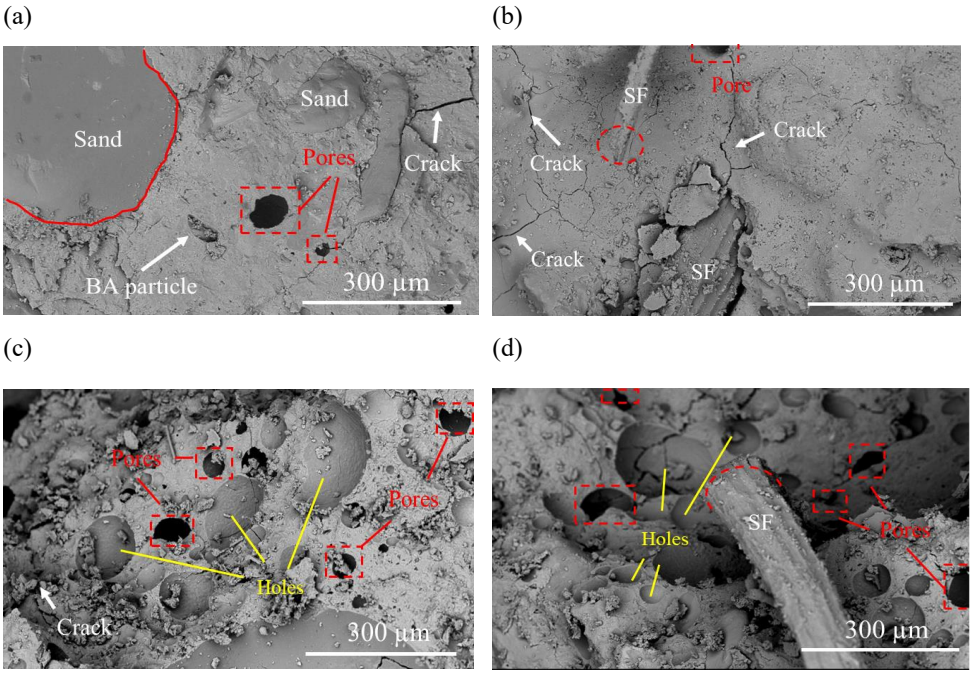

Fig. 7.13 SEM micrographs of typical mortar specimens (C-control and F- fibers): (a) MSWI BA25-C and (b) MSWI BA25-F; (c) MSWI BA75-C and (d) MSWI BA75-F.

In summary, compared with the low MSWI BA replacement level, more pores and holes can be generated within the mortar specimens at the high replacement, negatively affecting strength development. However, the fiber addition can effectively reduce such pores and holes through a physical filling role although certain delays cement hydration due to the polysaccharide release.

7.3.4 Leaching behavior

Besides the strength factor, the leaching issue is another key factor in the feasibility of using MSWI BA to replace sand in building composites. The leaching behaviors of the examined mortar specimens are shown in **Table 7.5**.

It can observed that the leaching values of almost all mortars are below the threshold values set in the Dutch Soil Quality Decree [266]. The concentrations of sulfate, Cr, Zn, and Mo are significantly below the legislation limit value regardless of MSWI BA replacement and SF inclusion. This is closely related to cement hydration products, which incorporate some

contaminant ions into their structure and immobilize these ions [345, 346]. The leaching value variation of chloride and Ba is remarkable, depending on the sand replacement level and SF incorporation. Specifically regarding the leaching value of chloride, only a 25% replacement level can meet the threshold requirement without SF addition. By contrast, the replacement level with MSWI BA can be up to 50% when under SF incorporation. Similar behavior was also found in cases of other contaminant ions. These phenomena suggest that the application of SF in cementitious systems can effectively immobilize contaminant ions, especially some heavy metal ions. Previous studies by scholars [347, 348] have shown that the presence of the capillaries with a large diameter can effectivley treat wastewater especially dyes and heavy metal ions. Therefore, the leaching immobilization in this study is highly related to the hollow-lumen structure of SF, which absorbs the leachate of specimens via physical capillary role during mixing, casting, and early curing.

Table 7.5 Leaching of chloride and sulphate and heavy metal cations present in the leachates for raw materials (cement, MSWI BA, and mortars) and experimental samples (C-control and F- fibers).

Samples		**Leaching value (mg/kg d.m.)**					
		Chloride	Sulphate	Ba	Cr	Zn	Mo
MSWI BA		4870	2390	0.59	0.44	12.64	0.7
CEM I 52.5 R [240]		322	52	30000	0.5	<0.01	0.2
MSWI BA0	C	38.3	81.6	16.1	0.07	0.25	0.03
	F	34.6	60.8	13.6	0.05	0.15	0.03
MSWI BA25	C	549	51.5	26.1	0.05	0.43	0.05
	F	313	42.9	18.3	0.07	0.25	0.05
MSWI BA50	C	1054	55.1	31.4	0.06	0.52	0.11
	F	545	43.6	21.3	0.08	0.29	0.06
MSWI BA75	C	1438	51.8	32.7	0.08	0.52	0.09
	F	698	45.1	21.0	0.11	0.40	0.08
MSWI BA100	C	1381	45.2	31.05	0.12	0.70	0.11
	F	768	47.0	18.9	0.14	0.54	0.1
LL		616	1730	22	0.6	0.9	1

Noting: mg/kg d.m. *refers to the mg per kg of dry matter;* **LL** *refers to the legislation limit of the building materials that have not been molded [266].*

Therefore, SF addition can effectively immobilize the contaminant ions from the mortars containing MSWI BA. That means green SF incorporation can help increase the sand replacement level with MSWI BA, thus further enhancing the utilization rate of hazardous solid waste.

7.3.5 Environmental impact and economic evaluation

Environmental impact

To evaluate the environmental impact of produced specimens, the amount of CO_2 emissions generated was calculated within the Simapro software during the production process. In this work, the CO_2 emission of MSWI BA only considers its transport generation, not considering its production process generation. This is because MSWI BA is burned waste by-products, not actively produced by humans [292]. That means the transport category here just consists of the transport of packed sisal fiber and sand. The transport distance is set as 250 km, based on the longest straight line distance in the Netherlands [307]. The result of the CO_2 emissions is shown in **Fig. 7.14**.

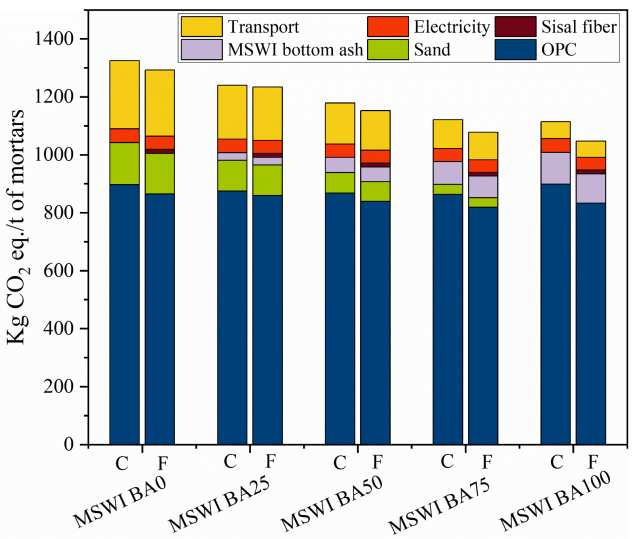

Fig. 7.14 CO_2 emissions of the produced specimens (C-control and F- fibers).

It can be observed that the processing in all mortars within MSWI BA emits a lower amount of CO_2 as compared with the pure mortar process, 1324.5 kg CO_2 eq./t in the MSWI BA0-C and

1292.4 kg CO_2 eq./t in MSWI BA0-F, respectively. Additionally, the CO_2 emission of the corresponding mortar decreases as MSWI BA incorporation increases. The decrease is attributed to the increased substitution ratios with MSWI BA in mortars. Compared with all control mortars, a reduction in CO_2 emission can be observed in their counterpart fiber-reinforced mortars, especially under high replacement levels with MSWI BA. High MSWI BA content generates more pores/voids, meaning incorporating much more low-embodied energy SF into the mortars, consequently lowering the CO_2 emission of its process. Consequently, the inclusion of SF in mortar specimens containing MSWI BA sand has a great advantage in reducing carbon emission footprint.

Economic evaluation

To assess the feasibility and practicality of the specimens, the corresponding preparation cost was calculated. The detailed price date is referred to in **Table 5.7** and the standard sand is 139 €/m^3. Accordingly, the cost of specimen preparation is calculated, as shown in **Fig. 7.15**.

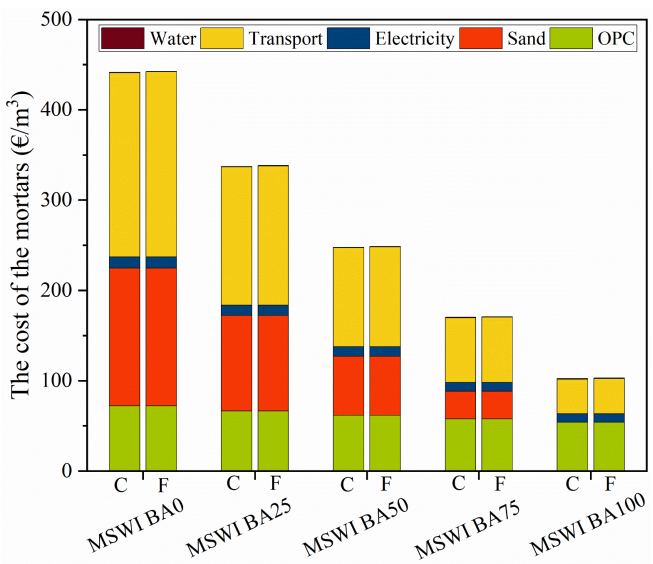

Fig. 7.15 The cost of the produced specimens (C-control and F- fibers).

Fig. 7.15 indicates that as the substitution level with MSWI BA increases, the cost of produced specimens considerably decreases. At the 25% replacement level, the cost of produced mortar specimens is about 23.6% lower than that of pure mortars. Interestingly, the cost of the fiber-

reinforced mortars almost remained constant compared with the control mortars under the same substitution level. This is mainly because SF addition fills the pores within the mortar containing MSWI BA, instead of changing the total mortar structure volume. Additionally, the transport cost of raw material SF is quite low due to its lightweight. Consequently, the cost variation resulting from added SF can be disregarded.

In other words, even though the addition of SF led to a slight increase in cost at the same MSWI BA sand substitution level, it effectively enhances the sand replacement with MSWI BA within specimens by improving specimen properties. This, in turn, results in significant cost reduction and economic benefits.

7.4 Conclusion

This research aims to explore a feasible solution to poor mechanical strength and contaminant leaching issues concerning using the waste by-product MSWI BA as a substitute for natural sand in conventional mortars/concretes. For this, this study introduces sisal fiber and investigates the effects of sisal incorporation on the workability, mechanical properties, and fractography micro performance of the mortars containing MSWI BA sands, while also evaluating environmental impacts, especially toxic leaching behavior, and economic benefits. The conclusions can be drawn as follows:

(1) The utilization of MSWI BA as a substitute for river silica sand appears promising. MSWI BA exhibits similar particle size distribution and density properties with fine silica sands. Additionally, the irregular shape and rough surface of MSWI BA are noted to enhance interfacial bonding, resulting in higher strength properties of mortar/concrete.

(2) Regarding workability, an increased flowability diameter of the mortar as the MSWI BA content increases. By contrast, the addition of SF was observed to reduce the flowability diameter, attributed to the water absorption nature of SF.

(3) Substituting sand with MSWI BA significantly reduces the compressive strength, Young's modulus, and UPV value of the mortar. However, the incorporation of SF enhances these properties in the corresponding mortars. Notably, a highly linear relationship was obtained between compressive strength, Young's modulus, and UPV, which suggested that non-

destructive UPV can be an effective means for estimating the compressive-behavior mechanical properties of this type of mortar mixture containing MSWI BA sand.

(4) Through three-point bending tests, flexural strength, and fracture toughness generally increase upon the addition of SF. Comparative analysis between experiment results and simulated results confirms that Hirsch's theoretical simulation for predicting the tensile modulus and strength of the fiber-reinforced composites applies to SF-reinforced mortars containing MSWI BA sand.

(5) The incorporation of SF can yield remarkably positive environmental impacts. In the leaching test, it was demonstrated that SF effectively mitigates the leaching of certain heavy metal ions, chloride, and sulfate anions, irrespective of the replacement level. Ultimately, the addition of SF enables the replacement of MSWI BA sand to comply with Dutch legislation thresholds for shaped building materials. In assessing the CO_2 emissions associated with the use of MSWI BA sand, it was found that mortar using MSWI BA sand has lower emissions compared to the control mortar using standard river sands; the addition of SF can further reduce CO_2 emissions.

(6) In terms of cost calculation, it is found that using MSWI BA sands significantly decreases the preparation cost. As the replacement level increases, the corresponding cost continues to decrease. Due to the extremely low cost of SF, its addition does not significantly impact the overall cost variation.

Therefore, the addition of SF is a cost-effective way to solve the challenges of using MSWI BA sands in mortar specimens. This not only remarkably increases MSWI BA sand substitution level and enhances the mechanical properties of the related products but also contributes to sustainability, offering both environmental friendliness and economic benefits. Further investigations are warranted to evaluate the efficacy of incorporating other natural fibers in mortar specimens containing MSWI BA sand.

CHAPTER 8

8. Conclusions and recommendations

The thesis focuses on the development of sustainable building composites through the application of natural fibers and MSWI BA. Toward this path, natural fiber-reinforced composites and MSWI BA-based sustainable composites, respectively, are explored. The conclusions drawn from this work, along with corresponding recommendations for future study, are summarized as follows.

8.1 Conclusions for presented work

8.1.1 Durability of natural fiber-reinforced composites

Chapter 2 to Chapter 4 focus on the durability improvement of hemp fiber-reinforced cement composites (HFRCCs) and bio-based insulation composites via fiber treatments. In the study of HFRCCs, the fiber modification effects, mechanical strength, microstructure properties, interfacial bonding, and degradation behavior are evaluated and discussed. To improve the poor fiber-matrix interface property of HFRCCs, caused by the swelling and shrinking behavior of the hydrophilic hemp fibers, the fiber surface was purposefully modified by introducing a low-cost hydrophobic agent, namely alkyl ketene dimer (AKD). The experimental results revealed that the AKD modification can change the hydrophilic characteristic of hemp fibers. The AKD-modified fiber can effectively improve the interfacial bonding and compatibility between the fibers and the cement matrix in comparison with unmodified fibers. As a result, the highest increment of mechanical strength of the composites from 7 d to 28 d of curing was observed in the AKD-modified fiber-reinforced cement composites. The compressive and flexural strength effectively increased up to 53 MPa and 8 MPa, respectively.

Furthermore, to prevent fiber degradation in alkaline cement composites, ZrO_2 was used to coat hemp fibers. According to the thermogravimetric analysis test, the ZrO_2 film can act as a thermal insulator, providing protection that enables the modified hemp fibers to exhibit good thermal stability and effectively mitigate or even prevent rapid alkaline degradation. In addition, it was found that the surface of fibers without ZrO_2 exhibited more cement hydration products, such as portlandite and ettringite. While the surface of ZrO_2-modified fibers in cement composites had fewer hydration products, primarily in the form of C-S-H phases. Importantly, the composites reinforced with ZrO_2-modified fibers retain their high mechanical strength, even after long-term wetting-drying cycles. Finally, based on alkali resistance tests, fibers coated with ZrO_2 film demonstrated superior resistance to both hydrolysis and mineralization.

In terms of bio-based insulation composites, to mitigate the risk of mould growth, which negatively affects durability, hydrophobic modification using AKD was proposed. The experimental investigation revealed that AKD hydrophobic modification enables improved hygrothermal performance and better mould growth resistance capacity of bio-based composites. Notably, modified grass composites exhibit higher porosity, significantly reduced water absorption, lower thermal conductivity, and better mould resistance compared to modified mycelium composites, making them more suitable as insulation materials. Furthermore, hygrothermal simulation results further reveal that AKD modification can effectively enhance the mould resistance of bio-based composites and their suitability to various climate conditions by reducing their hygroscopic properties, particularly for grass composites.

8.1.2 Recycling MSWI BA into building composites

From Chapter 5 to Chapter 7, it is demonstrated that despite many technological barriers, MSWI BA can be successfully utilized as a sustainable building material. This is achieved with the addition of natural fibers, which serve a dual role of filler and contaminant absorbent. The filling and absorbing properties of natural fibers help to which can effectively address the two key problems associated with the use of MSWI BA in different cementitious composites: low strength and contaminant leaching.

As supplementary cementitious materials, MSWI BA was milled to partially replace the cement powder. To address the abovementioned two issues, sisal fibers and oil palm fibers were incorporated into the MSWI BA-based binder composites. The effects of incorporating these

two types of fiber on the composites containing MSWI BA were compared. It was found that when the maximum replacement with MSWI BA increased to 30% the 28-d compressive strength of the blended binder with sisal fibers was about 85% higher than the reference binder. The leaching of contaminants from the crushed MSWI BA-based cement binders is almost far below the limit values of Dutch legislation. Furthermore, MSWI BA-based cement binders with natural fibers have lower greenhouse gas (GHG) emissions and production costs in comparison with pure cement binders.

In the manufacturing process of cold-bonded lightweight aggregate using milled MSWI BA, finely cut sisal fibers were added. The incorporation of sisal fibers improved the production efficiency of coarse manufactured aggregates, with an increase of up to 66.5% at a 70% replacement level of MSWI BA. Moreover, the surface roughness and strength were improved due to the addition of sisal fibers. In the system of the CEM-MSWI BA matrix, the fiber incorporation not only accelerates the cement hydration reaction but also fills the pore generated from the swelling of metallic aluminum in MSWI BA, achieving the strength enhancement of the aggregates. More importantly, some contaminant ions including chloride, chromium, and copper from MSWI BA, could be effectively absorbed and solidified by the sisal fibers.

Apart from the abovementioned applications, the incorporation of sisal fibers is proposed to improve the substitution level of MSWI BA as sand in mortar composites. While the workability increased with higher replacement levels of MSWI BA sands, the mechanical strength properties exhibited a decreased trend due to the increased pore formation according to morphology observation. Conversely, the addition of sisal fibers can increase the mechanical strength of corresponding mortar specimens. The leaching behavior was controlled with the addition of sisal fibers, meeting the Dutch requirement on shaped building materials.

8.2 Recommendations for future studies

This thesis systematically studies the valorization of natural fibers and MSWI BA for the development of sustainable building materials. A series of engineering performances including mechanical strength, microstructure properties, hygrothermal performance, leaching behavior, and sustainability were evaluated. The presented results can provide information and guidance for the management of waste biomass fibers and MSWI BA to achieve an eco-friendly society. Nonetheless, some remaining issues are still in demand for further research, which are as below:

- In the investigation of the interfacial bonding of hemp fiber-reinforced cement composites, mechanical strength, compatibility calculation, and SEM observation have been studied and proven in this thesis. More effective methods and characterization of interface bonding should be applied such as pull-out tests, interfacial transition zones, and molecular simulation.

- In the durability study on using ZrO_2 to modify the fibers as the reinforcement in the cementitious composites, to effectively and reasonably evaluate the durability of modified fiber-reinforced cement composites, the resulting composites should be placed in the practical conditions to evaluate their durability.

- When MSWI BA is used as supplemental cementitious materials, the incorporation of either sisal fiber or oil palm fibers is fixed at a low percentage value. Therefore, it is recommended to optimize the additional amount of these fibers in the composite containing MSWI BA.

- The MSWI BA-based lightweight aggregates under the sisal fiber incorporation show better mechanical strength and decreased leaching behavior. However, this investigation is currently on the aggregate level. A further study on the performance of incorporating them into concrete composites needs to be conducted.

- In the study of incorporating sisal fibers in mortars containing MSWI BA sands, a durability assessment under outdoor conditions should be conducted in order to better evaluate the feasibility of real-scale application.

Bibliography

[1] M.W. Doyle & D.G. Havlick, Infrastructure and the environment, *Annual Review of Environment and Resources* **34**, 349-373 (2009).

[2] P.N. Balaguru & S.P. Shah, Cement Based Materials: Fiber-reinforced cement composites, *Mc Graw Hill International Editions*, (1992).

[3] N. Tkachenko, K. Tang, M. McCarten, S. Reece, D. Kampmann, C. Hickey, M. Bayaraa, P. Foster, C. Layman & C. Rossi, Global database of cement production assets and upstream suppliers, *Scientific Data* **10**(1), 696 (2023).

[4] M. Jaganmohan, Global cement production 1995-2023, *US Geological Survey*, (2024).

[5] Global Carbon Project-Carbon dioxide emissions from the manufacture of cement worldwide from 1960 to 2022 (in million metric tons). https://www.statista.com/statistics/1299532/carbon-dioxide-emissions-worldwide-cement-manufacturing/ (accessed July 1st, 2024).

[6] The Paris Agreement (UNFCCC). https://unfccc.int/process-and-meetings/the-paris-agreement/the-paris-agreement (accessed Nov. 13th, 2023).

[7] O. Onuaguluchi & N. Banthia, Plant-based natural fiber reinforced cement composites: A review, *Cement and Concrete Composites* **68**, 96-108 (2016).

[8] D. Chung, Improving cement-based materials by using silica fume, *Journal of Materials Science* **37**, 673-682 (2002).

[9] R. Helmuth, Fly ash in cement and concrete, *The National Academies of Sciences, Engineering, and Medicin*, *Washington, United States* (1987).

[10] E. Özbay, M. Erdemir & H.İ. Durmuş, Utilization and efficiency of ground granulated blast furnace slag on concrete properties–A review, *Construction and Building Materials* **105**, 423-434 (2016).

[11] X. Li, Y. Lv, B. Ma, Q. Chen, X. Yin & S. Jian, Utilization of municipal solid waste incineration bottom ash in blended cement, *Journal of Cleaner Production* **32**, 96-100 (2012).

[12] R. Cioffi, F. Colangelo, F. Montagnaro & L. Santoro, Manufacture of artificial aggregate using MSWI bottom ash, *Waste Management* **31**(2), 281-288 (2011).

[13] F. de Andrade Silva, B. Mobasher & R.D. Toledo Filho, Cracking mechanisms in durable sisal fiber reinforced cement composites, *Cement and Concrete Composites* **31**(10), 721-730 (2009).

[14] Z. Li, X. Wang & L. Wang, Properties of hemp fiber reinforced concrete composites, *Composites Part A: Applied Science and Manufacturing* **37**(3), 497-505 (2006).

[15] K. Kochova, Mechanical and physical properties of fiber-cement composites using alternative natural fibers (Doctoral Thesis, *Eindhoven University of Technology*, 2022).

[16] K. Kochova, F. Gauvin, K. Schollbach & H.J.H. Brouwers, Using alternative waste coir fibers as a reinforcement in cement-fiber composites, *Construction and Building Materials* **231**, 117121 (2020).

[17] R. Shetty, R. Pai, A.B. Barboza & V.P. Gandhi, Processing, mechanical charaterization and its tribological study of discontinously reinforced caryota urens fiber polyester composites, *ARPN Journal of Engineering and Applied Sciences* **13**(12), 3920-3928 (2018).

[18] F. Kurpiel, Fiber-cement siding is tomorrow's growth product, *Wood Technology* **125**(1), 50-54 (1998).

[19] X. Zhao, X. Wei, Y. Guo, C. Qiu, S. Long, Y. Wang & H. Qiu, Industrial hemp—An old but versatile bast fiber crop, *Journal of Natural Fibers* **19**(13), 6269-6282 (2022).

[20] J. Petit, E.M. Salentijn, M.J. Paulo, C. Thouminot, B.J. Dinter, G. Magagnini, H.J. Gusovius, K. Tang, S. Amaducci & S. Wang, Genetic variability of morphological, flowering, and biomass quality traits in hemp (Cannabis sativa L.), *Frontiers in Plant Science* **11**, 102 (2020).

[21] S.F. Santos, R.S. Teixeira & H.S. Junior, Sustainable and nonconventional construction materials using inorganic bonded fiber composites: Interfacial transition zone between lignocellulosic fiber and matrix in cement-based composites, *Elsevier (Woodhead Publishing)*, *Duxford, United Kingdom* (2017).

[22] S.D. Petroudy, Advanced high strength natural fibre composites in construction: Physical and mechanical properties of natural fibers, *Elsevier (Woodhead Publishing)*, *Duxford, United Kingdom* (2017).

[23] J.F. Vincent, A unified nomenclature for plant fibres for industrial use, *Applied Composite Materials* **7**, 269-271 (2000).

[24] D. Fengel & G. Wegener, Wood: chemistry, ultrastructure, reactions, *Walter de Gruyter*, *Berlin, Germany* (2011).

[25] C.A. Hill, Wood modification: chemical, thermal and other processes, *John Wiley & Sons*, *Chichester, United Kingdom* (2007).

[26] Z. Azwa, B. Yousif, A. Manalo & W. Karunasena, A review on the degradability of polymeric composites based on natural fibres, *Materials & Design* **47**, 424-442 (2013).

[27] J. Wei & C. Meyer, Utilization of rice husk ash in green natural fiber-reinforced cement composites: Mitigating degradation of sisal fiber, *Cement and Concrete Research* **81**, 94-111 (2016).

[28] M. Aziz, P. Paramasivam & S. Lee, Prospects for natural fibre reinforced concretes in construction, *International Journal of Cement Composites and Lightweight Concrete* **3**(2), 123-132 (1981).

[29] J. Wei & C. Meyer, Degradation mechanisms of natural fiber in the matrix of cement composites, *Cement and Concrete Research* **73**, 1-16 (2015).

[30] C.H. Koh, F. Gauvin, K. Schollbach & H.J.H. Brouwers, Investigation of material characteristics and hygrothermal performances of different bio-based insulation composites, *Construction and Building Materials* **346**, (2022).

[31] A. Keulen, A. van Zomeren, P. Harpe, W. Aarnink, H. Simons & H.J.H. Brouwers, High performance of treated and washed MSWI bottom ash granulates as natural aggregate replacement within earth-moist concrete, *Waste Management* **49**, 83-95 (2016).

[32] V. Kumar & N. Garg, The chemical and physical origin of incineration ash reactivity in cementitious systems, *Resources, Conservation and Recycling* **177**, 106009 (2022).

[33] M. Šyc, F.G. Simon, J. Hykš, R. Braga, L. Biganzoli, G. Costa, V. Funari & M. Grosso, Metal recovery from incineration bottom ash: State-of-the-art and recent developments, *Journal of Hazardous Materials* **393**, 122433 (2020).

[34] Y. Xia, P. He, L. Shao & H. Zhang, Metal distribution characteristic of MSWI bottom ash in view of metal recovery, *Journal of Environmental Sciences* **52**, 178-189 (2017).

[35] S. Wong, A.X.Y. Mah, A.H. Nordin, B.B. Nyakuma, N. Ngadi, R. Mat, N.A.S. Amin, W.S. Ho & T.H. Lee, Emerging trends in municipal solid waste incineration ashes research: a bibliometric analysis from 1994 to 2018, *Environmental Science and Pollution Research* **27**, 7757-7784 (2020).

[36] N.M. Alderete, A.M. Joseph, P. Van den Heede, S. Matthys & N. De Belie, Effective and sustainable use of municipal solid waste incineration bottom ash in concrete regarding strength and durability, *Resources, Conservation and Recycling* **167**, 105356 (2021).
[37] X. Dou, F. Ren, M.Q. Nguyen, A. Ahamed, K. Yin, W.P. Chan & V.W.C. Chang, Review of MSWI bottom ash utilization from perspectives of collective characterization, treatment and existing application, *Renewable and Sustainable Energy Reviews* **79**, 24-38 (2017).
[38] Y. Liu, Y. Li, X. Li & Y. Jiang, Leaching behavior of heavy metals and PAHs from MSWI bottom ash in a long-term static immersing experiment, *Waste Management* **28**(7), 1126-1136 (2008).
[39] C. Wiles & P. Shepherd, Beneficial use and recycling of municipal waste combustion residues-a comprehensive resource document, *National Renewable Energy Lab*, *Colorado, United States* (1999).
[40] Q. Alam, Valorization of municipal solid waste incineration bottom ash: chemical nature, leachability and treatments of hazardous elements (Doctoral Thesis, *Eindhoven University of Technology*, 2019).
[41] Q. Alam, M.V.A. Florea, K. Schollbach & H.J.H. Brouwers, A two-stage treatment for Municipal Solid Waste Incineration (MSWI) bottom ash to remove agglomerated fine particles and leachable contaminants, *Waste Management* **67**, 181-192 (2017).
[42] Q. Alam, K. Schollbach, M. Rijnders, C. van Hoek, S. van der Laan & H.J.H. Brouwers, The immobilization of potentially toxic elements due to incineration and weathering of bottom ash fines, *Journal of Hazardous Materials* **379**, 120798 (2019).
[43] H. Luo, Y. Cheng, D. He & E. Yang, Review of leaching behavior of municipal solid waste incineration (MSWI) ash, *Science of The Total Environment* **668**, 90-103 (2019).
[44] E. Awwad, M. Mabsout, B. Hamad, M.T. Farran & H. Khatib, Studies on fiber-reinforced concrete using industrial hemp fibers, *Construction and Building Materials* **35**, 710-717 (2012).
[45] Z. Li, L. Wang & X. Wang, Compressive and flexural properties of hemp fiber reinforced concrete, *Fibers and Polymers* **5**, 187-197 (2004).
[46] B. Çomak, A. Bideci & Ö.S. Bideci, Effects of hemp fibers on characteristics of cement based mortar, *Construction and Building Materials* **169**, 794-799 (2018).
[47] G. Ruano, F. Bellomo, G. Lopez, A. Bertuzzi, L. Nallim & S. Oller, Mechanical behaviour of cementitious composites reinforced with bagasse and hemp fibers, *Construction and Building Materials* **240**, 117856 (2020).
[48] F. Benmahiddine, F. Bennai, R. Cherif, R. Belarbi, A. Tahakourt & K. Abahri, Experimental investigation on the influence of immersion/drying cycles on the hygrothermal and mechanical properties of hemp concrete, *Journal of Building Engineering* **32**, 101758 (2020).
[49] S. Parveen, S. Rana & R. Fangueiro, Sustainable and nonconventional construction materials using inorganic bonded fiber composites: Macro-and nanodimensional plant fiber reinforcements for cementitious composites, *Elsevier (Woodhead Publishing)*, *Duxford, United Kingdom* (2017).
[50] M.J. John, B. Francis, K. Varughese & S. Thomas, Effect of chemical modification on properties of hybrid fiber biocomposites, *Composites Part A: Applied Science and Manufacturing* **39**(2), 352-363 (2008).
[51] G. Ferrara, M. Pepe, E. Martinelli & R. Dias Tolêdo Filho, Influence of an impregnation treatment on the morphology and mechanical behaviour of flax yarns embedded in hydraulic lime mortar, *Fibers* **7**(4), 30 (2019).
[52] R. Sepe, F. Bollino, L. Boccarusso & F. Caputo, Influence of chemical treatments on mechanical properties of hemp fiber reinforced composites, *Composites Part B: Engineering* **133**, 210-217 (2018).

[53] F. Bollino, V. Giannella, E. Armentani & R. Sepe, Mechanical behavior of chemically-treated hemp fibers reinforced composites subjected to moisture absorption, *Journal of Materials Research and Technology* **22**, 762-775 (2023).

[54] S.R. Ferreira, F. de Andrade Silva, P.R.L. Lima & R.D. Toledo Filho, Effect of hornification on the structure, tensile behavior and fiber matrix bond of sisal, jute and curauá fiber cement based composite systems, *Construction and Building Materials* **139**, 551-561 (2017).

[55] J. Claramunt, M. Ardanuy & J.A. García-Hortal, Effect of drying and rewetting cycles on the structure and physicochemical characteristics of softwood fibres for reinforcement of cementitious composites, *Carbohydrate Polymers* **79**(1), 200-205 (2010).

[56] M. Fidelis, Development and mechanical characterization of jute textile reinforced concrete (Doctoral Thesis, *Universidade Federal do Rio de Janeiro*, 2012).

[57] Y. Ohama, Handbook of polymer-modified concrete and mortars: properties and process technology, *Elsevier (William Andrew)*, *New Jersey, United States* (1995).

[58] K. Bilba & M.-A. Arsene, Silane treatment of bagasse fiber for reinforcement of cementitious composites, *Composites Part A: Applied Science and Manufacturing* **39**(9), 1488-1495 (2008).

[59] E.P. Plueddemann, Silane coupling agents: Nature of adhesion through silane coupling agents, *Springer*, (1991).

[60] Y. Xie, C.A. Hill, Z. Xiao, H. Militz & C. Mai, Silane coupling agents used for natural fiber/polymer composites: A review, *Composites Part A: Applied Science and Manufacturing* **41**(7), 806-819 (2010).

[61] L. Boulos, M.R. Foruzanmehr, A. Tagnit-Hamou, S. Elkoun & M. Robert, Wetting analysis and surface characterization of flax fibers modified with zirconia by sol-gel method, *Surface and Coatings Technology* **313**, 407-416 (2017).

[62] G. Garnier, J. Wright, L. Godbout & L. Yu, Wetting mechanism of alkyl ketene dimers on cellulose films, *Colloids and Surfaces A: Physicochemical and Engineering Aspects* **145**(1-3), 153-165 (1998).

[63] W. Zhang, X. Yao, S. Khanal & S. Xu, A novel surface treatment for bamboo flour and its effect on the dimensional stability and mechanical properties of high density polyethylene/bamboo flour composites, *Construction and Building Materials* **186**, 1220-1227 (2018).

[64] N. Angin, S. Caylak, M. Ertas & A.D. Cavdar, Effect of alkyl ketene dimer on chemical and thermal properties of polylactic acid (PLA) hybrid composites, *Sustainable Materials and Technologies* **32**, e00386 (2022).

[65] K. Missoum, F. Martoïa, M.N. Belgacem & J. Bras, Effect of chemically modified nanofibrillated cellulose addition on the properties of fiber-based materials, *Industrial Crops and Products* **48**, 98-105 (2013).

[66] A. Mohanty, M. Misra & L.T. Drzal, Surface modifications of natural fibers and performance of the resulting biocomposites: An overview, *Composite Interfaces* **8**(5), 313-343 (2001).

[67] H. Zhang, Effect of a novel coupling agent, alkyl ketene dimer, on the mechanical properties of wood–plastic composites, *Materials & Design* **59**, 130-134 (2014).

[68] S. Candamano, F. Crea, L. Coppola, P. De Luca & D. Coffetti, Influence of acrylic latex and pre-treated hemp fibers on cement based mortar properties, *Construction and Building Materials* **273**, 121720 (2021).

[69] M. Rahimi, A. Omran & A. Tagnit-Hamou, Role of homogenization and surface treatment of flax fiber on performance of cement-based composites, *Cleaner Materials* **3**, 100037 (2022).

[70] K. Vandepitte, S. Vasile, S. Vermeire, M. Vanderhoeven, W. Van der Borght, J. Latré, A. De Raeve & V. Troch, Hemp (Cannabis sativa L.) for high-value textile applications: The effective long fiber yield and quality of different hemp varieties, processed using industrial flax equipment, *Industrial Crops and Products* **158**, 112969 (2020).

[71] H. Zhang, B. Wang, A. Xie & Y. Qi, Experimental study on dynamic mechanical properties and constitutive model of basalt fiber reinforced concrete, *Construction and Building Materials* **152**, 154-167 (2017).

[72] X. Zheng, Z. Liu, T. Fu, S. Easa, W. Liu & R. Qiu, Performance Enhancement of Asphalt Mixtures Enabled by Bamboo Fibers and Acrylated Epoxidized Soybean Oil, *ACS Sustainable Chemistry & Engineering* **11**(15), 5867-5875 (2023).

[73] EN 196-1. Methods of Testing Cement-Part 1: Determination of Strength. *European Committee for Standardization* (2005).

[74] X. Wu, H. Mou, H. Fan, J. Yin, Y. Liu & J. Liu, Improving the flexibility and durability of aged paper with bacterial cellulose, *Materials Today Communications* **32**, 103827 (2022).

[75] B. Barr, K. Liu & R. Dowers, A toughness index to measure the energy absorption of fibre reinforced concrete, *International Journal of Cement Composites and Lightweight Concrete* **4**(4), 221-227 (1982).

[76] F. Sarker, P. Potluri, S. Afroj, V. Koncherry, K.S. Novoselov & N. Karim, Ultrahigh performance of nanoengineered graphene-based natural jute fiber composites, *ACS Applied Materials & Interfaces* **11**(23), 21166-21176 (2019).

[77] W. Shen, H. Zhang & R. Ettl, Chemical composition of "AKD vapour" and its implication to AKD vapour sizing, *Cellulose* **12**, 641-652 (2005).

[78] A. Valadez-Gonzalez, J. Cervantes-Uc, R. Olayo & P. Herrera-Franco, Effect of fiber surface treatment on the fiber–matrix bond strength of natural fiber reinforced composites, *Composites Part B: Engineering* **30**(3), 309-320 (1999).

[79] B. Arminger, W. Gindl-Altmutter, J. Keckes & C. Hansmann, Facile preparation of superhydrophobic wood surfaces via spraying of aqueous alkyl ketene dimer dispersions, *RSC advances* **9**(42), 24357-24367 (2019).

[80] F. Veloso de Carvalho, K. Pal, F. Gomes de Souza Junior, R. Dias Toledo Filho, T. Moraes de Almeida, E. Daher Pereira, S. Thode Filho, M. Galal Aboelkheir, V. Corrêa Costa, N. Ricardo Barbosa de Lima & F. da Silveira Maranhão, Polyaniline and magnetite on curaua fibers for molecular interface improvement with a cement matrix, *Journal of Molecular Structure* **1233**, 130101 (2021).

[81] J. Zhuang, M. Li, Y. Pu, A.J. Ragauskas & C.G. Yoo, Observation of potential contaminants in processed biomass using fourier transform infrared spectroscopy, *Applied Sciences* **10**(12), 4345 (2020).

[82] W. Liu, A. Mohanty, L. Drzal, P. Askel & M. Misra, Effects of alkali treatment on the structure, morphology and thermal properties of native grass fibers as reinforcements for polymer matrix composites, *Journal of Materials Science* **39**(3), 1051-1054 (2004).

[83] N. Sgriccia, M. Hawley & M. Misra, Characterization of natural fiber surfaces and natural fiber composites, *Composites Part A: Applied Science and Manufacturing* **39**(10), 1632-1637 (2008).

[84] J. Biagiotti, D. Puglia, L. Torre, J.M. Kenny, A. Arbelaiz, G. Cantero, C. Marieta, R. Llano Ponte & I. Mondragon, A systematic investigation on the influence of the chemical treatment of natural fibers on the properties of their polymer matrix composites, *Polymer Composites* **25**(5), 470-479 (2004).

[85] P.N. Nelson, Chain Length and Thermal Sensitivity of the Infrared Spectra of a Homologous Series of Anhydrous Silver(I) n-Alkanoates, *International Journal of Spectroscopy* **2016**, 1-9 (2016).

[86] X. Song, F. Chen & F. Liu, Preparation and characterization of alkyl ketene dimer (AKD) modified cellulose composite membrane, *Carbohydrate Polymers* **88**(2), 417-421 (2012).
[87] S. Beddu, A. Basri, Z.C. Muda, F. Farahlina, D. Mohamad, Z. Itam, N.L.M. Kamal & T. Sabariah, Comparison of thermomechanical properties of cement mortar with kenaf and polypropylene fibers, *IOP Conference Series: Materials Science and Engineering* **1144**(1), 012036 (2021).
[88] S.A. Pasca, I.D. Hartley, M.E. Reid & R.W. Thring, Evaluation of Compatibility between Beetle-Killed Lodgepole Pine (Pinus Contorta var. Latifolia) Wood with Portland Cement, *Materials* **3**(12), 5311-5319 (2010).
[89] F. Ahmad, H.S. Choi & M.K. Park, A Review: Natural Fiber Composites Selection in View of Mechanical, Light Weight, and Economic Properties, *Macromolecular Materials and Engineering* **300**(1), 10-24 (2015).
[90] Z.W. Bin Na, Wood-cement compatibility review, *Wood Research* **59**(5), 813-826 (2014).
[91] D. Miller & A. Moslemi, Wood-cement composites: effect of model compounds on hydration characteristics and tensile strength, *Wood and Fiber Science* **23**(4), 472-482 (1991).
[92] G. Mascolo, M.C. Mascolo, A. Vitale & O. Marino, Microstructure evolution of lime putty upon aging, *Journal of Crystal Growth* **312**(16-17), 2363-2368 (2010).
[93] A. Myerson, Handbook of industrial crystallization, *Elsevier (Butterworth-Heinemann)*, *Massachusetts, United States* (2002).
[94] P. He, M. Wang, S. Fu, D. Jia, S. Yan, J. Yuan, J. Xu, P. Wang & Y. Zhou, Effects of Si/Al ratio on the structure and properties of metakaolin based geopolymer, *Ceramics International* **42**(13), 14416-14422 (2016).
[95] X. Cheng, Y. Li, C. Li, D. Li & Z. Xu, Effect of pretreatment on fabrication of natural fibroin fiber/apatite composites using alternate soaking method, *Journal of Inorganic Materials* **26**(1), 43-48 (2011).
[96] N. Zhang, H. Ye, D. Pan & Y. Zhang, Effects of alkali-treated kenaf fiber on environmentally friendly geopolymer-kenaf composites: Black liquid as the regenerated activator of the geopolymer, *Construction and Building Materials* **297**, 123787 (2021).
[97] A.V. Boehm, S. Meininger, A. Tesch, U. Gbureck & F.A. Müller, The mechanical properties of biocompatible apatite bone cement reinforced with chemically activated carbon fibers, *Materials* **11**(2), 192 (2018).
[98] B. Mohr, J. Biernacki & K. Kurtis, Supplementary cementitious materials for mitigating degradation of kraft pulp fiber-cement composites, *Cement and Concrete Research* **37**(11), 1531-1543 (2007).
[99] M.Y.A. Mollah, Y.N. Tsai & D.L. Cocke, An FTIR investigation of cement based solidification/stabilization systems doped with cadmium, *Journal of Environmental Science & Health Part A* **27**(5), 1213-1227 (1992).
[100] M.Y. Mollah, M. Kesmez & D.L. Cocke, An X-ray diffraction (XRD) and Fourier transform infrared spectroscopic (FT-IR) investigation of the long-term effect on the solidification/stabilization (S/S) of arsenic (V) in Portland cement type-V, *Science of the Total Environment* **325**(1-3), 255-262 (2004).
[101] T. Richard, L. Mercury, F. Poulet & L. d'Hendecourt, Diffuse reflectance infrared Fourier transform spectroscopy as a tool to characterise water in adsorption/confinement situations, *Journal of Colloid and Interface Science* **304**(1), 125-136 (2006).
[102] K. Suzuki, T. Nishikawa & S. Ito, Formation and carbonation of CSH in water, *Cement and Concrete research* **15**(2), 213-224 (1985).
[103] M.Y.A. Mollah, W. Yu, R. Schennach & D.L. Cocke, A Fourier transform infrared spectroscopic investigation of the early hydration of Portland cement and the influence of sodium lignosulfonate, *Cement and Concrete Research* **30**(2), 267-273 (2000).

[104] M. Yousuf, A. Mollah, J.R. Pargat & D.L. Cocke, An infrared spectroscopic examination of cement-based solidification/stabilization systems-Portland types V and IP with zinc, *Journal of Environmental Science & Health, Part A* **27**(6), 1503-1503 (1992).
[105] J. Bensted & S.P. Varma, Some applications of infrared and raman spectroscopy in cement chemistry: Part 3-hydration of Portland cement and its constituents, *Cement Technology* **5**(5), 440-445 (1974).
[106] M. Criado, A. Fernández-Jiménez & A. Palomo, Alkali activation of fly ash: Effect of the SiO_2/Na_2O ratio: Part I: FTIR study, *Microporous & Mesoporous Materials* **106**(1-3), 180-191 (2007).
[107] W. Tahri, B. Samet, S. Baklouti, F. Pacheco-Torgal & C. Jesus, Mechanical Performance of Geopolymeric Mortars Based on Natural Clay, Fly Ash and Metakaolin, *European Mortar Summit, Lisboa, Portugal*, (2015).
[108] J. Da, S.A. Neto, A. Torre & A.P. Kirchheim, Effects of sulfates on the hydration of Portland cement - A review, *Construction and Building Materials* **279**, 122428 (2021).
[109] G.W. Lee & Y.C. Choi, Effect of abaca natural fiber on the setting behavior and autogenous shrinkage of cement composite, *Journal of Building Engineering* **56**, 104719 (2022).
[110] F. Kesikidou & M. Stefanidou, Natural fiber-reinforced mortars, *Journal of Building Engineering* **25**, 100786 (2019).
[111] J. Zuo, Y. Wu & K. Wu, Seebeck Effect and Mechanical Properties of Carbon Nanotube-Carbon Fiber/Cement Nanocomposites, *Fullerenes, Nanotubes, and Carbon nanostructures* **23**(5), 383-391 (2015).
[112] Balasubramanian, J. Chandrashekaran & D. Selvan, Experimental Investigation of Natural Fiber Reinforced Concrete in Construction Industry, *International Research Journal of Engineering and Technology* **2**(1), 179-182 (2015).
[113] K. Korniejenko, E. Frczek, E. Pytlak & M. Adamski, Mechanical Properties of Geopolymer Composites Reinforced with Natural Fibers, *Procedia Engineering* **151**, 388-393 (2016).
[114] Z. Tang, Z. Li, J. Hua, S. Lu & L. Chi, Enhancing the damping properties of cement mortar by pretreating coconut fibers for weakened interfaces, *Journal of Cleaner Production* **379**, 134662 (2022).
[115] F. Pacheco-Torgal & S. Jalali, Cementitious building materials reinforced with vegetable fibres: A review, *Construction and Building Materials* **25**(2), 575-581 (2011).
[116] K. Kochova, K. Schollbach, F. Gauvin & H.J.H. Brouwers, Effect of saccharides on the hydration of ordinary Portland cement, *Construction and Building Materials* **150**, 268-275 (2017).
[117] B. Sun, W. Zhao, G. Cai, T. Noguchi & W. Wang, A novel strength prediction model of mortars with different types of cement and SCMs, *Structural Concrete* **23**(2), 1214-1225 (2022).
[118] J. Khedari, B. Suttisonk, N. Pratinthong & J. Hirunlabh, New lightweight composite construction materials with low thermal conductivity, *Cement and Concrete Composites* **23**(1), 65-70 (2001).
[119] A. Quiroga, V. Marzocchi & I. Rintoul, Influence of wood treatments on mechanical properties of wood–cement composites and of Populus Euroamericana wood fibers, *Composites Part B: Engineering* **84**, 25-32 (2016).
[120] V. Puri, P. Chakrabortty & S. Majumdar, A review of low cost housing technologies in India, *Advances in Structural Engineering: Materials* **3**, 1943-1955 (2015).
[121] H. Song, T. Liu & F. Gauvin, Enhancing mechanical performance of green fiber cement composites: Role of eco-friendly alkyl ketene dimer on surfaces of hemp fibers, *Journal of Materials Research and Technology* **28**, 3121-3132 (2023).

[122] R. De Gutiérrez, L. Diaz & S. Delvasto, Effect of pozzolans on the performance of fiber-reinforced mortars, *Cement and Concrete Composites* **27**(5), 593-598 (2005).

[123] Y. Ban, W. Zhi, M. Fei, W. Liu, D. Yu, T. Fu & R. Qiu, Preparation and performance of cement mortar reinforced by modified bamboo fibers, *Polymers* **12**(11), 2650 (2020).

[124] J.E. Mejia-Ballesteros, L. Rodier, R. Filomeno, H. Savastano Jr, J. Fiorelli & M.F. Rojas, Influence of the fiber treatment and matrix modification on the durability of eucalyptus fiber reinforced composites, *Cement and Concrete Composites* **124**, 104280 (2021).

[125] B. Zukowski, E.R.F. dos Santos, Y.G. dos Santos Mendonça, F. de Andrade Silva & R.D. Toledo Filho, The durability of SHCC with alkali treated curaua fiber exposed to natural weathering, *Cement and Concrete Composites* **94**, 116-125 (2018).

[126] G.H.D. Tonoli, M.N. Belgacem, G. Siqueira, J. Bras, H. Savastano Jr & F.R. Lahr, Processing and dimensional changes of cement based composites reinforced with surface-treated cellulose fibres, *Cement and Concrete Composites* **37**, 68-75 (2013).

[127] L. Boulos, M.R. Foruzanmehr, A. Tagnit-Hamou & M. Robert, The effect of a zirconium dioxide sol-gel treatment on the durability of flax reinforcements in cementitious composites, *Cement and Concrete Research* **115**, 105-115 (2019).

[128] M. Canovas, N. Selva & G. Kawiche, New economical solutions for improvement of durability of Portland cement mortars reinforced with sisal fibres, *Materials and Structures* **25**, 417-422 (1992).

[129] K. Kamiya, S. Sakka & Y. Tatemichi, Preparation of glass fibres of the ZrO_2-SiO_2 and Na_2O-ZrO_2-SiO_2 systems from metal alkoxides and their resistance to alkaline solution, *Journal of Materials Science* **15**, 1765-1771 (1980).

[130] T. Jung & R. Subramanian, Alkali resistance enhancement of basalt fibers by hydrated zirconia films formed by the sol-gel process, *Journal of Materials Research* **9**(4), 1006-1013 (1994).

[131] E.M. Salentijn, Q. Zhang, S. Amaducci, M. Yang & L.M. Trindade, New developments in fiber hemp (Cannabis sativa L.) breeding, *Industrial Crops and Products* **68**, 32-41 (2015).

[132] C. Wang, Y. Zhang, H. Tan & X. Du, Non-calcined ZrO_2 sol-coated hollow glass fibre membrane: Preparation, microstructure, and dye separation, *Ceramics International* **47**(9), 12906-12915 (2021).

[133] J.L. Stapper, F. Gauvin & H.J.H. Brouwers, Influence of short-term degradation on coir in natural fibre-cement composites, *Construction and Building Materials* **306**, 124906 (2021).

[134] H. Wang, R. Postle, R. Kessler & W. Kessler, Removing pectin and lignin during chemical processing of hemp for textile applications, *Textile Research Journal* **73**(8), 664-669 (2003).

[135] R. Shanks, A. Hodzic & D. Ridderhof, Composites of poly (lactic acid) with flax fibers modified by interstitial polymerization, *Journal of Applied Polymer Science* **99**(5), 2305-2313 (2006).

[136] L. Boulos, M.R. Foruzanmehr & M. Robert, Evolution of the interfacial transition zone and the degradation mechanism of zirconia treated flax fabric reinforced cementitious composites, *Construction and Building Materials* **190**, 120-130 (2018).

[137] A.K. Both, D. Choudhry & C.L. Cheung, Valorization of hemp fibers into biocomposites via one-step pectin-based green fabrication process, *Journal of Applied Polymer Science* **140**(10), e53586 (2023).

[138] J.T. Mhlongo, Y. Nuapia, B. Tlhaole, O.T. Mahlangu & A. Etale, Optimization of hemp bast microfiber production using response surface modelling, *Processes* **10**(6), 1150 (2022).

[139] A. Hakamy, F. Shaikh & I.M. Low, Thermal and mechanical properties of hemp fabric-reinforced nanoclay–cement nanocomposites, *Journal of Materials Science* **49**, 1684-1694 (2014).
[140] J. de Almeida Melo Filho, F. de Andrade Silva & R.D. Toledo Filho, Degradation kinetics and aging mechanisms on sisal fiber cement composite systems, *Cement and Concrete Composites* **40**, 30-39 (2013).
[141] D. Sarkar, D. Mohapatra, S. Ray, S. Bhattacharyya, S. Adak & N. Mitra, Synthesis and characterization of sol–gel derived ZrO_2 doped Al_2O_3 nanopowder, *Ceramics International* **33**(7), 1275-1282 (2007).
[142] J. Liao, D. Zhou, B. Yang, R. Liu & Q. Zhang, Sol–gel preparation and photoluminescence properties of tetragonal ZrO_2: Y^{3+}, Eu^{3+} nanophosphors, *Optical Materials* **35**(2), 274-279 (2012).
[143] F. Deschner, F. Winnefeld, B. Lothenbach, S. Seufert, P. Schwesig, S. Dittrich, F. Goetz-Neunhoeffer & J. Neubauer, Hydration of Portland cement with high replacement by siliceous fly ash, *Cement and Concrete Research* **42**(10), 1389-1400 (2012).
[144] H.F.W. Taylor, Cement chemistry *(2nd ed.)*, *Thomas Telford*, *London, United Kingdom* (1997).
[145] I. Richardson & G. Groves, The incorporation of minor and trace elements into calcium silicate hydrate (C-S-H) gel in hardened cement pastes, *Cement and Concrete Research* **23**(1), 131-138 (1993).
[146] D. Bonen & S. Diamond, Interpretation of Compositional Patterns Found by Quantitative Energy Dispersive X-ray Analysis for Cement Paste Constituents, *Journal of the American Ceramic Society* **77**(7), 1875-1882 (1994).
[147] A.J. Connelly, K.P. Travis, R.J. Hand, N.C. Hyatt & E. Maddrell, Composition–structure relationships in simplified nuclear waste glasses: 2. The effect of ZrO_2 additions, *Journal of the American Ceramic Society* **94**(1), 137-144 (2011).
[148] A. Paul, Chemical durability of glasses; a thermodynamic approach, *Journal of Materials Science* **12**, 2246-2268 (1977).
[149] Y. Zhang, Z. Yang & J. Jiang, Insight into ions adsorption at the CSH gel-aqueous electrolyte interface: from atomic-scale mechanism to macroscopic phenomena, *Construction and Building Materials* **321**, 126179 (2022).
[150] X. An, R. Zhang, L. Liu, J. Yang, Z. Tian, G. Yang, H. Cao, Z. Cheng, Y. Ni & H. Liu, Ozone pretreatment facilitating cellulase hydrolysis of unbleached bamboo pulp for improved fiber flexibility, *Industrial Crops and Products* **178**, 114577 (2022).
[151] A.B. Akinyemi, E.T. Omoniyi & G. Onuzulike, Effect of microwave assisted alkali pretreatment and other pretreatment methods on some properties of bamboo fibre reinforced cement composites, *Construction and Building Materials* **245**, 118405 (2020).
[152] M.M. Camargo, E. Adefrs Taye, J.A. Roether, D. Tilahun Redda & A.R. Boccaccini, A review on natural fiber-reinforced geopolymer and cement-based composites, *Materials* **13**(20), 4603 (2020).
[153] G. Ren, T. Chen, X. Gao & A. Su, Insights into thermal stability and interface bond performance of sisal fiber in ultra-high performance concrete under different curing conditions, *Cement and Concrete Composites* **137**, 104910 (2023).
[154] D. Gomes dos Santos, A. Barbosa de Lima & P. de Sousa Costa, The effect of the drying temperature on the moisture removal and mechanical properties of sisal fibers, *Defect and Diffusion Forum* **380**, 66-71 (2017).
[155] M. Cai, H. Takagi, A.N. Nakagaito, M. Katoh, T. Ueki, G.I. Waterhouse & Y. Li, Influence of alkali treatment on internal microstructure and tensile properties of abaca fibers, *Industrial Crops and Products* **65**, 27-35 (2015).
[156] P. Saha, S. Manna, S.R. Chowdhury, R. Sen, D. Roy & B. Adhikari, Enhancement of tensile strength of lignocellulosic jute fibers by alkali-steam treatment, *Bioresource Technology* **101**(9), 3182-3187 (2010).

[157] X. Wang, L. Dou, Z. Li, L. Yang, J. Yu & B. Ding, Flexible hierarchical ZrO_2 nanoparticle-embedded SiO_2 nanofibrous membrane as a versatile tool for efficient removal of phosphate, *ACS Applied Materials & Interfaces* **8**(50), 34668-34676 (2016).

[158] G. Ramakrishna & T. Sundararajan, Studies on the durability of natural fibres and the effect of corroded fibres on the strength of mortar, *Cement and Concrete Composites* **27**(5), 575-582 (2005).

[159] N. Tabassum, D. Kumar, D. Verma, R.A. Bohara & M. Singh, Zirconium oxide (ZrO_2) nanoparticles from antibacterial activity to cytotoxicity: A next-generation of multifunctional nanoparticles, *Materials Today Communications* **26**, 102156 (2021).

[160] V.D. Pizzol, L.M. Mendes, H. Savastano Jr, M. Frías, F. Davila, M.A. Cincotto, V.M. John & G.H.D. Tonoli, Mineralogical and microstructural changes promoted by accelerated carbonation and ageing cycles of hybrid fiber–cement composites, *Construction and Building Materials* **68**, 750-756 (2014).

[161] L. Zhao, S. Zhu, H. Wu, H. Liang, C. Liu, W. Liu, W. Zhou & Y. Song, The improved resistance against the degradation of sisal fibers under the environment of cement hydration by surface coating of graphene oxide (GO) based membranes, *Construction and Building Materials* **305**, 124694 (2021).

[162] R.D. Tolêdo Filho, K. Scrivener, G.L. England & K. Ghavami, Durability of alkali-sensitive sisal and coconut fibres in cement mortar composites, *Cement and Concrete Composites* **22**(2), 127-143 (2000).

[163] R. Simhan, Chemical durability of ZrO_2 containing glasses, *Journal of Non-Crystalline Solids* **54**(3), 335-343 (1983).

[164] M. Chikhi, B. Agoudjil, A. Boudenne & A. Gherabli, Experimental investigation of new biocomposite with low cost for thermal insulation, *Energy and Buildings* **66**, 267-273 (2013).

[165] A. Kumar, K. Staněk, P. Ryparová, P. Hajek & J. Tywoniak, Hydrophobic treatment of wood fibrous thermal insulator by octadecyltrichlorosilane and its influence on hygric properties and resistance against moulds, *Composites Part B: Engineering* **106**, 285-293 (2016).

[166] B.P. Jelle, Traditional, state-of-the-art and future thermal building insulation materials and solutions–Properties, requirements and possibilities, *Energy and Buildings* **43**(10), 2549-2563 (2011).

[167] M. Alam, H. Singh & M. Limbachiya, Vacuum Insulation Panels (VIPs) for building construction industry–A review of the contemporary developments and future directions, *Applied Energy* **88**(11), 3592-3602 (2011).

[168] F. Pacheco-Torgal, Eco-efficient construction and building materials research under the EU Framework Programme Horizon 2020, *Construction and Building Materials* **51**, 151-162 (2014).

[169] E. Latif, M.A. Ciupala, S. Tucker, D.C. Wijeyesekera & D.J. Newport, Hygrothermal performance of wood-hemp insulation in timber frame wall panels with and without a vapour barrier, *Building and Environment* **92**, 122-134 (2015).

[170] A. Abdou & I. Budaiwi, The variation of thermal conductivity of fibrous insulation materials under different levels of moisture content, *Construction and Building Materials* **43**, 533-544 (2013).

[171] P.L. Hurtado, A. Rouilly, V. Vandenbossche & C. Raynaud, A review on the properties of cellulose fibre insulation, *Building and Environment* **96**, 170-177 (2016).

[172] S. Panyakaew & S. Fotios, New thermal insulation boards made from coconut husk and bagasse, *Energy and Buildings* **43**(7), 1732-1739 (2011).

[173] S. Kumfu & T. Jintakosol, Thermal insulation produced from pineapple leaf fiber and natural rubber latex, *Advanced Materials Research* **506**, 453-456 (2012).

[174] R.v.d. Meiracker, J. Vredenbregt, V.d. Boer, J. Gumbs & S. Fransen, The reuse of grass waste in southwest Drenthe *Commissioned by Municipality Hoogeveen, Wageningen, The Netherlands* (2015).
[175] Koh, F. Gauvin, K. Schollbach & H.J.H. Brouwers, Investigation of material characteristics and hygrothermal performances of different bio-based insulation composites, *Construction and Building Materials* **346**, 128440 (2022).
[176] V. Guna, M. Ilangovan, K. Adithya, A.K. CV, C. Srinivas, S. Yogesh, G. Nagananda, K. Venkatesh & N. Reddy, Biofibers and biocomposites from sabai grass: A unique renewable resource, *Carbohydrate Polymers* **218**, 243-249 (2019).
[177] L. Lu, X. Wang, S. Li, Y. Tang & X. Mai, Thermal performance of lonicera rupicola grass as a building insulation composite material, *Advanced Composites and Hybrid Materials* **6**(1), 8 (2023).
[178] M. Jones, T. Huynh, C. Dekiwadia, F. Daver & S. John, Mycelium composites: a review of engineering characteristics and growth kinetics, *Journal of Bionanoscience* **11**(4), 241-257 (2017).
[179] M. Pelletier, G. Holt, J. Wanjura, E. Bayer & G. McIntyre, An evaluation study of mycelium based acoustic absorbers grown on agricultural by-product substrates, *Industrial Crops and Products* **51**, 480-485 (2013).
[180] M. Haneef, L. Ceseracciu, C. Canale, I.S. Bayer, J.A. Heredia-Guerrero & A. Athanassiou, Advanced materials from fungal mycelium: fabrication and tuning of physical properties, *Scientific Reports* **7**(1), 41292 (2017).
[181] X. Zhang, X. Fan, C. Han, Y. Li, E. Price, G. Wnek, Y.-T.T. Liao & X.B. Yu, Novel strategies to grow natural fibers with improved thermal stability and fire resistance, *Journal of Cleaner Production* **320**, 128729 (2021).
[182] F.V. Appels, S. Camere, M. Montalti, E. Karana, K.M. Jansen, J. Dijksterhuis, P. Krijgsheld & H.A. Wösten, Fabrication factors influencing mechanical, moisture-and water-related properties of mycelium-based composites, *Materials & Design* **161**, 64-71 (2019).
[183] M. Zhang, Z. Zhang, R. Zhang, Y. Peng, M. Wang & J. Cao, Lightweight, thermal insulation, hydrophobic mycelium composites with hierarchical porous structure: Design, manufacture and applications, *Composites Part B: Engineering* **266**, 111003 (2023).
[184] M. Jones, A. Mautner, S. Luenco, A. Bismarck & S. John, Engineered mycelium composite construction materials from fungal biorefineries: A critical review, *Materials & Design* **187**, 108397 (2020).
[185] P. Johansson, T. Svensson & A. Ekstrand-Tobin, Validation of critical moisture conditions for mould growth on building materials, *Building and Environment* **62**, 201-209 (2013).
[186] E. Vereecken & S. Roels, Review of mould prediction models and their influence on mould risk evaluation, *Building and Environment* **51**, 296-310 (2012).
[187] S.S. Peeters, Assessing Modifications on Mycelium-Based Composites and the Effects on Fungal Degradation and Material Properties (Master thesis, *Eindhoven University of Technology Eindhoven*, 2023).
[188] A. Lozhechnikova, K. Vahtikari, M. Hughes & M. Österberg, Toward energy efficiency through an optimized use of wood: The development of natural hydrophobic coatings that retain moisture-buffering ability, *Energy and Buildings* **105**, 37-42 (2015).
[189] ASTM C1498-01. Standard test method for hygroscopic sorption isotherms of building materials. *American Society of Testing and Materials* (2017).
[190] The engineering toolBox: Saturated salt solutions and control of air humidity. https://www.engineeringtoolbox.com/salt-humidity-d_1887.html (accessed Aug. 26th, 2023).

[191] EN-ISO 12572:2001. Hygrothermal performance of building materials and products: Determination of water vapour transmission properties. *European Union & International Organization for Standardization* (2001).

[192] EAD 040005-00-1201. Factory-made thermal and/or acoustic insulation products made of vegetable or animal fibres. *European Organization for Technical Assessment* (2015).

[193] ISO 846:2019. Plastrics - Evaluation of the action of microorganisms. *International Organization for Standardization* (2019).

[194] WUFI software (WUFI 6). https://wufi.de/en/software/ (accessed Dec. 20th, 2023).

[195] Climate. OneBuilding.Org (Repository of free climate data for building performance simulation). https://climate.onebuilding.org/default.html (accessed Feb. 2nd, 2024).

[196] L. Huang, X. Song, L. Cui, S. Gao, F. Chen, S. Wang & J. Liu, Preparation and characterization of AKD sizing agent by "one-pot cooking", *Nordic Pulp & Paper Research Journal* **33**(2), 317-326 (2018).

[197] E. Frinhani & R. Oliveira, The applicability of natural colorants in papermaking, *Tappi Journal* **5**(7), 3-7 (2006).

[198] K. Adenekan & B. Hutton-Prager, Sticky hydrophobic behavior of cellulose substrates impregnated with alkyl ketene dimer (AKD) via sub-and supercritical carbon dioxide, *Colloids and Surfaces A: Physicochemical and Engineering Aspects* **560**, 154-163 (2019).

[199] C. Liang & R. Marchessault, Infrared spectra of crystalline polysaccharides. I. Hydrogen bonds in native celluloses, *Journal of Polymer Science* **37**(132), 385-395 (1959).

[200] W. Sonderegger & P. Niemz, Thermal conductivity and water vapour transmission properties of wood-based materials, *European Journal of Wood and Wood Products* **67**(3), 313-321 (2009).

[201] O. Vololonirina, M. Coutand & B. Perrin, Characterization of hygrothermal properties of wood-based products–Impact of moisture content and temperature, *Construction and Building Materials* **63**, 223-233 (2014).

[202] T. Alioua, B. Agoudjil, N. Chennouf, A. Boudenne & K. Benzarti, Investigation on heat and moisture transfer in bio-based building wall with consideration of the hysteresis effect, *Building and Environment* **163**, 106333 (2019).

[203] Y.A. Cengel & J.M. Cimbala, Fluid mechanics: fundamentals and applications (Si Units), *McGraw Hill*, *San Franciso, United States* (2010).

[204] H. Viitanen, J. Vinha, K. Salminen, T. Ojanen, R. Peuhkuri, L. Paajanen & K. Lähdesmäki, Moisture and bio-deterioration risk of building materials and structures, *Journal of Building Physics* **33**(3), 201-224 (2010).

[205] F. Domínguez-Muñoz, B. Anderson, J.M. Cejudo-López & A. Carrillo-Andrés, Uncertainty in the thermal conductivity of insulation materials, *Energy and Buildings* **42**(11), 2159-2168 (2010).

[206] H. Viitanen, M. Krus, T. Ojanen, V. Eitner & D. Zirkelbach, Mold risk classification based on comparative evaluation of two established growth models, *Energy Procedia* **78**, 1425-1430 (2015).

[207] S.H. Kamarullah, M.M. Mydin, W.S. Omar, S.S. Harith, B.H. Noor, N.Z. Alias, S. Manap & R. Mohamad, Surface morphology and chemical composition of Napier grass fibers, *Malaysian Journal of Analytical Sciences* **19**(4), 889-895 (2015).

[208] A. Komuraiah, N.S. Kumar & B.D. Prasad, Chemical composition of natural fibers and its influence on their mechanical properties, *Mechanics of Composite Materials* **50**, 359-376 (2014).

[209] C. Koh, F. Gauvin, K. Schollbach & H.J.H. Brouwers, Upcycling wheat and barley straws into sustainable thermal insulation: Assessment and treatment for durability, *Resources, Conservation and Recycling* **198**, 107161 (2023).
[210] S.H. Ryu, H.J. Moon & J.T. Kim, Evaluation of the influence of hygric properties of wallpapers on mould growth rates using hygrothermal simulation, *Energy and Buildings* **98**, 113-118 (2015).
[211] Y. Xue, Y. Fan, Z. Wang, W. Gao, Z. Sun & J. Ge, Facilitator of moisture accumulation in building envelopes and its influences on condensation and mould growth, *Energy and Buildings* **277**, 112528 (2022).
[212] M. Ali, M.O. Oladokun, S.B. Osman, S. Mohd Din, M.S. Ibrahim & F. Yusof, Hygrothermal performance of building envelopes in the tropics under operative conditions: condensation and mould growth risk appraisal, *Jurnal Teknologi* **78**(5), (2016).
[213] A. Maalouf & A. Mavropoulos, Re-assessing global municipal solid waste generation, *Waste Manag. Res.* **41**(4), 936-847 (2022).
[214] P. Tang, M.V.A. Florea, P. Spiesz & H.J.H. Brouwers, Application of thermally activated municipal solid waste incineration (MSWI) bottom ash fines as binder substitute, *Cement and Concrete Composites* **70**, 194-205 (2016).
[215] H. Cheng & Y. Hu, Municipal solid waste (MSW) as a renewable source of energy: Current and future practices in China, *Bioresource Technology* **101**(11), 3816-3824 (2010).
[216] J. Chimenos, M. Segarra, M. Fernández & F. Espiell, Characterization of the bottom ash in municipal solid waste incinerator, *Journal of Hazardous Materials* **64**(3), 211-222 (1999).
[217] J.R. Pan, C. Huang, J.-J. Kuo & S.-H. Lin, Recycling MSWI bottom and fly ash as raw materials for Portland cement, *Waste Management* **28**(7), 1113-1118 (2008).
[218] M. Ferraris, M. Salvo, A. Ventrella, L. Buzzi & M. Veglia, Use of vitrified MSWI bottom ashes for concrete production, *Waste Management* **29**(3), 1041-1047 (2009).
[219] N. De Belie, A.M. Joseph & S. Matthys, Reactivity of municipal solid waste incineration ashes as a supplementary cementitious material, *15th International Congress on the Chemistry of Cement (ICCC19), Prague, Czech Republic*, (2019).
[220] G. Pecqueur, C. Crignon & B. Quénée, Behaviour of cement-treated MSWI bottom ash, *Waste Management* **21**(3), 229-233 (2001).
[221] L. Biganzoli, L. Gorla, S. Nessi & M. Grosso, Volatilisation and oxidation of aluminium scraps fed into incineration furnaces, *Waste Management* **32**(12), 2266-2272 (2012).
[222] Y. Liu, K.S. Sidhu, Z. Chen & E.-H. Yang, Alkali-treated incineration bottom ash as supplementary cementitious materials, *Construction and Building Materials* **179**, 371-378 (2018).
[223] N. Saikia, G. Mertens, K. Van Balen, J. Elsen, T. Van Gerven & C. Vandecasteele, Pre-treatment of municipal solid waste incineration (MSWI) bottom ash for utilisation in cement mortar, *Construction and Building Materials* **96**, 76-85 (2015).
[224] J.-E. Aubert, B. Husson & N. Sarramone, Utilization of municipal solid waste incineration (MSWI) fly ash in blended cement: Part 2. Mechanical strength of mortars and environmental impact, *Journal of Hazardous Materials* **146**(1-2), 12-19 (2007).

[225] A.M. Joseph, R. Snellings, P. Nielsen, S. Matthys & N. De Belie, Pre-treatment and utilisation of municipal solid waste incineration bottom ashes towards a circular economy, *Construction and Building Materials* **260**, 120485 (2020).
[226] M. Gori, B. Bergfeldt, G. Pfrang-Stotz, J. Reichelt & P. Sirini, Effect of short-term natural weathering on MSWI and wood waste bottom ash leaching behaviour, *Journal of Hazardous Materials* **189**(1-2), 435-443 (2011).
[227] P. Tang, M.V.A. Florea, P. Spiesz & H.J.H. Brouwers, Characteristics and application potential of municipal solid waste incineration (MSWI) bottom ashes from two waste-to-energy plants, *Construction and Building Materials* **83**, 77-94 (2015).
[228] Q. Alam, K. Schollbach, M.V.A. Florea & H.J.H. Brouwers, Investigating washing treatment to minimize leaching of chlorides and heavy metals from MSWI bottom ash, *4th International Conference on Sustainable Solid Waste Management,* Limasol, Cyprus, (2016).
[229] A. Polettini & R. Pomi, The leaching behavior of incinerator bottom ash as affected by accelerated ageing, *Journal of Hazardous Materials* **113**(1-3), 209-215 (2004).
[230] X. Sun & Y. Yi, Acid washing of incineration bottom ash of municipal solid waste: Effects of pH on removal and leaching of heavy metals, *Waste Management* **120**, 183-192 (2021).
[231] Z. Chen, J.-S. Li, D. Xuan, C.S. Poon & X. Huang, Effect of alkaline washing treatment on leaching behavior of municipal solid waste incineration bottom ash, *Environmental Science and Pollution Research* **30**(1), 1966-1978 (2023).
[232] Y. Zheng, J. Wang, Y. Zhu & A. Wang, Research and application of kapok fiber as an absorbing material: A mini review, *Journal of Environmental Sciences* **27**, 21-32 (2015).
[233] N.A. Zubair, R.M. Moawia, M.M. Nasef, M. Hubbe & M. Zakeri, A critical review on natural fibers modifications by graft copolymerization for wastewater treatment, *Journal of Polymers and the Environment* **30**(4), 1199-1227 (2022).
[234] A. Kausar, S.T. Zohra, S. Ijaz, M. Iqbal, J. Iqbal, I. Bibi, S. Nouren, N. El Messaoudi & A. Nazir, Cellulose-based materials and their adsorptive removal efficiency for dyes: A review, *International Journal of Biological Macromolecules*, (2022).
[235] M. Hanafi, E. Aydin & A. Ekinci, Engineering properties of basalt fiber-reinforced bottom ash cement paste composites, *Materials* **13**(8), 1952 (2020).
[236] B.A. Akinyemi & C. Dai, Development of banana fibers and wood bottom ash modified cement mortars, *Construction and Building Materials* **241**, 118041 (2020).
[237] A. Mohanty, M.a. Misra & G. Hinrichsen, Biofibres, biodegradable polymers and biocomposites: An overview, *Macromolecular Materials and Engineering* **276**(1), 1-24 (2000).
[238] S. Shinoj, R. Visvanathan, S. Panigrahi & M. Kochubabu, Oil palm fiber (OPF) and its composites: A review, *Industrial Crops and products* **33**(1), 7-22 (2011).
[239] Y. Luo, K. Klima, H.J.H. Brouwers & Q. Yu, Effects of ladle slag on Class F fly ash geopolymer: Reaction mechanism and high temperature behavior, *Cement and Concrete Composites* **129**, 104468 (2022).
[240] E. Loginova, K. Schollbach, M. Proskurnin & H.J.H. Brouwers, Municipal solid waste incineration bottom ash fines: Transformation into a minor additional constituent for cements, *Resources, Conservation and Recycling* **166**, 105354 (2021).

[241] M.U. Hossain, C.S. Poon, I.M. Lo & J.C. Cheng, Comparative LCA on using waste materials in the cement industry: A Hong Kong case study, *Resources, Conservation and Recycling* **120**, 199-208 (2017).
[242] T. Kim, S. Tae & C.U. Chae, Analysis of environmental impact for concrete using LCA by varying the recycling components, the compressive strength and the admixture material mixing, *Sustainability* **8**(4), 389 (2016).
[243] ISO 14044:2006. Environmental Management. Life Cycle Assessment. Requirements and Guidelines. *International Organization for Standardization* (2006).
[244] M. Margallo, R. Aldaco & A. Irabien, Life cycle assessment of bottom ash management from a municipal solid waste incinerator (MSWI), *Chemical Engineering Transactions* **35**, 871-876 (2013).
[245] B. Meyer, Scories d'ordures incinérées pour béton, *Bulletin du ciment.* **54**(7), 1-7 (1986).
[246] P. Filipponi, A. Polettini, R. Pomi & P. Sirini, Physical and mechanical properties of cement-based products containing incineration bottom ash, *Waste Management* **23**(2), 145-156 (2003).
[247] Y. Song, B. Li, E.-H. Yang, Y. Liu & T. Ding, Feasibility study on utilization of municipal solid waste incineration bottom ash as aerating agent for the production of autoclaved aerated concrete, *Cement and Concrete Composites* **56**, 51-58 (2015).
[248] O. Gencel, S.M.S. Kazmi, M.J. Munir, G. Kaplan, O.Y. Bayraktar, D.O. Yarar, A. Karimipour & M.R. Ahmad, Influence of bottom ash and polypropylene fibers on the physico-mechanical, durability and thermal performance of foam concrete: An experimental investigation, *Construction and Building Materials* **306**, 124887 (2021).
[249] G. Vaickelionis & R. Vaickelioniene, Cement hydration in the presence of wood extractives and pozzolan mineral additives, *Ceramics Silikaty* **50**(2), 115 (2006).
[250] M. Rachmat & T. Salsabilla, Analysis of hexagonal paving block as a better paving shape, *IOP Conference Series: Materials Science and Engineering,* (2019).
[251] Z. Chen & E.-H. Yang, Early age hydration of blended cement with different size fractions of municipal solid waste incineration bottom ash, *Construction and Building Materials* **156**, 880-890 (2017).
[252] S. Ajouguim, J. Page, C. Djelal, M. Waqif & L. Saâdi, Impact of Alfa fibers morphology on hydration kinetics and mechanical properties of cement mortars, *Construction and Building Materials* **293**, 123514 (2021).
[253] G. Fang & M. Zhang, The evolution of interfacial transition zone in alkali-activated fly ash-slag concrete, *Cement and Concrete Research* **129**, 105963 (2020).
[254] X. Gao, Q. Yu & H.J.H. Brouwers, Reaction kinetics, gel character and strength of ambient temperature cured alkali activated slag–fly ash blends, *Construction and Building Materials* **80**, 105-115 (2015).
[255] S. Liu, L. Wang, Y. Gao, B. Yu & W. Tang, Influence of fineness on hydration kinetics of supersulfated cement, *Thermochimica Acta* **605**, 37-42 (2015).
[256] M.C.G. Juenger & H.M. Jennings, New insights into the effects of sugar on the hydration and microstructure of cement pastes, *Cement and Concrete Research* **32**(3), 393-399 (2002).
[257] S. Chakraborty, S.P. Kundu, A. Roy, B. Adhikari & S.B. Majumder, Effect of jute as fiber reinforcement controlling the hydration characteristics of cement matrix, *Industrial & Engineering Chemistry Research* **52**(3), 1252-1260 (2013).
[258] V. Caprai, F. Gauvin, K. Schollbach & H.J.H. Brouwers, MSWI bottom ash as binder replacement in wood cement composites, *Construction and Building Materials* **196**, 672-680 (2019).
[259] Q. Wang, S. Li, S. Pan, X. Cui, D.J. Corr & S.P. Shah, Effect of graphene oxide on the hydration and microstructure of fly ash-cement system, *Construction and Building Materials* **198**, 106-119 (2019).

[260] V. Caprai, K. Schollbach, M.V.A. Florea & H.J.H. Brouwers, Evaluation of municipal solid waste incineration filter cake as supplementary cementitious material, *Construction and Building Materials* **250**, 118833 (2020).
[261] J. Yao, Q. Kong, H. Zhu, Y. Long & D. Shen, Content and fractionation of Cu, Zn and Cd in size fractionated municipal solid waste incineration bottom ash, *Ecotoxicology and Environmental Safety* **94**, 131-137 (2013).
[262] H. Lutz & C. Ludwig, Heavy metal evaporation from fly ash in inert and oxidizing atmospheres **5**, *Paul Scherrer Institute, Switzerland* 17-18 (2002).
[263] M. Díaz-Bautista, R. Álvarez-Rodríguez, C. Clemente-Jul & A. Mastral, AFBC of coal with tyre rubber. Influence of the co-combustion variables on the mineral matter of solid by-products and on Zn lixiviation, *Fuel* **106**, 10-20 (2013).
[264] A.R. Martin, M.A. Martins, O.R. da Silva & L.H. Mattoso, Studies on the thermal properties of sisal fiber and its constituents, *Thermochimica Acta* **506**(1-2), 14-19 (2010).
[265] Z. Yang, S. Tian, L. Liu, X. Wang & Z. Zhang, Recycling ground MSWI bottom ash in cement composites: Long-term environmental impacts, *Waste Management* **78**, 841-848 (2018).
[266] Regulation of the State Secretary for Housing, Planning and the Environment and the State Secretary for Transport: Preliminary draft of the Soil Quality Regulation https://rwsenvironment.eu/subjects/soil/legislation-and/soil-quality-decree/ (accessed 12 February, 2023).
[267] L.A. Sormunen, A. Kalliainen, P. Kolisoja & R. Rantsi, Combining mineral fractions of recovered MSWI bottom ash: Improvement for utilization in civil engineering structures, *Waste and Biomass Valorization* **8**, 1467-1478 (2017).
[268] P. Tang, W. Chen, D. Xuan, Y. Zuo & C.S. Poon, Investigation of cementitious properties of different constituents in municipal solid waste incineration bottom ash as supplementary cementitious materials, *Journal of Cleaner Production* **258**, 120675 (2020).
[269] S. Zhang, Z. Ghouleh, Z. He, L. Hu & Y. Shao, Use of municipal solid waste incineration bottom ash as a supplementary cementitious material in dry-cast concrete, *Construction and Building Materials* **266**, 120890 (2021).
[270] P. Nielsen, M. Quaghebeur, B. Laenen, R. Kumps & P. Van Bommel, The use of MSWI-bottom ash as aggregate in concrete—limitations and possible solutions, *The 7th International Conference on the Environmental and Technical Implications of Construction with Alternative Materials (WASCON), Lyon, France*, (2009).
[271] U. Müller & K. Rübner, The microstructure of concrete made with municipal waste incinerator bottom ash as an aggregate component, *Cement and Concrete Research* **36**(8), 1434-1443 (2006).
[272] F. Tajra, M. Abd Elrahman & D. Stephan, The production and properties of cold-bonded aggregate and its applications in concrete: A review, *Construction and Building Materials* **225**, 29-43 (2019).
[273] J. Liu, Z. Li, W. Zhang, H. Jin, F. Xing & L. Tang, The impact of cold-bonded artificial lightweight aggregates produced by municipal solid waste incineration bottom ash (MSWIBA) replace natural aggregates on the mechanical, microscopic and environmental properties, durability of sustainable concrete, *Journal of Cleaner Production* **337**, 130479 (2022).
[274] P. Tang & H.J.H. Brouwers, Integral recycling of municipal solid waste incineration (MSWI) bottom ash fines (0–2 mm) and industrial powder wastes by cold-bonding pelletization, *Waste Management* **62**, 125-138 (2017).

[275] P. Tang, M.V.A. Florea & H.J.H. Brouwers, Employing cold bonded pelletization to produce lightweight aggregates from incineration fine bottom ash, *Journal of Cleaner Production* **165**, 1371-1384 (2017).
[276] P. Shafigh, U.J. Alengaram, H.B. Mahmud & M.Z. Jumaat, Engineering properties of oil palm shell lightweight concrete containing fly ash, *Materials & Design* **49**, 613-621 (2013).
[277] A.A. Agra, A. Nicolodi, B.D. Flores, I.V. Flores, G.L.R. da Silva, A.C.F. Vilela & E. Osório, Automated procedure for coke microstructural characterization in imagej software aiming industrial application, *Fuel* **304**, 121374 (2021).
[278] E. Loginova, K. Schollbach, M. Proskurnin & H.J.H. Brouwers, Mechanical performance and microstructural properties of cement mortars containing MSWI BA as a minor additional constituent, *Case Studies in Construction Materials* **18**, e01701 (2023).
[279] W. Juimo, T. Cherradi, L. Abidi & L. Oliveira, Characterisation of natural pozzolan of" djoungo"(cameroon) as lightweight aggregate for ligtweight concrete, *GEOMATE Journal* **11**(27), 2782-2789 (2016).
[280] W.C. Krumbein, Measurement and geological significance of shape and roundness of sedimentary particles, *Journal of Sedimentary Research* **11**(2), 64-72 (1941).
[281] Y. Hiramatsu & Y. Oka, Determination of the tensile strength of rock by a compression test of an irregular test piece, *International Journal of Rock Mechanics and Mining Sciences & Geomechanics Abstracts* **3**(2), 89-90 (1966).
[282] A. Petrillo, F. Colangelo, I. Farina, M. Travaglioni, C. Salzano & R. Cioffi, Multi-criteria analysis for Life Cycle Assessment and Life Cycle Costing of lightweight artificial aggregates from industrial waste by double-step cold bonding palletization, *Journal of Cleaner Production* **351**, 131395 (2022).
[283] X. Shang, J. Chang, J. Yang, X. Ke & Z. Duan, Life cycle sustainable assessment of natural vs artificial lightweight aggregates, *Journal of Cleaner Production* **367**, 133064 (2022).
[284] A.B. López-García, M. Uceda-Rodríguez, S. León-Gutiérrez, C.J. Cobo-Ceacero & J.M. Moreno-Maroto, Eco-efficient transformation of mineral wool wastes into lightweight aggregates at low firing temperature and associated environmental assessment, *Construction and Building Materials* **345**, 128294 (2022).
[285] I. Tanaka, M. Koishi & K. Shinohara, A study on the process for formation of spherical cement through an examination of the changes of powder properties and electrical charges of the cement and its constituent materials during surface modification, *Cement and Concrete Research* **32**(1), 57-64 (2002).
[286] S. Ahmad, R. Kothari, H.M. Singh, V. Tyagi, B. Singh & A. Sari, Experimental investigation of microalgal harvesting with low cost bottom ash: Influence of temperature and pH with zeta potential and thermodynamic function, *Environmental Technology & Innovation* **22**, 101376 (2021).
[287] V.H. Vargas, R.R. Paveglio, P.d.S. Pauletto, N.P.G. Salau & L.G. Dotto, Sisal fiber as an alternative and cost-effective adsorbent for the removal of methylene blue and reactive black 5 dyes from aqueous solutions, *Chemical Engineering Communications* **207**(4), 523-536 (2020).
[288] I. Zafar, K. Rashid & M. Ju, Synthesis and characterization of lightweight aggregates through geopolymerization and microwave irradiation curing, *Journal of Building Engineering* **42**, 102454 (2021).
[289] A.R. de Azevedo, M.T. Marvila, B.A. Tayeh, D. Cecchin, A.C. Pereira & S.N. Monteiro, Technological performance of açaí natural fibre reinforced cement-based mortars, *Journal of Building Engineering* **33**, 101675 (2021).

[290] G. Huang, K. Yang, L. Chen, Z. Lu, Y. Sun, X. Zhang, Y. Feng, Y. Ji & Z. Xu, Use of pretreatment to prevent expansion and foaming in high-performance MSWI bottom ash alkali-activated mortars, *Construction and Building Materials* **245**, 118471 (2020).

[291] E. Güneyisi, M. Gesoğlu, Ö. Pürsünlü & K. Mermerdaş, Durability aspect of concretes composed of cold bonded and sintered fly ash lightweight aggregates, *Composites Part B: Engineering* **53**, 258-266 (2013).

[292] J. Liu, Z. Li, W. Zhang, H. Jin, F. Xing & L. Tang, The impact of cold-bonded artificial lightweight aggregates produced by municipal solid waste incineration bottom ash (MSWIBA) replace natural aggregates on the mechanical, microscopic and environmental properties, durability of sustainable concrete, *Journal of Cleaner Production* **337**, (2022).

[293] X. Qiao, M. Tyrer, C.S. Poon & C. Cheeseman, Novel cementitious materials produced from incinerator bottom ash, *Resources, Conservation and Recycling* **52**(3), 496-510 (2008).

[294] A. Mezencevova, V. Garas, H. Nanko & K.E. Kurtis, Influence of thermomechanical pulp fiber compositions on internal curing of cementitious materials, *Journal of Materials in Civil Engineering* **24**(8), 970-975 (2012).

[295] S. Kawashima & S.P. Shah, Early-age autogenous and drying shrinkage behavior of cellulose fiber-reinforced cementitious materials, *Cement and Concrete Composites* **33**(2), 201-208 (2011).

[296] M. Dadkhah & J.-M. Tulliani, Damage Management of Concrete Structures with Engineered Cementitious Materials and Natural Fibers: A Review of Potential Uses, *Sustainability* **14**(7), 3917 (2022).

[297] Y. Gao, L.-Q. Liu, S.-Z. Zu, K. Peng, D. Zhou, B.-H. Han & Z. Zhang, The effect of interlayer adhesion on the mechanical behaviors of macroscopic graphene oxide papers, *ACS Nano* **5**(3), 2134-2141 (2011).

[298] F. Zhao, K. Xu, H. Ren, L. Ding, J. Geng & Y. Zhang, Combined effects of organic matter and calcium on biofouling of nanofiltration membranes, *Journal of Membrane Science* **486**, 177-188 (2015).

[299] L. Aggarwal & J. Singh, Effect of plant fibre extractives on properties of cement, *Cement and Concrete Composites* **12**(2), 103-108 (1990).

[300] M.O. Eloget, Suitability of Sisal Juice Extract as a Retarder in Cement Concrete (Doctoral thesis, *Jomo Kenyatta University of Agriculture and Technology*, 2022).

[301] T.D. Duong, K.L. Nguyen & M. Hoang, Competitive sorption of Na^+ and Ca^{2+} ions on unbleached kraft fibres—A kinetics and equilibrium study, *Journal of Colloid and Interface Science* **301**(2), 446-451 (2006).

[302] P. Jongvisuttisun, J. Leisen & K.E. Kurtis, Key mechanisms controlling internal curing performance of natural fibers, *Cement and Concrete Research* **107**, 206-220 (2018).

[303] C.M. Futalan, A.E.S. Choi, H.G.O. Soriano, M.K.B. Cabacungan & J.C. Millare, Modification strategies of kapok fiber composites and its application in the adsorption of heavy metal ions and dyes from aqueous solutions: A systematic review, *International Journal of Environmental Research and Public Health* **19**(5), 2703 (2022).

[304] A. Bismarck, A.K. Mohanty, I. Aranberri-Askargorta, S. Czapla, M. Misra, G. Hinrichsen & J. Springer, Surface characterization of natural fibers; surface properties and the water up-take behavior of modified sisal and coir fibers, *Green Chemistry* **3**(2), 100-107 (2001).

[305] N.S.A. Rahman, M.F. Yhaya, B. Azahari & W.R. Ismail, Utilisation of natural cellulose fibres in wastewater treatment, *Cellulose* **25**, 4887-4903 (2018).

[306] P. Piantone, F. Bodénan & L. Chatelet-Snidaro, Mineralogical study of secondary mineral phases from weathered MSWI bottom ash: implications for the modelling and trapping of heavy metals, *Applied Geochemistry* **19**(12), 1891-1904 (2004).

[307] Maps of The Netherlands. https://www.worldatlas.com/maps/netherlands (accessed May 20th, 2023).
[308] The leading B2B e-commerce platform for global trade. https://www.alibaba.com/ (accessed Dec. 10th, 2023).
[309] J. Xiao, H. Zhang, X. Hu, T. Ding & X. Xiao, Impact assessment of river sand resource shortage under different policy scenarios in China, *Low-carbon Materials and Green Construction* **1**(1), 16 (2023).
[310] J. Zhang, D. Li & Y. Wang, Toward intelligent construction: Prediction of mechanical properties of manufactured-sand concrete using tree-based models, *Journal of Cleaner Production* **258**, 120665 (2020).
[311] P. Brown O. and Peduzzi, Driven to extraction: can sand mining be sustainable? *Hoffmann Centre, Chatham House, United Kingdom*, (2019).
[312] J. Yao, H. Song, Y. Li, Y. Cui, M. Chai & W. Ling, Mechanism of macro-and microscopic performance of cement mortars influenced by municipal solid waste incineration bottom ash as sand substitution, *Construction and Building Materials* **397**, 132317 (2023).
[313] V. Caprai, A. Lazaro & H.J.H. Brouwers, Waterglass impregnation of municipal solid waste incineration bottom ash applied as sand replacement in mortars, *Waste Management* **86**, 87-96 (2019).
[314] B. Verbinnen, P. Billen, J. Van Caneghem & C. Vandecasteele, Recycling of MSWI bottom ash: a review of chemical barriers, engineering applications and treatment technologies, *Waste and Biomass Valorization* **8**, 1453-1466 (2017).
[315] J.R. Minane, F. Becquart, N.E. Abriak & C. Deboffe, Upgraded Mineral Sand Fraction from MSWI Bottom Ash: An Alternative Solution for the Substitution of Natural Aggregates in Concrete Applications, *International High-Performance Built Environment Conference,* (2016).
[316] M.S.H.M. Sani, F. Muftah & Z. Muda, The properties of special concrete using washed bottom ash (WBA) as partial sand replacement, *International Journal of Sustainable Construction Engineering and Technology* **1**(2), 65-76 (2010).
[317] I.A. Rahman, H. Hamdam & A.M.A. Zaidi, Assessment of recycled aggregate concrete, *Modern Applied Science* **3**(10), 47-54 (2009).
[318] K. Yan, H. Sun, F. Gao, D. Ge & L. You, Assessment and mechanism analysis of municipal solid waste incineration bottom ash as aggregate in cement stabilized macadam, *Journal of Cleaner Production* **244**, 118750 (2020).
[319] EN 1015-3:1999. Methods of test for mortar for masonry - Part 3: Determination of consistence of fresh mortar (by flow table). *European Standard* (1999).
[320] H. Nguyen, T. Fujii, K. Okubo & V. Carvelli, Cement mortar reinforced with recycled carbon fiber and CFRP waste, *17th European Conference on Composite Materials, Munich, Germany*, (2016).
[321] H. Song, T. Liu, F. Gauvin & H.J.H. Brouwers, Improving the interface compatibility and mechanical performances of the cementitious composites by low-cost alkyl ketene dimer modified fibers, *Construction and Building Materials* **395**, 132186 (2023).
[322] I. Farina, F. Fabbrocino, G. Carpentieri, M. Modano, A. Amendola, R. Goodall, L. Feo & F. Fraternali, On the reinforcement of cement mortars through 3D printed polymeric and metallic fibers, *Composites Part B: Engineering* **90**, 76-85 (2016).
[323] N. Schneider & D. Stephan, Reactivation of a retarded suspension of ground granulated blast-furnace slag, *Materials* **9**(3), 174 (2016).

[324] Q. Liu, A. Singh, J. Xiao, B. Li & V.W. Tam, Workability and mechanical properties of mortar containing recycled sand from aerated concrete blocks and sintered clay bricks, *Resources, Conservation and Recycling* **157**, 104728 (2020).
[325] F. de Andrade Silva, B. Mobasher, C. Soranakom & R.D. Toledo Filho, Effect of fiber shape and morphology on interfacial bond and cracking behaviors of sisal fiber cement based composites, *Cement and Concrete Composites* **33**(8), 814-823 (2011).
[326] P. Lertwattanaruk & A. Suntijitto, Properties of natural fiber cement materials containing coconut coir and oil palm fibers for residential building applications, *Construction and Building Materials* **94**, 664-669 (2015).
[327] A. Wongsa, R. Kunthawatwong, S. Naenudon, V. Sata & P. Chindaprasirt, Natural fiber reinforced high calcium fly ash geopolymer mortar, *Construction and Building Materials* **241**, 118143 (2020).
[328] J. Pera, L. Coutaz, J. Ambroise & M. Chababbet, Use of incinerator bottom ash in concrete, *Cement and Concrete Research* **27**(1), 1-5 (1997).
[329] B. Bahja, A. Elouafi, A. Tizliouine & L. Omari, Morphological and structural analysis of treated sisal fibers and their impact on mechanical properties in cementitious composites, *Journal of Building Engineering* **34**, 102025 (2021).
[330] Y.M. Wei, B. Tomita, Y. Hiramatsu, A. Miyatake & T. Fujii, Study of hydration behaviors of wood-cement mixtures: compatibility of cement mixed with wood fiber strand obtained by the water-vapor explosion process, *Journal of Wood Science* **48**, 365-373 (2002).
[331] B. Muñoz-Sánchez, M.J. Arévalo-Caballero & M.C. Pacheco-Menor, Influence of acetic acid and calcium hydroxide treatments of rubber waste on the properties of rubberized mortars, *Materials and Structures* **50**, 1-16 (2017).
[332] T.U. Mohammed & M.N. Rahman, Effect of types of aggregate and sand-to-aggregate volume ratio on UPV in concrete, *Construction and Building Materials* **125**, 832-841 (2016).
[333] ImageJ (Image Processing and Analysis in Java). https://imagej.net/ij/ij/ (accessed March 5th, 2023).
[334] M. Ardanuy, J. Claramunt & R.D. Toledo Filho, Cellulosic fiber reinforced cement-based composites: A review of recent research, *Construction and Building Materials* **79**, 115-128 (2015).
[335] T. Ding, J. Xiao, S. Zou & X. Zhou, Anisotropic behavior in bending of 3D printed concrete reinforced with fibers, *Composite Structures* **254**, 112808 (2020).
[336] D. Raghavendher, S. Kumar & D. Singh, Incinerator bottom ash as a supplementary material for green concrete and mortar, *Materials Today: Proceedings* **93**(3), 189-195 (2023).
[337] V. Caprai, K. Schollbach & H.J.H. Brouwers, Influence of hydrothermal treatment on the mechanical and environmental performances of mortars including MSWI bottom ash, *Waste Management* **78**, 639-648 (2018).
[338] H. Ghanem, J. Khatib & A. Elkordi, Effect of partial replacement of sand by MSWI-BA on the properties of mortar, *BAU Journal-Science and Technology* **1**(2), 4 (2020).
[339] M.R. Irshidat, N. Al-Nuaimi & M. Rabie, Potential utilization of municipal solid waste incineration ashes as sand replacement for developing sustainable cementitious binder, *Construction and Building Materials* **312**, 125488 (2021).
[340] Z. Yang, R. Ji, L. Liu, X. Wang & Z. Zhang, Recycling of municipal solid waste incineration by-product for cement composites preparation, *Construction and Building Materials* **162**, 794-801 (2018).

[341] K.-t. Lau, P.-y. Hung, M.-H. Zhu & D. Hui, Properties of natural fibre composites for structural engineering applications, *Composites Part B: Engineering* **136**, 222-233 (2018).
[342] Y.S. Munde & R.B. Ingle, Theoretical modeling and experimental verification of mechanical properties of natural fiber reinforced thermoplastics, *8th International Conference Interdisciplinarity in Engineering,* (2015).
[343] G. Kalaprasad, K. Joseph, S. Thomas & C. Pavithran, Theoretical modelling of tensile properties of short sisal fibre-reinforced low-density polyethylene composites, *Journal of Materials Science* **32**, 4261-4267 (1997).
[344] C. Juarez, A. Duran, P. Valdez & G. Fajardo, Performance of "Agave lecheguilla" natural fiber in portland cement composites exposed to severe environment conditions, *Building and Environment* **42**(3), 1151-1157 (2007).
[345] P. Tang & H.J.H. Brouwers, The durability and environmental properties of self-compacting concrete incorporating cold bonded lightweight aggregates produced from combined industrial solid wastes, *Construction and Building Materials* **167**, 271-285 (2018).
[346] I. Garcia-Lodeiro, V. Carcelen-Taboada, A. Fernández-Jiménez & A. Palomo, Manufacture of hybrid cements with fly ash and bottom ash from a municipal solid waste incinerator, *Construction and Building Materials* **105**, 218-226 (2016).
[347] A.L. Cazetta, A.M. Vargas, E.M. Nogami, M.H. Kunita, M.R. Guilherme, A.C. Martins, T.L. Silva, J.C. Moraes & V.C. Almeida, NaOH-activated carbon of high surface area produced from coconut shell: Kinetics and equilibrium studies from the methylene blue adsorption, *Chemical Engineering Journal* **174**(1), 117-125 (2011).
[348] Q. Hou, H. Zhou, W. Zhang, Q. Chang, J. Yang, C. Xue & S. Hu, Boosting adsorption of heavy metal ions in wastewater through solar-driven interfacial evaporation of chemically-treated carbonized wood, *Science of the Total Environment* **759**, 144317 (2021).

List of abbreviations and symbols

Abbreviation

AKD	Alkyl ketene dimer
BA	Bottom ash
EDS	Energy dispersive spectrometry
FTIR	Fourier transform infrarood spectrometrie
GHG	Greenhouse gas
HF	Hemp fibers
HFRCCs	Hemp fiber-reinforced cement composites
IBA	Incinerator bottom ash
IC	Ion chromatography
ICP-AES	Inductively coupled plasma-atomic emission spectrometry
LCA	Life cycle assessment
LOI	Loss on ignition
MSWI BA	Municipal solid waste incineration bottom ash
MSWI BA-BCBs	Municipal solid waste incineration bottom ash-based cement binders
NFRCCs	Natural fiber-reinforced cement composites
OPC	Ordinary Portland cement
PSD	Particle size distribution
SEM	Scanning electron microscope
SF	Sisal fibers
SLWAs	Synthesized lightweight aggregates
SQD	Soil quality decree
TGA	Thermogravimetric analysis
UPV	Ultrasonic Pulse Velocity
WAC	Water absorption capacity
WAT	Water absorption test
XRD	X-ray diffraction
XRF	X-ray fluorescence

Symbols

A (m^2)	Area
I_t (%)	Toughness index
mg/kg d.m.	Mg per kg of dry matter
$\rho_{envelop}$ (g/cm^3)	Envelop density
ρ_{true} (g/cm^3)	True density
ρ_{bulk} (g/cm^3)	Bulk density
$\rho_{apparent}$ (g/cm^3)	Apparent density
ρ_w (g/cm^3)	Water density
W_{sat} (kg)	Saturated weight
W_{dried} (kg)	Dried weight
φ (%)	porosity
Ψ	Sphericity
Ra (µm)	Surface roughness
RH (%)	Relative humidity
δ_{air} (kg/m*s*Pa)	Water vapor permeability of air
g (kg/m^2•s)	Water vapour transmission rate
λ (W/m*k)	Thermal conductivity
H (J/m^3)	Enthalpy
P (Pa)	Pressure
T (°C)	Temperature
µ (dimensionless)	Vapor diffusion resistance factor
D_w (m^2/s)	Liquid transport coefficient
ΔP (Pa)	Partial pressure difference of water vapor
Δt (s)	Time interval
D (m)	Thickness
$\sigma_{crushing}$ (MPa)	Crushing strength
V (Km/s)	Ultrasonic pulse velocity

List of publications

Peer-Reviewed Journal Publications

1. H. Song, T. Liu, F. Gauvin, and H.J.H. Brouwers. Improving the interface compatibility and mechanical performances of the cementitious composites by low-cost alkyl ketene dimer modified fibers. *Construction and Building Materials* 395 (2023): 132186.
2. H. Song, T. Liu, and F. Gauvin. Enhancing mechanical performance of green fiber cement composites: Role of eco-friendly alkyl ketene dimer on surfaces of hemp fibers. *Journal of Materials Research and Technology* 28 (2023): 3121-3132.
3. H. Song, T. Liu, F. Gauvin, and H.J.H. Brouwers. Evaluation of zirconia modification on the durability of natural fiber-reinforced cement composites using accelerated aging. *Journal of Building Engineering* 84 (2024):108632.
4. H. Song, T. Liu, and F. Gauvin. Application of plant fibers incorporation on municipal solid waste incineration (MSWI) bottom ash as binder substitute: mechanical strength and leaching evaluation. *Submitted.*
5. H. Song, T. Liu, F. Gauvin, and H.J.H. Brouwers. Investigation of sisal fiber incorporation on engineering properties and sustainability of lightweight aggregates produced from municipal solid waste incinerated bottom ash. *Construction and Building Materials* 413 (2024): 134943.
6. H. Song, T. Liu, J. Li, F. Gauvin, W. Chen, and H.J.H. Brouwers. MSWI bottom ash as sand in mortars: the effect of sisal fibers. *Submitted*.
7. H. Song, K. Hon, F. Gauvin, S. Pantaleo, F. Berger, W. Chen, and H.J.H. Brouwers. Durability assessment of alkyl ketene dimer hydrophobic treatment of bio-based thermal insulation materials. *Resource, Conservation and Recycling.* Accepted.
8. H. Song, T. Luinenburg, F. Gauvin, and H.J.H. Brouwers. Carbonization coated treatment of municipal solid waste incineration bottom ash and its feasibility as sand in mortars: mechanical properties and leaching behavior. *In preparation.*
9. H. Song, J. Zeng, F. Gauvin, and H.J.H. Brouwers. Prediction of tensile performance of reinforced cementitious composites by plant fibers using machine learning. *In preparation.*

Patent Applications

1. H. Song, T. Liu, F. Gauvin and H.J.H. Brouwers. Cementitious paste and concrete with bottom ash and natural fibers. *P099273NL.*

Conference Proceedings

1. H. Song, T. Liu, F. Gauvin and H.J.H Brouwers, Investigations on the effect of surface treatment of hemp fibers on the mechanical and micro performance of fiber cement composites", Proceeding of the International Conference organized by Wuhan University of Technology, The 3rd International Conference on Sustainable Building Materials (ICSBM 2023), Wuhan, China, September 2023 (Poster).
2. H. Song, F. Gauvin, and H.J.H. Brouwers, "Surface treatment of hemp fibers for reinforcement of cementitious composites", 7th International Conference Non-Traditional Cement & Concrete (NTCC), Brno, Czech Republic, June 2023 (Presentation).
3. H. Song, F. Gauvin and H.J.H. Brouwers, Investigations on the effect of surface treatment of hemp fibers on the mechanical and micro-performance of fiber-cement composites, 4th International Conference on the Chemistry of Construction Materials, Karlsruhe Institute of Technology, Germany, September 2022. (Poster).

Curriculum vitae

Helong Song was born in Dengzhou, Henan Province, China on February 2nd, 1994. After finishing his primary, middle, and high school educations in Dengzhou, he started to study at Tianjin University of Science and Technology (TUST) in September 2013. In June 2017, he received his bachelor's degree majoring in Light Chemical Engineering (Biomass Resource Engineering). In September 2017, he started to study at the School of Light Industry and Engineering at South China University of Technology (SCUT) as a master student, supervised by Prof. Huiming Fan, majoring in ancient book restoration, solid waste recycling and their applications and machine equipment development, earning his master's degree in August 2019. In November 2019, he started his Ph.D. study under the supervision of Prof. H.J.H. (Jos) Brouwers, Prof. Wei Chen, and Dr. Florent Gauvin at Eindhoven University of Technology (TU/e), Eindhoven, the Netherlands. His Ph.D. research topic is related to the application of natural fibers and municipal solid waste incineration (MSWI) bottom ash into building materials.

Bouwstenen is een publicatiereeks
van de Faculteit Bouwkunde,
Technische Universiteit Eindhoven.
Zij presenteert resultaten van
onderzoek en andere activiteiten op
het vakgebied der Bouwkunde,
uitgevoerd in het kader van deze
Faculteit.

Bouwstenen en andere proefschriften van de
TU/e zijn online beschikbaar via:
https://research.tue.nl/

Reeds verschenen in de serie
Bouwstenen

nr 1
Elan: A Computer Model for Building Energy Design: Theory and Validation
Martin H. de Wit
H.H. Driessen
R.M.M. van der Velden

nr 2
Kwaliteit, Keuzevrijheid en Kosten: Evaluatie van Experiment Klarendal, Arnhem
J. Smeets
C. le Nobel
M. Broos
J. Frenken
A. v.d. Sanden

nr 3
Crooswijk: Van 'Bijzonder' naar 'Gewoon'
Vincent Smit
Kees Noort

nr 4
Staal in de Woningbouw
Edwin J.F. Delsing

nr 5
Mathematical Theory of Stressed Skin Action in Profiled Sheeting with Various Edge Conditions
Andre W.A.M.J. van den Bogaard

nr 6
Hoe Berekenbaar en Betrouwbaar is de Coëfficiënt k in x-ksigma en x-ks?
K.B. Lub
A.J. Bosch

nr 7
Het Typologisch Gereedschap: Een Verkennende Studie Omtrent Typologie en Omtrent de Aanpak van Typologisch Onderzoek
J.H. Luiten

nr 8
Informatievoorziening en Beheerprocessen
A. Nauta
Jos Smeets (red.)
Helga Fassbinder (projectleider)
Adrie Proveniers
J. v.d. Moosdijk

nr 9
Strukturering en Verwerking van Tijdgegevens voor de Uitvoering van Bouwwerken
ir. W.F. Schaefer
P.A. Erkelens

nr 10
Stedebouw en de Vorming van een Speciale Wetenschap
K. Doevendans

nr 11
Informatica en Ondersteuning van Ruimtelijke Besluitvorming
G.G. van der Meulen

nr 12
Staal in de Woningbouw, Korrosie-Bescherming van de Begane Grondvloer
Edwin J.F. Delsing

nr 13
Een Thermisch Model voor de Berekening van Staalplaatbetonvloeren onder Brandomstandigheden
A.F. Hamerlinck

nr 14
De Wijkgedachte in Nederland: Gemeenschapsstreven in een Stedebouwkundige Context
K. Doevendans
R. Stolzenburg

nr 15
Diaphragm Effect of Trapezoidally Profiled Steel Sheets: Experimental Research into the Influence of Force Application
Andre W.A.M.J. van den Bogaard

nr 16
Versterken met Spuit-Ferrocement: Het Mechanische Gedrag van met Spuit-Ferrocement Versterkte Gewapend Betonbalken
K.B. Lubir
M.C.G. van Wanroy

nr 17
De Tractaten van Jean Nicolas Louis Durand
G. van Zeyl

nr 18
Wonen onder een Plat Dak: Drie Opstellen over Enkele Vooronderstellingen van de Stedebouw
K. Doevendans

nr 19
Supporting Decision Making Processes: A Graphical and Interactive Analysis of Multivariate Data
W. Adams

nr 20
Self-Help Building Productivity: A Method for Improving House Building by Low-Income Groups Applied to Kenya 1990-2000
P. A. Erkelens

nr 21
De Verdeling van Woningen: Een Kwestie van Onderhandelen
Vincent Smit

nr 22
Flexibiliteit en Kosten in het Ontwerpproces: Een Besluitvormingondersteunend Model
M. Prins

nr 23
Spontane Nederzettingen Begeleid: Voorwaarden en Criteria in Sri Lanka
Po Hin Thung

nr 24
Fundamentals of the Design of Bamboo Structures
Oscar Arce-Villalobos

nr 25
Concepten van de Bouwkunde
M.F.Th. Bax (red.)
H.M.G.J. Trum (red.)

nr 26
Meaning of the Site
Xiaodong Li

nr 27
Het Woonmilieu op Begrip Gebracht: Een Speurtocht naar de Betekenis van het Begrip 'Woonmilieu'
Jaap Ketelaar

nr 28
Urban Environment in Developing Countries
editors: Peter A. Erkelens
George G. van der Meulen (red.)

nr 29
Stategische Plannen voor de Stad: Onderzoek en Planning in Drie Steden
prof.dr. H. Fassbinder (red.)
H. Rikhof (red.)

nr 30
Stedebouwkunde en Stadsbestuur
Piet Beekman

nr 31
De Architectuur van Djenné: Een Onderzoek naar de Historische Stad
P.C.M. Maas

nr 32
Conjoint Experiments and Retail Planning
Harmen Oppewal

nr 33
Strukturformen Indonesischer Bautechnik: Entwicklung Methodischer Grundlagen für eine 'Konstruktive Pattern Language' in Indonesien
Heinz Frick arch. SIA

nr 34
Styles of Architectural Designing: Empirical Research on Working Styles and Personality Dispositions
Anton P.M. van Bakel

nr 35
Conjoint Choice Models for Urban Tourism Planning and Marketing
Benedict Dellaert

nr 36
Stedelijke Planvorming als Co-Produktie
Helga Fassbinder (red.)

nr 37
Design Research in the Netherlands
editors: R.M. Oxman
M.F.Th. Bax
H.H. Achten

nr 38
Communication in the Building Industry
Bauke de Vries

nr 39
Optimaal Dimensioneren van Gelaste Plaatliggers
J.B.W. Stark
F. van Pelt
L.F.M. van Gorp
B.W.E.M. van Hove

nr 40
Huisvesting en Overwinning van Armoede
P.H. Thung
P. Beekman (red.)

nr 41
Urban Habitat: The Environment of Tomorrow
George G. van der Meulen
Peter A. Erkelens

nr 42
A Typology of Joints
John C.M. Olie

nr 43
Modeling Constraints-Based Choices for Leisure Mobility Planning
Marcus P. Stemerding

nr 44
Activity-Based Travel Demand Modeling
Dick Ettema

nr 45
Wind-Induced Pressure Fluctuations on Building Facades
Chris Geurts

nr 46
Generic Representations
Henri Achten

nr 47
Johann Santini Aichel: Architectuur en Ambiguiteit
Dirk De Meyer

nr 48
Concrete Behaviour in Multiaxial Compression
Erik van Geel

nr 49
Modelling Site Selection
Frank Witlox

nr 50
Ecolemma Model
Ferdinand Beetstra

nr 51
Conjoint Approaches to Developing Activity-Based Models
Donggen Wang

nr 52
On the Effectiveness of Ventilation
Ad Roos

nr 53
Conjoint Modeling Approaches for Residential Group preferences
Eric Molin

nr 54
Modelling Architectural Design Information by Features
Jos van Leeuwen

nr 55
A Spatial Decision Support System for the Planning of Retail and Service Facilities
Theo Arentze

nr 56
Integrated Lighting System Assistant
Ellie de Groot

nr 57
Ontwerpend Leren, Leren Ontwerpen
J.T. Boekholt

nr 58
Temporal Aspects of Theme Park Choice Behavior
Astrid Kemperman

nr 59
Ontwerp van een Geïndustrialiseerde Funderingswijze
Faas Moonen

nr 60
Merlin: A Decision Support System for Outdoor Leisure Planning
Manon van Middelkoop

nr 61
The Aura of Modernity
Jos Bosman

nr 62
Urban Form and Activity-Travel Patterns
Daniëlle Snellen

nr 63
Design Research in the Netherlands 2000
Henri Achten

nr 64
Computer Aided Dimensional Control in Building Construction
Rui Wu

nr 65
Beyond Sustainable Building
editors: Peter A. Erkelens
Sander de Jonge
August A.M. van Vliet
co-editor: Ruth J.G. Verhagen

nr 66
Das Globalrecyclingfähige Haus
Hans Löfflad

nr 67
Cool Schools for Hot Suburbs
René J. Dierkx

nr 68
A Bamboo Building Design Decision Support Tool
Fitri Mardjono

nr 69
Driving Rain on Building Envelopes
Fabien van Mook

nr 70
Heating Monumental Churches
Henk Schellen

nr 71
Van Woningverhuurder naar Aanbieder van Woongenot
Patrick Dogge

nr 72
Moisture Transfer Properties of Coated Gypsum
Emile Goossens

nr 73
Plybamboo Wall-Panels for Housing
Guillermo E. González-Beltrán

nr 74
The Future Site-Proceedings
Ger Maas
Frans van Gassel

nr 75
Radon transport in Autoclaved Aerated Concrete
Michel van der Pal

nr 76
The Reliability and Validity of Interactive Virtual Reality Computer Experiments
Amy Tan

nr 77
Measuring Housing Preferences Using Virtual Reality and Belief Networks
Maciej A. Orzechowski

nr 78
Computational Representations of Words and Associations in Architectural Design
Nicole Segers

nr 79
Measuring and Predicting Adaptation in Multidimensional Activity-Travel Patterns
Chang-Hyeon Joh

nr 80
Strategic Briefing
Fayez Al Hassan

nr 81
Well Being in Hospitals
Simona Di Cicco

nr 82
Solares Bauen: Implementierungs- und Umsetzungs-Aspekte in der Hochschulausbildung in Österreich
Gerhard Schuster

nr 83
Supporting Strategic Design of Workplace Environments with Case-Based Reasoning
Shauna Mallory-Hill

nr 84
ACCEL: A Tool for Supporting Concept Generation in the Early Design Phase
Maxim Ivashkov

nr 85
Brick-Mortar Interaction in Masonry under Compression
Ad Vermeltfoort

nr 86
Zelfredzaam Wonen
Guus van Vliet

nr 87
Een Ensemble met Grootstedelijke Allure
Jos Bosman
Hans Schippers

nr 88
On the Computation of Well-Structured Graphic Representations in Architectural Design
Henri Achten

nr 89
De Evolutie van een West-Afrikaanse Vernaculaire Architectuur
Wolf Schijns

nr 90
ROMBO Tactiek
Christoph Maria Ravesloot

nr 91
External Coupling between Building Energy Simulation and Computational Fluid Dynamics
Ery Djunaedy

nr 92
Design Research in the Netherlands 2005
editors: Henri Achten
Kees Dorst
Pieter Jan Stappers
Bauke de Vries

nr 93
Ein Modell zur Baulichen Transformation
Jalil H. Saber Zaimian

nr 94
Human Lighting Demands: Healthy Lighting in an Office Environment
Myriam Aries

nr 95
A Spatial Decision Support System for the Provision and Monitoring of Urban Greenspace
Claudia Pelizaro

nr 96
Leren Creëren
Adri Proveniers

nr 97
Simlandscape
Rob de Waard

nr 98
Design Team Communication
Ad den Otter

nr 99
Humaan-Ecologisch Georiënteerde Woningbouw
Juri Czabanowski

nr 100
Hambase
Martin de Wit

nr 101
Sound Transmission through Pipe Systems and into Building Structures
Susanne Bron-van der Jagt

nr 102
Het Bouwkundig Contrapunt
Jan Francis Boelen

nr 103
A Framework for a Multi-Agent Planning Support System
Dick Saarloos

nr 104
Bracing Steel Frames with Calcium Silicate Element Walls
Bright Mweene Ng'andu

nr 105
Naar een Nieuwe Houtskeletbouw
F.N.G. De Medts

nr 106 and 107
Niet gepubliceerd

nr 108
Geborgenheid
T.E.L. van Pinxteren

nr 109
Modelling Strategic Behaviour in Anticipation of Congestion
Qi Han

nr 110
Reflecties op het Woondomein
Fred Sanders

nr 111
On Assessment of Wind Comfort by Sand Erosion
Gábor Dezsö

nr 112
Bench Heating in Monumental Churches
Dionne Limpens-Neilen

nr 113
RE. Architecture
Ana Pereira Roders

nr 114
Toward Applicable Green Architecture
Usama El Fiky

nr 115
Knowledge Representation under Inherent Uncertainty in a Multi-Agent System for Land Use Planning
Liying Ma

nr 116
Integrated Heat Air and Moisture Modeling and Simulation
Jos van Schijndel

nr 117
Concrete Behaviour in Multiaxial Compression
J.P.W. Bongers

nr 118
The Image of the Urban Landscape
Ana Moya Pellitero

nr 119
The Self-Organizing City in Vietnam
Stephanie Geertman

nr 120
A Multi-Agent Planning Support System for Assessing Externalities of Urban Form Scenarios
Rachel Katoshevski-Cavari

nr 121
Den Schulbau Neu Denken, Fühlen und Wollen
Urs Christian Maurer-Dietrich

nr 122
Peter Eisenman Theories and Practices
Bernhard Kormoss

nr 123
User Simulation of Space Utilisation
Vincent Tabak

nr 125
In Search of a Complex System Model
Oswald Devisch

nr 126
Lighting at Work: Environmental Study of Direct Effects of Lighting Level and Spectrum on Psycho-Physiological Variables
Grazyna Górnicka

nr 127
Flanking Sound Transmission through Lightweight Framed Double Leaf Walls
Stefan Schoenwald

nr 128
Bounded Rationality and Spatio-Temporal Pedestrian Shopping Behavior
Wei Zhu

nr 129
Travel Information: Impact on Activity Travel Pattern
Zhongwei Sun

nr 130
Co-Simulation for Performance Prediction of Innovative Integrated Mechanical Energy Systems in Buildings
Marija Trčka

nr 131
Niet gepubliceerd

nr 132
Architectural Cue Model in Evacuation Simulation for Underground Space Design
Chengyu Sun

nr 133
Uncertainty and Sensitivity Analysis in Building Performance Simulation for Decision Support and Design Optimization
Christina Hopfe

nr 134
Facilitating Distributed Collaboration in the AEC/FM Sector Using Semantic Web Technologies
Jacob Beetz

nr 135
Circumferentially Adhesive Bonded Glass Panes for Bracing Steel Frame in Façades
Edwin Huveners

nr 136
Influence of Temperature on Concrete Beams Strengthened in Flexure with CFRP
Ernst-Lucas Klamer

nr 137
Sturen op Klantwaarde
Jos Smeets

nr 139
Lateral Behavior of Steel Frames with Discretely Connected Precast Concrete Infill Panels
Paul Teewen

nr 140
Integral Design Method in the Context of Sustainable Building Design
Perica Savanović

nr 141
Household Activity-Travel Behavior: Implementation of Within-Household Interactions
Renni Anggraini

nr 142
Design Research in the Netherlands 2010
Henri Achten

nr 143
Modelling Life Trajectories and Transport Mode Choice Using Bayesian Belief Networks
Marloes Verhoeven

nr 144
Assessing Construction Project Performance in Ghana
William Gyadu-Asiedu

nr 145
Empowering Seniors through Domotic Homes
Masi Mohammadi

nr 146
An Integral Design Concept for Ecological Self-Compacting Concrete
Martin Hunger

nr 147
Governing Multi-Actor Decision Processes in Dutch Industrial Area Redevelopment
Erik Blokhuis

nr 148
A Multifunctional Design Approach for Sustainable Concrete
Götz Hüsken

nr 149
Quality Monitoring in Infrastructural Design-Build Projects
Ruben Favié

nr 150
Assessment Matrix for Conservation of Valuable Timber Structures
Michael Abels

nr 151
Co-simulation of Building Energy Simulation and Computational Fluid Dynamics for Whole-Building Heat, Air and Moisture Engineering
Mohammad Mirsadeghi

nr 152
External Coupling of Building Energy Simulation and Building Element Heat, Air and Moisture Simulation
Daniel Cóstola

nr 153
Adaptive Decision Making In Multi-Stakeholder Retail Planning
Ingrid Janssen

nr 154
Landscape Generator
Kymo Slager

nr 155
Constraint Specification in Architecture
Remco Niemeijer

nr 156
A Need-Based Approach to Dynamic Activity Generation
Linda Nijland

nr 157
Modeling Office Firm Dynamics in an Agent-Based Micro Simulation Framework
Gustavo Garcia Manzato

nr 158
Lightweight Floor System for Vibration Comfort
Sander Zegers

nr 159
Aanpasbaarheid van de Draagstructuur
Roel Gijsbers

nr 160
'Village in the City' in Guangzhou, China
Yanliu Lin

nr 161
Climate Risk Assessment in Museums
Marco Martens

nr 162
Social Activity-Travel Patterns
Pauline van den Berg

nr 163
Sound Concentration Caused by Curved Surfaces
Martijn Vercammen

nr 164
Design of Environmentally Friendly Calcium Sulfate-Based Building Materials: Towards an Improved Indoor Air Quality
Qingliang Yu

nr 165
Beyond Uniform Thermal Comfort on the Effects of Non-Uniformity and Individual Physiology
Lisje Schellen

nr 166
Sustainable Residential Districts
Gaby Abdalla

nr 167
Towards a Performance Assessment Methodology using Computational Simulation for Air Distribution System Designs in Operating Rooms
Mônica do Amaral Melhado

nr 168
Strategic Decision Modeling in Brownfield Redevelopment
Brano Glumac

nr 169
Pamela: A Parking Analysis Model for Predicting Effects in Local Areas
Peter van der Waerden

nr 170
A Vision Driven Wayfinding Simulation-System Based on the Architectural Features Perceived in the Office Environment
Qunli Chen

nr 171
Measuring Mental Representations Underlying Activity-Travel Choices
Oliver Horeni

nr 172
Modelling the Effects of Social Networks on Activity and Travel Behaviour
Nicole Ronald

nr 173
Uncertainty Propagation and Sensitivity Analysis Techniques in Building Performance Simulation to Support Conceptual Building and System Design
Christian Struck

nr 174
Numerical Modeling of Micro-Scale Wind-Induced Pollutant Dispersion in the Built Environment
Pierre Gousseau

nr 175
Modeling Recreation Choices over the Family Lifecycle
Anna Beatriz Grigolon

nr 176
Experimental and Numerical Analysis of Mixing Ventilation at Laminar, Transitional and Turbulent Slot Reynolds Numbers
Twan van Hooff

nr 177
Collaborative Design Support: Workshops to Stimulate Interaction and Knowledge Exchange Between Practitioners
Emile M.C.J. Quanjel

nr 178
Future-Proof Platforms for Aging-in-Place
Michiel Brink

nr 179
Motivate: A Context-Aware Mobile Application for Physical Activity Promotion
Yuzhong Lin

nr 180
Experience the City: Analysis of Space-Time Behaviour and Spatial Learning
Anastasia Moiseeva

nr 181
Unbonded Post-Tensioned Shear Walls of Calcium Silicate Element Masonry
Lex van der Meer

nr 182
Construction and Demolition Waste Recycling into Innovative Building Materials for Sustainable Construction in Tanzania
Mwita M. Sabai

nr 183
Durability of Concrete with Emphasis on Chloride Migration
Przemysław Spiesz

nr 184
Computational Modeling of Urban Wind Flow and Natural Ventilation Potential of Buildings
Rubina Ramponi

nr 185
A Distributed Dynamic Simulation Mechanism for Buildings Automation and Control Systems
Azzedine Yahiaoui

nr 186
Modeling Cognitive Learning of Urban Networks in Daily Activity-Travel Behavior
Şehnaz Cenani Durmazoğlu

nr 187
Functionality and Adaptability of Design Solutions for Public Apartment Buildings in Ghana
Stephen Agyefi-Mensah

nr 188
A Construction Waste Generation Model for Developing Countries
Lilliana Abarca-Guerrero

nr 189
Synchronizing Networks: The Modeling of Supernetworks for Activity-Travel Behavior
Feixiong Liao

nr 190
Time and Money Allocation Decisions in Out-of-Home Leisure Activity Choices
Gamze Zeynep Dane

nr 191
How to Measure Added Value of CRE and Building Design
Rianne Appel-Meulenbroek

nr 192
Secondary Materials in Cement-Based Products: Treatment, Modeling and Environmental Interaction
Miruna Florea

nr 193
Concepts for the Robustness Improvement of Self-Compacting Concrete: Effects of Admixtures and Mixture Components on the Rheology and Early Hydration at Varying Temperatures
Wolfram Schmidt

nr 194
Modelling and Simulation of Virtual Natural Lighting Solutions in Buildings
Rizki A. Mangkuto

nr 195
Nano-Silica Production at Low Temperatures from the Dissolution of Olivine - Synthesis, Tailoring and Modelling
Alberto Lazaro Garcia

nr 196
Building Energy Simulation Based Assessment of Industrial Halls for Design Support
Bruno Lee

nr 197
Computational Performance Prediction of the Potential of Hybrid Adaptable Thermal Storage Concepts for Lightweight Low-Energy Houses
Pieter-Jan Hoes

nr 198
Application of Nano-Silica in Concrete
George Quercia Bianchi

nr 199
Dynamics of Social Networks and Activity Travel Behaviour
Fariya Sharmeen

nr 200
Building Structural Design Generation and Optimisation including Spatial Modification
Juan Manuel Davila Delgado

nr 201
Hydration and Thermal Decomposition of Cement/Calcium-Sulphate Based Materials
Ariën de Korte

nr 202
Republiek van Beelden:
De Politieke Werkingen van het Ontwerp in Regionale Planvorming
Bart de Zwart

nr 203
Effects of Energy Price Increases on Individual Activity-Travel Repertoires and Energy Consumption
Dujuan Yang

nr 204
Geometry and Ventilation:
Evaluation of the Leeward Sawtooth Roof Potential in the Natural Ventilation of Buildings
Jorge Isaac Perén Montero

nr 205
Computational Modelling of Evaporative Cooling as a Climate Change Adaptation Measure at the Spatial Scale of Buildings and Streets
Hamid Montazeri

nr 206
Local Buckling of Aluminium Beams in Fire Conditions
Ronald van der Meulen

nr 207
Historic Urban Landscapes:
Framing the Integration of Urban and Heritage Planning in Multilevel Governance
Loes Veldpaus

nr 208
Sustainable Transformation of the Cities:
Urban Design Pragmatics to Achieve a Sustainable City
Ernesto Antonio Zumelzu Scheel

nr 209
Development of Sustainable Protective Ultra-High Performance Fibre Reinforced Concrete (UHPFRC):
Design, Assessment and Modeling
Rui Yu

nr 210
Uncertainty in Modeling Activity-Travel Demand in Complex Uban Systems
Soora Rasouli

nr 211
Simulation-based Performance Assessment of Climate Adaptive Greenhouse Shells
Chul-sung Lee

nr 212
Green Cities:
Modelling the Spatial Transformation of the Urban Environment using Renewable Energy Technologies
Saleh Mohammadi

nr 213
A Bounded Rationality Model of Short and Long-Term Dynamics of Activity-Travel Behavior
Ifigeneia Psarra

nr 214
Effects of Pricing Strategies on Dynamic Repertoires of Activity-Travel Behaviour
Elaheh Khademi

nr 215
Handstorm Principles for Creative and Collaborative Working
Frans van Gassel

nr 216
Light Conditions in Nursing Homes: Visual Comfort and Visual Functioning of Residents
Marianne M. Sinoo

nr 217
Woonsporen: De Sociale en Ruimtelijke Biografie van een Stedelijk Bouwblok in de Amsterdamse Transvaalbuurt
Hüseyin Hüsnü Yegenoglu

nr 218
Studies on User Control in Ambient Intelligent Systems
Berent Willem Meerbeek

nr 219
Daily Livings in a Smart Home: Users' Living Preference Modeling of Smart Homes
Erfaneh Allameh

nr 220
Smart Home Design: Spatial Preference Modeling of Smart Homes
Mohammadali Heidari Jozam

nr 221
Wonen: Discoursen, Praktijken, Perspectieven
Jos Smeets

nr 222
Personal Control over Indoor Climate in Offices: Impact on Comfort, Health and Productivity
Atze Christiaan Boerstra

nr 223
Personalized Route Finding in Multimodal Transportation Networks
Jianwe Zhang

nr 224
The Design of an Adaptive Healing Room for Stroke Patients
Elke Daemen

nr 225
Experimental and Numerical Analysis of Climate Change Induced Risks to Historic Buildings and Collections
Zara Huijbregts

nr 226
Wind Flow Modeling in Urban Areas Through Experimental and Numerical Techniques
Alessio Ricci

nr 227
Clever Climate Control for Culture: Energy Efficient Indoor Climate Control Strategies for Museums Respecting Collection Preservation and Thermal Comfort of Visitors
Rick Kramer

nr 228
Fatigue Life Estimation of Metal Structures Based on Damage Modeling
Sarmediran Silitonga

nr 229
A multi-agents and occupancy based strategy for energy management and process control on the room-level
Timilehin Moses Labeodan

nr 230
Environmental assessment of Building Integrated Photovoltaics: Numerical and Experimental Carrying Capacity Based Approach
Michiel Ritzen

nr 231
Performance of Admixture and Secondary Minerals in Alkali Activated Concrete: Sustaining a Concrete Future
Arno Keulen

nr 232
World Heritage Cities and Sustainable Urban Development: Bridging Global and Local Levels in Monitoring the Sustainable Urban Development of World Heritage Cities
Paloma C. Guzman Molina

nr 233
Stage Acoustics and Sound Exposure in Performance and Rehearsal Spaces for Orchestras: Methods for Physical Measurements
Remy Wenmaekers

nr 234
Municipal Solid Waste Incineration (MSWI) Bottom Ash: From Waste to Value Characterization, Treatments and Application
Pei Tang

nr 235
Large Eddy Simulations Applied to Wind Loading and Pollutant Dispersion
Mattia Ricci

nr 236
Alkali Activated Slag-Fly Ash Binders: Design, Modeling and Application
Xu Gao

nr 237
Sodium Carbonate Activated Slag: Reaction Analysis, Microstructural Modification & Engineering Application
Bo Yuan

nr 238
Shopping Behavior in Malls
Widiyani

nr 239
Smart Grid-Building Energy Interactions: Demand Side Power Flexibility in Office Buildings
Kennedy Otieno Aduda

nr 240
Modeling Taxis Dynamic Behavior in Uncertain Urban Environments
Zheng Zhong

nr 241
Gap-Theoretical Analyses of Residential Satisfaction and Intention to Move
Wen Jiang

nr 242
Travel Satisfaction and Subjective Well-Being: A Behavioral Modeling Perspective
Yanan Gao

nr 243
Building Energy Modelling to Support the Commissioning of Holistic Data Centre Operation
Vojtech Zavrel

nr 244
Regret-Based Travel Behavior Modeling: An Extended Framework
Sunghoon Jang

nr 245
Towards Robust Low-Energy Houses: A Computational Approach for Performance Robustness Assessment using Scenario Analysis
Rajesh Reddy Kotireddy

nr 246
Development of sustainable and functionalized inorganic binder-biofiber composites
Guillaume Doudart de la Grée

nr 247
A Multiscale Analysis of the Urban Heat Island Effect: From City Averaged Temperatures to the Energy Demand of Individual Buildings
Yasin Toparlar

nr 248
Design Method for Adaptive Daylight Systems for buildings covered by large (span) roofs
Florian Heinzelmann

nr 249
Hardening, high-temperature resistance and acid resistance of one-part geopolymers
Patrick Sturm

nr 250
Effects of the built environment on dynamic repertoires of activity-travel behaviour
Aida Pontes de Aquino

nr 251
Modeling for auralization of urban environments: Incorporation of directivity in sound propagation and analysis of a framework for auralizing a car pass-by
Fotis Georgiou

nr 252
Wind Loads on Heliostats and Photovoltaic Trackers
Andreas Pfahl

nr 253
Approaches for computational performance optimization of innovative adaptive façade concepts
Roel Loonen

nr 254
Multi-scale FEM-DEM Model for Granular Materials: Micro-scale boundary conditions, Statics, and Dynamics
Jiadun Liu

nr 255
Bending Moment - Shear Force Interaction of Rolled I-Shaped Steel Sections
Rianne Willie Adriana Dekker

nr 256
Paralympic tandem cycling and handcycling: Computational and wind tunnel analysis of aerodynamic performance
Paul Fionn Mannion

nr 257
Experimental characterization and numerical modelling of 3D printed concrete: Controlling structural behaviour in the fresh and hardened state
Robert Johannes Maria Wolfs

nr 258
Requirement checking in the building industry: Enabling modularized and extensible requirement checking systems based on semantic web technologies
Chi Zhang

nr 259
A Sustainable Industrial Site Redevelopment Planning Support System
Tong Wang

nr 260
Efficient storage and retrieval of detailed building models: Multi-disciplinary and long-term use of geometric and semantic construction information
Thomas Ferdinand Krijnen

nr 261
The users' value of business center concepts for knowledge sharing and networking behavior within and between organizations
Minou Weijs-Perrée

nr 262
Characterization and improvement of aerodynamic performance of vertical axis wind turbines using computational fluid dynamics (CFD)
Abdolrahim Rezaeiha

nr 263
In-situ characterization of the acoustic impedance of vegetated roofs
Chang Liu

nr 264
Occupancy-based lighting control: Developing an energy saving strategy that ensures office workers' comfort
Christel de Bakker

nr 265
Stakeholders-Oriented Spatial Decision Support System
Cahyono Susetyo

nr 266
Climate-induced damage in oak museum objects
Rianne Aleida Luimes

nr 267
Towards individual thermal comfort: Model predictive personalized control of heating systems
Katarina Katic

nr 268
Modelling and Measuring Quality of Urban Life: Housing, Neighborhood, Transport and Job
Lida Aminian

nr 269
Optimization of an aquifer thermal energy storage system through integrated modelling of aquifer, HVAC systems and building
Basar Bozkaya

nr 270
Numerical modeling for urban sound propagation: developments in wave-based and energy-based methods
Raúl Pagán Muñoz

nr 271
Lighting in multi-user office environments: improving employee wellbeing through personal control
Sanae van der Vleuten-Chraibi

nr 272
A strategy for fit-for-purpose occupant behavior modelling in building energy and comfort performance simulation
Isabella I. Gaetani dell'Aquila d'Aragona

nr 273
Een architectuurhistorische waardestelling van naoorlogse woonwijken in Nederland: Het voorbeeld van de Westelijke Tuinsteden in Amsterdam
Eleonore Henriette Marie Mens

nr 274
Job-Housing Co-Dependent Mobility Decisions in Life Trajectories
Jia Guo

nr 275
A user-oriented focus to create healthcare facilities: decision making on strategic values
Emilia Rosalia Catharina Maria Huisman

nr 276
Dynamics of plane impinging jets at moderate Reynolds numbers – with applications to air curtains
Adelya Khayrullina

nr 277
Valorization of Municipal Solid Waste Incineration Bottom Ash - Chemical Nature, Leachability and Treatments of Hazardous Elements
Qadeer Alam

nr 278
Treatments and valorization of MSWI bottom ash - application in cement-based materials
Veronica Caprai

nr 279
Personal lighting conditions of office workers - input for intelligent systems to optimize subjective alertness
Juliëtte van Duijnhoven

nr 280
Social influence effects in tourism travel: air trip itinerary and destination choices
Xiaofeng Pan

nr 281
Advancing Post-War Housing: Integrating Heritage Impact, Environmental Impact, Hygrothermal Risk and Costs in Renovation Design Decisions
Lisanne Claartje Havinga

nr 282
Impact resistant ultra-high performance fibre reinforced concrete: materials, components and properties
Peipeng Li

nr 283
Demand-driven Science Parks: The Perceived Benefits and Trade-offs of Tenant Firms with regard to Science Park Attributes
Wei Keat Benny Ng

nr 284
Raise the lantern; how light can help to maintain a healthy and safe hospital environment focusing on nurses
Maria Petronella Johanna Aarts

nr 285
Modelling Learning and Dynamic Route and Parking Choice Behaviour under Uncertainty
Elaine Cristina Schneider de Carvalho

nr 286
Identifying indoor local microclimates for safekeeping of cultural heritage
Karin Kompatscher

nr 287
Probabilistic modeling of fatigue resistance for welded and riveted bridge details. Resistance models and estimation of uncertainty.
Davide Leonetti

nr 288
Performance of Layered UHPFRC under Static and Dynamic Loads: Effects of steel fibers, coarse aggregates and layered structures
Yangyueye Cao

nr 289
Photocatalytic abatement of the nitrogen oxide pollution: synthesis, application and long-term evaluation of titania-silica composites
Yuri Hendrix

nr 290
Assessing knowledge adoption in post-disaster reconstruction: Understanding the impact of hazard-resistant construction knowledge on reconstruction processes of self-recovering communities in Nepal and the Philippines
Eefje Hendriks

nr 291
Locating electric vehicle charging stations: A multi-agent based dynamic simulation
Seheon Kim

nr 292
De invloed van Lean Management op de beheersing van het bouwproces
Wim van den Bouwhuijsen

nr 293
Neighborhood Environment and Physical Activity of Older Adults
Zhengying Liu

nr 294
Practical and continuous luminance distribution measurements for lighting quality
Thijs Willem Kruisselbrink

nr 295
Auditory Distraction in Open-Plan Study Environments in Higher Education
Pieternella Elizabeth Braat-Eggen

nr 296
Exploring the effect of the sound environment on nurses' task performance: an applied approach focusing on prospective memory
Jikke Reinten

nr 297
Design and performance of water resistant cementitious materials– Mechanisms, evaluation and applications
Zhengyao Qu

nr 298
Design Optimization of Seasonal Thermal Energy Storage Integrated District Heating and Cooling System: A Modeling and Simulation Approach
Luyi Xu

nr 299
Land use and transport: Integrated approaches for planning and management
Zhongqi Wang

nr 300
Multi-disciplinary optimization of building spatial designs: co-evolutionary design process simulations, evolutionary algorithms, hybrid approaches
Sjonnie Boonstra

nr 301
Modeling the spatial and temporal relation between urban land use, temperature, and energy demand
Hung-Chu Chen

nr 302
Seismic retrofitting of masonry walls with flexible deep mounted CFRP strips
Ömer Serhat Türkmen

nr 303
Coupled Aerostructural Shape and Topology Optimization of Horizontal-Axis Wind Turbine Rotor Blades
Zhijun Wang

nr 304
Valorization of Recycled Waste Glass and Converter Steel Slag as Ingredients for Building Materials: Hydration and Carbonation Studies
Gang Liu

nr 305
Low-Carbon City Development based on Land Use Planning
Gengzhe Wang

nr 306
Sustainable energy transition scenario analysis for buildings and neighborhoods - Data driven optimization
Shalika Saubhagya Wickramarachchi Walker

nr 307
In-between living and manufactured: an exploratory study on biobuilding components for building design
Berrak Kirbas Akyurek

nr 308
Development of alternative cementitious binders and functionalized materials: design, performance and durability
Anna Monika Kaja

nr 309
Development a morphological approach for interactive kinetic façade design: Improving multiple occupants' visual comfort
Seyed Morteza Hosseini

nr 310
PV in urban context: modeling and simulation strategies for analyzing the performance of shaded PV systems
Ádám Bognár

nr 311
Life Trajectory, Household Car Ownership Dynamics and Home Renewable Energy Equipment Adoption
Gaofeng Gu

nr 312
Impact of Street-Scale Built Environment on Walking/Cycling around Metro Stations
Yanan Liu

nr 313
Advances in Urban Traffic Network Equilibrium Models and Algorithms
Dong Wang

nr 314
Development of an uncertainty analysis framework for model-based consequential life cycle assessment: application to activity-based modelling and life cycle assessment of multimodal mobility
Paul Martin Baustert

nr 315
Variable stiffness and damping structural joints for semi-active vibration control
Qinyu Wang

nr 316
Understanding Carsharing-Facilitating Neighborhood Preferences
Juan Wang

nr 317
Dynamic alignment of Corporate Real Estate to business strategies: An empirical analysis using historical data and in-depth modelling of decision making
Howard Cooke

nr 318
Local People Matter: Towards participatory governance of cultural heritage in China
Ji Li

nr 319
Walkability and Walkable Healthy Neighborhoods
Bojing Liao

nr 320
Light directionality in design of healthy offices: exploration of two methods
Parisa Khademagha

nr 321
Room acoustic modeling with the time-domain discontinuous Galerkin method
Huiqing Wang

nr 322
Sustainable insulating lightweight materials for enhancing indoor building performance: miscanthus, aerogel and nano-silica
Yuxuan Chen

nr 323
Computational analysis of the impact of façade geometrical details on wind flow and pollutant dispersion
Xing Zheng

nr 324
Analysis of urban wind energy potential around high-rise buildings in close proximity using computational fluid dynamics
Yu-Hsuan Jang

nr 325
A new approach to automated energy performance and fault detection and diagnosis of HVAC systems: Development of the 4S3F method
Arie Taal

nr 326
Innovative Admixtures for Modifying Viscosity and Volume Change of Cement Composites
Hossein Karimi

nr 327
Towards houses with low grid dependency: A simulation-based design optimization approach
Zahra Mohammadi

nr 328
Activation of demand flexibility for heating systems in buildings: Real-life demonstration of optimal control for power-to-heat and thermal energy storage
Christian Finck

nr 329
A computational framework for analysis and optimisation of automated solar shading systems
Samuel B. de Vries

nr 330
Challenges and potential solutions for cultural heritage adaptive reuse: a comparative study employing the Historic Urban Landscape approach
Nadia Pintossi

nr 331
Shared control in office lighting systems
Tatiana Aleksandrovna Lashina

nr 332
Comfort in Urban Public Spaces
You Peng

nr 333
Numerical modelling of metal soap formation in historical oil paintings
Gerardus Johannes Anna Maria Eumelen

nr 334
A transdisciplinary decision-making approach to food-water-energy nexus: A guide towards sustainable development
Maryam Ghodsvali

nr 335
Numerical modelling of transient low-frequency sound propagation and vibration in buildings
Indra Sihar

nr 336
Characterization of impact sound from lightweight joist floors
Yi Qin

nr 337
Cities for Children: Supporting Children and Caregivers in Participatory Urban Planning
Özlemnur Ataol

nr 338
Engaging the unengaged: Exploring citizen participation in nature-based solutions in China
Li Dai

nr 339
Municipal Solid Waste Incineration Residues: analysis, treatments, and applications
Ekaterina Loginova

nr 340
Enhancing the Uptake of Nature-Based Solutions in Urban Settings: An Information Systems Approach
Shahryar Ershad Sarabi

nr 341
Work Schedule Arrangements in Two-Adult Households with Children
Bilin Han

nr 342
Increasing awareness of urban cultural heritage using digital technologies: empirical design and analysis of a new multi-media web platform
Benshuo Wang

nr 343
Mechanical and physical properties of fibre-cement composites using alternative natural fibres
Katerina Kochova

nr 344
Numerical and experimental investigation of urban microclimate in a real compact heterogeneous urban area
Nestoras Antoniou

nr 345
Examining in-class activities to facilitate academic achievement in higher education: A framework for optimal indoor environmental conditions
Henk W. Brink

nr 346
High-temperature resistant geopolymers: composition, microstructure and performance
Kinga Malgorzata Klima

nr 347
Individual and household decision-making in shared parking
Qianqian Yan

nr 348
In-situ formation of LDHs in Alkali activated binders
Tao Liu

nr 349
Condition assessment of concrete sewer pipes through an integrated experimental-numerical approach
Irene C. Scheperboer

nr 350
In situ PU-based characterization of sound absorbing materials for room acoustic modeling purposes
Baltazar Briere de La Hosseraye

nr 351
Uncertainty analysis and management in building energy data mining: A bottom-up approach considering the temporal and spatial aspect of data
Waqas Khan

nr 352
Personalized Heating Control Systems to improve thermal comfort and reduce energy consumption
Michal Veselý

nr 353
Restorative value of the urban greenscape: Urban residential streets as restorative environments
Robert P. van Dongen

nr 354
Urban ventilation and the compact Mediterranean city: numerical investigations of the dynamic relationships between density, morphology and wind flow
Olga Palusci

nr 355
Data science for buildings: a multi-scale approach bridging occupants to smart-city energy planning
Julien Leprince

nr 356
Class Association Rule Models for Predicting Transportation Mode Choice
Jiajia Zhang

nr 357
Acceptance and use of autonomous vehicles
Zhihui Tian

nr 358
Consumer Acceptance of Crowdshipping Services
Chenyu Wang

nr 359
Determinants of habitual participation in leisure-time physical activity and active travel in life trajectories
Xiaoyue Chen

nr 360
Analysis of Citizens' Motivation and Intention Using Modern Information Technology in Urban Planning Public Participation
Wenshu Li

nr 361
Linking smart and physical port cities. Port-city interface areas: from obsolete/isolated to smart environments.
Mercè de Miguel Capdevila

nr 362
Assessment and improvement of indoor thermal comfort and energy demand of Chinese heritage apartment buildings under climate change
Muxi Lei

nr 363
Indoor airflow and heat transfer in a cross-ventilated generic building: wind tunnel experiments and computational fluid dynamics analyses
Katarina Kosutova

nr 364
A Robotic Construction Simulation Platform for Light-weight Prefabricated Structures. Lifetime prediction of vertical-axis wind turbines based on CFD simulations and high-cycle fatigue modeling
Aiyu Zhu

nr 365
Lifetime prediction of vertical-axis wind turbines based on CFD simulations and high-cycle fatigue modeling
Feiyu Geng

nr 366
Computational modeling of convective heat transfer at building surfaces
Samy Iousef

nr 367
Numerical simulation of the atmospheric boundary layer with application to natural ventilation
Raffaele Vasaturo

nr 368
Bouwen zonder scrupules. De Nederlandse bouwnijverheid tijdens de bezetting en de eerste jaren van wederopbouw (1940-1950)
Geert-Jan Mellink

nr 369
Factors Promoting a Positive Experienced Neighborhood Public Space--A Virtual Environment-based analysis.
Yuwen Zhao

nr 370
Place quality making in high-speed railway station areas: Devising place quality indicators for urban design, beyond the transport-land use divide
Jinglun Du

nr 371
Sustainable Bio-based Adsorptive Concrete for Phosphorus Removal
Fan Wu

nr 372
The physical workplace as a resource for mental health: A salutogenic approach to a mentally healthy workplace design at home and at the office
Lisanne Bergefurt

nr 373
High-end application of basic oxygen furnace steel slag as sustainable building materials
Muhammad Jawad Ahmed

nr 374
Energy-Efficient Urban Rail Transit Operations: Models, Algorithms, and Applications
Kang Huang

nr 375
Household Energy Efficiency Adoption: Influencing Factors and Diffusion Interventions
Hua Du

nr 376
High-temperature resistant geopolymer-based materials out of industrial residuals.
Yan Luo

nr 377
A Simulation Approach Exploring the Impacts of Land Use Variables on Travel Behavior.
Xiaoming Lyu

nr 378
Understanding and modelling individual preferences for Mobility as a Service
Valeria Caiati

nr 379
Linking the physical and digital built environment - Enabling occupant-centric decision-making using cross-domain semantic digital twins
Alex Donkers

nr 380
Indoor Air Quality in Daycare Centers: Assessing and Mitigating Indoor Exposure on Young Children
Hailin Zheng

nr 381
A Data-Driven Approach to Understanding Visitors' Behavior to Reduce the Negative Effects of Tourism in Historical Cities
Sezi Karayazi

nr 382
Wind effects on internal depressurization for asbestos abatement
Anjali Radhakrishnan Jayakumari

nr 383
Spatiotemporal Graph Convolutional Neural Network for Robust and Accurate Traffic Flow Prediction
Yutian Liu

nr 384
Photo-responsive functional aluminosilicate cementitious materials - Design, Performance and Durability
Daoru Liu

nr 385
High-end applications of basic oxygen furnace slag as a cementitious binder. Phase Assemblage, Mechanical & Chemical Activation, Composites Application
Winnie Franco Santos

nr 386
Towards improved performance modelling of distributed PV systems in the built environment
Bin Meng

nr 387
Development of sustainable insulation materials. Design, performance and applications
Alex Koh Chuen Hon

nr 388
Simulations of Sandwich Panel Systems under Fire: Two-Scale Methods for Connections, Pyrolysis for Insulation, Experimental Validations
Qingfeng Xu

nr 389
Long-term Mechanical Performance of the Flax Fiber Reinforced Polymer Composites Considering the Environmental Effects
Bowen Xu

nr 390
Quality engineering and control for digital fabrication with concrete
Derk Bos

nr 391
Structural Engineering of 3D Printed Strain Hardening Cementitious Composites. From micro-scale analysis to application
Karsten Nefs

nr 392
Children's Outdoor Play in the Digital Age; The Role of Digital Interventions in Stimulating Children's Outdoor Play Behavior
Avin Khalilollahi

nr 393
Biophilic design and integrating nature in architecture: Guidelines for three-dimensional green spaces to innovate architectural typologies and create impact for sustainability
Weijie Zhong

nr 394
Crafting Smart Homes: Innovative Design Strategies to Enhance Housing Quality for Ageing Well
Chuan Ma

Developing building composites that are both sustainable and high-performance is crucial for the construction industry. This work focuses on the valorization of natural fibers (i.e. plant-based) as well as Municipal Solid Waste Incineration (MSWI) bottom ash. The thesis starts with providing potential solutions such as fiber modification to technical barriers when utilizing natural fibers in cementitious composites (e.g., interface property and durability). Then, bio-based composites without cementitious binders for thermal insulation applications are studied and a potential approach to enhance their durability is proposed. Furthermore, recycling MSWI bottom ash in building materials such as supplementary cementitious materials, synthesized lightweight aggregates, and sand substitutes is investigated with emphasis on their mechanical strength and environmental aspects. A method with natural fiber incorporation is proposed to enhance these properties. Overall, this thesis aims to develop cost-effective and eco-friendly strategies to address key challenges in recycling natural fibers and MSWI bottom ash for building composites, promoting their practical application.

DEPARTMENT OF THE BUILT ENVIRONMENT

TU/e EINDHOVEN UNIVERSITY OF TECHNOLOGY